

Planet-hosting cool stars: constraining M dwarf properties with visible and infrared spectra

A DISSERTATION SUBMITTED TO THE GRADUATE DIVISION OF THE
UNIVERSITY OF HAWAII AT MĀNOA IN PARTIAL FULFILLMENT OF THE
REQUIREMENTS FOR THE DEGREE OF

DOCTOR OF PHILOSOPHY
IN
ASTRONOMY

July 9, 2013

By
Andrew Withycombe Mann

Dissertation Committee:

Eric Gaidos, Chairperson
J. Patrick Henry
John Rayner
Nader Haghighipour
Edward R. D. Scott

© Copyright 2013
by
Andrew W. Mann
All Rights Reserved

To my parents, Donald and Linda Mann.

Acknowledgements

No one does a thesis alone, and this work is no different. Special thanks goes to my mentor, Eric Gaidos, who has provided the time, resources, advice, funding, and assistance to make this work possible. In particular, without his thick layer of red ink on every manuscript I've written, it's likely that my research would not have had the impact it has, as most of my early manuscript drafts were only marginally intelligible. I feel my growth as a scientist is mostly due to his guidance over the course of my thesis.

Thanks to the members of my thesis committee: Eric Gaidos, John Rayner, Nader Haghhipour, Pat Henry, and Ed Scott, for coming to meetings on time, listening attentively, and providing sage advice.

Financial support for this work was provided by NSF grant AST-0908419, NASA grants NNX10AI90G and NNX11AC33G (Origins of Solar Systems) to Eric Gaidos, US Department of Energy contract DE-AC02-05CH11231 to Greg Aldering, as well as as well as NSF grants AST 06-07757 and AST 09-08419 to Sebastien Lepine.

Thanks to Nadine Manset at the Canada-France-Hawaii Telescope (CFHT) for her management of the queue observations. The CFHT is operated by the National Research Council of Canada, the Institut National des Sciences de l'Univers of the Centre National de la Recherche Scientifique of France, and the University of Hawaii.

Some of the data presented in this thesis were obtained from the Multimission Archive at the Space Telescope Science Institute (MAST). STScI is operated by the Association of Universities for Research in Astronomy, Inc., under NASA contract NAS5-26555. Support for MAST for non-HST data is provided by the NASA Office of Space Science via grant NNX09AF08G and by other grants and contracts.

Thanks to Greg Aldering for his support of the SuperNova Integral Field Spectrograph (SNIFS). SNIFS on the UH 2.2-m telescope is part of the Nearby Supernova Factory project, a scientific collaboration among the Centre de Recherche Astronomique de Lyon, Institut de Physique Nucléaire de Lyon, Laboratoire de Physique Nucléaire et des Hautes Energies, Lawrence Berkeley National Laboratory, Yale University, University of Bonn, Max Planck Institute for Astrophysics, Tsinghua Center for Astrophysics, and the Centre de Physique des Particules de Marseille.

Thanks to the regular attendees of writing session; Jenny Shih, Geoff Matthews, Chao-Ling Hung, Kelly Lockhart, and William Best, for providing a productive workspace. On the opposite end, thanks to my officemates; Zach Gazak, Lauren Stephenson, and Ryan Swindle, for keeping me from working too hard.

Special thanks to Kirsten Larson and Jenny Shih for being generally entertaining friends.

This work would not have been possible with the large amount of IRTF and UH2.2m time, both from the IfA TAC, and also engineering time from Alan Tokunaga, John Rayner, Mark Willman, and Colin Aspin, and the IRTF and UH2.2m TOs and support staff.

This thesis relied heavily on data from the Infrared Telescope Facility (IRTF). The IRTF is operated by the University of Hawaii under Cooperative Agreement no. NNX-08AE38A with the National Aeronautics and Space Administration, Science Mission Directorate, Planetary Astronomy Program.

This thesis includes data collected by the Kepler mission. Funding for the Kepler mission is provided by the NASA Science Mission Directorate.

I also owe a great deal to Phil Muirhead and Adam Kraus, who recognized my work early on in my thesis and made me more confident about my skills as a researcher. Their career and life advise proved to be just as almost as important as the science advise I got from collaborators. Thanks to Mike Liu, Andrew Howard, and the rest of the low-mass group at IfA, for giving me a place to bounce of ideas, and forcing me to give regular talks on my research. Thanks to Sebastien Lepine and John Brewer for their useful comments on my manuscripts.

Thanks to _____ (left blank to represent all the people I forgot to thank).

Thanks most of all to Chao-Ling, for putting up with late nights observing, long work hours, and my generally busy schedule.

Abstract

M dwarfs have become attractive targets for exoplanet searches. Smaller planets can be detected around stars with smaller radii (via the transit technique) or lower mass (via the radial velocity technique). Planets in the habitable zone of an M dwarf are closer in, and thus easier to detect, than those orbiting in the habitable zone of Solar-type stars. However, studying M dwarfs is difficult due to their intrinsic faintness and poorly established stellar parameters (radius, metallicity, etc.). For this dissertation I have worked to mitigate these problems with the goals of finding new transiting planets and establishing the role of stellar metallicity on the size and occurrence of transiting planets around M dwarfs.

I describe a new approach to search for planetary transits around M dwarfs by slewing between targets several degrees apart on the sky. This method improves the efficiency of transit searches by enabling one to monitor multiple, separated, M dwarfs simultaneously from the ground.

I show that the bright, late-type stars targeted by the *Kepler* spacecraft are predominately misclassified or unclassified giant stars. The level of giant star contamination has a significant impact on the metallicity distribution of the *Kepler* M star sample as well as the calculated planet occurrence.

I significantly improve on techniques to measure M dwarf metallicities. Using wide binaries with a Solar-type primary and an M dwarf companion as calibrator stars, I perform an unbiased search for metal-sensitive features in visible and near-infrared spectra. This yields a list of spectral lines (or regions) that I then use to develop a series empirical calibrations (valid over different wavelength regimes) of M dwarf metallicities accurate to better than 0.1 dex.

Lastly, I apply this technique to *Kepler* late K and M dwarf targets and planet hosts. I find that late-type stars hosting Neptune-sized and smaller planets have a metallicity distribution indistinguishable from that of the sample with no detected planets. This suggests that planet formation must be efficient in collecting material from the disk, or that disk masses for M dwarfs are more massive than basic scaling would suggest.

Table of Contents

Acknowledgements	iv
Abstract	vi
List of Tables	ix
List of Figures	x
Chapter 1: Introduction	1
1.1 Transiting Planets	1
1.2 The Planet-Metallicity correlation	2
1.3 M Dwarfs: promises and perils	3
1.4 Kepler	5
1.5 This Study	6
Chapter 2: Ground-Based Submillimagnitude CCD Photometry of Bright Stars Using Snapshot Observations	13
2.1 Introduction	13
2.2 Observations	16
2.3 Sources of Noise	18
2.3.1 Scintillation Noise	20
2.3.2 Extinction	21
2.3.3 Short-Term Atmospheric Transparency Variations	22
2.3.4 Detector Noise	25
2.4 Strategies to Minimize Noise	28
2.4.1 CCD Regions and Signal Levels	28
2.4.2 Choice of Filter	31
2.4.3 Degree of Defocusing	33
2.4.4 Integration time	35
2.4.5 Choice of Comparison Star	35
2.5 Comparison to Observations	37
2.5.1 Total Errors	37
2.5.2 Correlated (Red) Noise	39
2.6 Discussion	41
2.6.1 Methods of Submillimagnitude Photometry	41
2.6.2 Performance of a Hypothetical Transit Search	42
Chapter 3: They might be giants: luminosity class, planet occurrence, and planet-metallicity relation of the coolest <i>Kepler</i> target stars	53

3.1	Introduction	53
3.2	Sample, Observations, and Reduction	56
3.3	Luminosity Class	67
3.3.1	Training Sets	67
3.3.2	Spectroscopic Determination of Luminosity Class	68
3.3.3	Photometric Determination of Luminosity Class	70
3.3.4	Application of training sets to the <i>Kepler</i> sample	70
3.3.5	Giant Star Fraction	75
3.4	Planet occurrence	75
3.4.1	Nonparametric Estimation	75
3.4.2	Parametric Likelihood estimation	78
3.5	Planet-host Metallicities	80
3.6	Discussion	81
Chapter 4: Prospecting in late-type dwarfs:		
	a calibration of infrared and visible spectroscopic metallicities of late-K and M dwarfs spanning 1.5 dex	93
4.1	Introduction	94
4.2	Sample	95
4.3	Observations and Reduction	99
4.3.1	ESPaDOnS/CFHT	99
4.3.2	SpeX/IRTF	99
4.3.3	SNIFS/UH2.2m	100
4.3.4	Construction of a combined M dwarf Spectrum	100
4.4	Deriving Stellar Parameters	101
4.4.1	FGK Metallicities	101
4.4.2	Late-K/M Dwarf Spectral Types	105
4.5	Identifying Metal-Sensitive Indices	105
4.6	Determination of M dwarf Metallicities	110
4.7	Assessing and Recalibrating Existing Techniques	116
4.7.1	$\zeta_{\text{TiO/CaH}}$	116
4.7.2	$J - K$ Metallicities	120
4.7.3	K -band Metallicities	121
4.7.4	H -band Metallicities	121
4.8	Summary and Discussion	122
Chapter 5: Testing the Metal of Late-Type Kepler Planet Hosts with Iron-Clad Methods		132
5.1	Introduction	132
5.2	Sample	135
5.2.1	KOI Sample	135
5.2.2	<i>Kepler</i> Non-KOI Sample	135
5.3	Observations And Reduction	137
5.4	Determination of [Fe/H] and R_*	137
5.5	Results	146
5.6	Discussion	148
Chapter 6: Conclusions		158
6.1	Summary	158

6.2 Future Outlook	159
------------------------------	-----

List of Tables

2.1	Observing Conditions	18
2.2	Photometry Experiments	20
2.3	Estimated Error/Noise Budget	37
3.1	Parameters of Observed <i>Kepler</i> Targets	59
3.1	Parameters of Observed <i>Kepler</i> Targets	60
3.1	Parameters of Observed <i>Kepler</i> Targets	61
3.1	Parameters of Observed <i>Kepler</i> Targets	62
3.1	Parameters of Observed <i>Kepler</i> Targets	63
3.1	Parameters of Observed <i>Kepler</i> Targets	64
3.1	Parameters of Observed <i>Kepler</i> Targets	65
3.1	Parameters of Observed <i>Kepler</i> Targets	66
3.2	Definitions of Spectroscopic Indices	68
4.1	Wide Binary Sample	97
4.1	Wide Binary Sample	98
4.1	Wide Binary Sample	99
4.2	Parameters of Primary Stars observed at CFHT	102
4.3	Corrections Applied to Primary Star Metallicities	103
4.4	Continuum Regions Used	108
4.5	Metal-sensitive Features	111
4.5	Metal-sensitive Features	113
4.6	Metallicity Calibration Statistics	116
4.7	Assessment of Previous Metallicity Indicators	116
4.8	Stars Observed from Woolf et al. (2009)	119
5.1	KOI Stellar Parameters	140
5.1	KOI Stellar Parameters	141
5.2	non-KOI Stellar Parameters	142
5.2	non-KOI Stellar Parameters	144
5.3	Summary of Metallicity Distributions	147

List of Figures

2.1	Theoretical normalized light curves of stars transited by planets on 4 day orbits, compared with the photometric precision obtained from space - <i>Kepler</i> 30 minute (Jenkins et al. 2010) and COROT (Aigrain et al. 2009) - and a practical limit from the ground (5×10^{-4}). Limb darkening is included as described in Claret (2000). A stellar mass-radius relation $R_* \sim M_*^{1.06}$ (appropriate for M dwarfs) is used. Ground-based photometry can be sufficiently stable to detect and characterize super-Earth- to Neptune sizes planets around M dwarf stars.	15
2.2	Aitoff projection of trajectory of telescope pointings for constellation observations, designed to minimize slew time. The circle is approximately the size of the full Moon. Although a given target is usually several degrees away from the next target, the slew time is not significantly longer than the readout time (~ 20 s). The constellation technique enabled us to concurrently search for transits around eight target stars.	19
2.3	Approximate transmission (bottom) and emission (top) of the atmosphere on a clear night over Mauna Kea with B , SDSS g , SDSS r , SDSS i , SDSS z , and narrow z filters multiplied by the SNIFS CCD quantum efficiency. There is a discontinuity at ~ 5200 Å in the emission caused by low QE near the edge of the blue and red channels of the SNIFS integral field unit. Our observations were taken predominantly in SDSS z , although some were taken in SDSS r . Scattering affects the filters blueward of 5500 Å whereas molecular (chiefly H ₂ O and O ₂) absorption lines contaminate the r and z passbands. A narrow z filter (J. Johnson, private communication) can mitigate errors from both molecular absorption and scattering.	23
2.4	Photometric error in observations with the SDSS r (top left), SDSS z (top right), B (bottom left), and narrow z filters produced by a difference in spectral type between comparison and target star as a function of airmass (both using the SNIFS detector). The target star has an effective temperature of 4000 K and $\log g = 4.5$	24

2.5	Fractional error as a function of rms image motion within a bad region (high pixel response variation), a good region (low pixel response variation), and at the center of the SNIFS science-grade imaging detector. These curves were generated by taking a defocused image and shifting it around a map of the detector response produced from a series of ~ 225 flats taken with varying exposure times through the SDSS r (top) and SDSS z (bottom) filters. Nonfilled points are for a pixel response map with a flat-field correction (median of 10 twilight flats). We assume no changes within the defocused PSF except position on the detector. Note that the good/bad regions used are comprised of different sets of pixels for the two different filters used.	27
2.6	<i>Top:</i> Mean of eight defocused images of a $V = 13$ star, each with an integration time of 30 s. <i>Bottom:</i> Standard deviation of pixel values from the mean. All images have the same spatial scale ($\sim 8''$ on a side), but not the same intensity scale. The highest peak in the PSF is due to coma in the UH 2.2 m optics (C. Aspin, private communication 2010; Behr 1973).	29
2.7	Histogram of the χ^2 values of a fit to pairs of individual pixel values vs. median detector values in a series of 150 dome flats. The theoretical distribution derived from a Monte Carlo analysis (based on Poisson statistics) is shown as a dashed line. We only include data from the bottom half of the SNIFS imaging science-grade detector (the region we use for transit imaging). We consider pixels with $\chi^2 > 240$ as poorly behaved and worth avoiding. These represent $\lesssim 0.1\%$ of the total number of pixels.	30
2.8	Comparison of photometric precision with and without flat-fielding. Dome flats are used when there is an insufficient quantity of high-S/N twilight flats from a given night. Although in some cases the precision is better with flats, on average, the precision is better without flat-fielding.	32
2.9	Curve of growth (vs. radius in arcseconds) of the mean of eight defocused images of a star obtained with the SNIFS/UH 2.2 m (solid line), and the S/N in an aperture of a given radius relative to the maximum value (dotted line).	34
2.10	Total predicted noise as a function of exposure time (<i>top left</i>) for a $m_z = 9$ star. Also shown is the total noise (<i>top right</i>), optimal defocus radius (<i>bottom right</i>), and exposure time (<i>bottom left</i>), corresponding to the setup with the lowest theoretical noise as a function of z magnitude. We perform these calculations based on noise from Poisson statistics, read and electronic pickup noise, scintillation, sky background, and atmospheric transparency fluctuations. We have assumed 1.5 minutes for readout and slew time between stars and that the comparison and target star are of identical flux and spectral type. Note that for our stars (mostly late K and early M dwarfs) $V - z \sim 1.8$ (Covey et al. 2007).	36

2.11 Light curves of eight stars using the constellation method along with rms using a reference signal constructed from stars observed immediately before and after the target (left), and from all seven other target stars (right). Cadence for these observations is ~ 1 observation every 17 minutes, which is sufficient to sample a transit (transits typically last $\gtrsim 1$ hr). All light curves were normalized to 1, and then each was offset in increments of 0.01 for plotting. Although using more comparison stars improves the S/N, we achieve the best overall photometric precision for each target star using a reference signal built from the stars observed immediately after and before it.	38
2.12 Precision of each of our observations vs. our estimated theoretical precision calculated for each observation. The dashed line marks where observed precision matches theoretical precision.	40
2.13 Average number of photometric observing nights before a transit is detected in a snapshot survey of M dwarf stars with a Doppler signal above the specified threshold. In making this calculation, we take into account setup, slew, twilight, and integration time, and we use precision levels attained in our SNIFS observations. A planet population similar to those around G-type stars is assumed (see Section 2.6.2 for details)	45
3.1 <i>Kepler</i> magnitude vs. $J - H$ color for Quarter 0-2 <i>Kepler</i> target stars with $K_P - J > 2$ (grey circles), KOIs (black stars), and targets with spectra from this program (red circles). Our observing bins (see Section 3.2) are marked by blue lines. There is a clear difference between the colors of bright ($K_P < 14$) and dim ($K_P > 14$) <i>Kepler</i> target stars, resulting in a very different distribution of colors. The great majority of KOIs are faint, and have bluer $J - H$ colors. For this reason we divide the sample into $J - H$ bins, and treat bright ($K_P < 14$) and dim ($K_P > 14$) <i>Kepler</i> target stars as two independent samples.	57
3.2 Distribution of KIC effective temperatures and $K_P - J$ colors for target stars (grey circles and grey solid histogram) and KOIs (black stars and black dashed histogram). The bulk of the stars in our spectroscopic sample are M dwarfs ($T_{eff} < 4000 K$) if we assume KIC T_{eff} values are accurate. Histograms for KOIs and observe targets offset slightly from each other for clarity (although the bins for each sample are the same). Note that not all stars have effective temperatures listed in the KIC; points lacking T_{eff} values are not shown in the center plot or bottom histogram, but are included in the $K_P - J$ histogram.	58

3.3	SNIFS spectra of an M dwarf (top) and M giant (bottom) of similar T_{eff} ($\simeq 3600$ K) and magnitude ($K_P \simeq 14$). Approximate regions for each of the six indices we use for giant/dwarf discrimination, as well as the TiO5 band, are marked in grey. B 1 refers to a mix of atomic lines (Ba II, Fe I, Mn I, and Ti I) which overlap at the resolution of SNIFS ($\simeq 1300$). The TiO5 molecular band is used as a probe of spectral type, although it is also sensitive to metallicity (Lépine et al. 2007). Other atomic and molecular lines are generally much weaker in late type giant stars (Reid & Hawley 2005). Indeed, the Na I (8172-8197Å) and K I (7669-7705Å) doublets are significantly weaker in the giant spectrum while they are both quite strong in the dwarf.	69
3.4	Measured strengths of each gravity-sensitive spectral feature vs. the strength of the TiO5 band for <i>Kepler</i> late-type target stars with spectra from this program. Bright ($K_P < 14$) targets are shown as red colored circles while faint ($K_P > 14$) observed targets are shown as blue colored circles. The two-dimensional PDFs defined by our training set of giants (dashed line) and dwarfs (solid line) are overlaid. Contours of the PDF correspond to 68%, and 90%, intervals for the given training set. By using all spectral features, we positively identify each star with spectra as a giant or a dwarf with $> 99\%$ certainty.	71
3.5	Similar to Figure 3.4 except using gravity-sensitive color-color relations. Each dot corresponds to a bright (red) or faint (blue) late-type <i>Kepler</i> target star. Contours are shown for the two training sets, corresponding to 68 and 90% PDF intervals. We apply this cut to <i>Kepler</i> target stars with $J - H > 0.52$ or $K_P - J > 2.0$, although only a subsample of this set is shown for clarity. Most stars fall well inside either the dwarf or giant sequence, however, even when all color relations are used, $\simeq 3\%$ of the sample still have an ambiguous luminosity class assignments. Most of these stars lack photometry in one or more band.	72
3.6	Weights for each of the color relations used for our photometric determination of luminosity class. Weights are determined by applying the giant and dwarf PDFs derived from half of the training set to the other half (after adding Poisson noise to the data). Weights are set to 0 for all X outside of our training sets. Weights tend to be low in regions where the giant and dwarf training set PDFs overlap, or in regions where data is sparse.	74
3.7	Effective temperatures computed by fitting our spectra to models from the BT-SETTL version of PHOENIX (Allard et al. 2011) as a function of the KIC assigned effective temperature for giants (left) and dwarfs (right). The dotted line indicates equality. Errors are estimated as part of our model fitting procedure (errors on KIC temperatures are taken to be 135 K (Brown et al. 2011). For both giants and dwarfs there is a clear 100-200 K offset between our spectroscopically determined temperatures and the KIC temperatures. This is most likely a consequence of the models used, as Castelli & Kurucz (2004) models used to fit KIC photometry to effective temperatures are unreliable below 4000 K.	77

3.8	Planet occurrence with giant stars removed (solid line) or using KIC $\log g > 4.0$, using isochrones from DSEP (black) or from Yonsei-Yale (red) calculated by Monte Carlo analysis. The left plot is calculated using nonparametric MC estimate, and the right uses a parametric MC estimate. For both plots, we consider planets with radii $2R_{\oplus} < R_P < 32_{\oplus}$ and periods $P < 50$ days, and stars with effective temperatures $3400 < T_{eff} < 4100$. A full description of our analysis is given in Section 3.4.	80
3.9	Median $g - r$ colors as a function of $J - H$ colors for <i>Kepler</i> target stars with: Earth to Neptune sized planet candidates (dotted/dashed line, diamonds), KIC $\log g > 4.0$ (solid line, asterisks), $> 90\%$ likelihood of being dwarfs based on their colors (dotted line, triangles), $> 90\%$ likelihood of being giants (dashed line, circles). The 1σ errors are calculated for the median in each bin by bootstrap resampling. Bins for all data sets are the same, but each point is offset slightly from the bin center for clarity. There is a statistically significant offset between the KIC $\log g > 4.0$ sample and the planet hosts when we consider stars with $0.58 < J - H < 0.66$, however, this offset is no longer present when misidentified giant stars are removed from the sample. Indeed, our dwarf control sample closely tracks the colors of the planet-hosting stellar population.	82
3.10	Scatter plot of a sample of <i>Kepler</i> dwarf stars (blue triangles), giant stars (red circles), and giant stars labeled as dwarfs (KIC $\log g > 4.0$) by the KIC (black crosses) in $g - r$ vs $J - H$ space. An equal number of data points are shown from each subset (giants/dwarfs/misidentified giants) to highlight the <i>relative</i> distributions. The histograms on the bottom and right side show the 1-D distribution in each color (coloring matches the center plot). Histograms are normalized to a peak value of 1 and the median of each histogram is marked with a dotted line (of the corresponding color). Although giant stars cover a range of $J - H$ colors, those that were mislabeled as dwarfs are more concentrated around $J - H \simeq 0.61$. The distribution of misidentified giants is bluer than the dwarf distribution. Thus if the misidentified giant stars are not properly removed the dwarf sample will appear bluer (more metal poor) than the KOI distribution (which contains almost no misidentified giants).	83
4.1	Comparison of metallicities from Ramírez et al. (2007) and those from SPOCS (Valenti & Fischer 2005) for the 112 stars present in both samples. The [Fe/H] values are quite consistent once corrected for a systematic offset of 0.08 dex. The remaining scatter is only $\simeq 0.06$ dex. Assuming SPOCS [Fe/H] values are accurate to 0.03 dex, this implies [Fe/H] metallicities from Ramírez et al. (2007) are accurate to $\simeq 0.05$ dex. We perform a similar analysis for all other metallicity sources (see Table 4.3).	104

4.2	Spectral types derived from the H ₂ O-K2 index (RA12) vs. those derived from TiO and CaH indices at visible wavelengths. The dashed line indicates a perfect agreement and typical errors are shown in the bottom right of the plot. For spectral types later than M1 the different techniques agree, but for earlier-type stars the H ₂ O-K2 index tends to return a later spectral type than visible wavelength indices.	106
4.3	Results of our systematic search to find the features that best correlate with [Fe/H] in late-K or M dwarf spectra. Feature centers (shown on the X axis) and widths are changed incrementally covering a range of widths (20 Å to 100 Å) and feature centers (0.35 μm to 2.4 μm). Red points indicate the R _{rand} ² values derived from randomly reassigning primary star metallicities and repeating our process 1000 times (the 99.9% highest resulting R _{ap} ² values are shown). In this particular analysis, we fit for [Fe/H], and fit the pseudo-continuum using just the continuum regions immediately blueward and redward of a given feature. A range of feature widths are shown, which results in some range to the distribution for a given central wavelength. Although there are > 400,000 unique combinations of feature center and width, only 15,000 are shown for simplicity.	109
4.4	Distribution of R _{ap} ² values as a function of feature center and width for the K-band (left) and red end of the visible wavelengths (right). The visible wavelength distribution is based on our analysis using just K5.5–M2 dwarfs. Data points which do not have R _{ap} ² > R _{rand} ² are white (i.e. not shown). Surprisingly, there is not much change in R _{ap} ² as a function of the selected width for a given feature in the K-band, however we do see a trend towards smaller widths in the visible wavelengths.	112
4.5	Metallicity for the primary star vs. derived metallicity of the late K or M dwarf companion based on Equations (4.8)-(4.17). Calibrations for [Fe/H] are shown on the left plots, while those for [M/H] are shown on the right plots. Statistics on the quality of the fit can be found in Table 4.6. Y axis error bars shown are based on 1 σ Gaussian errors for the primary star metallicity (see Section 4.4.1). Error bars for the K/M dwarf metallicity are the 1 σ standard deviation of 1000 recalculations of the K/M dwarf metallicity after adding noise to each spectrum consistent with its S/N.	115
4.6	Metallicity of the primary star ([Fe/H] to the left and [M/H] to the right) vs. the ζ parameter as defined by Lépine et al. (2007) and using the calibration of Lépine et al. (2013). It has been shown that the effectiveness of ζ varies as a function of spectral type, so we break up our sample into four spectral type ranges in the plot. The best-fit lines from Equations 4.25 and 4.25 are shown as dotted lines. We add in a sample of 22 stars from Woolf et al. (2009, open symbols) to our own wide binary sample (filled points). Our measurements of ζ do accurately identify metal-poor stars identified in Woolf et al. (2009), however, ζ only identifies one of our wide binary stars as a subdwarf.	118

5.1 Distribution of reduced proper motions for spectroscopically confirmed late K and M giants (black) and dwarfs (grey, hashed) from Mann et al. (2012). Stars with questionable proper motions (error in proper motion > 25 mas yr^{-1}) were excluded. We utilized a reduced proper motion cut of $H_J > 7.5$ (shown as a vertical dashed line) to remove interloping giant stars from our non-KOI sample.	136
5.2 Metallicity of the primary (FGK) dwarf from M13 vs. metallicity for the late K or M dwarf companion derived using Equation 5.2. The dashed line indicates equality. The binary sample covers the full range of metallicities and spectral types in our KOI and non-KOI sample.	138
5.3 Metallicities from Muirhead et al. (2012a) (top) or from Dressing & Charbonneau (2013) (bottom) as a function of those derived from our own program. The dashed lines indicate equality. We have added artificial scatter ($\simeq 0.01$ dex) to metallicities from Dressing & Charbonneau (2013) for clarity. Typical errors are shown in the bottom right of each plot. Note that Muirhead et al. (2012a) use [M/H] instead of [Fe/H]. Our metallicities are mostly within 1σ (reduced $\chi^2 \simeq 1$) of those from Muirhead et al. (2012a), with the exception of those with $[\text{Fe}/\text{H}] < -0.3$ which are more discrepant. Our [Fe/H] values greatly differ (reduced $\chi^2 > 3$) from those of Dressing & Charbonneau (2013).145	
5.4 Metallicity distribution of <i>Kepler</i> late K and M targets with no detected transit (black), Earth-sized KOIs ($R_P < 2R_{\oplus}$, magenta-grey dashed), Neptune sized KOIs ($2R_{\oplus} < R_P < 8R_{\oplus}$, blue), and Jupiter-sized KOIs ($8R_{\oplus} < R_P$, red, hashed). Bin sizes and locations are identical for all distributions, but the histograms are slightly offset for clarity. Arrows above the plot indicate the median of each distribution. Note that the black and blue arrows are nearly overlapping. For multi-planet systems we use the radius of the largest detected planet in the system.	146
5.5 Left: median $g - r$ colors of the metal-rich (blue) and metal-poor (red) samples of <i>Kepler</i> dwarfs for three $J - H$ color bins centered at 0.575, 0.625, and 0.675. Bin sizes and locations are identical for all distributions, but are slightly offset for clarity. The scatter in $g - r$ colors for a given metallicity range and $J - H$ bin are determined through bootstrap resampling. For all three $J - H$ bins, the two metallicity groups are indistinguishable at 2σ . Right: [Fe/H] vs. $g - r$ for two different $J - H$ bins, with the best-fit line shown. For both bins, the best fit lines are consistent with a slope of 0, and yield coefficients of determination (R^2) of 0.01 and 0.07, respectively. An F-test detects no significant improvement from the regression for either bin. Thus no significant correlation between $g - r$ vs. $J - H$ and [Fe/H] is found. 150	

Chapter 1

Introduction

After more than a century of effort, astronomers finally discovered the first extrasolar planets in late 1995 (e.g., Mayor & Queloz 1995). Surprisingly, the first planets discovered were very different from what we see in our Solar System. Although there were some discovered planets with similar orbital periods and eccentricities to Jupiter (e.g., Butler & Marcy 1996), most of the first $\simeq 30$ detected extrasolar planets had short orbital periods (< 10 days) and masses \gtrsim Jupiter, or were further out but with eccentricities $\gtrsim 0.2$ (Butler et al. 2004a). It is now understood that the close-in “hot-Jupiter” planets are present around only $\simeq 1\%$ of Solar-type stars (Marcy et al. 2005), but were the first discovered because of significant detection bias.

The first extrasolar planets were discovered through the radial velocity (RV) technique, which works by measuring the relative Doppler shift of the stellar spectrum due to the gravitational interaction between the star and planet. The amplitude of the observed Doppler shift, K , is larger (and hence easier to detect) for more massive planets ($K \propto M_P \sin(i)$, where i is the planet’s inclination with respect to our line of sight, and M_P is the planet’s mass) and smaller semi-major axes ($K \propto a^{-1/2}$, where a is the semi-major axis). Thus RV planet surveys tend to find planets that are massive, and close to their parent star.

1.1 Transiting Planets

Charbonneau et al. (2000) was the first to report detecting a transiting planet, i.e., a planet that crosses between its parent star and our line of sight. While a planet is transiting, the observed visual brightness of the star drops a small amount proportional to $(R_P/R_*)^2$, where R_P is the planet radius and R_* is the stellar radius. Transit light curves can be used to constrain the orbital inclination i (in fact the mere fact that a transit occurs puts tight limits on i), which, when combined with RV measurements, yields M_P (RV alone only gives lower limits on planet mass due to the $\sin(i)$ term). Planetary mass can then be combined with radius from the transit light curve to calculate such critically important quantities as surface gravity and average planet density. Planet density can provide insight into the planetary composition and interior structure (Seager et al. 2007; Miller & Fortney 2011; Rogers et al. 2011), and enables important tests of planet formation scenarios (Raymond et al. 2005, 2008). this makes transiting planets more scientifically informative than their non-transiting counterparts.

Unfortunately, planets that transit their stars are rare. The probability that a random planet alignment produces a transit $\simeq R_*/a$. Thus for close-in planets ($a < 0.1$) the transit probability will typically be $\sim 5\%$, but for a planet orbiting a Solar-type star at 1 AU, the transit probability is only 0.47%. Their rarity means that transit surveys must target thousands of stars to find just a handful of planets. Such surveys as the Wide Angle Search for Planets (WASP and SuperWASP, Pollacco et al. 2006)), and the Hungarian-made Automated Telescope Network (HAT-Net, Bakos et al. 2004) target hundreds of thousands of stars to find a few dozen transiting planets.

As of mid 2013, the number of confirmed transiting planetary systems was 245¹. This diverse sample has enabled the study of the distribution of planetary radii (and densities when RV measurements are available) across a range of orbital periods (Baraffe et al. 2010; Batygin & Stevenson 2010), and around a diverse sample of stellar hosts (Howard et al. 2012).

Even when a planet it is found to transit, constraining planetary parameters from the light curve is not always straight forward. An accurate planet radius requires a similarly accurate stellar radius. Further, if there are significant degeneracies between light curve observables. For example, transit depth changes as a function of the size of the planet, but also changes as a function of stellar limb-darkening.

Typical transit depths are small; $\sim 1\%$ for gas giants, $\sim 0.1\%$ for Neptune-sized objects, and $\sim 0.01\%$ for Earth-sized planets, assuming a Solar-type star. Measuring such small changes in flux accurately enough to characterize the planet necessitates reducing (or correcting for) sources of photometric error that might otherwise be ignored for all-sky absolute photometry. Error sources such as atmospheric scintillation (Young 1993; Dravins et al. 1997), atmospheric transparency variations (Hill et al. 1994), and noise from the CCD detector (Newberry 1991) all become important when measuring changes in flux of $\ll 1\%$.

Variations in the atmosphere can be mitigated by doing *differential* photometry, i.e., measuring the flux of a given star with respect to one or more comparison stars in the same field of view. This technique has been used to achieve better than 0.1% photometric precision for ground based observations (e.g., Johnson et al. 2009; Southworth et al. 2009), enabling the study of Neptune-sized and larger planets around Solar-type stars and smaller planets around late-type stars (see Section 1.3).

1.2 The Planet-Metallicity correlation

Spectroscopic analyses of nearby planet hosts reveal a strong correlation between the metallicity of stars and the likelihood that they harbor giant planets (Santos et al. 2004; Fischer & Valenti 2005). Gonzalez (1997) first noticed this trend using just 4 detected planets. Gonzalez (1997) argued that if these planets formed outside their current orbits and migrated inward while the star was still young (a scenario suggested by Lin et al. 1996), then most of the disk material between the planet and star could have accreted onto the star in the process. Because the convective region of a Solar-type star is only $\sim 3\%$ of the mass of the star, a small amount of accreted material can lead to a significant increase in the *observed* metallicity of the star.

¹<http://exoplanet.eu/>

However, the planet-metallicity correlation was found to hold for stars hosting giant planets at higher semi-major axes (Santos et al. 2004; Fischer & Valenti 2005), which probably formed in situ. Further, the trend was found even in M dwarfs and evolved stars that host giant planet (Johnson et al. 2010). Both M dwarfs and evolved stars have much larger convective envelopes than their Solar-type counterparts, mitigating any dilution from inward falling planets, suggesting that the metal-enrichment is primordial, rather than an artifact of pollution onto the star.

The metal-enrichment of giant planet hosts is seen in the context of the core accretion theory (Pollack et al. 1996). Under core accretion, a rocky core forms through the coagulation of planetesimals until it is sufficiently massive to accrete a gaseous envelope. Once the core reaches a critical mass ($5\text{--}10M_{\oplus}$, Hubickyj et al. 2005) hydrostatic equilibrium is no longer possible, and a phase of rapid gas accretion occurs. To form a giant planet, runaway accretion must take place in the $\simeq 2\text{--}6$ Myr timescale on which disks are observed to dissipate (Haisch et al. 2001; Evans et al. 2009). Compared to their metal-poor counterparts, metal-rich disks have longer lifetimes (Yasui et al. 2009) and harbor a higher density of solid material compared to lower-metallicity disks. Thus metal-rich stars have more giant planets because planetesimals accrete faster in denser, metal-rich disks, *and* have more time to form giant-planet cores before the gas dissipates (Ida & Lin 2004, 2005a).

Improvements in RV and transit survey precision led to the discovery of Neptune-mass and smaller objects (e.g., McArthur et al. 2004; Butler et al. 2004b; Bonfils et al. 2005). This included a large number of super-Earths (e.g., Charbonneau et al. 2009), which occupy a mass range between Earth and Uranus (Haghjipour 2011). As more Earth- to Neptune-mass objects were discovered, it became clear that unlike gas giants, smaller planets were not significantly more common around metal-rich Solar-type stars (Sousa et al. 2008).

Theory suggested that there should be some point at which metallicity matters, even for small planets (Gonzalez et al. 2001; Johnson & Li 2012). (Johnson & Li 2012) argued that this critical metallicity is $[\text{Fe}/\text{H}]_{\text{crit}} \sim -1.5 + \log(a/1\text{AU})$ for a Solar-type star. Unfortunately, existing RV and transit surveys preferentially target nearby, bright stars. Most stars in the solar neighborhood are near solar metallicity (Casagrande et al. 2011) and thus well above $[\text{Fe}/\text{H}]_{\text{crit}}$ for planet semi-major axes < 10 AU. Although there are a few surveys specifically targeting metal-poor systems (e.g., Sozzetti et al. 2006), they are insensitive (or only weakly sensitive) to Neptune-mass and smaller planets (Sozzetti et al. 2009). Thus, although they can draw conclusions about the role of metallicity on the frequency of giant planets, they can say little about the critical metallicity for the formation of smaller planets.

1.3 M Dwarfs: promises and perils

M dwarfs represent a potential ‘shortcut’ to finding habitable planets. Their small size and mass mean that a planet of equal size, mass, and orbit will be more easily detected (larger transit depth and RV amplitude) around an M dwarf than a Solar-type star. The circumstellar habitable zone, the region around a star within which a planet could support liquid water at the surface, is closer in for M dwarfs than for Solar-type stars, making detection easier. M dwarfs are also much more numerous than solar-type stars, representing more than 70% of the stars in the solar neighborhood (Henry et al. 1994).

M dwarfs offer an opportunity to search for the critical metallicity for planet formation. Williams & Cieza (2011) and Andrews et al. (2013) showed that there is a correlation between stellar mass and the protoplanetary disk mass (albeit with significant scatter). Assuming a correlation between disk mass and disk density, planet formation will be less efficient around an M dwarf than a Solar-type star. Thus the critical metallicity for planet formation will likely be higher around an M dwarf (since the need for material is higher), and thus more easily tested.

M dwarfs may hold the key to testing planet formation models. Johnson et al. (2010) demonstrated that giant planets are less frequent around M dwarfs than Solar-type stars, while Howard et al. (2012) found that small (Neptune-sized and smaller) planets are *more* common around late K and M dwarfs than more massive stars. However, Fressin et al. (2013) found no correlation between the presence of small planets and the mass of the star. The shape and nature of the correlation between stellar mass and planet frequency (for different planet sizes) has implications for planet formation models (Ida & Lin 2005b) and even planet migration models (Lin & Papaloizou 1986). Since M0 to M4 span almost a factor of three in mass, while the entire FGK sequence covers only a factor of $\simeq 2$ in mass, M dwarfs provide additional leverage to test any relation between host star mass and planetary properties.

Although M dwarfs present a great opportunity, they also present a number of challenges. M dwarfs are intrinsically faint, with luminosities $< 8\%$ that of the Sun. In part because of their faintness, M dwarfs were largely ignored in early exoplanet surveys. Most RV and transit surveys work at visible wavelengths, where M dwarfs are > 50 times fainter. Some RV surveys have moved to the near infrared (e.g., Bean et al. 2010; Barrick et al. 2012) where M dwarfs are brighter, but must deal with higher background, sky variability, and telluric lines (Seifahrt et al. 2010; Muirhead et al. 2011).

M dwarf parameters are also difficult to estimate. M dwarf effective temperatures (T_{eff}) can be estimated by comparing their spectral energy distribution or spectrum to atmospheric models (Casagrande et al. 2008; Rojas-Ayala et al. 2012; Lépine et al. 2013). However, there is significantly discrepancy between different techniques (Lépine et al. 2013). Further, there are systematic differences between M dwarf temperatures measured using spectra and those measured for nearby stars, where bolometric fluxes and angular sizes are known (Boyajian et al. 2012; Rojas-Ayala 2013).

Empirical measurements of M dwarf masses and radii from eclipsing binaries and nearby interferometric targets are inconsistent with each other (Torres et al. 2010; Boyajian et al. 2012), possibly due to inflation of tight binaries from increased activity and/or interacting magnetic fields (Kraus et al. 2011). Further, both interferometric and eclipsing binary measurements disagree with stellar models (Dotter et al. 2008; Boyajian et al. 2012). Since planet parameters are tied directly to the stellar parameters (for example, transit depth is $\propto R_P/R_*$), estimating M dwarf masses, radii, and metallicities are critical to understanding their planets.

The presence of diatomic and triatomic molecules and increased number of atomic lines in M dwarf photospheres creates line confusion, complicating measurements of the continuum in their stellar spectra (Mould 1976; Allard et al. 2011). This makes it difficult to estimate their metallicities ([Fe/H] and [M/H]). Instead, many relied on empirical measurements of M dwarf metallicities, such as their position on a color-magnitude diagram

(Schlaufman & Laughlin 2010), and calibrated their technique using wide binaries whose components are assumed to have the same metallicity. Rojas-Ayala et al. (2010) and Terrien et al. (2012) developed a technique to measure M dwarf metallicities using *K*- and *H*-band spectra (respectively). However, these techniques have limited effective range in metallicity and spectral type due to the small number (~ 20) of binary calibrator stars in their samples. A robust study of M dwarf planet host metallicities requires more accurate and versatile methods.

1.4 Kepler

The NASA *Kepler* mission (Borucki et al. 2010) has been monitoring stars since 2009 with the goal of discovering Earth-size planets in the circumstellar habitable zone (a region where liquid water could exist). *Kepler* simultaneously monitors $\simeq 150,000$ stars spanning the mass range from a small sample of O and B type stars to M dwarfs, as well as 5000-10000 evolved stars (Batalha et al. 2010).

Kepler searches for transiting planets around these stars by taking 6 second exposures, which are then added together on the telescope into short-cadence (total time of 54 seconds) or long-cadence (total time of 1626 seconds) data for download (Koch et al. 2010). The majority of the targets are observed in long-cadence mode, while short-cadence is reserved for special targets (e.g., planet hosts, astroseismology targets). *Kepler* is capable of remarkable photometric precision. In long-cadence mode, *Kepler* can measure flux changes of $\lesssim 30$ parts per million (0.003%) for stars $7 < K_P < 10$ (where K_P is the *Kepler* magnitude, which is comparable to *V* for Solar-type stars), and $\lesssim 300$ parts per million (0.03%) for stars $10 < K_P < 14$ (Koch et al. 2010)

Kepler has revolutionized the science of exoplanets by discovering more than 2000 exoplanet candidates (Batalha et al. 2013). It is estimated that $\lesssim 10\%$ of these candidates are false positives (Morton & Johnson 2011) with the exception of candidates with deep transits (Santerne et al. 2012; Colón et al. 2012), which are more likely to be confused with grazing or blended eclipsing binaries. As of early 2013, the *Kepler* planet candidate list represented more than a 4 fold increase in the total number of discovered planets prior to *Kepler*. This sample has enabled the study of exoplanet statistics based on large data sets, including studies of planet occurrence (Howard et al. 2012), multi-planet systems (Fabrycky et al. 2012), and correlations between stellar and planet properties (Buchhave et al. 2012).

Only about 3000 of the *Kepler* target stars are M dwarfs (Batalha et al. 2010), in large part due to the faintness of M dwarfs in the *Kepler* bandpass (similar to *V + R*) and the magnitude limit of the survey. However, as of early 2013, the *Kepler* M dwarf sample included 95 detected transiting planet candidates (Batalha et al. 2013; Dressing & Charbonneau 2013), far more than the number detected from the ground.

Parameters for stars in the *Kepler* field are largely drawn from the *Kepler* Input Catalog (KIC, Brown et al. 2011), which includes *griz* photometry, as well as stellar T_{eff} , [Fe/H], and radius values derived from the available photometry and utilizing the atmospheric models of Castelli & Kurucz (2004) and stellar evolutionary models of Han et al. (2009). Unfortunately, the available colors are degenerate with metallicity, $\log g$ and T_{eff} , resulting in only rough stellar parameters (errors in T_{eff} of 200 K, radius of 30%, and almost completely unconstrained metallicities). The situation is worse for the M dwarfs because

the Castelli & Kurucz (2004) and Han et al. (2009) models are inconsistent with empirical measurements of late K and M dwarfs (Boyajian et al. 2012).

1.5 This Study

Here I describe research aimed at resolving many of the difficulties with M dwarfs discussed above. This work will cover both detection and characterization of planets around bright, nearby, M dwarfs with the goal of studying the M dwarf planet occurrence and the distribution of M dwarf planet host metallicities. In Chapter 2, I discuss the development of the snapshot photometric technique, designed to aid in detecting Neptune-sized and larger planets around M dwarfs by searching multiple stars simultaneously. I go on to describe how searching for transits from the ground requires a precise understanding and careful mitigation of errors that are negligible for absolute photometry.

In Chapter 3, I show that late-type (\simeq K5 and later) stars targeted by the *Kepler* spacecraft are predominantly giant stars, how this finding impacts calculations of late K and M dwarf planet occurrence, and that the high level of giant contamination has led to erroneous conclusions about the metallicity distribution of the *Kepler* target stars.

In Chapter 4, I describe our method to measure late K and M dwarf metallicities using visible and/or NIR spectra. This method is calibrated using wide binaries with a Solar-type primary and a late K or M dwarf companion. I show how our technique significantly improves on previous work by using a larger and more diverse sample, and by systematically searching for all metal-sensitive lines in late K and M dwarf spectra.

In Chapter 5, I discuss how we apply our method to measure M dwarf metallicities to *Kepler* targets. Our results demonstrate that there is no significant correlation between the presence of Neptune-sized and smaller planets and the metallicity of the host star for late K and M dwarfs, consistent with what is seen for FGK dwarfs. I also briefly discuss some theoretical implications of these findings.

I conclude in Chapter 6 by summarizing our work and briefly discussing the future direction of work on characterizing the whole *Kepler* catalog, not just the M dwarfs or planet candidate hosts.

References

- Allard, F., Homeier, D., & Freytag, B. 2011, in Astronomical Society of the Pacific Conference Series, Vol. 448, 16th Cambridge Workshop on Cool Stars, Stellar Systems, and the Sun, ed. C. Johns-Krull, M. K. Browning, & A. A. West, 91
- Andrews, S. M., Rosenfeld, K. A., Kraus, A. L., & Wilner, D. J. 2013, ArXiv e-prints
- Bakos, G., Noyes, R. W., Kovács, G., Stanek, K. Z., Sasselov, D. D., & Domsa, I. 2004, PASP, 116, 266
- Baraffe, I., Chabrier, G., & Barman, T. 2010, Reports on Progress in Physics, 73, 016901
- Barrick, G. A., Vermeulen, T., Baratchart, S., Reshetov, V. A., Wang, S.-Y., Dolon, F., Hernandez, O., Pepe, F., Bouchy, F., Dunn, J., Dupieux, M., Gallou, G., Larrieu, M., Fonteneau, A., Moreau, F., Wildi, F., Parès, L. P., Thomas, J. N., Yan, C.-H., Doyon, R., Donati, J.-F., Vallée, P., Artigau, É., Delfosse, X., Rabou, P., Thibault, S., Kouach, D., & Loop, D. 2012, in Society of Photo-Optical Instrumentation Engineers (SPIE) Conference Series, Vol. 8451, Society of Photo-Optical Instrumentation Engineers (SPIE) Conference Series
- Batalha, N. M., Borucki, W. J., Koch, D. G., Bryson, S. T., Haas, M. R., Brown, T. M., Caldwell, D. A., Hall, J. R., Gilliland, R. L., Latham, D. W., Meibom, S., & Monet, D. G. 2010, ApJ, 713, L109
- Batalha, N. M., Rowe, J. F., Bryson, S. T., Barclay, T., Burke, C. J., Caldwell, D. A., Christiansen, J. L., Mullally, F., Thompson, S. E., Brown, T. M., Dupree, A. K., Fabrycky, D. C., Ford, E. B., Fortney, J. J., Gilliland, R. L., Isaacson, H., Latham, D. W., Marcy, G. W., Quinn, S. N., Ragozzine, D., Shporer, A., Borucki, W. J., Ciardi, D. R., Gautier, III, T. N., Haas, M. R., Jenkins, J. M., Koch, D. G., Lissauer, J. J., Rapin, W., Basri, G. S., Boss, A. P., Buchhave, L. A., Carter, J. A., Charbonneau, D., Christensen-Dalsgaard, J., Clarke, B. D., Cochran, W. D., Demory, B.-O., Desert, J.-M., Devore, E., Doyle, L. R., Esquerdo, G. A., Everett, M., Fressin, F., Geary, J. C., Girouard, F. R., Gould, A., Hall, J. R., Holman, M. J., Howard, A. W., Howell, S. B., Ibrahim, K. A., Kinemuchi, K., Kjeldsen, H., Klaus, T. C., Li, J., Lucas, P. W., Meibom, S., Morris, R. L., Prša, A., Quintana, E., Sanderfer, D. T., Sasselov, D., Seader, S. E., Smith, J. C., Steffen, J. H., Still, M., Stumpe, M. C., Tarter, J. C., Tenenbaum, P., Torres, G., Twicken, J. D., Uddin, K., Van Cleve, J., Walkowicz, L., & Welsh, W. F. 2013, ApJS, 204, 24

- Batygin, K. & Stevenson, D. J. 2010, ApJ, 714, L238
- Bean, J. L., Seifahrt, A., Hartman, H., Nilsson, H., Wiedemann, G., Reiners, A., Dreizler, S., & Henry, T. J. 2010, ApJ, 713, 410
- Bonfils, X., Forveille, T., Delfosse, X., Udry, S., Mayor, M., Perrier, C., Bouchy, F., Pepe, F., Queloz, D., & Bertaux, J.-L. 2005, A&A, 443, L15
- Borucki, W. J., Koch, D., Basri, G., Batalha, N., Brown, T., Caldwell, D., Caldwell, J., Christensen-Dalsgaard, J., Cochran, W. D., DeVore, E., Dunham, E. W., Dupree, A. K., Gautier, T. N., Geary, J. C., Gilliland, R., Gould, A., Howell, S. B., Jenkins, J. M., Kondo, Y., Latham, D. W., Marcy, G. W., Meibom, S., Kjeldsen, H., Lissauer, J. J., Monet, D. G., Morrison, D., Sasselov, D., Tarter, J., Boss, A., Brownlee, D., Owen, T., Buzasi, D., Charbonneau, D., Doyle, L., Fortney, J., Ford, E. B., Holman, M. J., Seager, S., Steffen, J. H., Welsh, W. F., Rowe, J., Anderson, H., Buchhave, L., Ciardi, D., Walkowicz, L., Sherry, W., Horch, E., Isaacson, H., Everett, M. E., Fischer, D., Torres, G., Johnson, J. A., Endl, M., MacQueen, P., Bryson, S. T., Dotson, J., Haas, M., Kolodziejczak, J., Van Cleve, J., Chandrasekaran, H., Twicken, J. D., Quintana, E. V., Clarke, B. D., Allen, C., Li, J., Wu, H., Tenenbaum, P., Verner, E., Bruhwiler, F., Barnes, J., & Prsa, A. 2010, Science, 327, 977
- Boyajian, T. S., von Braun, K., van Belle, G., McAlister, H. A., ten Brummelaar, T. A., Kane, S. R., Muirhead, P. S., Jones, J., White, R., Schaefer, G., Ciardi, D., Henry, T., López-Morales, M., Ridgway, S., Gies, D., Jao, W.-C., Rojas-Ayala, B., Parks, J. R., Sturmann, L., Sturmann, J., Turner, N. H., Farrington, C., Goldfinger, P. J., & Berger, D. H. 2012, ApJ, 757, 112
- Brown, T. M., Latham, D. W., Everett, M. E., & Esquerdo, G. A. 2011, AJ, 142, 112
- Buchhave, L. A., Latham, D. W., Johansen, A., Bizzarro, M., Torres, G., Rowe, J. F., Batalha, N. M., Borucki, W. J., Brugamyer, E., Caldwell, C., Bryson, S. T., Ciardi, D. R., Cochran, W. D., Endl, M., Esquerdo, G. A., Ford, E. B., Geary, J. C., Gilliland, R. L., Hansen, T., Isaacson, H., Laird, J. B., Lucas, P. W., Marcy, G. W., Morse, J. A., Robertson, P., Shporer, A., Stefanik, R. P., Still, M., & Quinn, S. N. 2012, Nature, 486, 375
- Butler, R. P. & Marcy, G. W. 1996, ApJ, 464, L153
- Butler, R. P., Marcy, G. W., Fischer, D. A., Vogt, S. S., Tinney, C. G., Jones, H. R. A., Penny, A. J., & Apps, K. 2004a, in IAU Symposium, Vol. 202, Planetary Systems in the Universe, ed. A. Penny, 3
- Butler, R. P., Vogt, S. S., Marcy, G. W., Fischer, D. A., Wright, J. T., Henry, G. W., Laughlin, G., & Lissauer, J. J. 2004b, ApJ, 617, 580
- Casagrande, L., Flynn, C., & Bessell, M. 2008, MNRAS, 389, 585
- Casagrande, L., Schönrich, R., Asplund, M., Cassisi, S., Ramírez, I., Meléndez, J., Bensby, T., & Feltzing, S. 2011, A&A, 530, A138

- Castelli, F. & Kurucz, R. L. 2004, ArXiv Astrophysics e-prints
- Charbonneau, D., Berta, Z. K., Irwin, J., Burke, C. J., Nutzman, P., Buchhave, L. A., Lovis, C., Bonfils, X., Latham, D. W., Udry, S., Murray-Clay, R. A., Holman, M. J., Falco, E. E., Winn, J. N., Queloz, D., Pepe, F., Mayor, M., Delfosse, X., & Forveille, T. 2009, *Nature*, 462, 891
- Charbonneau, D., Brown, T. M., Latham, D. W., & Mayor, M. 2000, *ApJ*, 529, L45
- Colón, K. D., Ford, E. B., & Morehead, R. C. 2012, ArXiv e-prints
- Dotter, A., Chaboyer, B., Jevremović, D., Kostov, V., Baron, E., & Ferguson, J. W. 2008, *ApJS*, 178, 89
- Dravins, D., Lindegren, L., Mezey, E., & Young, A. T. 1997, *PASP*, 109, 173
- Dressing, C. D. & Charbonneau, D. 2013, *ApJ*, 767, 95
- Evans, N. J., Dunham, M. M., Jørgensen, J. K., Enoch, M. L., Merín, B., van Dishoeck, E. F., Alcalá, J. M., Myers, P. C., Stapelfeldt, K. R., Huard, T. L., Allen, L. E., Harvey, P. M., van Kempen, T., Blake, G. A., Koerner, D. W., Mundy, L. G., Padgett, D. L., & Sargent, A. I. 2009, *ApJS*, 181, 321
- Fabrycky, D. C., Lissauer, J. J., Ragozzine, D., Rowe, J. F., Agol, E., Barclay, T., Batalha, N., Borucki, W., Ciardi, D. R., Ford, E. B., Geary, J. C., Holman, M. J., Jenkins, J. M., Li, J., Morehead, R. C., Shporer, A., Smith, J. C., Steffen, J. H., & Still, M. 2012, ArXiv e-prints
- Fischer, D. A. & Valenti, J. 2005, *ApJ*, 622, 1102
- Fressin, F., Torres, G., Charbonneau, D., Bryson, S. T., Christiansen, J., Dressing, C. D., Jenkins, J. M., Walkowicz, L. M., & Batalha, N. M. 2013, *ApJ*, 766, 81
- Gonzalez, G. 1997, *MNRAS*, 285, 403
- Gonzalez, G., Brownlee, D., & Ward, P. 2001, *Icarus*, 152, 185
- Haghighipour, N. 2011, *Contemporary Physics*, 52, 403
- Haisch, Jr., K. E., Lada, E. A., & Lada, C. J. 2001, *ApJ*, 553, L153
- Han, S.-I., Kim, Y.-C., Lee, Y.-W., Yi, S. K., Kim, D.-G., & Demarque, P. 2009, New Yonsei-Yale (Y^2) Isochrones and Horizontal-Branch Evolutionary Tracks with Helium Enhancements, ed. Richtler, T. & Larsen, S., 33
- Henry, T. J., Kirkpatrick, J. D., & Simons, D. A. 1994, *AJ*, 108, 1437
- Hill, F., Fischer, G., Forgach, S., Grier, J., Leibacher, J. W., Jones, H. P., Jones, P. B., Kupke, R., Stebbins, R. T., & Clay, D. W. 1994, *Sol. Phys.*, 152, 351

- Howard, A. W., Marcy, G. W., Bryson, S. T., Jenkins, J. M., Rowe, J. F., Batalha, N. M., Borucki, W. J., Koch, D. G., Dunham, E. W., Gautier, III, T. N., Van Cleve, J., Cochran, W. D., Latham, D. W., Lissauer, J. J., Torres, G., Brown, T. M., Gilliland, R. L., Buchhave, L. A., Caldwell, D. A., Christensen-Dalsgaard, J., Ciardi, D., Fressin, F., Haas, M. R., Howell, S. B., Kjeldsen, H., Seager, S., Rogers, L., Sasselov, D. D., Steffen, J. H., Basri, G. S., Charbonneau, D., Christiansen, J., Clarke, B., Dupree, A., Fabrycky, D. C., Fischer, D. A., Ford, E. B., Fortney, J. J., Tarter, J., Girouard, F. R., Holman, M. J., Johnson, J. A., Klaus, T. C., Machalek, P., Moorhead, A. V., Morehead, R. C., Ragozzine, D., Tenenbaum, P., Twicken, J. D., Quinn, S. N., Isaacson, H., Shporer, A., Lucas, P. W., Walkowicz, L. M., Welsh, W. F., Boss, A., Devore, E., Gould, A., Smith, J. C., Morris, R. L., Prsa, A., Morton, T. D., Still, M., Thompson, S. E., Mullally, F., Endl, M., & MacQueen, P. J. 2012, ApJS, 201, 15
- Hubickyj, O., Bodenheimer, P., & Lissauer, J. J. 2005, Icarus, 179, 415
- Ida, S. & Lin, D. N. C. 2004, ApJ, 616, 567
- . 2005a, Progress of Theoretical Physics Supplement, 158, 68
- . 2005b, ApJ, 626, 1045
- Johnson, J. A., Aller, K. M., Howard, A. W., & Crepp, J. R. 2010, PASP, 122, 905
- Johnson, J. A., Winn, J. N., Cabrera, N. E., & Carter, J. A. 2009, ApJ, 692, L100
- Johnson, J. L. & Li, H. 2012, ApJ, 751, 81
- Koch, D. G., Borucki, W. J., Basri, G., Batalha, N. M., Brown, T. M., Caldwell, D., Christensen-Dalsgaard, J., Cochran, W. D., DeVore, E., Dunham, E. W., Gautier, III, T. N., Geary, J. C., Gilliland, R. L., Gould, A., Jenkins, J., Kondo, Y., Latham, D. W., Lissauer, J. J., Marcy, G., Monet, D., Sasselov, D., Boss, A., Brownlee, D., Caldwell, J., Dupree, A. K., Howell, S. B., Kjeldsen, H., Meibom, S., Morrison, D., Owen, T., Reitsema, H., Tarter, J., Bryson, S. T., Dotson, J. L., Gazis, P., Haas, M. R., Kolodziejczak, J., Rowe, J. F., Van Cleve, J. E., Allen, C., Chandrasekaran, H., Clarke, B. D., Li, J., Quintana, E. V., Tenenbaum, P., Twicken, J. D., & Wu, H. 2010, ApJ, 713, L79
- Kraus, A. L., Tucker, R. A., Thompson, M. I., Craine, E. R., & Hillenbrand, L. A. 2011, ApJ, 728, 48
- Lépine, S., Hilton, E. J., Mann, A. W., Wilde, M., Rojas-Ayala, B., Cruz, K. L., & Gaidos, E. 2013, AJ, 145, 102
- Lin, D. N. C., Bodenheimer, P., & Richardson, D. C. 1996, Nature, 380, 606
- Lin, D. N. C. & Papaloizou, J. 1986, ApJ, 309, 846
- Marcy, G., Butler, R. P., Fischer, D., Vogt, S., Wright, J. T., Tinney, C. G., & Jones, H. R. A. 2005, Progress of Theoretical Physics Supplement, 158, 24
- Mayor, M. & Queloz, D. 1995, Nature, 378, 355

- McArthur, B. E., Endl, M., Cochran, W. D., Benedict, G. F., Fischer, D. A., Marcy, G. W., Butler, R. P., Naef, D., Mayor, M., Queloz, D., Udry, S., & Harrison, T. E. 2004, ApJ, 614, L81
- Miller, N. & Fortney, J. J. 2011, ApJ, 736, L29
- Morton, T. D. & Johnson, J. A. 2011, ApJ, 738, 170
- Mould, J. R. 1976, A&A, 48, 443
- Muirhead, P. S., Edelstein, J., Erskine, D. J., Wright, J. T., Mutterspaugh, M. W., Covey, K. R., Wishnow, E. H., Hamren, K., Andelson, P., Kimber, D., Mercer, T., Halverson, S. P., Vanderburg, A., Mondo, D., Czeszumska, A., & Lloyd, J. P. 2011, PASP, 123, 709
- Newberry, M. V. 1991, PASP, 103, 122
- Pollacco, D. L., Skillen, I., Collier Cameron, A., Christian, D. J., Hellier, C., Irwin, J., Lister, T. A., Street, R. A., West, R. G., Anderson, D., Clarkson, W. I., Deeg, H., Enoch, B., Evans, A., Fitzsimmons, A., Haswell, C. A., Hodgkin, S., Horne, K., Kane, S. R., Keenan, F. P., Maxted, P. F. L., Norton, A. J., Osborne, J., Parley, N. R., Ryans, R. S. I., Smalley, B., Wheatley, P. J., & Wilson, D. M. 2006, PASP, 118, 1407
- Pollack, J. B., Hubickyj, O., Bodenheimer, P., Lissauer, J. J., Podolak, M., & Greenzweig, Y. 1996, Icarus, 124, 62
- Raymond, S. N., Barnes, R., & Mandell, A. M. 2008, MNRAS, 384, 663
- Raymond, S. N., Quinn, T., & Lunine, J. I. 2005, ApJ, 632, 670
- Rogers, L. A., Bodenheimer, P., Lissauer, J. J., & Seager, S. 2011, ApJ, 738, 59
- Rojas-Ayala, B. 2013, in European Physical Journal Web of Conferences, Vol. 47, European Physical Journal Web of Conferences, 9004
- Rojas-Ayala, B., Covey, K. R., Muirhead, P. S., & Lloyd, J. P. 2010, ApJ, 720, L113
- . 2012, ApJ, 748, 93
- Santerne, A., Díaz, R. F., Moutou, C., Bouchy, F., Hébrard, G., Almenara, J.-M., Bonomo, A. S., Deleuil, M., & Santos, N. C. 2012, A&A, 545, A76
- Santos, N. C., Israeliian, G., & Mayor, M. 2004, A&A, 415, 1153
- Schlaufman, K. C. & Laughlin, G. 2010, A&A, 519, A105
- Seager, S., Kuchner, M., Hier-Majumder, C. A., & Militzer, B. 2007, ApJ, 669, 1279
- Seifahrt, A., Käufl, H. U., Zängl, G., Bean, J. L., Richter, M. J., & Siebenmorgen, R. 2010, A&A, 524, A11
- Sousa, S. G., Santos, N. C., Mayor, M., Udry, S., Casagrande, L., Israeliian, G., Pepe, F., Queloz, D., & Monteiro, M. J. P. F. G. 2008, A&A, 487, 373

- Southworth, J., Hinse, T. C., Jørgensen, U. G., Dominik, M., Ricci, D., Burgdorf, M. J., Hornstrup, A., Wheatley, P. J., Anguita, T., Bozza, V., Novati, S. C., Harpsøe, K., Kjærgaard, P., Liebig, C., Mancini, L., Masi, G., Mathiasen, M., Rahvar, S., Scarpetta, G., Snodgrass, C., Surdej, J., Thöne, C. C., & Zub, M. 2009, MNRAS, 396, 1023
- Sozzetti, A., Torres, G., Latham, D. W., Carney, B. W., Stefanik, R. P., Boss, A. P., Laird, J. B., & Korzennik, S. G. 2006, ApJ, 649, 428
- Sozzetti, A., Torres, G., Latham, D. W., Stefanik, R. P., Korzennik, S. G., Boss, A. P., Carney, B. W., & Laird, J. B. 2009, ApJ, 697, 544
- Terrien, R. C., Mahadevan, S., Bender, C. F., Deshpande, R., Ramsey, L. W., & Bochanski, J. J. 2012, ApJ, 747, L38
- Torres, G., Andersen, J., & Giménez, A. 2010, A&A Rev., 18, 67
- Williams, J. P. & Cieza, L. A. 2011, ARA&A, 49, 67
- Yasui, C., Kobayashi, N., Tokunaga, A. T., Saito, M., & Tokoku, C. 2009, ApJ, 705, 54
- Young, A. T. 1993, The Observatory, 113, 41

Chapter 2

Ground-Based Submillimagnitude CCD Photometry of Bright Stars Using Snapshot Observations

Published as Mann, Andrew W.; Gaidos, Eric; Aldering, Greg; 2011, PASP, 123, 1273

Abstract

We demonstrate ground-based submillimagnitude ($< 10^{-3}$) photometry of widely separated bright stars using snapshot CCD imaging. We routinely achieved this photometric precision by (1) choosing nearby comparison stars of a similar magnitude and spectral type, (2) defocusing the telescope to allow high signal ($> 10^7 e^-$) to be acquired in a single integration, (3) pointing the telescope so that all stellar images fall on the same detector pixels, and (4) using a region of the CCD detector that is free of nonlinear or aberrant pixels. We describe semiautomated observations with the Supernova Integrated Field Spectrograph (SNIFS) on the University of Hawaii 2.2m telescope on Mauna Kea, with which we achieved photometric precision as good as 5.2×10^{-4} (0.56 mmag) with a 5 minute cadence over a 2 hr interval. In one experiment, we monitored eight stars, each separated by several degrees, and achieved submillimagnitude precision with a cadence (per star) of ~ 17 minutes. Our snapshot technique is suitable for automated searches for planetary transits among multiple bright stars.

2.1 Introduction

High-precision stellar photometry is used to detect planets orbiting other stars, exploiting the phenomena of a transit (Charbonneau et al. 2000), a secondary eclipse (Charbonneau et al. 2007), or a microlensing event (Bond et al. 2004). Although photometry from space can be vastly more precise - *Kepler* achieves $\sim 2 \times 10^{-5}$ in 30 minutes with $V \sim 10$ stars (Koch et al. 2010) - the preponderance of astronomical resources are on the ground and must contend with absorption, scattering, and scintillation by the atmosphere. Ground-based searches have been able to detect Neptune- to Jupiter-sized planets on close-in, transiting orbits around solar-mass stars (e.g., Henry et al. 2000b; Pollacco et al. 2006; Gillon et al.

2007), a multi-Earth-mass planet around an M dwarf (Charbonneau et al. 2009), and planets on more distant orbits around M stars: (e.g., Gould et al. 2010).

Relative photometric stability of a few millimagnitudes on the timescale of minutes to hours is sufficient to detect the transit of a Jupiter-sized planet (Figure 2.1). However, superior stability is required to resolve degeneracies between the unknown impact parameter, size of the star, and limb-darkening effects, and to search for transit timing variation indicative of other, unseen planets (Winn et al. 2009; Southworth 2010). Furthermore, high-precision Doppler studies are now detecting Earth- to Neptune-mass planets on short-period orbits (Mayor et al. 2009; Howard et al. 2009; Lo Curto et al. 2010; Vogt et al. 2010). The transit depth of these objects, even around smaller M stars, is at most a few millimagnitudes (Figure 2.1). Signal-to-noise ratio (S/N) can be improved by phasing data with the known or hypothetical orbital period (Holman et al. 2006; Winn et al. 2007; Gillon et al. 2007), but the gains from phasing (and binning) are limited by time-correlated (red) noise, which has a $(1/f)^\gamma$ varying power spectral density, and does not decrease as the square root of the number of observations (Pont et al. 2006). Rather, photometric stability better than 10^{-3} (~ 1 mmag) in a single observation is required.

To surpass a precision of 10^{-3} , $\sim 10^7$ electrons must be acquired per integration. However, the dynamic range of optical CCD detectors limit the number of electrons in a single pixel to $\sim 10^5$. One method to avoid exceeding the linear range is to read out the detector at a rate of many hertz and to co-add the signal from multiple reads with low read noise (Souza et al. 2006). Another is to spread the signal over hundreds of pixels by shaping the point-spread function (PSF) with orthogonal charge transfer (Howell et al. 2003, 2005; Tonry et al. 2005; Johnson et al. 2009) or by defocusing the telescope (e.g., Gillon et al. 2009; Winn et al. 2009; Southworth et al. 2009). Longer integration times reduce scintillation noise and lower the fraction of time spent reading out the detector.

The deleterious effects of the atmosphere can be reduced by performing differential photometry with one or more comparison stars observed in the same field of view as the target star. That correction's accuracy will be limited by the signal from the comparison star (or collection of comparison stars). This technique commonly achieves photometric stability better than 1 mmag on ground-based observations of variable stars and exoplanet transits (Moutou et al. 2004; Tonry et al. 2005; Hartman et al. 2005; Johnson et al. 2009; Gillon et al. 2009; Winn et al. 2009; Southworth et al. 2009, 2010).

A larger telescope can collect more signal but, all else being equal, its detector will have a smaller field of view with which to include a suitable comparison star. For a given *f*-number, the field of view of a telescope with a specified imaging detector is inversely proportional to the aperture *D*. The number-flux relation for nearby stars has an approximate slope of -1.5 , thus for a given integration time, the signal from the brightest comparison star in the field of any target star scales as $D^2 \times D^{-4/3}$, or $D^{2/3}$ (not considering binaries). In principle, there is a modest advantage with larger telescope aperture. However, for a typical CCD field of view of $10'$, the probability of an equally bright comparison star appearing in the same field becomes large (i.e., 80% at a galactic latitude of 30°) only by an apparent magnitude of 13 (Zombeck 2007). This brightness is at the limit of current Doppler techniques, and would exclude those systems most amenable to follow-up observations.

If a more suitable comparison star can be found in a separate, but nearby field, observations of the target and reference can be obtained by slewing the telescope between

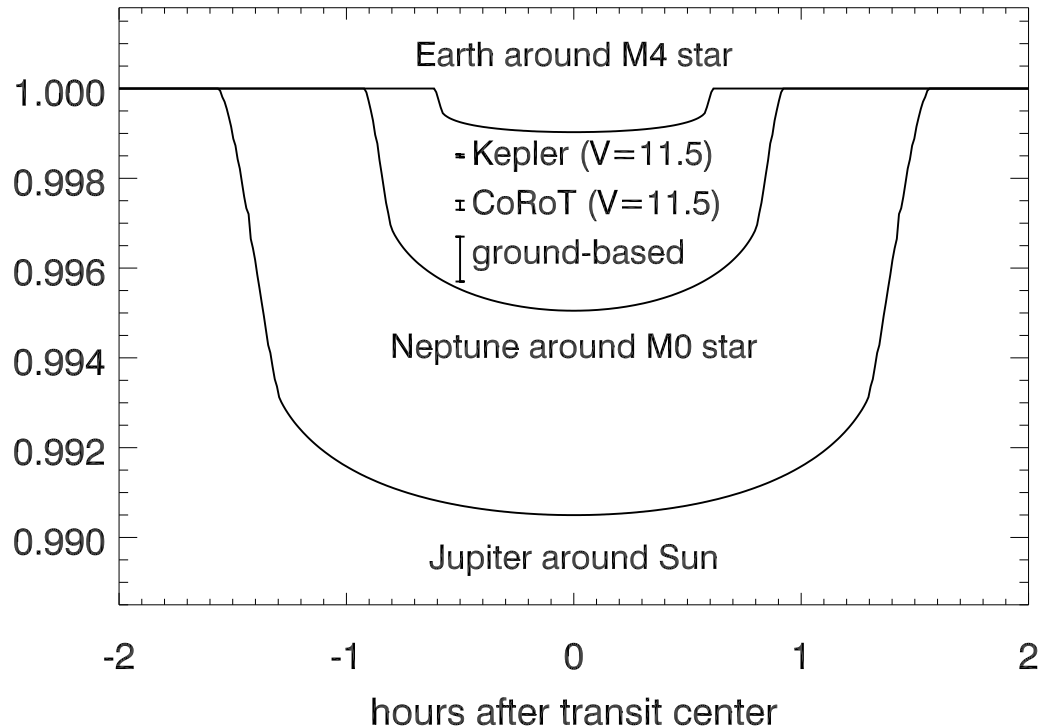


Figure 2.1: Theoretical normalized light curves of stars transited by planets on 4 day orbits, compared with the photometric precision obtained from space - *Kepler* 30 minute (Jenkins et al. 2010) and COROT (Aigrain et al. 2009) - and a practical limit from the ground (5×10^{-4}). Limb darkening is included as described in Claret (2000). A stellar mass-radius relation $R_* \sim M_*^{1.06}$ (appropriate for M dwarfs) is used. Ground-based photometry can be sufficiently stable to detect and characterize super-Earth- to Neptune sizes planets around M dwarf stars.

the two positions, and the exposure time can be adjusted to acquire equal signal from each star. The comparison star could also be the target of a transit search. These sequential observations will be neither simultaneous nor through the same column of the atmosphere. This technique has been employed for decades with single-channel photomultiplier tubes (PMTs) and has been applied to studies of (and searches for) exoplanet transits and stellar variability, commonly taking advantage of automatic telescopes (e.g., Genet et al. 1987; Young et al. 1991; Henry 1999; Henry et al. 2000a; Grauer et al. 2008). One of the seminal articles on the subject, Young et al. (1991), describes the limits of photometry when slewing between stars and making use of high-speed robotic telescopes. The authors suggest that the limit of ground-based automated photometry is ~ 1 mmag when all sources of error are properly handled. Henry (1999) and Henry et al. (2000a) use automatic photoelectric telescopes, all less than 1 m in aperture, and achieve photometric precision $\gtrsim 1$ mmag for single observations by observing a set of approximately four stars at a time, of which three are comparison stars. They claim their precision is limited more by variability of comparison stars than by noise inherent to the technique. So far, none of these efforts have been able to achieve consistent precision of less than 1 mmag.

By combining the single-channel PMT techniques with a high-performance CCD, we have routinely achieved submillimagnitude relative photometry with respect to one or more comparison stars under photometric conditions. Unlike with PMTs, we are able to do simultaneous sky measurement and can take advantage of high quantum efficiencies. We slew between multiple stars of similar spectral types and apparent magnitude, but separated by several degrees on the sky. Our snapshot method combines (1) semiautomated observations while rapidly slewing between target and comparison stars, (2) telescope defocusing to achieve the requisite photon counts, and (3) precision CCD photometry practices (discussed later). Here, we present data obtained using the SuperNova Integral Field Spectrograph (SNIFS) on the University of Hawaii UH2.2 m telescope at Mauna Kea Observatory. In Section 2.2 we describe our observations, including the instrument, telescope, and targets. In Section 2.3 we quantify the major sources of error, and in Section 2.4 we discuss our efforts to mitigate these sources of noise. In Section 2.5 we combine our noise sources using a simple noise model and compare with the noise from our observations. In Section 2.6 we discuss our findings in the form of guidelines for other observers, and we conclude with a simulated example of the technique’s intended application; a search for shallow ($\gtrsim 2$ mmag) planetary transits around stars that exhibit a Doppler signal.

2.2 Observations

SNIFS is mounted on the south bent Cassegrain port of the UH 2.2 m telescope located atop Mauna Kea. SNIFS is an integral field spectrograph (Aldering et al. 2002; Lantz et al. 2004) originally designed for spectrophotometric observations of Type Ia supernovae for the Nearby Supernovae Factory project (Pereira et al. 2010). SNIFS consists of blue and red spectrograph channels, along with an imaging channel, mounted behind a common shutter. The imaging channel consists of two E2V 2048×4096 CCD detectors (CCD44-82-B23), one a high-quality science-grade device dedicated to imaging and the other an excellent engineering-grade device used for guiding. Each $15 \mu\text{m}$ pixel subtends $0.137''$ and the field

of view is 9.35' on a side. The gain for the relevant amplifier of the imaging detector is 1.58 e⁻/DN and the readout noise is 4 e⁻, or 6 e⁻ if electronic pickup noise is included. The telescope control system is accessed by the SNIFS instrument computer, allowing the observer to run scripts that include telescope slews and offsets for target acquisition, focus changes, and guiding as described in Antilogus et al. (2008).

Our target and comparison stars are bright ($V < 13$) late K and early M main-sequence stars that are the targets of a combined Doppler-transit planet search (Lépine & Gaidos 2011). These stars are drawn from the proper-motion-selected SUPERBLINK catalog survey based on V - J color and color-magnitude relationships (Lépine 2005). Candidate targets are first screened using low-resolution spectra to confirm spectral type, determine metallicity, and remove those with strong H α emission (potentially active or flaring stars, Kowalski et al. 2009). Stars are then monitored for barycenter motion with the High Resolution Spectrometer on the Keck I telescope (Apps et al. 2010). Targets showing significant radial velocity variation are then monitored for transits. The full catalog comprises more than 13,000 M and K dwarf stars, and thus the nearest available comparison star from the catalog is usually no more than 2–3° away.

Observations were obtained between 2010 June 22 and 2011 January 15, usually within 7 days of a full Moon. Photometric observations presented here usually took up approximately half of each observing night. Observing conditions are presented in Table 2.1. Seeing was measured each time the telescope was focused: it is the full width at half-maximum of the PSF at optimal focus, interpolated between discrete focus settings. Data on atmospheric extinction were obtained from the SkyProbe of the Canada-France-Hawaii Telescope (CFHT), which images Tycho stars around the boresight of that telescope through B and V filters, and determines extinction by comparing the observed signals to reference values (Steinbring et al. 2009). We report the median, standard deviation, and 95 percentile values of all the measurements in a night, excluding the first 10 and last 10 observations made near sunset and sunrise. The SkyProbe data often contain high-extinction artifacts created when the telescope slews, so we check the SkyProbe data against videos from the UH 2.2m all-sky camera¹, which can provide visual confirmation of clouds. While extinction during the nights of June 22–24, July 27–29, and January 15 was low and constant (extinction of $\lesssim 0.2$ mag is considered photometric), extinction during June 27–30 and January 15 was more variable; variation in extinction is more detrimental to relative photometry than the absolute value of the extinction. Only June 30 showed evidence of (thin) clouds in the all-sky camera, predominately during the first few hours of the night. We also report the estimated precipitable water vapor (PWV) above Mauna Kea Observatories for each night, based on the mean of the 225 GHz optical depth (τ_{225}) measurements from the Caltech Submillimeter Observatory, and using the conversion PWV = $20 \times (\tau_{225} - 0.016)$ mm (Davis et al. 1997). These values are germane because of H₂O absorption features between 6000 and 10,000 Å, i.e., in the SDSS r , i , and z passbands.

A single observation cycle consisted of (1) the acquisition of a smaller (800 × 800) image to locate the star after a slew, (2) calculation of the centroid of the focused stellar PSF, and the required offset to place the star at the desired location on the CCD, while at the same time (3) defocusing of the telescope by a specified amount, (4) acquisition

¹<http://uh22data2.ifa.hawaii.edu/public/allsky/index.php>

Table 2.1. Observing Conditions

UTC date	Seeing ^a (")	Extinction ^b (mag)			Mean PWV ^c (mm)
		Median	std dev	95% value	
2010 Jun 22	0.75	0.187	0.026	0.238	1.05
2010 Jun 24	0.78, 1.07	0.198	0.045	0.240	1.13
2010 Jun 25	0.61	0.180	0.082	0.241	1.15
2010 Jun 27	0.99, 0.74, 0.81, 0.84	0.225	0.197	0.942	2.48
2010 Jun 29	0.87, 0.71	0.237	0.198	0.894	1.83
2010 Jun 30	0.68, 0.73	0.237	0.202	0.949	1.43
2010 Jul 27	0.73	0.213	0.073	0.319	1.55
2010 Jul 30	1.02, 1.03	0.207	0.093	0.248	0.85
2010 Sep 15	0.96, 1.12	0.215	0.173	0.922	1.07
2011 Jan 15	0.83, 0.88	0.183	0.056	0.221	1.74

^aFrom SNIFS focus images.

^bCFHT SkyProbe (V band) values.

^cBased on mean of Caltech Submillimeter Observatory 225 GHz tau measurements.

of the image for photometry, (5) slewing to the next target while the image is read out, and (6) refocusing the telescope. To minimize readout time, only the bottom 1024 rows of each CCD/amplifier combination were used to image the target. For short slews, a single observation cycle requires \sim 2 minutes to complete. Nearly all observations were performed through the SDSS z passband, although some were performed with SDSS r (Fukugita et al. 1996).

Observations are done in one of four different semiautomated modes, (1) a target with a comparison star(s) in the same field of view, (2) single-set snapshot, consisting of a single set of stars (usually one target and one to two comparison stars) of similar spectral type and magnitude, and permitting the shortest cadence, (3) survey snapshot, where we observe two or more sets, with the stars in a set separated by less than a few degrees, but with the sets separated by as much as 30° , and (4) constellation mode, where we repeat a sequence of observations of a large number of neighboring stars in a circuit, each star serves as a potential comparison star for every other star in the constellation (Figure 2.2).

2.3 Sources of Noise

When the target and comparison stars are in the same field of view, differential photometry between the two is performed through nearly the same air column. In snapshot photometry of stars separated by a degree or more, observations are neither simultaneous nor made through the same path in the atmosphere. Inhomogeneities and atmospheric transmission fluctuations (ATFs) will produce errors, but these can be mitigated by judicious choices of passband, allowable airmass, and comparison star, as well as information about the atmosphere itself (Stubbs et al. 2007). Here, we discuss each noise source, including an estimate of the amount of noise from each source in our observations. We discuss some basic strategies for minimizing these sources of error in Section 2.4, and in Section 2.5 we

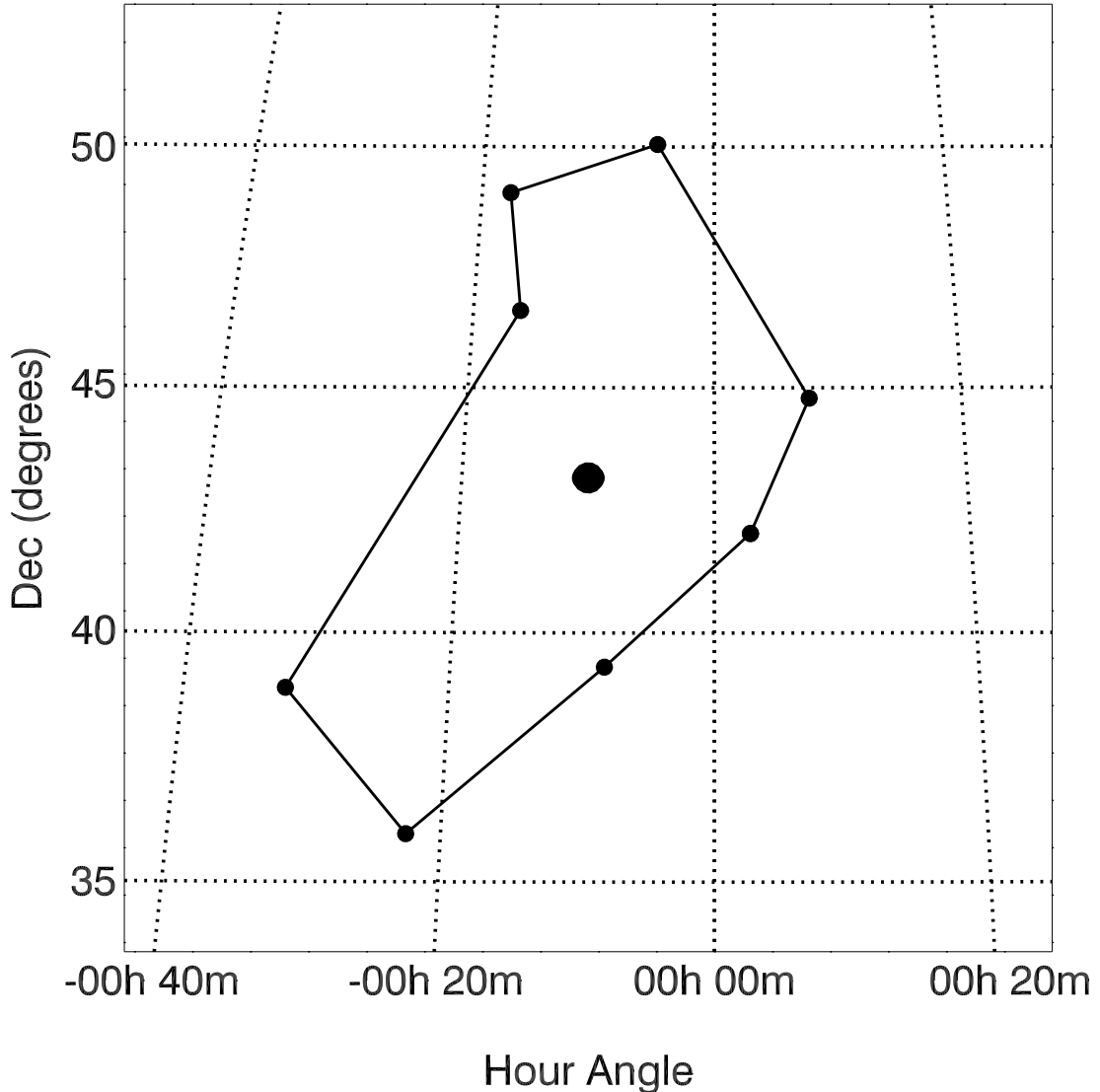


Figure 2.2: Aitoff projection of trajectory of telescope pointings for constellation observations, designed to minimize slew time. The circle is approximately the size of the full Moon. Although a given target is usually several degrees away from the next target, the slew time is not significantly longer than the readout time (~ 20 s). The constellation technique enabled us to concurrently search for transits around eight target stars.

Table 2.2. Photometry Experiments

UTC Date	Experiment ^c	Integrations (sec)	Cadence (min)	Aper. rad. (pixels)	Target	Signal ^a Reference	rms ^b $\times 10^{-4}$
2010 Jul 27	Snapshot (8-star)	9 × 19	17	80	15.8	...	5.4 (5.8)
2010 Jul 27	Snapshot (8-star)	9 × 31	17	75	11.7	...	6.0 (7.0)
2010 Jul 27	Snapshot (8-star)	9 × 22	17	90	15.7	...	8.9 (5.2)
2010 Jul 27	Snapshot (8-star)	9 × 30	17	75	14.2	...	7.3 (8.0)
2010 Jul 27	Snapshot (8-star)	9 × 13	17	80	11.8	...	8.3 (9.0)
2010 Jul 27	Snapshot (8-star)	9 × 23	17	85	16.3	...	7.8 (6.9)
2010 Jul 27	Snapshot (8-star)	9 × 13	17	75	13.6	...	6.5 (7.5)
2010 Jul 27	Snapshot (8-star)	9 × 18	17	75	14.0	...	8.4 (8.0)
2010 Jul 31	Common field	15 × 88	2.4	65, 80	8.4	13.6	9.7 (—)
2010 Jul 27	Common field	13 × 22	5.5	60, 85	13.1	12.5	8.4 (—)
2011 Jan 15	<i>r</i> Filter test	20 × 50	9.6	85	17.1	16.8	9.2 (9.5)
2011 Jan 15	<i>z</i> Filter test	20 × 50	9.6	80	18.0	17.6	8.5 (7.5)
2011 Jan 15	Exposure time tests	22 × 25	18.1	65	8.0	7.1	11.5 (11.7)
2011 Jan 15	Exposure time tests	22 × 50	18.1	75	16.1	14.0	9.8 (10.1)
2011 Jan 15	Exposure time tests	22 × 100	18.1	90	31.9	27.8	8.0 (11.5)

^a 10^6 e⁻ per integration.

^bValue in parentheses is theoretical precision (see Section 2.5 and Table 2.3).

^cWith the exception of the January 15 filter tests, all data listed here were taken with the *z* filter.

combine all noise sources to predict the noise level for each observation to be compared with the actual precision.

To compare with snapshot observations, we twice conducted an experiment in which two stars of similar spectral type and *z*-band magnitude that fortuitously fell within the same field of view were continuously observed (cadence, 2.4, 5.5 minutes). The rms of the photometry was 9.7×10^{-4} and 8.4×10^{-4} (Table 2.2). Noise from these observations is primarily due to scintillation, noise from the detector (see §§2.3.1 and 2.3.4, respectively), and Poisson noise. In these experiments the comparison stars were of comparable fluxes as the target (total counts $\sim 1 \times 10^7$ e⁻). Total signal detected in both tests was similar to that of our snapshot observations, where median signal is $\sim 1.4 \times 10^7$ e⁻ for both target and comparison stars, yielding Poisson noise of $\sim 2.7 \times 10^{-4}$ for each integration. The precision for these experiments was not better than that for our snapshot experiments.

2.3.1 Scintillation Noise

Scintillation noise is caused by fluctuations of the atmosphere's refractive index, which lead to phase distortion in the plane light wave passing through the atmosphere to an entrance aperture of the telescope. Scintillation noise from a telescope on Mauna Kea (4200 m elevation) is approximately

$$\sigma_s \approx 1.6 z^{7/4} D^{-2/3} t^{-1/2} \left(\frac{\lambda}{5500} \right)^{-7/12} \text{ mmag}, \quad (2.1)$$

where D is the diameter of the telescope in meters, z is the airmass, t is the integration time in seconds, and λ is the wavelength in angstroms (Young 1993; Birney et al. 2006). Equation (2.1) is only approximate, as scintillation also varies seasonally, with the speed and direction of the wind (Young 1974; Dravins et al. 1998; Birney et al. 2006) and with conditions in the upper atmosphere (Heasley et al. 1996). For example, the true value of the airmass exponent is ~ 2 when observing in the same direction as the wind and is ~ 1.5 when observing perpendicular to it, and the wavelength dependency vanishes for larger telescopes (Roddier 1981). More rigorous methods of calculating scintillation can be found in Kenyon et al. (2006) and Kornilov (2011), but with proper modification of the airmass term for wind direction and no wavelength dependency, equation (2.1) is consistent within 20% of scintillation measurements from Mauna Kea (Dainty et al. 1982; Gilliland et al. 1993; Cherubini et al. 2008) under conditions similar to those of our observations. With wind modifications and without the wavelength term, equation (2.1) gives a median value per star of 2.4×10^{-4} for noise due to scintillation in our observations. It becomes the dominant contribution to the error budget at exposure times if less than 15 sec.

2.3.2 Extinction

First-order extinction: Our target and comparison stars, although close on the sky, will have a nonnegligible difference in airmass. For an observation of stars lasting several hours, the differential airmass of the target and comparison star(s), $\chi = X_{\text{targ}} - X_{\text{comp}}$, will change. For small values of χ , and assuming no significant change in the extinction coefficient, the fractional change in the normalized relative flux will be $\delta f \approx 0.4 \ln(10)E(\lambda)\Delta\chi$, where $E(\lambda)$ is the extinction coefficient in magnitudes and airmass and $\Delta\chi$ is the change in airmass difference over the course of an observation. A typical value of $\Delta\chi$ in 2 hr for a well-selected comparison star is 0.003. Assuming an extinction coefficient for photometric conditions of ~ 0.04 mag airmass $^{-1}$ in SDSS z (McCord & Clark 1979; Hodgkin et al. 2009), the change in flux of the target star relative to the comparison star will be $\sim 10^{-4}$. Even for comparison stars within 5° of the target, values of greater than 0.01 for $\Delta\chi$ are possible, and the resulting change in flux could be as much as $\sim 4 \times 10^{-4}$. If large values of $\Delta\chi$ combine with higher extinction coefficients (i.e., nonphotometric or high mean PWV), the systematic effect can be larger than $\sim 10^{-3}$. However, the resulting trend is systematic and can be removed with $\sim 10^{-4}$ precision provided that the extinction coefficient is measured (or known) to better than 0.01 mag airmass $^{-1}$.

Second-order extinction: If the target and comparison stars do not have the same spectral energy distributions over the passband $\Delta\lambda$, changes in the extinction by the atmosphere with airmass and time will produce trends in their relative signals. The effect will be proportional to $\Delta\lambda^2$. Second-order extinction error was analyzed by (among others) Young et al. (1991) and Everett & Howell (2001). Young et al. (1991) estimate the size of the effect by observing two stars differing in $B-V$ by 0.3 mag and find that the difference in B extinction of the two stars is ~ 7 mmag airmass $^{-1}$, although other estimates are notably smaller: e.g., Everett & Howell (2001). The color effect is smaller in redder passbands, with stars of later spectral type, and with narrower bandwidth filters. In the case in which the spectral energy distributions of the target and comparison stars are known, a correction can be made.

We estimate second-order extinction errors with respect to a typical target star in our observations (4000 K and $\log g = 4.5$). We convolve model spectra of Kurucz (1991) with the transmission curve of the SDSS r , SDSS z (Fukugita et al. 1996), B , or a narrow custom z (J. Johnson 2011 private communication) filter, the quantum efficiency of the EV2 detector, and a model of atmospheric transmission. Figure 2.3 shows the profile of each of these filters multiplied by the SNIFS transmission and with an approximation of the atmosphere above Mauna Kea. Our atmosphere model is based on low-resolution spectra of standard stars taken with SNIFS, combined with the HITRAN software (Rothman et al. 2009) in regions where our spectra are incomplete or contaminated by features of our standards. Figure 2.4 shows the expected change (systematic error) in flux ratio ($F_{target}/F_{comparison}$, normalized to 1), as a function of airmass, for the SDSS r , SDSS z , B , and narrow z filters. We assume that the target and comparison stars are observed through identical airmass. We find the size of the effect in the B band to be approximately $2.5 \text{ mmag airmass}^{-1}$ for a comparison star with (B-V) color difference of 0.3, which is significantly smaller than that found by Young et al. (1991). The difference is likely due to the difference in atmosphere above the observatories (Mauna Kea versus Mount Hopkins), different instrument profiles, and the choice of later spectral type stars for our calculations. For our observations in the SDSS z filter, we calculate a median fractional error of only 4.5×10^{-5} , which is a benefit of choosing comparison stars of a similar spectral type to the target star and working at longer wavelengths, where the differences in stellar spectra are smaller.

2.3.3 Short-Term Atmospheric Transparency Variations

Snapshot observations are not simultaneous ($\gtrsim 2$ min lag), and variations in the atmosphere will produce error. Hill et al. (1994) find the average power spectrum of transparency fluctuations in the atmosphere above Mauna Kea to obey

$$\log P(\nu) = -9.84 - 1.50 \log \nu, \quad (2.2)$$

where ν is the frequency in hertz. Equation (2.2) is based on an average over 691 clear days. An individual night could have significantly higher or lower ATFs, which makes this source of noise particularly difficult to estimate for any given observation. Regardless, the spectrum contains no coherence time within the timescale of our observations, and the photometric stability improves with decreasing time between target and comparison star observations (shorter cadence), although with diminishing returns. We make use of equation (2.2) to estimate the noise from atmospheric variations between observations of target and comparison stars. In general, the variance due to ATF is

$$\sigma_{ATF}^2 = \left\langle \left| \int_0^{t'} D(t) S(t) dt \right|^2 \right\rangle, \quad (2.3)$$

where $D(t)$ and $S(t)$ are functions that describe the transparency fluctuations and integration windows respectively, and $\langle \rangle$ represents the time-averaged expectation. We

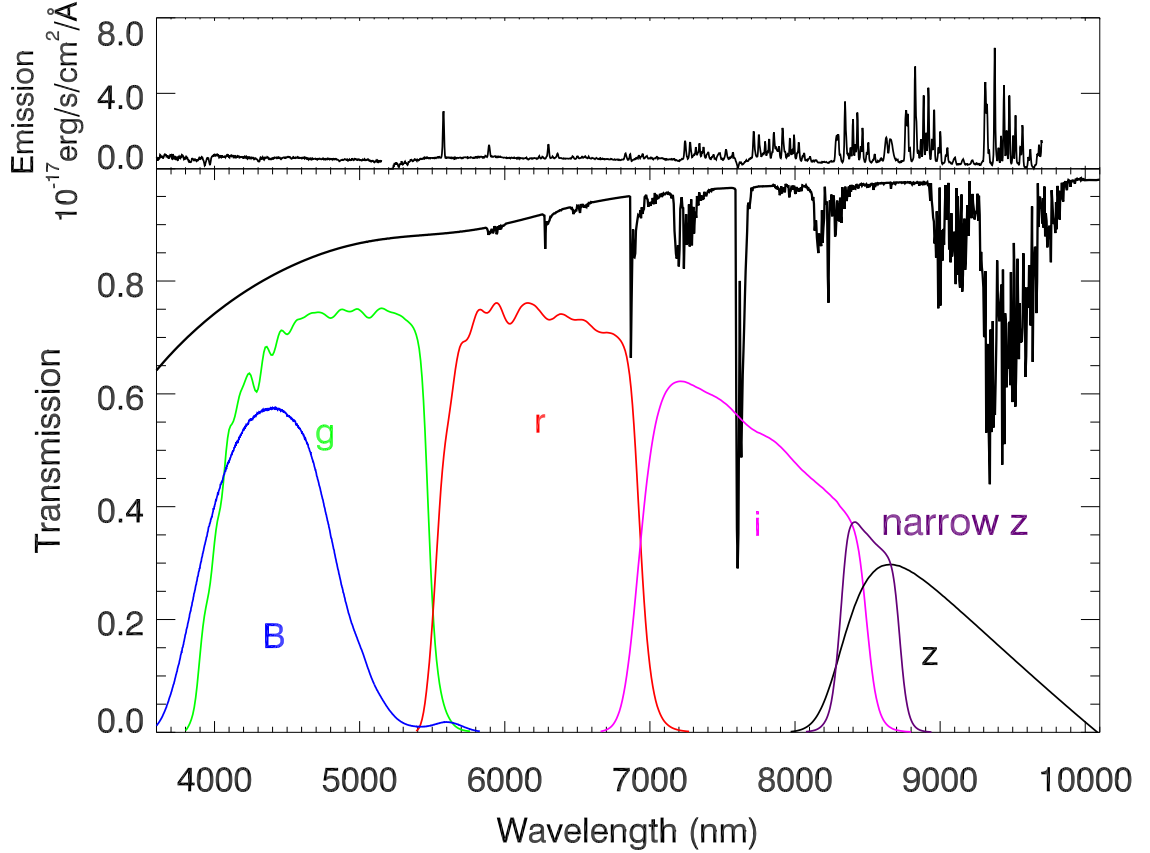


Figure 2.3: Approximate transmission (bottom) and emission (top) of the atmosphere on a clear night over Mauna Kea with B , SDSS g , SDSS r , SDSS i , SDSS z , and narrow z filters multiplied by the SNIFS CCD quantum efficiency. There is a discontinuity at $\sim 5200 \text{ \AA}$ in the emission caused by low QE near the edge of the blue and red channels of the SNIFS integral field unit. Our observations were taken predominantly in SDSS z , although some were taken in SDSS r . Scattering affects the filters blueward of 5500 \AA whereas molecular (chiefly H_2O and O_2) absorption lines contaminate the r and z passbands. A narrow z filter (J. Johnson, private communication) can mitigate errors from both molecular absorption and scattering.

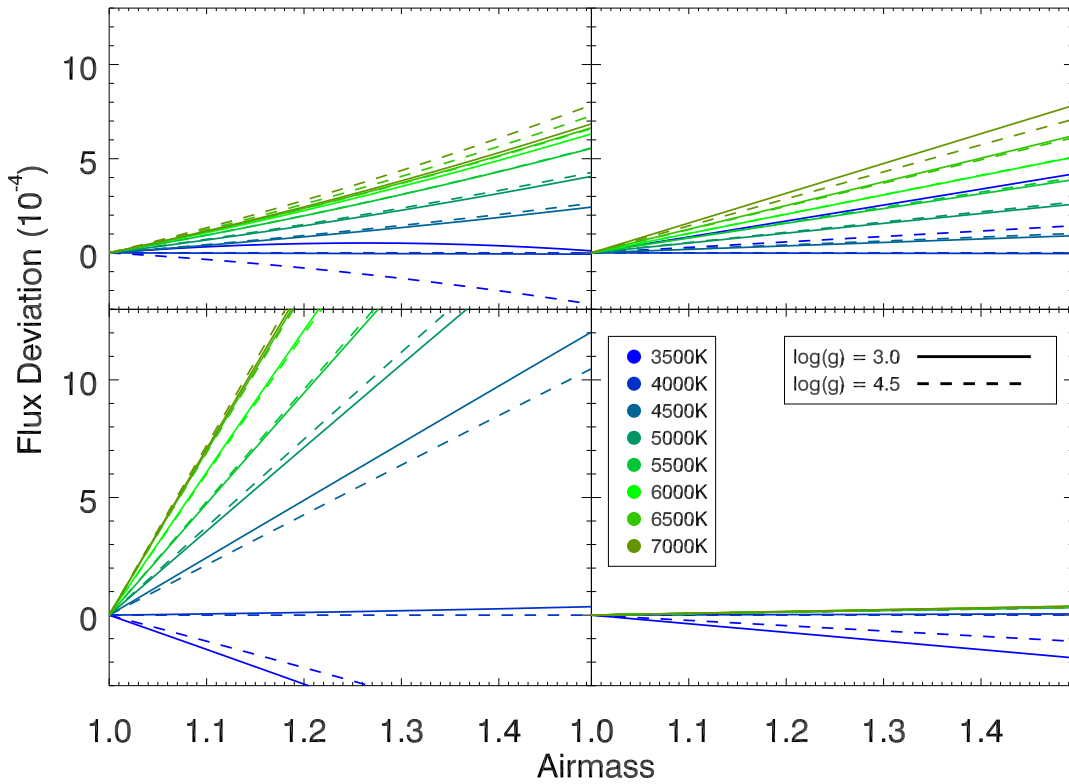


Figure 2.4: Photometric error in observations with the SDSS r (top left), SDSS z (top right), B (bottom left), and narrow z filters produced by a difference in spectral type between comparison and target star as a function of airmass (both using the SNIFS detector). The target star has an effective temperature of 4000 K and $\log g = 4.5$.

assume that our observations behave as a function of the form

$$S(t) = \begin{cases} 1 & : t \in T_{targ} \\ -1 & : t \in T_{comp} \\ 0 & : t \notin T_{targ} \cup T_{comp} \end{cases}, \quad (2.4)$$

where T_{targ} and T_{comp} are the times over which we are integrating on the target and comparison star respectively. We can represent $S(t)$ and $D(t)$ as Fourier transforms $D(\omega)$ and $S(\omega)$ and substitute into equation 2.3. After some simplification, we find

$$\sigma_{ATF}^2 \approx \left\langle \int_0^{\omega'} (D(\omega))^2 (S(\omega))^2 d\omega \right\rangle, \quad (2.5)$$

where $D(\omega)^2 = P(\omega)$, and ω' is the angular frequency over which $D(\omega)$ and $S(\omega)$ are defined. Equation (2.2) covers a significant portion of the optical spectrum, whereas we are interested in the z band, where the atmosphere is more transparent. We assume that $P(\omega)$ at the z -band scales linearly with the Hill et al. (1994) power spectrum and we derive a scalar coefficient based on our atmosphere model discussed previously and information gathered from the CFHT SkyProbe (Steinbring et al. 2009). Our atmosphere model gives us the average atmospheric transparency for SDSS z (or any other bandpass) to compare with Hill et al. (1994). We use the CFHT SkyProbe data to derive a scale factor between transparency fluctuations of Hill et al. (1994) and that of the V -band. This is consistent with the results of our atmospheric model; i.e., the amplitude of transparency fluctuations scales with average transparency fluctuations, thus enabling us to properly adjust equation (2.2) to any bandpass within the range of our atmosphere model. For our observations, the median noise due to transparency fluctuations is 2.8×10^{-4} and is typically smaller than Poisson and scintillation noise.

2.3.4 Detector Noise

No CCD has a perfectly uniform response rate, even when corrected with flat-fields. We calculated the error due to pixel response nonuniformities combined with motion of the defocused image around a given coordinate centroid, ignoring changes within the defocused PSF and chip nonlinearities. To accomplish this, we took 225 dome flats in 2010 June with exposure times from 2 to 15 s; 150 flats were taken using the SDSS z filter, and the remaining 75 were taken with SDSS r . All flat-fields were obtained within a period of 5 hr. Count levels varied from 5×10^3 to 3.8×10^4 e⁻ (typical levels for the signal in one of our defocused images). For each filter, we performed a linear least-squares fit of electron counts in each pixel versus median electron counts (for the chip of interest), assuming Poisson and read-noise variance. The result was a pixel-by-pixel map of the CCD's response for each filter. The median count was used instead of exposure time to remove effects of lamp variation. We created a model defocused PSF and scanned it over the 1024^2 region of interest in our detector response map to find the region(s) of the CCD with the most uniform pixel response. In general, the CCD's behavior was similar in both filters, although variation of the pixel response for the best (most uniform) regions was slightly better when using the r filter (rms pixel response $\sim 0.7\%$) than it was when using the z filter (rms $\sim 0.8\%$). For

either filter, even small PSF motions (< 3 pixels) on a bad region (very nonuniform pixel response) can cause noticeable ($> 3 \times 10^{-4}$) variations in received flux. Large motions (> 15 pixels) around a well-behaved region (highly uniform pixel response) can create similarly large variations in flux. Because we use a good region on the chip, typical rms motions for our observations (< 5 pixels) contribute minimal noise ($\lesssim 1 \times 10^{-4}$ for z and $\lesssim 0.8 \times 10^{-4}$ for r) to the total error budget (Figure 2.5).

Pixel-to-pixel variations in the response of the detector can be removed to a certain extent with dome and/or sky flats. However, using flats introduces additional noise to the data, because quantum efficiency variations among the CCD pixels are wavelength-dependent, the dome lamp (or sky) will not have the same spectrum as the target, and master flats composed of numerous, high-S/N flats still have noticeable Poisson noise. Twilight flats will better match the spectral energy background distribution of the data frames; however, it is difficult to get a large number of high-S/N twilight flats in the relatively short twilight window. These and many other errors associated with flat-fielding are discussed more thoroughly in (among others) Newberry (1991), Tobin (1993), Manfroid (1995), and Manfroid et al. (2001).

Noises brought about by flat-fielding may be significant, compared with the $\lesssim 10^{-4}$ sized errors induced from inaccurate detector response (Figure 2.5). For example, consider a master flat composed of 10 twilight flats, each with $\sim 20000 \text{ e}^- \text{ pixel}^{-1}$, and defocused target/comparison stars spread over 1000 pixels. Taking into account Poisson noise only, the error associated with flat-fielding to the light curve will be $\sim 1 \times 10^{-4}$, putting it on par with other noise from detector nonuniformity. Further, when we apply a median of 10 twilight flats to our dense grid of 150 flats (we assume the grid of flats to be a more accurate map of the detector) the predicted errors created by image motion do not improve significantly, as shown in Figure 2.5. Applying a flat-field correction improves precision when using a mediocre region of the chip, and/or when the image is drifting $\gg 10$ pixels. Since we make use of a very flat region of the chip, and image motions are small, flat-field corrections may actually *add* noise.

Detector nonlinearities are small for most science-grade instruments, but they can become important for photometry at submillimagnitude precision. For a single observation the recorded flux will be approximately

$$S \approx \sum_i (x_i - \alpha x_i^2), \quad (2.6)$$

where x_i is the normalized incident intensity on any given pixel, and α is the level of nonlinearity in the pertinent range. If the incident flux is $\bar{x} + r$, where r is normally distributed with standard deviation σ , then the difference between the signal of any two observations, S_j and S_k , will be

$$S_j - S_k \approx \sum_i [2\alpha(r_{ij} - r_{ik}) + \alpha(r_{ij}^2 - r_{ik}^2)]. \quad (2.7)$$

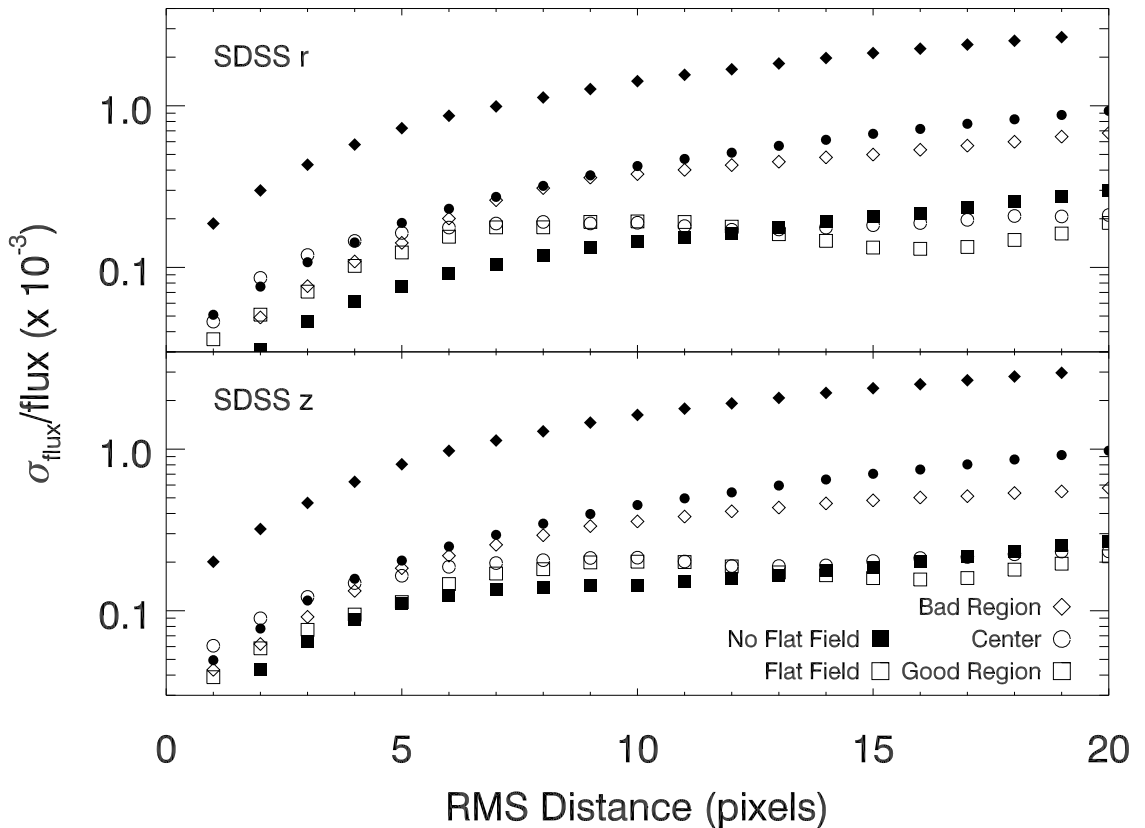


Figure 2.5: Fractional error as a function of rms image motion within a bad region (high pixel response variation), a good region (low pixel response variation), and at the center of the SNIFS science-grade imaging detector. These curves were generated by taking a defocused image and shifting it around a map of the detector response produced from a series of ~ 225 flats taken with varying exposure times through the SDSS r (top) and SDSS z (bottom) filters. Nonfilled points are for a pixel response map with a flat-field correction (median of 10 twilight flats). We assume no changes within the defocused PSF except position on the detector. Note that the good/bad regions used are comprised of different sets of pixels for the two different filters used.

The distribution of $S_j - S_k$ will have an average of zero, but a nonzero standard deviation. If we ignore terms of higher order than σ^2 , then the latter will be:

$$rms \sim \frac{\sqrt{2}\alpha\sigma^2}{\sqrt{N}}, \quad (2.8)$$

where N is the total number of pixels. A typical aperture size for our observations contains $N \sim 1.5 \times 10^4$ pixels. σ can vary significantly between observations, but is no higher than 1.0 and is often less than 0.1. In 2005 a series of dome flats were taken to determine the flux range over which the SNIFS E2V CCD is linear, which we use to estimate α . Exposure times varied between 2 and 55 s and were interleaved to reduce any time-varying effects. All exposures were taken within a few hours. The region containing the lower 200 pixels of the photometric chip and relevant amplifier was found to be linear to $0.15\% \pm 0.08\%$ between 7×10^3 and 1×10^5 e⁻. The rms of these measurements is 0.16%, most of which is due to variations in lamp brightness. Since we require the chip to be linear to better than 0.1% for submillimagnitude photometry, we aim to keep the maximum flux in any given pixel below 5.0×10^4 e⁻, where the CCD is linear to better than 10^{-3} . Thus for flux levels consistent with the majority of our observations, $\alpha \lesssim 0.0015$. Using 1.0 as an upper limit on σ , the noise due to nonlinearities is only 1.7×10^{-5} .

Another potential source of error is variation in the *shape* of the PSF, combined with fixed calibration errors in the pixel response. Even with sufficient defocusing, phase errors from seeing will induce fluctuations across the face of the image. The result is that, although total flux may be conserved, flux will be redistributed between pixels, which will produce uncertainties to the extent that pixel responses are not perfectly calibrated. If the PSF did not vary, such calibration uncertainties would not produce time variations. Figure 2.6 shows the rms difference between eight individual images and the mean. The stellar wings are mostly constant, but there is significant variability in the shape of the core annulus, particularly at its inner and outer edges. We estimate the magnitude of such an error by assuming that the calibration suffers from errors having a fixed Gaussian distribution with $\sigma = 1\%$. The error calculated from the eight images is only 4×10^{-5} , which is a consequence of summing uncorrelated errors over the more than 10^4 pixels with which the signal is acquired.

2.4 Strategies to Minimize Noise

2.4.1 CCD Regions and Signal Levels

Large pixel nonlinearities, like those seen in some near-infrared detectors, can be corrected by applying fits to an intensity series for each pixel and then implementing the corrections to the detected flux (Vacca et al. 2004). Pixel nonlinearities can also be mitigated in differential photometry by using the same pixels and similar flux levels and exposure times. More subtle nonlinearities and time-variable pixel responses are difficult to independently measure and remove, but cannot be ignored when submillimagnitude precision is required. One solution is to identify those pixels that are poorly behaved (highly nonlinear and/or time-variable pixels) and avoid them. It is *not* possible to simply mask these pixels during image processing, because that sensitizes the total signal to small changes in the position or

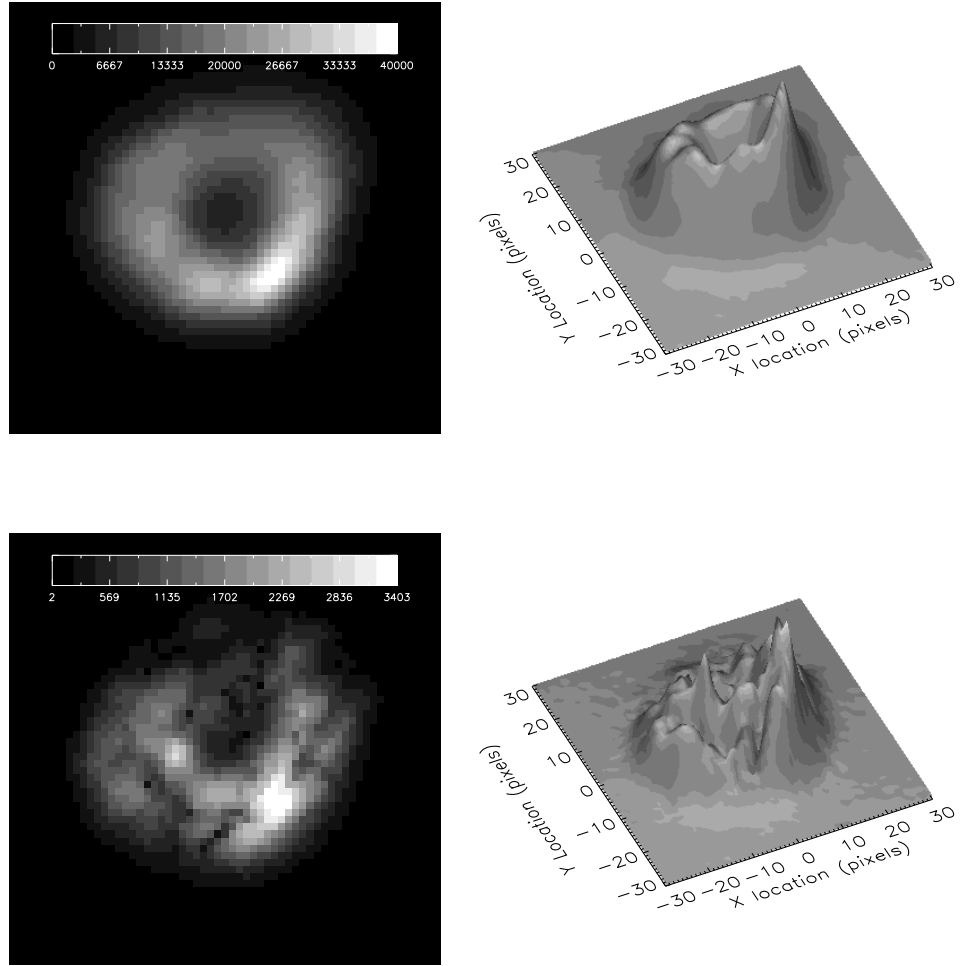


Figure 2.6: *Top:* Mean of eight defocused images of a $V = 13$ star, each with an integration time of 30 s. *Bottom:* Standard deviation of pixel values from the mean. All images have the same spatial scale ($\sim 8''$ on a side), but not the same intensity scale. The highest peak in the PSF is due to coma in the UH 2.2 m optics (C. Aspin, private communication 2010; Behr 1973).

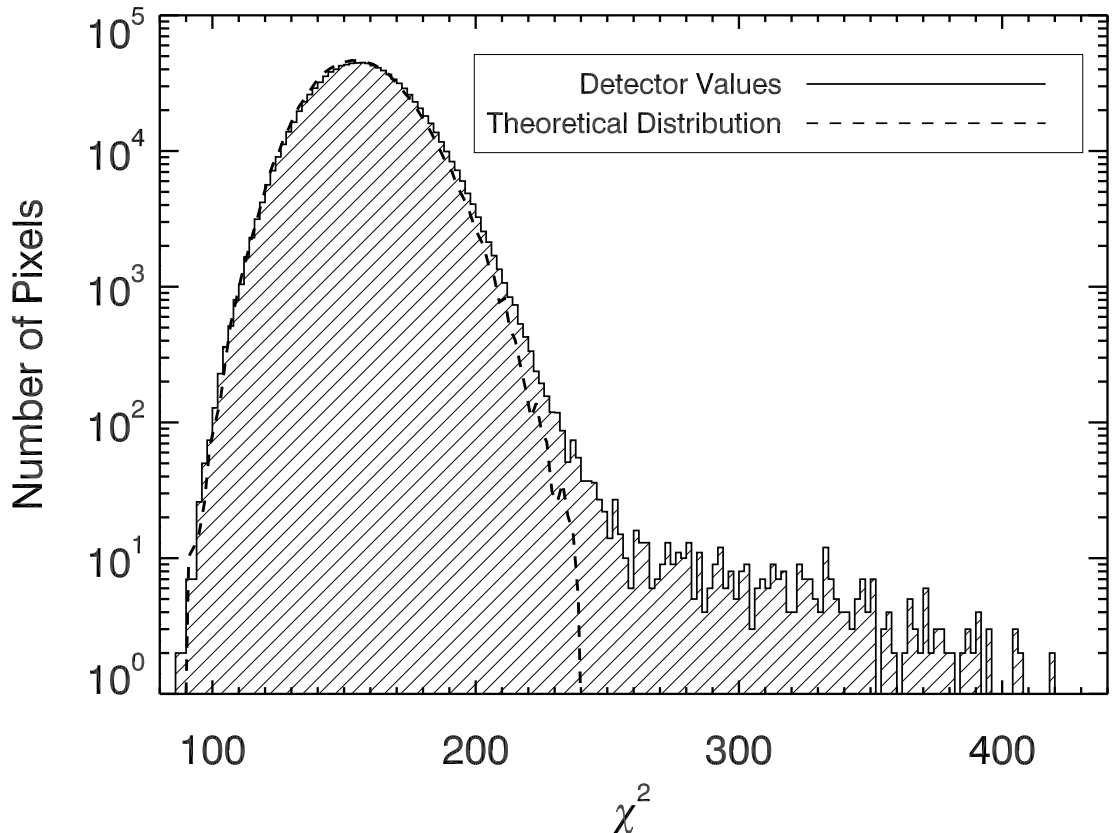


Figure 2.7: Histogram of the χ^2 values of a fit to pairs of individual pixel values vs. median detector values in a series of 150 dome flats. The theoretical distribution derived from a Monte Carlo analysis (based on Poisson statistics) is shown as a dashed line. We only include data from the bottom half of the SNIFS imaging science-grade detector (the region we use for transit imaging). We consider pixels with $\chi^2 > 240$ as poorly behaved and worth avoiding. These represent $\lesssim 0.1\%$ of the total number of pixels.

shape of the PSF. Our strategy for dealing with noise related to the detector is threefold, we locate the range of signal over which the detector is sufficiently linear (discussed in Section 2.3.4), identify regions of the detector containing pixels with uniform response rates, and minimize the motion of the defocused image between integrations.

We used the series of flats taken in 2010 (discussed in Section 2.3.4) to locate time-variable or highly nonlinear pixels on the SNIFS E2V detector. We identified pixels that have the highest χ^2 values for a linear fit. Figure 2.7 shows a histogram of the χ^2 values for pixel across the 1024^2 region of the detector used for photometry. Because our flat experiment is designed to locate the best and worst regions on the detector the absolute variation from linearity is not as important as the identification of pixels that show higher levels of nonlinearity (higher χ^2) than others. $\lesssim 0.1\%$ of pixels have χ^2 values above the expected distribution ($\chi^2 > 240$) and are predominantly concentrated in a few areas (e.g., near the edges of the detector), making poorly behaved pixels easier to avoid.

Our data indicate that the best precision is achieved *without* flat-fielding, provided that images are placed in good (flat) regions of the chip and that image motion is small (rms < 10 pixels). Figure 2.8 shows a comparison of precision with and without flat-fielding. For light curves built with flat-fielding we use twilight flats where available, and dome flats elsewhere. Although some light curves benefit from the use of flat-fields, applying flat-field corrections to most of our data worsened the precision. Instead, noise from errors in pixel response are minimized by using the same (good) region of the chip for all observations with a given filter (see Figure 2.5 for a comparison of noise from good and bad regions of the CCD) and by keeping image motion small from integration to integration. SNIFS' automated acquisition and position of the target/comparison stars is more than sufficient to keep image motion below 5 pixels. Flat-fielding will have more beneficial results for detectors with higher interpixel QE variations or higher image drift between integrations.

2.4.2 Choice of Filter

Choice of bandpass filter is a tradeoff between the desire to maximize signal from the star and to minimize the contribution from wavelengths that are affected by scintillation, scattering (by aerosols and molecules), and absorption by O₂ and H₂O (Stubbs et al. 2007). Observations through redder filters will have lower first- *and* second-order extinction (see §2.3.2). Stellar variability is a significant source of noise in the *V* band for as much as 20% of M dwarfs on 12 hr timescales (Hartman et al. 2011; Ciardi et al. 2011). However, observing at longer wavelengths reduces the spot-photosphere contrast, reducing noise from stellar rotation and spots. Among the redder SDSS filters, *i* is seriously compromised by molecular bands (Figure 2.3), *z* is bracketed by two H₂O bands, although the low quantum efficiency of most CCDs redward of 9000 Å mitigates H₂O contamination, while *r* is more affected by aerosol fluctuations. Use of a narrow *z* filter (if one is available) would almost completely eliminate second-order extinction error (Figure 2.4), due to its narrow bandwidth and red central wavelength (Figure 2.3). A narrow *z* filter would also reduce noise from scintillation and scattering from aerosols while avoiding a major H₂O line.

Observations in near-infrared filters are more affected by atmospheric emission than bluer bands, however, our data suggest that the overall noise from atmospheric emission and/or fringing is small. Fringing is present in SDSS *i* and *z* for SNIFS, but noise from fringing is minor compared with the rest of the sky background. Since we predominantly observe within 7 days of a full Moon, the dominant component of the sky background is scattered light from the Moon. Figure 2.3 includes an estimate of the atmospheric emission over Mauna Kea based on spectra taken from SNIFS. In the *z* band, integrated sky emission in a $\sim 7''$ radius, a typical defocus size, will be at least a factor of 100 smaller than the flux from a typical star ($m_z = 9$) in our program. In the narrow *z* band, this grows to 180, since the narrow *z*-filter transmission cuts off before the largest OH emission lines that contaminate the *z* band.

To test the performance of SDSS *z* and *r* filters we performed regular observations while interleaving exposures of *r* and *z* filters. We kept other controllable variables (exposure time, defocus, etc.) fixed between filter changes. The *z* band slightly outperformed the *r* filter overall (see Table 2.2), but not by as much as our total noise estimate predicts (see Section 2.5 for more on the noise model). The discrepancy could be due to underestimating

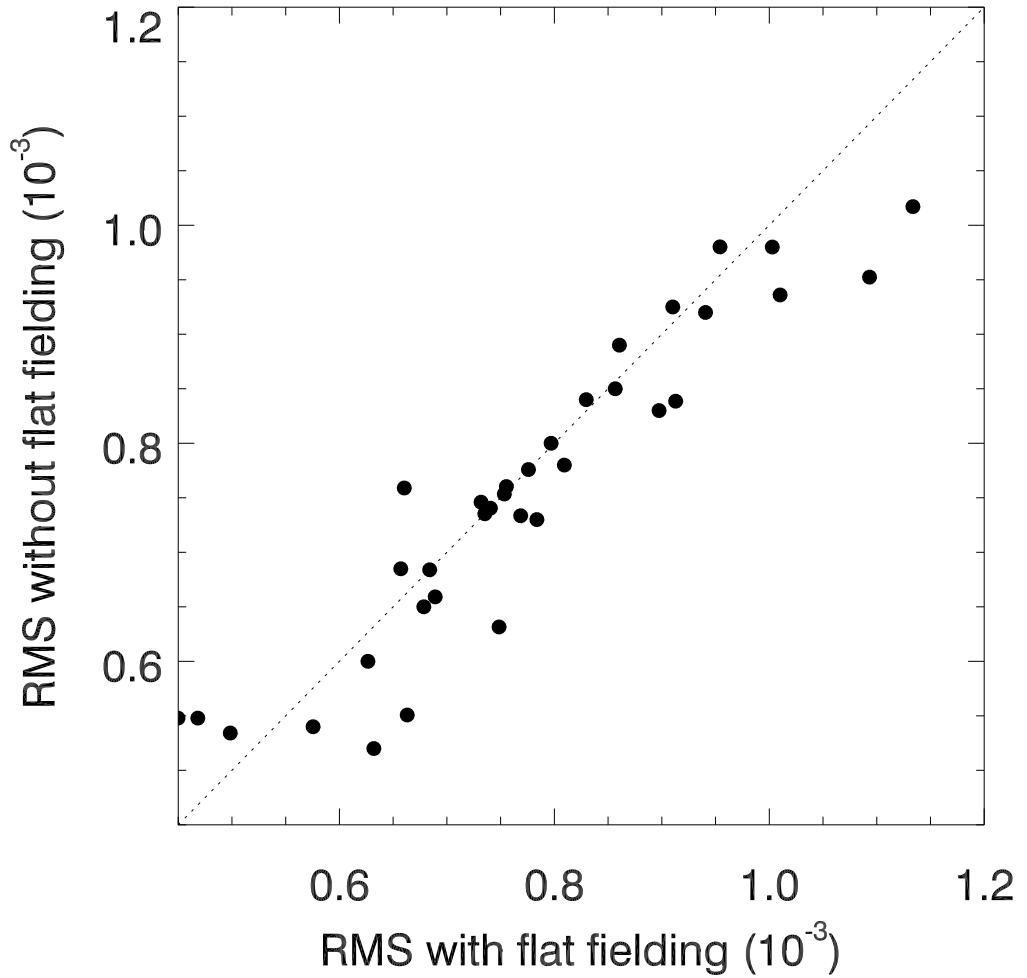


Figure 2.8: Comparison of photometric precision with and without flat-fielding. Dome flats are used when there is an insufficient quantity of high-S/N twilight flats from a given night. Although in some cases the precision is better with flats, on average, the precision is better without flat-fielding.

the effect of the H₂O line on the z filter, which is dependent on the PWV of that particular night and induces noise that cannot be easily modeled.

2.4.3 Degree of Defocusing

A minimum degree of defocusing is required for a fixed total signal from the star and linear range of the detector. For example, if the linear range of a CCD is 5×10^4 e⁻, then the acquisition of 2×10^7 e⁻ must take place over at least 400 pixels (for SNIFS, this is a circle 5'' across). Because the PSF is nonuniform, more pixels must actually be used to collect the signal and avoid saturation. Greater defocusing may be desirable for very bright stars to avoid integration times much shorter than the CCD read time and to minimize scintillation noise.

Figure 2.6 is the mean of eight 30 s integrations of a defocused $V \approx 13$ M star obtained through the SDSS z filter. Most of the signal is confined to an annulus with a $\sim 4''$ radius that represents an out-of-focus image of the telescope's primary mirror. The defocused PSF core is surrounded by a halo pattern, produced by the defocused convolution of the telescope pupil with the seeing, which extends out $\sim 10''$. The image is not axisymmetric because of coma in the telescope optics (C. Aspin, private communication 2010; Behr 1973). The area within the annulus is $\sim 10^3$ pixels, and the average signal per pixel is 1.7×10^4 e⁻, with a total signal of 1.6×10^7 e⁻. The total read and electronic pickup noise (200 e⁻) is much less than the photon noise (4×10^3 e⁻). The maximum S/N is achieved by summing the signal within an aperture of 8'' radius, if only photon noise, sky noise, read noise, and electronic pickup noise are considered (Figure 2.9).

More defocused images are less sensitive to motion of the stellar image on the CCD; however, the total read noise and probability of including ill-behaved pixels are greater. We consider the idealized case where the PSF is a circular aperture comprising N pixels, each of which gets $S \times N^{-1}$ signal (e⁻) and has read and electronic pickup noise σ_1 (e⁻ pixel⁻¹) and uncorrected response variation σ_2 , which we presume adds in quadrature. The variance from a single nonoverlapping pixel due to the last source of error is $S^2 N^{-2} \sigma_2^2$. If the centroid rms motion in pixels is δ then the number of pixels that are not common to a pair of stellar images is $\sim 2\pi\delta\sqrt{N/\pi}$. The total variance due to read noise and image jitter is

$$\sigma^2 \approx N\sigma_1^2 + 2N^{-3/2}\sqrt{\pi}\delta S^2\sigma_2^2. \quad (2.9)$$

Total read noise increases with N , but noise due to image jitter decreases. The number of pixels N_* that minimizes the total error is

$$N_* \approx (2\delta\sigma_2^2 S^2 \sigma_1^{-2})^{2/5}. \quad (2.10)$$

For $\delta = 3$ (the median centroid motion in pixels for our observations), $\sigma_2 = 0.01$, $\sigma_1 = 6$ e⁻, and $S = 10^7$ e⁻, and $N_* \approx 7.2 \times 10^3$: i.e., a circular region with diameter of ~ 96 pixels (13'') with total noise $\sigma = 6.6 \times 10^{-5}$ e⁻. N_* is sensitive to well depth, read noise, and the uncorrected pixel response noise, but can be estimated by experiments with defocused images. We are often forced to use higher defocus values than equation (2.10) suggests to keep the counts in the coma-induced peak in the linear range of the detector.

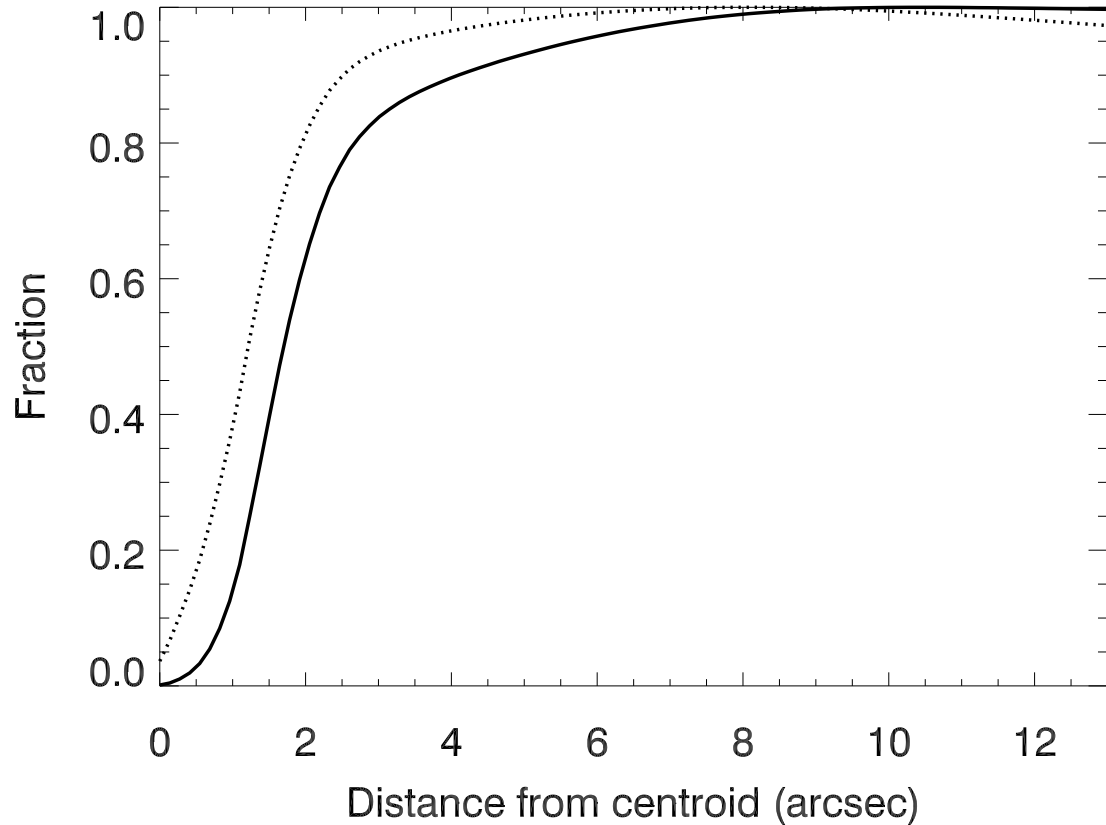


Figure 2.9: Curve of growth (vs. radius in arcseconds) of the mean of eight defocused images of a star obtained with the SNIFS/UH 2.2 m (solid line), and the S/N in an aperture of a given radius relative to the maximum value (dotted line).

2.4.4 Integration time

Poisson and scintillation noise decrease with integration time whereas noise from ATF will increase. Additionally, higher exposure times for a given star will require more defocusing, increasing contributions from read and sky noise. There exists an optimal exposure time that minimizes the total error from these sources. We estimate the optimal exposure time as a function of the magnitude of the star using our calculations for all of these sources of noise: ATF, scintillation, Poisson, read and electronic pickup, and sky. We use a model of our defocused images (including the coma-induced peak) to calculate the required defocus in order to satisfy equation (2.10) and to keep the flux below 5×10^4 e⁻/pixel (i.e., where the detector is linear to better than 0.001). We then calculate the total expected noise as a function of exposure time, assuming target and reference stars of identical flux and spectral type, yielding an optimal exposure time for a given stellar magnitude. We repeat this calculation for a range of magnitudes encompassing those in our survey (see Section 2.2). Figure 2.10 shows the optimal exposure times, defocused image radius, and calculated noise for the exposure time with the best expected precision. Our calculation overestimates exposure times for the brightest stars ($m_z \lesssim 8$), where the suggested level of defocusing becomes impractical.

In our exposure time tests, we interleave observations of a pair of stars ($m_z = 10.8$ and 11.4) using three sets of exposure times each (25s, 50s, 100s and 40s, 80s, 160 s, respectively). According to our applied noise model, the best precision should be obtained with the 50s and 80s integration times (Figure 2.10). However, the lowest total noise came from the highest exposure time (100s and 160s). Additionally, the 50/80s and the 100/160s exposure time sets beat the expected precision (see Table 2.2), suggesting that ATF may have been lower on that particular night, or that we might be averaging over stellar P-mode oscillations with longer exposure times (Young et al. 1991; Brown & Gilliland 1994; Henry 1999; Ciardi et al. 2011).

2.4.5 Choice of Comparison Star

There are noticeable gains from proper selection of a comparison star. Our collection of low-resolution spectra enables us to select comparison stars of a similar spectral type to our target, resulting in very small errors from second-order extinction (4.5×10^{-5}). If we replace all comparison stars with G dwarfs (6500 K), the median value becomes 3.0×10^{-4} , which would make it a more significant part of the error budget (Table 2.3). This is especially important with M-type target stars, which are intrinsically faint and are therefore less likely to be selected as comparison stars based on flux alone.

In principle, more comparison star observations will improve the S/N, but these additional observations will occur at increasingly earlier or later times and can engender greater systematic error due to changes in the atmosphere. We examine the constellation approach by linear construction of a reference signal \bar{s} for the j th observation of the i th star:

$$\bar{s}_{ij} = \sum_{kl} a_{ijkl} s_{kl}, \quad (2.11)$$

where s_{kl} is the flux, and the weighting function $a_{ijkl} = 0$ for $i = k$. In general, for nonzero values, a_{ijkl} will depend on the characteristics of the atmosphere, the cadence of

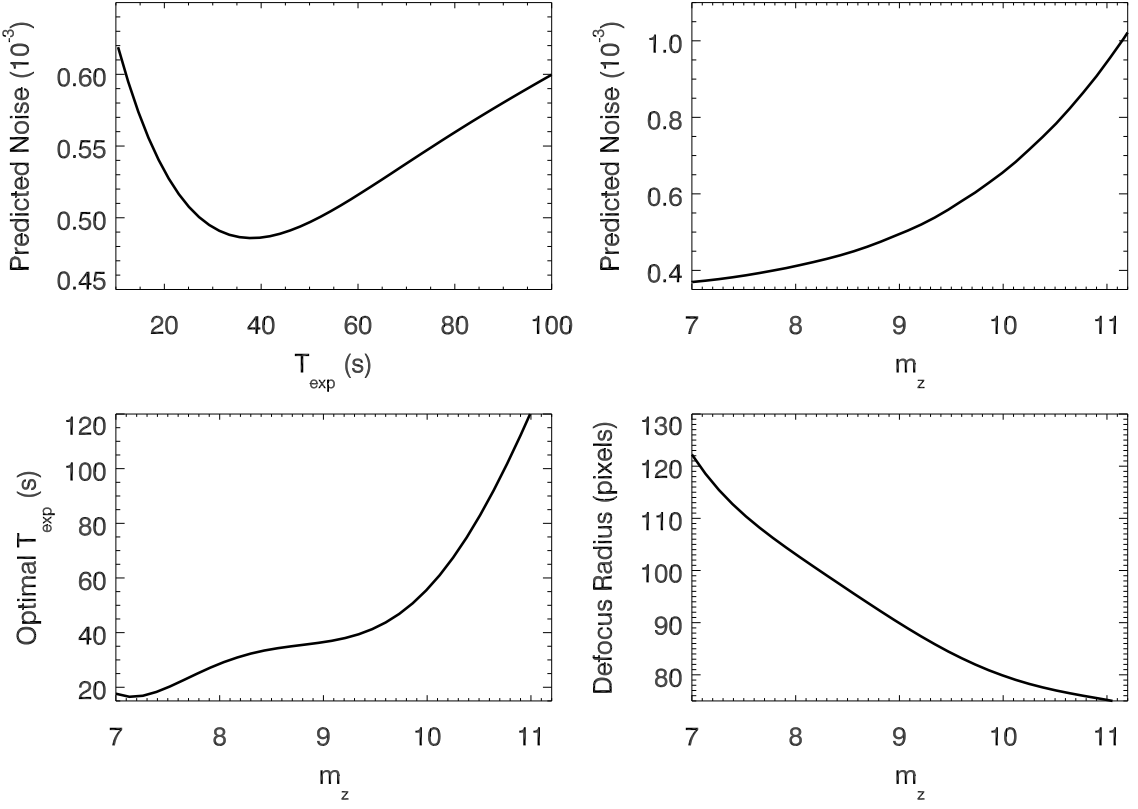


Figure 2.10: Total predicted noise as a function of exposure time (*top left*) for a $m_z = 9$ star. Also shown is the total noise (*top right*), optimal defocus radius (*bottom right*), and exposure time (*bottom left*), corresponding to the setup with the lowest theoretical noise as a function of z magnitude. We perform these calculations based on noise from Poisson statistics, read and electronic pickup noise, scintillation, sky background, and atmospheric transparency fluctuations. We have assumed 1.5 minutes for readout and slew time between stars and that the comparison and target star are of identical flux and spectral type. Note that for our stars (mostly late K and early M dwarfs) $V - z \sim 1.8$ (Covey et al. 2007).

Table 2.3. Estimated Error/Noise Budget

Noise Source ^a	Median 10^{-4}	Mean 10^{-4}
Poisson	4.8	4.9
Scintillation	3.4	3.3
Atmospheric transparency fluctuations	2.8	2.9
First-order extinction	1.0	0.91
Sky	0.99	1.3
Read and electronic pickup	0.86	0.93
Motion on chip	0.85	1.0
Second-order extinction	0.45	0.56
Shape changes	0.27	0.34
Chip/Amplifier nonlinearities	0.020	0.021

^aNoise for each star is based on our model applied to each observation (theoretical and actual precision shown in Figure 2.12). Noise is calculated per light curve (accounting for target and all comparison stars).

the observations, and the stability of the data from the stars ($i \neq k$) in the constellation. To keep the signal normalized, for all i, j we force:

$$\sum_{kl} a_{ijkl} = 1. \quad (2.12)$$

We use the constellation technique as an experiment to determine the a_{ijkl} that produces the best photometric precision. We compute a grid of reference signals for each star following equation (2.11) and apply a range of possible values for a_{ijkl} . For our observations, we find that the best precision is achieved most consistently when using a reference signal formed from the stars immediately before and after the target observation, i.e., $a_{ijkl} \sim 0$ for all $|i - k| \neq 1$ or $j \neq l$. This conclusion is consistent with our estimates of the noise from ATF (Section 2.3.3), which begin to overwhelm the noise budget when more than ~ 7 minutes passed between target and comparison star observation. However, the additional stars in the constellation can be used to identify and mitigate noise from aberrant data points (e.g., data contaminated by cosmic rays), or variable stars in the constellation. Figure 2.11 shows the precision for light curves built using the stars before and after the target observation alongside light curves (of the same stars) constructed using an equal weight of all available comparison stars.

2.5 Comparison to Observations

2.5.1 Total Errors

We calculate the total predicted error of each observation by adding the uncorrelated noise from both the target and comparison star(s) due to: scintillation, Poisson (of the star), sky (background), motion on the chip, change in shape of the defocused image, overall

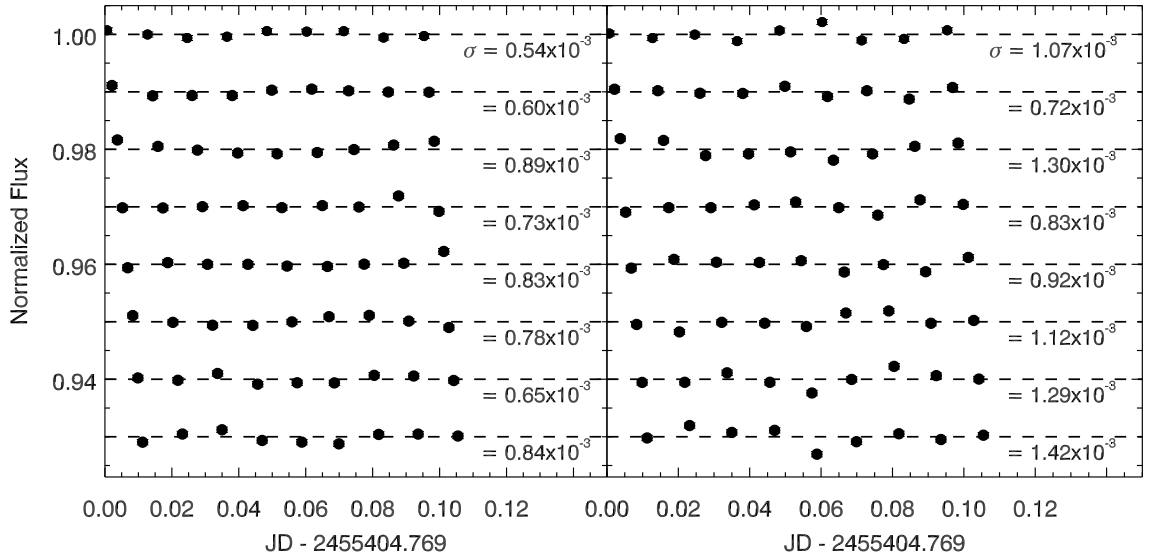


Figure 2.11: Light curves of eight stars using the constellation method along with rms using a reference signal constructed from stars observed immediately before and after the target (left), and from all seven other target stars (right). Cadence for these observations is ~ 1 observation every 17 minutes, which is sufficient to sample a transit (transits typically last $\gtrsim 1$ hr). All light curves were normalized to 1, and then each was offset in increments of 0.01 for plotting. Although using more comparison stars improves the S/N, we achieve the best overall photometric precision for each target star using a reference signal built from the stars observed immediately after and before it.

chip/amplifier nonlinearities, and readout (read plus electronic pickup noise), along with first- and second-order extinction and ATF. Noise from motion on the chip is estimated using our model of detector behavior (Section 2.3.4). The noise from the change in shape (changes in distribution of flux over the defocused image) is calculated assuming that the detector interpixel response suffers from 1% Gaussian variation. We correct for noise from first-order extinction when this noise source is greater than 1×10^{-4} and we know the extinction coefficient to better than $0.01 \text{ mag airmass}^{-1}$. Although specific levels for each term vary significantly between observations, the median values of Poisson noise are the largest, followed by noise from ATF, scintillation, first-order extinction, sky, read and electronic pickup, motion on the chip, second-order extinction, changes in shape of the PSF, and overall/amplifier nonlinearities (typical noise levels are listed in Table 2.3). The small relative size of many of these errors (second-order extinction, for example) is mostly due to judicious choices in each of our observations: e.g., wise choice of comparison stars, exposure times, and region of the detector used.

Figure 2.12 shows the precision of each observation versus the total theoretical noise for each observation. Although the mean of the predicted error is within 3% of the theoretical precision, there is significant scatter ($\text{rms} = 12\%$). We expect the major discrepancy to be in our estimate of error from ATF, which is difficult to calculate for any specific observation. Other noise terms are approximate, such as scintillation, which is only good to $\sim 20\%$ (even with modification for wind direction). We have also assumed no correlation between terms, which might be causing us to systematically underestimate noise. Additionally, stellar variability may contribute to the noise budget, e.g., P-mode oscillations, which can be noticeable for our targets (mostly late K and early M dwarfs) at our level of precision (Brown & Gilliland 1994; Henry 1999; Ciardi et al. 2011). Observations with short exposure times are especially susceptible to P-mode oscillations, as P-mode oscillations have timescales on the order of minutes (Young et al. 1991). Thus, our model correctly accounts for the overall magnitude of errors but cannot reliably predict the error of a specific observation.

2.5.2 Correlated (Red) Noise

The performance of most transit surveys is limited largely by time-correlated (red) noise, which limits gains in precision from binning/phasing data (Pont et al. 2006; Carter & Winn 2009). Red noise is also especially deleterious because it can mimic a signal of interest, leading to precise but inaccurate results. We expect to have some degree of time correlation in noise from extinction, ATF, and scintillation, which will manifest as a combination of white and red noise. Due to all these considerations, we analyze the level of red noise in our data. We estimate red noise from our comparison-star-corrected light curves using a wavelet-based method. The method, described in Carter & Winn (2009), determines parameters of noise formed as a combination of Gaussian (white) noise and noise with a power spectral density varying as $1/f^\gamma$. We test the simple case of $\gamma = 1$, as well as the case of $\gamma = 1.5$, implied by equation (2.2). No light curve shows red noise above 6×10^{-4} for either $\gamma = 1$ or $\gamma = 1.5$, and median red noise is only 2.8×10^{-4} , at least some of which is due to stellar variability. The low levels of red noise compared with total noise suggest that we are not being overly hindered by time-correlated noise sources. Thus data acquired using the snapshot technique can be binned to produce improved precision; after

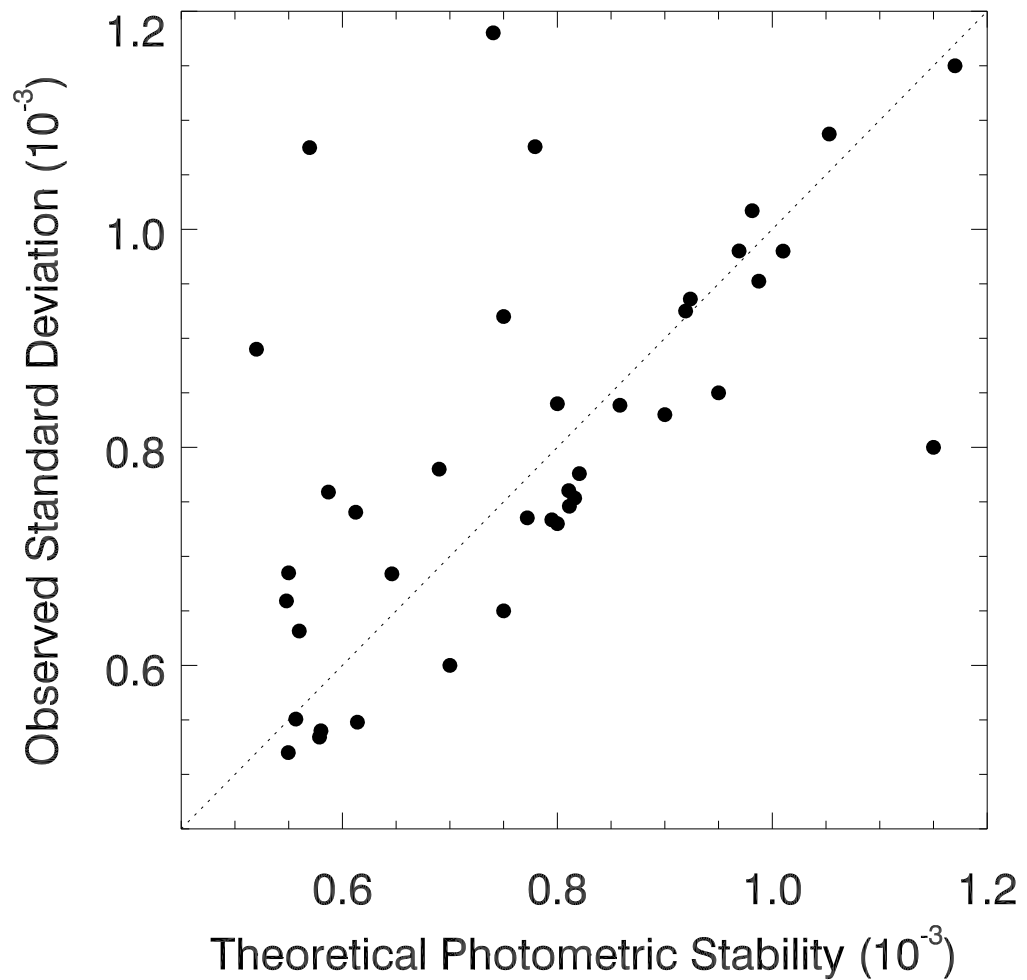


Figure 2.12: Precision of each of our observations vs. our estimated theoretical precision calculated for each observation. The dashed line marks where observed precision matches theoretical precision.

binning each observation to a cadence of less than 20 minutes, the median rms from our observations is 3.2×10^{-4} (all over intervals of at least 2 hr to ensure sufficient data points) and all binned light curves had rms of less than 10^{-3} . Further precision improvements can be made with additional binning; however, a cadence of greater than 20 minutes is impractical for detecting the presence of a transit.

2.6 Discussion

Using defocused snapshot photometry, we have consistently achieved submillimagnitude photometry from the summit of Mauna Kea under clear conditions. Our lowest photometric rms was 5.2×10^{-4} (with a 5 minute cadence) over a ~ 2 hr interval. Of our 38 experiments using the snapshot method, 32 of them had rms precision of less than 1×10^{-3} , and our median precision was 7.8×10^{-4} . We include our constellatio- mode observations, where we observe eight stars in sequence (Figure 2.11). Although our precision is not as good as the best recorded from the ground (e.g., Gilliland et al. 1993; Hartman et al. 2005), it is sufficient to detect the transit of a Neptune size planet around a dwarf M0 star or a $10M_{\oplus}$ super-Earth around an M4 star at 5σ significance. Further, our technique does not rely on a large number of comparison stars, yields submillimagnitude photometric precision consistently, and can be readily automated.

2.6.1 Methods of Submillimagnitude Photometry

Although our methods were optimized for the UH 2.2m telescope, SNIFS instrument, and Mauna Kea observing site, we give guidelines for achieving submillimagnitude photometry that can be followed by anyone. Some of these are recapitulated guidelines offered by Young et al. (1991) and Henry (1999).

Appropriate selection of comparison star: Optimal choice of comparison star is a tradeoff between minimizing the separation on the sky and using a star of comparable apparent brightness and spectral type. Submillimagnitude photometry becomes significantly more difficult with separations of more than a few minutes of slew time between target and comparison stars. Using more than two comparison stars provides no significant improvement (and usually yields inferior precision), as changes in the atmosphere grow larger than other sources of noise related to the comparison star(s) after just 7 minutes. Using two comparison stars is preferred over a single star in order to identify any signal that is the result of stellar variability instead of a transit. Large separations increase airmass differences, and give the atmosphere time (and distance) over which to change. Although stars of similar apparent brightness are preferred, this technique allows the observer to use different exposure times and focus settings for target and comparison stars. Thus, significantly dimmer or brighter comparison stars can be used with only minimal loss in precision. The spectral type of a comparison star should be similar to that of the target, especially if the stars are observed over a wide range of airmasses. It is not usually worthwhile to use comparison stars that require more than ~ 6 minutes of time between target and comparison star observation. Past this, the precision loss from atmospheric fluctuations overwhelms noise from a poor choice of comparison star.

Exposure times and defocusing: Integration times and the amount of defocus must be chosen so that the signal per pixel is within the linear range ($\ll 1\%$ nonlinear) of the detector. Young et al. (1991) suggest using shorter integrations to move rapidly between target and comparison stars. Our calculations and data indicate that the optimal exposure time depends on the tradeoffs between ATF and shot/scintillation noise, and it often exceeds 1 minute. Figure 2.10 shows how to scale exposure times and defocus radius with the brightness of the star, although the values may be significantly different for other telescopes. Assuming there are no stars that will overlap with the target when defocused, and that the detector has a sufficiently large region of well-behaved pixels, it is best to find the ideal exposure time for each star, and defocus as appropriate to keep flux levels below the nonlinear range of the detector.

Minimize time between observations: Making use of a smaller region of the chip will reduce overhead from CCD readout enough that the time between observations is usually limited by telescope/dome slew time. In the constellation method, a number of stars are observed in sequence to search for transits (Fig.s 2.2 and 2.11). In order to maximize observing efficiency and the number of targets that can be observed with the highest cadence (> 1 observation every 30 minutes), a time-efficient trajectory must connect the target stars. With an efficient path, the constellation technique can be expanded to observe a large number of stars in sequence at the cost of cadence. If the dome motion is slower than the motion of the telescope, the fastest path minimizes azimuthal moves.

Observe near meridian crossing: In addition to being at minimum airmass, objects near meridian crossing experience the smallest changes in airmass relative to nearby stars. When to observe is especially important when observing over longer periods of time (> 1 hr). For observations on the same set of stars lasting significantly longer than a few hours (producing large changes in the airmass difference), it will be necessary to take enough measurements of the extinction coefficient to constrain it to better than 0.01 mag airmass $^{-1}$ during the observation.

Selection of passband filter: We achieved similar photometric precision in both SDSS r and z passbands, possibly a result of higher scintillation noise in the former and contamination by the H₂O lines in the latter. A narrower z filter lacking the H₂O-affected wings (Figure 2.3) would avoid both of these problems, as well as reduce the size of second-order extinction.

Use of well-behaved regions of the detector: Regions of the detector containing nonlinearities, variable behavior, or significant nonuniformity must be avoided and cannot simply be corrected by flat-fielding (Figure 2.7). One significant advantage of the snapshot method is that images of the comparison star and target star can be placed in the same position on the detector. The rms of centroid motions (from integration to integration) should be kept to less than 10 pixels (Figure 2.5). Snapshot photometry only requires a field of view large enough to fit a single defocused star and enough surrounding field to estimate the sky background with an absolute error much less than that of the star.

2.6.2 Performance of a Hypothetical Transit Search

To close, we examine the performance of the photometric method described in this article using Monte Carlo simulations of a search for transiting planets around M dwarf stars. We

assume a telescope like the UH 2.2m at a photometric site such as Mauna Kea. The all-sky input catalog consists of 13,570 nearby late K and early M stars selected from photographic plate surveys based on their proper motions ($\mu > 0.15'' \text{ yr}^{-1}$) (Lépine & Shara 2005; Lépine & Gaidos 2011), and $V-J$ colors, where J -band magnitudes come from the Two Micron All Sky Survey, a near-infrared all-sky survey (Skrutskie et al. 2006). We estimate the effective temperature based on an average of $V-J$, $V-H$, $V-K$, and $J-K$ colors and temperature-color relations established by Houdashelt et al. (2000) and Casagrande et al. (2008). A bolometric correction is computed as per Houdashelt et al. (2000), assuming solar metallicity and surface gravity $\log g = 4.5$. Absolute magnitudes are calculated assuming a position on the main sequence (Lépine 2005). We make three separate estimates of the mass based on the near-infrared absolute magnitudes (Delfosse et al. 2000; Xia et al. 2008) and average them. Although a radius can be calculated from the Stefan-Boltzmann relation, we instead empirically infer it from the mass using the relation $R_* \approx M_*^{1.06}$ ($0.3M_\odot < M_* < 0.6M_\odot$) based on theoretical models (Baraffe et al. 1998) and supported by the available data on radius measurements of single stars (Demory et al. 2009).

We use the planet mass distribution $dn/d\log M_p = 0.39M_p^{0.48}$ (M in Earths) estimated by Howard et al. (2010) and the period distribution of Cumming et al. (2008): $dn/d\log(P) \sim P^{0.26}$ for $P = 2 - 2000$ days. These distributions are only known for solar-mass stars and may be different for M dwarfs (Raymond et al. 2007; Montgomery & Laughlin 2009). The recently released *Kepler* catalog of planet candidates contains ~ 1200 objects with estimated radii, but $\lesssim 3\%$ of them are around M dwarfs. We adopt the orbital eccentricity distribution derived by Shen & Turner (2008), recognizing that the distribution is well-constrained only for giant planets and that of low-mass planets may be significantly different (Pilat-Lohinger 2009; Mann et al. 2010). Inclination angles and longitudes of periaxis are drawn from isotropic distributions. For a mass-radius relationship we use the surprisingly simple formula $R_p = M_p^{0.5}$ (Earth units), which captures the overall trend for exoplanets of masses intermediate to those of Earth and Saturn. This diverges from the mass-radius relationship of rocky planets derived from interior models (e.g., Seager et al. 2007), possibly because of the tendency of more massive planets to have H/He envelopes. We assume that all planets above a mass of 125 Earths are the size of Jupiter (11.2 Earth radii).

The simulated observing program is constructed as follows. Days are first selected randomly from throughout the year. Sunset and sunrise are determined for the Mauna Kea summit, and observing begins and ends 30 minutes after and before sunset and sunrise, respectively. The short twilight interval is justified because our targets are bright and Rayleigh scattering from the sky is low in the z passband. A target is selected at random from an updated subset of the catalog that is found at an airmass below 1.4. We allow 2 minutes for the telescope to slew to each target and the instrument to set up, and we assume a fixed integration time of 2 minutes. Each target that is observed is placed on hold and will not be reobserved until at least 2 hours has elapsed (the typical duration of a transit). We do not consider the requirement that each target be observed a certain number of times each night because we ultimately sum the probability of detecting a transit over all observations, not all individual targets.

Detection requires a S/N ratio greater than 5 in a single observation. The transit signal is calculated using the limb-darkening model of Claret (2000). The total noise consists of shot

noise, scintillation noise, and other (atmospheric) noise (0.4 mmag) added in quadrature. The first two contributions are based on the performance of the SNIFS instrument and assume a SDSS z passband (see Section 2.3 for details). The detection probability is the product of the transit probability times the probability of detecting the transit averaged over 30,000 Monte Carlo realizations of planets. We can impose a Doppler detection criterion by performing the average only over those systems where the radial velocity amplitude exceeds a specified value. This simulates a scenario in which targets are first selected by Doppler observations for transit searches.

Figure 2.13 plots the average required number of clear nights per transit discovery as a function of the Doppler threshold. A higher threshold selects more massive planets on closer orbits; these are more likely to transit and are more readily detected if they do. For a 6 m s^{-1} threshold, the mass distribution of detected planets peaks at around $24 M_E$ (Neptune size). If 56% of nights are photometric (Steinbring et al. 2009), then a 1 yr survey of 6 m s^{-1} systems would produce 25 transiting systems. This would require a prohibitive number of Doppler-selected targets. In the absence of Doppler selection, a completely blind survey requires a more daunting average of 90 nights per detection, suggesting that this method is ideally suited for supplementing an existing Doppler or transit program rather than as a technique applied to a new transit survey.

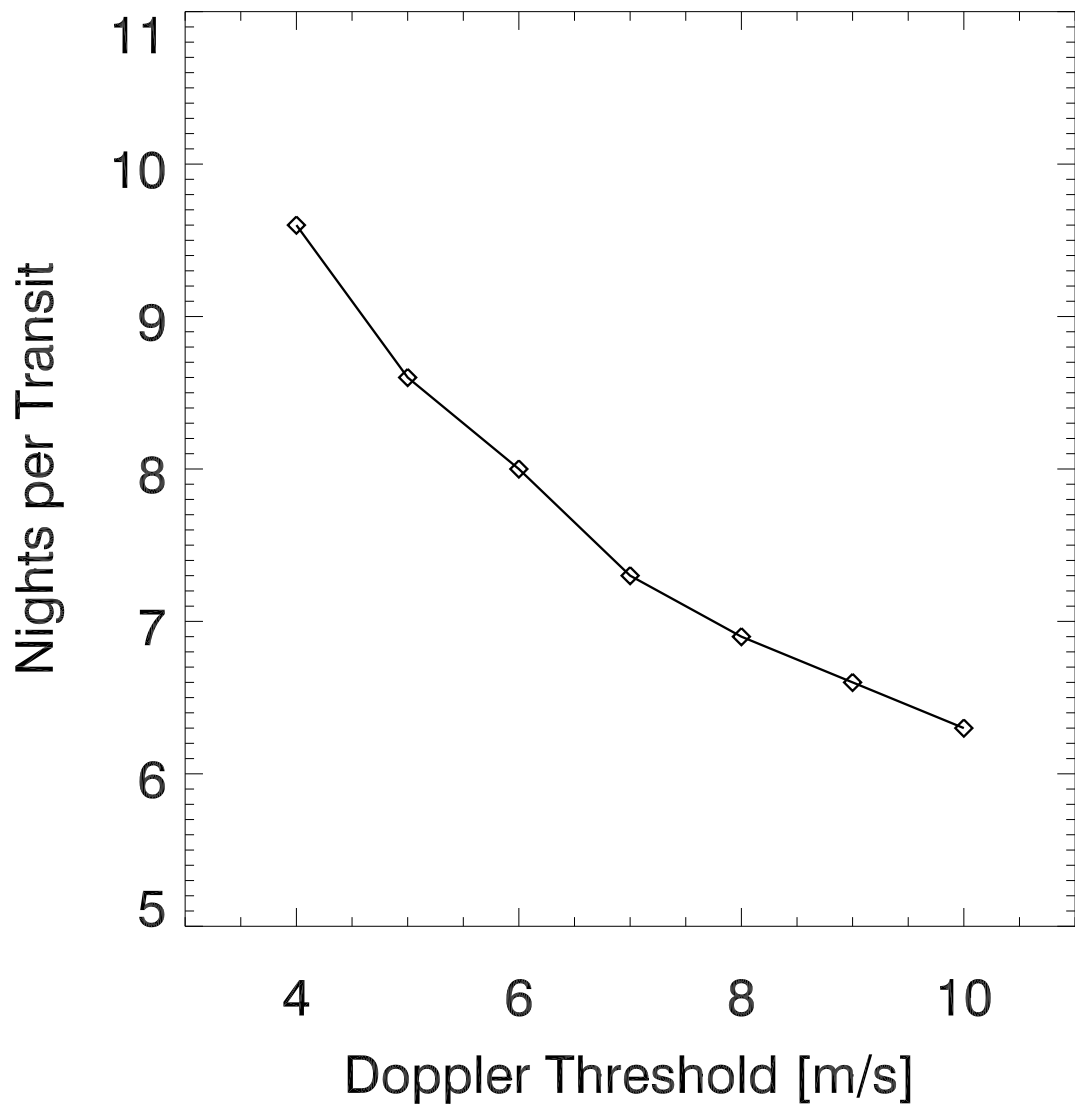


Figure 2.13: Average number of photometric observing nights before a transit is detected in a snapshot survey of M dwarf stars with a Doppler signal above the specified threshold. In making this calculation, we take into account setup, slew, twilight, and integration time, and we use precision levels attained in our SNIFS observations. A planet population similar to those around G-type stars is assumed (see Section 2.6.2 for details)

References

- Aigrain, S., Pont, F., Fressin, F., Alapini, A., Alonso, R., Auvergne, M., Barbieri, M., Barge, P., Bordé, P., Bouchy, F., Deeg, H., de La Reza, R., Deleuil, M., Dvorak, R., Erikson, A., Fridlund, M., Gondoin, P., Guterman, P., Jorda, L., Lammer, H., Léger, A., Llebaria, A., Magain, P., Mazeh, T., Moutou, C., Ollivier, M., Pätzold, M., Queloz, D., Rauer, H., Rouan, D., Schneider, J., Wuchter, G., & Zucker, S. 2009, *A&A*, 506, 425
- Aldering, G., Adam, G., Antilogus, P., Astier, P., Bacon, R., Bongard, S., Bonnaud, C., Copin, Y., Hardin, D., Henault, F., Howell, D. A., Lemonnier, J., Levy, J., Loken, S. C., Nugent, P. E., Pain, R., Pecontal, A., Pecontal, E., Perlmutter, S., Quimby, R. M., Schahmaneche, K., Smadja, G., & Wood-Vasey, W. M. 2002, in Proc. SPIE, ed. J. A. Tyson & S. Wolff, Vol. 4836, 61–72
- Antilogus, P., Thomas, R. C., Aldering, G., Aragon, C., Copin, Y., Gangler, E., Hornero, E., Pecontal, A., Poon, S., Runge, K., Scalzo, R., Bailey, S., Baltay, C., Buton, C., Bongard, S., Childress, M., Loken, S., Nugent, P., Pain, R., Pecontal, E., Pereira, R., Perlmutter, S., Rabinowitz, D., Rigaudier, G., Smadja, G., Tao, C., & Wu, C. 2008, in Proc. SPIE, Vol. 7016
- Apps, K., Clubb, K. I., Fischer, D. A., Gaidos, E., Howard, A., Johnson, J. A., Marcy, G. W., Isaacson, H., Giguere, M. J., Valenti, J. A., Rodriguez, V., Chubak, C., & Lepine, S. 2010, *PASP*, 122, 156
- Baraffe, I., Chabrier, G., Allard, F., & Hauschildt, P. H. 1998, *A&A*, 337, 403
- Behr, A. 1973, *A&A*, 28, 355
- Birney, D. S., Gonzalez, G., & Oesper, D. 2006, *Observational Astronomy - 2nd Edition* (Cambridge University Press)
- Bond, I. A., Udalski, A., Jaroszyński, M., Rattenbury, N. J., Paczyński, B., Soszyński, I., Wyrzykowski, L., Szymański, M. K., Kubiak, M., Szewczyk, O., Źebruń, K., Pietrzyński, G., Abe, F., Bennett, D. P., Eguchi, S., Furuta, Y., Hearnshaw, J. B., Kamiya, K., Kilmartin, P. M., Kurata, Y., Masuda, K., Matsubara, Y., Muraki, Y., Noda, S., Okajima, K., Sako, T., Sekiguchi, T., Sullivan, D. J., Sumi, T., Tristram, P. J., Yanagisawa, T., & Yock, P. C. M. 2004, *ApJ*, 606, L155
- Brown, T. M. & Gilliland, R. L. 1994, *ARA&A*, 32, 37

- Carter, J. A. & Winn, J. N. 2009, ApJ, 704, 51
- Casagrande, L., Flynn, C., & Bessell, M. 2008, MNRAS, 389, 585
- Charbonneau, D., Berta, Z. K., Irwin, J., Burke, C. J., Nutzman, P., Buchhave, L. A., Lovis, C., Bonfils, X., Latham, D. W., Udry, S., Murray-Clay, R. A., Holman, M. J., Falco, E. E., Winn, J. N., Queloz, D., Pepe, F., Mayor, M., Delfosse, X., & Forveille, T. 2009, Nature, 462, 891
- Charbonneau, D., Brown, T. M., Burrows, A., & Laughlin, G. 2007, Protostars and Planets V, 701
- Charbonneau, D., Brown, T. M., Latham, D. W., & Mayor, M. 2000, ApJ, 529, L45
- Cherubini, T., Businger, S., Lyman, R., & Chun, M. 2008, Journal of Applied Meteorology and Climatology, 47, 1140
- Ciardi, D. R., von Braun, K., Bryden, G., van Eyken, J., Howell, S. B., Kane, S. R., Plavchan, P., Ramírez, S. V., & Stauffer, J. R. 2011, AJ, 141, 108
- Claret, A. 2000, A&A, 363, 1081
- Covey, K. R., Ivezić, Ž., Schlegel, D., Finkbeiner, D., Padmanabhan, N., Lupton, R. H., Agüeros, M. A., Bochanski, J. J., Hawley, S. L., West, A. A., Seth, A., Kimball, A., Gogarten, S. M., Claire, M., Haggard, D., Kaib, N., Schneider, D. P., & Sesar, B. 2007, AJ, 134, 2398
- Cumming, A., Butler, R. P., Marcy, G. W., Vogt, S. S., Wright, J. T., & Fischer, D. A. 2008, PASP, 120, 531
- Dainty, J. C., Levine, B. M., Brames, B. J., & Odonnell, K. A. 1982, Appl. Opt., 21, 1196
- Davis, G. R., Naylor, D. A., Griffin, M. J., Clark, T. A., & Holland, W. S. 1997, Icarus, 130, 387
- Delfosse, X., Forveille, T., Ségransan, D., Beuzit, J., Udry, S., Perrier, C., & Mayor, M. 2000, A&A, 364, 217
- Demory, B.-O., Ségransan, D., Forveille, T., Queloz, D., Beuzit, J.-L., Delfosse, X., di Folco, E., Kervella, P., Le Bouquin, J.-B., Perrier, C., Benisty, M., Duvert, G., Hofmann, K.-H., Lopez, B., & Petrov, R. 2009, A&A, 505, 205
- Dravins, D., Lindegren, L., Mezey, E., & Young, A. T. 1998, PASP, 110, 1118
- Everett, M. E. & Howell, S. B. 2001, PASP, 113, 1428
- Fukugita, M., Ichikawa, T., Gunn, J. E., Doi, M., Shimasaku, K., & Schneider, D. P. 1996, AJ, 111, 1748
- Genet, R. M., Boyd, L. J., Kissell, K. E., Crawford, D. L., & Hall, D. S. 1987, PASP, 99, 660

- Gilliland, R. L., Brown, T. M., Kjeldsen, H., McCarthy, J. K., Peri, M. L., Belmonte, J. A., Vidal, I., Cram, L. E., Palmer, J., Frandsen, S., Parthasarathy, M., Petro, L., Schneider, H., Stetson, P. B., & Weiss, W. W. 1993, AJ, 106, 2441
- Gillon, M., Pont, F., Demory, B., Mallmann, F., Mayor, M., Mazeh, T., Queloz, D., Shporer, A., Udry, S., & Vuissoz, C. 2007, A&A, 472, L13
- Gillon, M., Smalley, B., Hebb, L., Anderson, D. R., Triaud, A. H. M. J., Hellier, C., Maxted, P. F. L., Queloz, D., & Wilson, D. M. 2009, A&A, 496, 259
- Gould, A., Dong, S., Gaudi, B. S., Udalski, A., Bond, I. A., Greenhill, J., Street, R. A., Dominik, M., Sumi, T., Szymański, M. K., Han, C., Allen, W., Bolt, G., Bos, M., Christie, G. W., DePoy, D. L., Drummond, J., Eastman, J. D., Gal-Yam, A., Higgins, D., Janczak, J., Kaspi, S., Kozłowski, S., Lee, C., Mallia, F., Maury, A., Maoz, D., McCormick, J., Monard, L. A. G., Moorhouse, D., Morgan, N., Natusch, T., Ofek, E. O., Park, B., Pogge, R. W., Polishook, D., Santallo, R., Shporer, A., Spector, O., Thornley, G., Yee, J. C., The μ FUN Collaboration, Kubiak, M., Pietrzyński, G., Soszyński, I., Szewczyk, O., Wyrzykowski, L., Ulaczyk, K., Poleski, R., The OGLE Collaboration, Abe, F., Bennett, D. P., Botzler, C. S., Douchin, D., Freeman, M., Fukui, A., Furusawa, K., Hearnshaw, J. B., Hosaka, S., Itow, Y., Kamiya, K., Kilmartin, P. M., Korpela, A., Lin, W., Ling, C. H., Makita, S., Masuda, K., Matsubara, Y., Miyake, N., Muraki, Y., Nagaya, M., Nishimoto, K., Ohnishi, K., Okumura, T., Perrott, Y. C., Philpott, L., Rattenbury, N., Saito, T., Sako, T., Sullivan, D. J., Sweatman, W. L., Tristram, P. J., von Seggern, E., Yock, P. C. M., The MOA Collaboration, Albrow, M., Batista, V., Beaulieu, J. P., Brillant, S., Caldwell, J., Calitz, J. J., Cassan, A., Cole, A., Cook, K., Coutures, C., Dieters, S., Dominis Prester, D., Donatowicz, J., Fouqué, P., Hill, K., Hoffman, M., Jablonski, F., Kane, S. R., Kains, N., Kubas, D., Marquette, J., Martin, R., Martioli, E., Meintjes, P., Menzies, J., Pedretti, E., Pollard, K., Sahu, K. C., Vinter, C., Wambsganss, J., Watson, R., Williams, A., Zub, M., The PLANET Collaboration, Allan, A., Bode, M. F., Bramich, D. M., Burgdorf, M. J., Clay, N., Fraser, S., Hawkins, E., Horne, K., Kerins, E., Lister, T. A., Mottram, C., Saunders, E. S., Snodgrass, C., Steele, I. A., Tsapras, Y., The RoboNet Collaboration, Jørgensen, U. G., Anguita, T., Bozza, V., Calchi Novati, S., Harpsøe, K., Hinse, T. C., Hundertmark, M., Kjærgaard, P., Liebig, C., Mancini, L., Masi, G., Mathiasen, M., Rahvar, S., Ricci, D., Scarpetta, G., Southworth, J., Surdej, J., Thöne, C. C., & MiNDSTEP Consortium, T. 2010, ApJ, 720, 1073
- Grauer, A. D., Neely, A. W., & Lacy, C. H. S. 2008, PASP, 120, 992
- Hartman, J. D., Bakos, G. Á., Noyes, R. W., Sipőcz, B., Kovács, G., Mazeh, T., Shporer, A., & Pál, A. 2011, AJ, 141, 166
- Hartman, J. D., Stanek, K. Z., Gaudi, B. S., Holman, M. J., & McLeod, B. A. 2005, AJ, 130, 2241
- Heasley, J. N., Janes, K., Labonte, B., Guenther, D., Mickey, D., & Demarque, P. 1996, PASP, 108, 385

- Henry, G. W. 1999, PASP, 111, 845
- Henry, G. W., Fekel, F. C., Henry, S. M., & Hall, D. S. 2000a, ApJS, 130, 201
- Henry, G. W., Marcy, G. W., Butler, R. P., & Vogt, S. S. 2000b, ApJ, 529, L41
- Hill, F., Fischer, G., Forgach, S., Grier, J., Leibacher, J. W., Jones, H. P., Jones, P. B., Kupke, R., Stebbins, R. T., & Clay, D. W. 1994, Sol. Phys., 152, 351
- Hodgkin, S. T., Irwin, M. J., Hewett, P. C., & Warren, S. J. 2009, MNRAS, 394, 675
- Holman, M. J., Winn, J. N., Latham, D. W., O'Donovan, F. T., Charbonneau, D., Bakos, G. A., Esquerdo, G. A., Hergenrother, C., Everett, M. E., & Pál, A. 2006, ApJ, 652, 1715
- Houdashelt, M. L., Bell, R. A., & Sweigart, A. V. 2000, AJ, 119, 1448
- Howard, A. W., Johnson, J. A., Marcy, G. W., Fischer, D. A., Wright, J. T., Henry, G. W., Giguere, M. J., Isaacson, H., Valenti, J. A., Anderson, J., & Piskunov, N. E. 2009, ApJ, 696, 75
- Howard, A. W., Marcy, G. W., Johnson, J. A., Fischer, D. A., Wright, J. T., Isaacson, H., Valenti, J. A., Anderson, J., Lin, D. N. C., & Ida, S. 2010, Science, 330, 653
- Howell, S. B., Everett, M. E., Tonry, J. L., Pickles, A., & Dain, C. 2003, PASP, 115, 1340
- Howell, S. B., VanOutryve, C., Tonry, J. L., Everett, M. E., & Schneider, R. 2005, PASP, 117, 1187
- Jenkins, J. M., Caldwell, D. A., Chandrasekaran, H., Twicken, J. D., Bryson, S. T., Quintana, E. V., Clarke, B. D., Li, J., Allen, C., Tenenbaum, P., Wu, H., Klaus, T. C., Van Cleve, J., Dotson, J. A., Haas, M. R., Gilliland, R. L., Koch, D. G., & Borucki, W. J. 2010, ApJ, 713, L120
- Johnson, J. A., Winn, J. N., Cabrera, N. E., & Carter, J. A. 2009, ApJ, 692, L100
- Kenyon, S. L., Lawrence, J. S., Ashley, M. C. B., Storey, J. W. V., Tokovinin, A., & Fossat, E. 2006, PASP, 118, 924
- Koch, D. G., Borucki, W. J., Basri, G., Batalha, N. M., Brown, T. M., Caldwell, D., Christensen-Dalsgaard, J., Cochran, W. D., DeVore, E., Dunham, E. W., Gautier, III, T. N., Geary, J. C., Gilliland, R. L., Gould, A., Jenkins, J., Kondo, Y., Latham, D. W., Lissauer, J. J., Marcy, G., Monet, D., Sasselov, D., Boss, A., Brownlee, D., Caldwell, J., Dupree, A. K., Howell, S. B., Kjeldsen, H., Meibom, S., Morrison, D., Owen, T., Reitsema, H., Tarter, J., Bryson, S. T., Dotson, J. L., Gazis, P., Haas, M. R., Kolodziejczak, J., Rowe, J. F., Van Cleve, J. E., Allen, C., Chandrasekaran, H., Clarke, B. D., Li, J., Quintana, E. V., Tenenbaum, P., Twicken, J. D., & Wu, H. 2010, ApJ, 713, L79
- Kornilov, V. G. 2011, Astronomy Letters, 37, 40
- Kowalski, A. F., Hawley, S. L., Hilton, E. J., Becker, A. C., West, A. A., Bochanski, J. J., & Sesar, B. 2009, AJ, 138, 633

- Kurucz, R. L. 1991, in NATO ASIC Proc. 341: Stellar Atmospheres - Beyond Classical Models, 441–+
- Lantz, B., Aldering, G., Antilogus, P., Bonnaud, C., Capoani, L., Castera, A., Copin, Y., Dubet, D., Gangler, E., Henault, F., Lemonnier, J.-P., Pain, R., Pecontal, A., Pecontal, E., & Smadja, G. 2004, in Society of Photo-Optical Instrumentation Engineers (SPIE) Conference Series, Vol. 5249, Society of Photo-Optical Instrumentation Engineers (SPIE) Conference Series, ed. L. Mazuray, P. J. Rogers, & R. Wartmann, 146–155
- Lépine, S. 2005, AJ, 130, 1680
- Lépine, S. & Gaidos, E. 2011, AJ, 142, 138
- Lépine, S. & Shara, M. M. 2005, AJ, 129, 1483
- Lo Curto, G., Mayor, M., Benz, W., Bouchy, F., Lovis, C., Moutou, C., Naef, D., Pepe, F., Queloz, D., Santos, N. C., Segransan, D., & Udry, S. 2010, A&A, 512, A48+
- Manfroid, J. 1995, A&AS, 113, 587
- Manfroid, J., Royer, P., Rauw, G., & Gosset, E. 2001, in Astronomical Society of the Pacific Conference Series, Vol. 238, Astronomical Data Analysis Software and Systems X, ed. F. R. Harnden Jr., F. A. Primini, & H. E. Payne, 373–+
- Mann, A. W., Gaidos, E., & Gaudi, B. S. 2010, ApJ, 719, 1454
- Mayor, M., Bonfils, X., Forveille, T., Delfosse, X., Udry, S., Bertaix, J., Beust, H., Bouchy, F., Lovis, C., Pepe, F., Perrier, C., Queloz, D., & Santos, N. C. 2009, A&A, 507, 487
- McCord, T. B. & Clark, R. N. 1979, PASP, 91, 571
- Montgomery, R. & Laughlin, G. 2009, Icarus, 202, 1
- Moutou, C., Pont, F., Bouchy, F., & Mayor, M. 2004, A&A, 424, L31
- Newberry, M. V. 1991, PASP, 103, 122
- Pereira, R., Aldering, G., Antilogus, P., Aragon, C., Bailey, S., Baltay, C., Bongard, S., Buton, C., Childress, M., Chotard, N., Copin, Y., Gangler, E., Loken, S., Nugent, P., Pain, R., Pecontal, E., Perlmutter, S., Rabinowitz, D., Rigaudier, G., Runge, K., Scalzo, R., Smadja, G., Fakhouri, H. K., Tao, C., Thomas, R. C., & Wu, C. 2010, in Proc. American Institute of Physics, ed. J.-M. Alimi & A. Fuözfa, Vol. 1241, 259–266
- Pilat-Lohinger, E. 2009, International Journal of Astrobiology, 8, 175
- Pollacco, D. L., Skillen, I., Collier Cameron, A., Christian, D. J., Hellier, C., Irwin, J., Lister, T. A., Street, R. A., West, R. G., Anderson, D., Clarkson, W. I., Deeg, H., Enoch, B., Evans, A., Fitzsimmons, A., Haswell, C. A., Hodgkin, S., Horne, K., Kane, S. R., Keenan, F. P., Maxted, P. F. L., Norton, A. J., Osborne, J., Parley, N. R., Ryans, R. S. I., Smalley, B., Wheatley, P. J., & Wilson, D. M. 2006, PASP, 118, 1407

- Pont, F., Zucker, S., & Queloz, D. 2006, MNRAS, 373, 231
- Raymond, S. N., Scalo, J., & Meadows, V. S. 2007, ApJ, 669, 606
- Roddier, F. 1981, Progress in optics. Volume 19. Amsterdam, North-Holland Publishing Co., 1981, p. 281-376., 19, 281
- Rothman, L. S., Gordon, I. E., Barbe, A., Benner, D. C., Bernath, P. F., Birk, M., Boudon, V., Brown, L. R., Campargue, A., Champion, J.-P., Chance, K., Coudert, L. H., Dana, V., Devi, V. M., Fally, S., Flaud, J.-M., Gamache, R. R., Goldman, A., Jacquemart, D., Kleiner, I., Lacome, N., Lafferty, W. J., Mandin, J.-Y., Massie, S. T., Mikhailenko, S. N., Miller, C. E., Moazzen-Ahmadi, N., Naumenko, O. V., Nikitin, A. V., Orphal, J., Perevalov, V. I., Perrin, A., Predoi-Cross, A., Rinsland, C. P., Rotger, M., Šimečková, M., Smith, M. A. H., Sung, K., Tashkun, S. A., Tennyson, J., Toth, R. A., Vandaele, A. C., & Vander Auwera, J. 2009, J. Quant. Spec. Radiat. Transf., 110, 533
- Seager, S., Kuchner, M., Hier-Majumder, C. A., & Militzer, B. 2007, ApJ, 669, 1279
- Shen, Y. & Turner, E. L. 2008, ApJ, 685, 553
- Skrutskie, M. F., Cutri, R. M., Stiening, R., Weinberg, M. D., Schneider, S., Carpenter, J. M., Beichman, C., Capps, R., Chester, T., Elias, J., Huchra, J., Liebert, J., Lonsdale, C., Monet, D. G., Price, S., Seitzer, P., Jarrett, T., Kirkpatrick, J. D., Gizis, J. E., Howard, E., Evans, T., Fowler, J., Fullmer, L., Hurt, R., Light, R., Kopan, E. L., Marsh, K. A., McCallon, H. L., Tam, R., Van Dyk, S., & Wheelock, S. 2006, AJ, 131, 1163
- Southworth, J. 2010, MNRAS, 408, 1689
- Southworth, J., Hinse, T. C., Jørgensen, U. G., Dominik, M., Ricci, D., Burgdorf, M. J., Hornstrup, A., Wheatley, P. J., Anguita, T., Bozza, V., Novati, S. C., Harpsøe, K., Kjærgaard, P., Liebig, C., Mancini, L., Masi, G., Mathiasen, M., Rahvar, S., Scarpetta, G., Snodgrass, C., Surdej, J., Thöne, C. C., & Zub, M. 2009, MNRAS, 396, 1023
- Southworth, J., Mancini, L., Novati, S. C., Dominik, M., Glitrup, M., Hinse, T. C., Jørgensen, U. G., Mathiasen, M., Ricci, D., Maier, G., Zimmer, F., Bozza, V., Browne, P., Bruni, I., Burgdorf, M., Dall’Ora, M., Finet, F., Harpsøe, K., Hundertmark, M., Liebig, C., Rahvar, S., Scarpetta, G., Skottfelt, J., Smalley, B., Snodgrass, C., & Surdej, J. 2010, MNRAS, 408, 1680
- Souza, S. P., Babcock, B. A., Pasachoff, J. M., Gulbis, A. A. S., Elliot, J. L., Person, M. J., & Gangestad, J. W. 2006, PASP, 118, 1550
- Steinbring, E., Cuillandre, J., & Magnier, E. 2009, PASP, 121, 295
- Stubbs, C. W., High, F. W., George, M. R., DeRose, K. L., Blondin, S., Tonry, J. L., Chambers, K. C., Granett, B. R., Burke, D. L., & Smith, R. C. 2007, PASP, 119, 1163
- Tobin, W. 1993, in IAU Colloq. 136: Stellar Photometry - Current Techniques and Future Developments, ed. C. J. Butler & I. Elliott, 304–+

- Tonry, J. L., Howell, S. B., Everett, M. E., Rodney, S. A., Willman, M., & VanOutryve, C. 2005, PASP, 117, 281
- Vacca, W. D., Cushing, M. C., & Rayner, J. T. 2004, PASP, 116, 352
- Vogt, S. S., Wittenmyer, R. A., Butler, R. P., O'Toole, S., Henry, G. W., Rivera, E. J., Meschiari, S., Laughlin, G., Tinney, C. G., Jones, H. R. A., Bailey, J., Carter, B. D., & Batygin, K. 2010, ApJ, 708, 1366
- Winn, J. N., Holman, M. J., Carter, J. A., Torres, G., Osip, D. J., & Beatty, T. 2009, AJ, 137, 3826
- Winn, J. N., Holman, M. J., & Fuentes, C. I. 2007, AJ, 133, 11
- Xia, F., Ren, S., & Fu, Y. 2008, Ap&SS, 314, 51
- Young, A. T. 1974, ApJ, 189, 587
- . 1993, The Observatory, 113, 41
- Young, A. T., Genet, R. M., Boyd, L. J., Borucki, W. J., Lockwood, G. W., Henry, G. W., Hall, D. S., Smith, D. P., Baliumas, S. L., Donahue, R., & Epand, D. H. 1991, PASP, 103, 221
- Zombeck, M. 2007, Handbook of Space Astronomy and Astrophysics: Third Edition (Cambridge University Press)

Chapter 3

They might be giants: luminosity class, planet occurrence, and planet-metallicity relation of the coolest *Kepler* target stars

Published as Mann, Andrew W.; Gaidos, Eric; Lpine, Sbastien; Hilton, Eric J.; 2012,
ApJ, 753, 90

Abstract

We estimate the stellar parameters of late K and early M type *Kepler* target stars. We obtain medium resolution visible spectra of 382 stars with $K_P - J > 2$ (\simeq K5 and later spectral type). We determine luminosity class by comparing the strength of gravity-sensitive indices (CaH, K I, Ca II, and Na I) to their strength in a sample of stars of known luminosity class. We find that giants constitute $96 \pm 1\%$ of the bright ($K_P < 14$) *Kepler* target stars, and $7 \pm 3\%$ of dim ($K_P > 14$) stars, significantly higher than fractions based on the stellar parameters quoted in the *Kepler* Input Catalog (KIC). The KIC effective temperatures are systematically $(110^{+15}_{-35}$ K) higher than temperatures we determine from fitting our spectra to PHOENIX stellar models. Through Monte Carlo simulations of the *Kepler* exoplanet candidate population, we find a planet occurrence of 0.36 ± 0.08 when giant stars are properly removed, somewhat higher than when a KIC $\log g > 4$ criterion is used (0.27 ± 0.05). Lastly, we show that there is no significant difference in $g - r$ color (a probe of metallicity) between late-type *Kepler* stars with transiting Earth-to-Neptune sized exoplanet candidates and dwarf stars with no detected transits. We show that a previous claimed offset between these two populations is most likely an artifact of including a large number of misidentified giants.

3.1 Introduction

The NASA *Kepler* mission (Borucki et al. 2010) has ushered exoplanet science into a new phase of analysis based on the statistics of large samples. Among the more elementary statistics derived from *Kepler* results are the planet occurrence around stars (Howard et al.

2012, henceforth H12), the distribution of planet size (or mass Wolfgang & Laughlin 2012; Gaidos et al. 2012), correlations between the presence of planets and the properties of the host stars (e.g. Schlaufman & Laughlin 2011, henceforth SL11), and the characteristics of multi-planet systems (Fabrycky et al. 2012). These findings yield important constraints on models of planet formation and evolution, and are best established for solar-type stars (late F through early K spectral types) because they constitute the vast majority of *Kepler* targets.

The results of *Kepler* were first preceded by the findings of radial velocity surveys of solar-type stars. More than 15% of dwarf stars have close-in (~ 0.25 AU) planets with orbital periods less than 50 days (Howard et al. 2010, 2012) and this fraction increases with orbital period (Mayor et al. 2011). The same authors find that planet occurrence is inversely related to planet mass or radius, with “super-Earths” outnumbering Jupiter-size planets by more than an order of magnitude. Around solar-type stars, the presence of giant planets is strongly correlated with super-solar metallicity (Gonzalez 1997; Santos et al. 2004; Fischer & Valenti 2005; Johnson et al. 2010), but this correlation does not appear to hold for smaller planets (Sousa et al. 2008; Bouchy et al. 2009; Mayor et al. 2011). As with results from *Kepler*, these findings are primarily for solar-type stars because many nearby representatives are bright enough for ground-based Doppler radial velocity observations.

Very cool (late K and early M type) dwarf stars have become popular targets of planet searches (e.g. Charbonneau et al. 2009; Vogt et al. 2010; Bean et al. 2010; Mann et al. 2011; Apps et al. 2010; Fischer et al. 2012). Planets around cool stars are easier to detect because of the stars’ smaller masses and radii. Furthermore, because these stars are less luminous, close-in and thus detectable planets can still orbit within the “habitable zone,” where an Earth-like planet would avoid the “snowball” or runaway greenhouse climate states (Gaidos et al. 2007). However, the statistics of planets around these stars are poorly established. These stars are underrepresented in magnitude-limited Doppler surveys as well as the *Kepler* target list. Only 2% of *Kepler* target stars are classified as possible M types (cooler than 4000 K), whereas $>70\%$ of all stars within 20 pc are M dwarfs (Henry et al. 1994; Chabrier 2003; Reid et al. 2004).

Nevertheless, *Kepler* data has been used to draw two important conclusions about late-type exoplanet hosts. First, H12 found that the frequency of stars with planets on close-in ($P < 50$ d) orbits rises with decreasing effective temperature through early K-type and that an even higher fraction of M dwarf stars may host such planets. Second, SL11 claimed that late K dwarf stars, but not solar-type stars, hosting super-Earth to Neptune sized candidate transiting planets are more metal rich than stars for which transits have not been detected. These findings offer potential tests of theories of planet formation (Fischer & Valenti 2005; Kennedy & Kenyon 2008; Cumming et al. 2008)

Kepler targets are selected from the *Kepler* input catalog (KIC) based on the ability of the mission to find transiting planets, especially in the habitable zone; ideally, the target catalog should consist exclusively of dwarf stars for which the signal of a transiting planet is largest, and exclude sub-giant and giant stars. Brown et al. (2011) used D51 (Mg Ib line) photometry and Sloan *g*-D51 color to exclude giants, however this is also sensitive to temperature and metallicity and is not available for all targets. The KIC includes Sloan (*griz*) and 2MASS (*JHK*) magnitudes; stellar parameters are estimated by forward modeling of the photometric data with the synthetic spectra of Castelli & Kurucz (2004),

and effective temperature T_{eff} , gravity log g , and metallicity [M/H] as free parameters. Stellar mass and distance are then estimated using luminosity, T_{eff} , and log g from the stellar evolutionary models of Girardi et al. (2000). The combination of stellar mass and log g then yields a stellar radius.

Brown et al. (2011) state that KIC radius estimates have average errors of 35% and are not reliable for stars cooler than 4000 K. H12 point out that, because of the difficulty in constraining log g , the radii of some stars, particularly sub-giants, may be underestimated by a factor of 2 or more in the KIC. Gaidos et al. (2012) found that consistency between the *Kepler* candidate planet catalog and the M2K Doppler survey could be achieved if the former was incomplete compared to estimates based on KIC radii. They further point out that *Kepler* planet candidates were conspicuously sparse among late K stars with colors that are shared by both dwarfs and giant stars. Finally, Muirhead et al. (2012) (henceforth M12) showe that KIC estimates for the radii of many *Kepler* M dwarfs hosting planets are smaller than KIC values by as much as a factor of two. This discrepancy is not to be confused with the 5-10% radius difference between radii of the most refined models and measurements by interferometry and observations of eclipsing binaries (e.g. López-Santiago et al. 2010; Kraus et al. 2011).

Reliable stellar parameters are a prerequisite for robust statistical analysis of planets, especially transiting planets. These are needed not only for stars for which planet candidates have been detected (referred to as Kepler Objects of Interest or KOIs), but also for the target sample as a whole. The radius of a planet producing a given transit depth is proportional to the radius of its host star. Likewise, the transit signal produced by a planet of a given radius - and hence its detectability around a star in the survey - also depends on stellar radius. If some target stars are actually larger or even giant stars, then planets are less likely to be detected in that sample, which means that the most likely occurrence rate of those planets is higher. For M dwarf stars in general, and particularly for the coolest *Kepler* target stars, parameters such as radius are uncertain or even very unreliable (e.g. Johnson et al. 2012, M12).

Brown et al. (2011) metallicities are reliable to 0.4 dex for solar-type stars, but are essentially useless for stars with $T_{eff} < 4000$. Instead, SL11 use Sloan $g - r$ colors for a given $J - H$ range (a proxy for spectral type) as an indicator of the amount of Fe line blanketing at blue wavelengths, and hence metallicity. They construct mean $g - r$ vs. $J - H$ loci for KOIs and *Kepler* stars without identified transits. They find a significant difference between the $g - r$ colors of the two populations for stars with $J - H \approx 0.62$, corresponding to late K-type stars. Based on stellar models, SL11 argue that the late-type KOIs are $\simeq 0.2$ dex more metal rich than *Kepler* targets with no detected transit. However, K giants are significantly bluer than dwarfs in $g - r$, for the same $J - H$ (Yanny et al. 2009). Thus, contamination of the *Kepler* target sample by giants would shift the locus of target stars to bluer $g - r$, but would not affect the KOI locus, as planets are less detectable, or completely undetectable around giant stars. Realizing this, SL11 constructed and analyzed artificial mixed data sets to estimate that a 10-30% contamination by giants would also produce the observed offset.

M12 use the equivalent widths of atomic lines in the K ($2.2 \mu\text{m}$) band (Rojas-Ayala et al. 2012) and their measurements of late-type KOIs' metallicities are consistent with, or slightly metal-poor (median [M/H] = -0.10) compared to the solar neighborhood (M/H

$\simeq -0.05$ Johnson & Apps 2009). SL11 and M12 are consistent with each other if the *Kepler* target list itself is biased toward metal-poor M dwarfs, or if the offset found by SL11 is due to high giant contamination in *Kepler* late-type target stars.

Moderate resolution spectra are nearly always sufficient to distinguish K and M giants from their dwarf cousins. In addition Ciardi et al. (2011) showed that some giant stars can be identified based on *JHK* photometry alone. In this paper, we combine moderate resolution spectra of a sample of Kepler targets with KIC photometry to refine the planet occurrence rate for late-type stars calculated by H12, and determine if the giant fraction is high enough to explain the color offset observed by SL11. In Section 3.2 we present spectroscopy of a representative sample of late-type *Kepler* target stars. In Section 3.3 we use both spectroscopy and photometry to derive luminosity classes and calculate the giant fraction for late-type *Kepler* target stars. In Section 3.4 we use this information, plus radii based on stellar evolutionary models, to refine the planet occurrence around these stars. In Section 3.5 we calculate and compare the mean $g - r$ colors (as metallicity proxies) of KOIs and a *bona fide* dwarf sample, and show how and why our results differ from those of SL11.

3.2 Sample, Observations, and Reduction

Because derived KIC parameters may not always be reliable, we instead select our sample using photometry. A sample of stars with $V - J > 2.5$ will include $> 98\%$ of all M dwarfs, as well as most of the K7 dwarfs in the sample (Lépine & Gaidos 2011, henceforth LG11). Although 2MASS J magnitudes are available for almost the entire sample, V magnitudes are not. *Kepler* magnitudes (K_P), however, are available for all target stars. For M0 stars, $K_P - V \simeq -0.43^1$ so we conservatively select stars with $K_P - J > 2$ observed in Quarters 0-2 by *Kepler* and retrieved from the Multimission Archive (STScI). We remove stars with a contaminating star within 1 arc second.

Bright *Kepler* target stars were selected in a fundamentally different way from dim stars (see Figure 3.1 and Batalha et al. 2010). We separately analyzed dim ($K_P > 14$) and bright ($K_P < 14$) stars. Bessell & Brett (1988) showed that giant stars tend to have more extreme $J - H$ colors than their dwarf counterparts. However, we wanted to investigate how *misidentified* giant stars in the KIC are distributed with $J - H$ color. Thus we further subdivided our sample into four $J - H$ color bins: $J - H \leq 0.70$, $0.70 < J - H \leq 0.76$, $0.76 < J - H \leq 0.82$, and $0.82 < J - H$ for the bright stars and $J - H \leq 0.62$, $0.62 < J - H \leq 0.65$, $0.65 < J - H \leq 0.68$, and $J - H > 0.68$ for the dim stars. Color bins were designed such that each contains a similar number of stars. We observed a sample of stars within each bin, selected randomly with respect to $J - H$. We observed more bright stars because they are more observationally accessible, although we observed targets spanning all *Kepler* magnitudes to detect trends with K_P . In total we observed 382 stars covering $6.5 < K_P < 16$, $0.40 < J - H < 1.00$ and KIC effective temperatures $3200 < T_{eff} < 5050$ K. The distribution of observed targets is shown in $J - H$ and KIC T_{eff} space in Figure 3.2. A list of observed targets is given in Table 3.1.

¹keplergo.arc.nasa.gov/CalibrationZeropoint.shtml

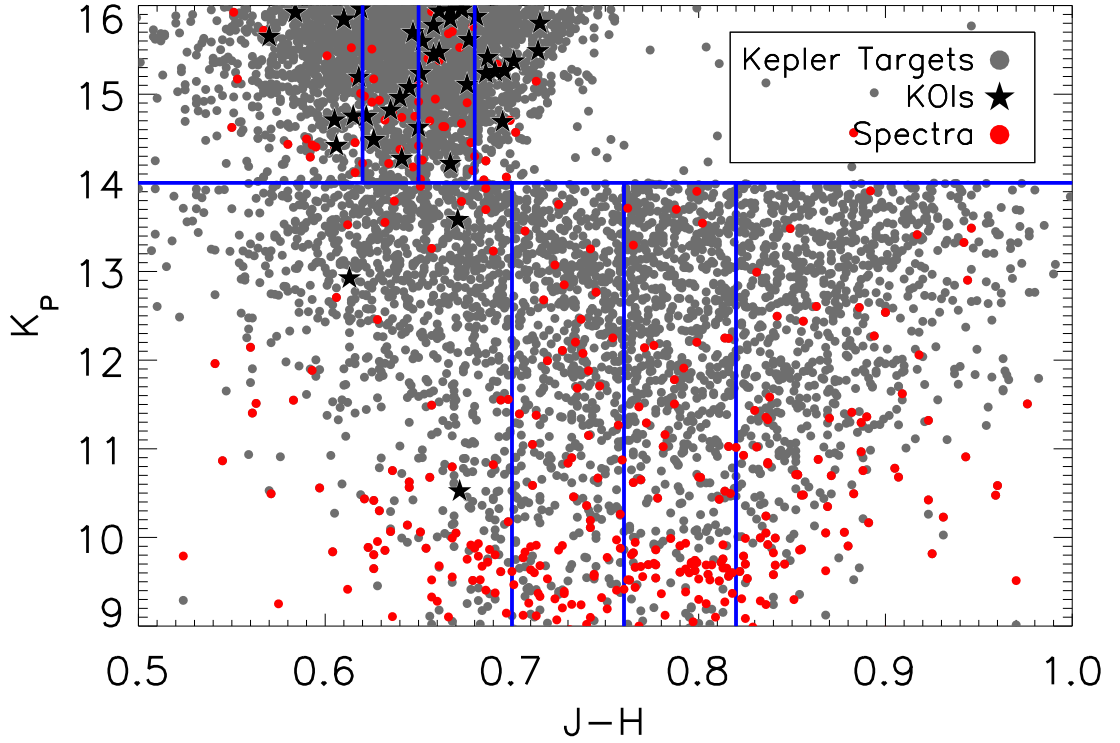


Figure 3.1: *Kepler* magnitude vs. $J - H$ color for Quarter 0-2 *Kepler* target stars with $K_P - J > 2$ (grey circles), KOIs (black stars), and targets with spectra from this program (red circles). Our observing bins (see Section 3.2) are marked by blue lines. There is a clear difference between the colors of bright ($K_P < 14$) and dim ($K_P > 14$) *Kepler* target stars, resulting in a very different distribution of colors. The great majority of KOIs are faint, and have bluer $J - H$ colors. For this reason we divide the sample into $J - H$ bins, and treat bright ($K_P < 14$) and dim ($K_P > 14$) *Kepler* target stars as two independent samples.

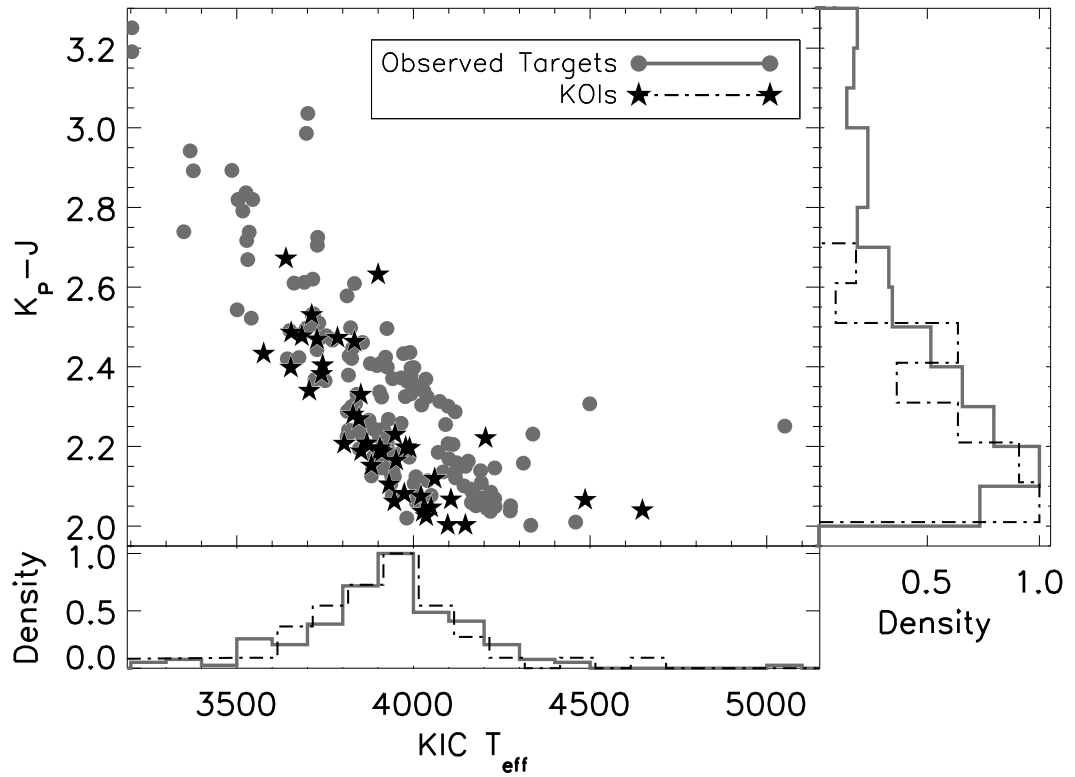


Figure 3.2: Distribution of KIC effective temperatures and $K_P - J$ colors for target stars (grey circles and grey solid histogram) and KOIs (black stars and black dashed histogram). The bulk of the stars in our spectroscopic sample are M dwarfs ($T_{\text{eff}} < 4000 K$) if we assume KIC T_{eff} values are accurate. Histograms for KOIs and observe targets offset slightly from each other for clarity (although the bins for each sample are the same). Note that not all stars have effective temperatures listed in the KIC; points lacking T_{eff} values are not shown in the center plot or bottom histogram, but are included in the $K_P - J$ histogram.

Table 3.1. Parameters of Observed *Kepler* Targets

KIC ID	KIC Parameters			Instrument ^a	Luminosity Class	Derived from Spectra	
	K_P	$\log g$	T_{eff} [K]			T_{eff} [K]	σ_T [K]
1026895	9.2	4.5	3977	CCDS	Giant	3900	60
1160867	9.5	4.6	3753	MkIII	Giant	4000	50
1865910 ^b	10.5	—	—	MkIII	Giant	3960	70
2017534 ^b	10.6	—	—	CCDS	Giant	4190	50
2141385	8.3	2.2	3897	CCDS	Giant	3760	90
2165574 ^b	11.3	—	—	MkIII	Giant	3850	60
2424191	11.9	4.4	3929	MkIII	Giant	3900	60
2578661 ^b	8.6	—	—	CCDS	Giant	4090	60
2716732 ^b	12.5	—	—	SNIFS	Giant	4000	40
2846564	9.9	0.6	3377	CCDS	Giant	3520	90
2847029	9.9	0.7	3368	CCDS	Giant	3430	110
2858435 ^b	12.1	—	—	MkIII	Giant	4080	60
2996015 ^b	9.6	—	—	MkIII	Giant	3690	90
2998002	8.8	1.8	4023	CCDS	Giant	3800	70
3001835 ^b	13.5	—	—	SNIFS	Giant	3800	60
3110253	12.6	4.4	3728	SNIFS	Giant	3630	60
3114424 ^b	10.4	—	—	MkIII	Giant	3870	60
3121983 ^b	13.7	—	—	SNIFS	Giant	3970	60
3131012	8.9	1.9	4147	CCDS	Giant	3930	50
3216051 ^b	13.8	—	—	SNIFS	Giant	3900	50
3218009	12.2	4.5	3717	SNIFS	Giant	3730	70
3218180 ^b	10.8	—	—	SNIFS	Giant	4020	50
3218308	13.8	4.3	3920	SNIFS	Dwarf	3770	60
3218445 ^b	10.6	—	—	MkIII	Giant	4020	50
3221040 ^b	9.7	—	—	CCDS	Giant	3700	80
3222519	11.8	4.6	3736	SNIFS	Giant	3730	70
3232795 ^b	9.2	—	—	CCDS	Giant	3850	60
3324261	8.7	1.9	3926	CCDS	Giant	3770	80
3328254	15.5	4.6	3676	SNIFS	Dwarf	3600	60
3344220	14.7	4.5	3907	SNIFS	Dwarf	3860	50
3347337 ^b	9.8	—	—	MkIII	Giant	3870	90
3357261	14.8	4.5	4008	SNIFS	Dwarf	4020	50
3424790 ^b	12.8	—	—	SNIFS	Giant	4030	50
3438817	14.0	4.5	3825	SNIFS	Dwarf	3650	70
3441157 ^b	8.0	—	—	CCDS	Giant	3920	60
3453029 ^b	9.4	—	—	CCDS	Giant	4170	50
3455303 ^b	12.3	—	—	SNIFS	Giant	3600	80
3455941 ^b	10.9	—	—	CCDS	Giant	4260	40
3544681 ^b	10.1	—	—	MkIII	Giant	3830	60
3548498 ^b	12.5	—	—	SNIFS	Giant	3800	60
3734205	9.9	2.0	4338	CCDS	Giant	4080	60
3749305 ^b	13.9	—	—	SNIFS	Giant	3660	50
3765622 ^b	9.8	—	—	CCDS	Giant	3600	80
3855090 ^b	8.9	—	—	CCDS	Giant	3960	60
3964632	10.8	4.4	3926	MkIII	Giant	3950	70
3964647	13.5	4.5	3717	SNIFS	Giant	3740	70
4035742 ^b	13.3	—	—	SNIFS	Giant	4030	50
4040917 ^b	8.0	—	—	CCDS	Giant	3940	60
4044462 ^b	11.5	—	—	MkIII	Giant	4240	40
4048788	11.7	2.4	4098	SNIFS	Giant	3860	70
4058863 ^b	13.9	—	—	SNIFS	Giant	3950	60
4060284	11.9	3.0	4001	SNIFS	Giant	3780	80
4060593	9.2	4.3	3874	CCDS	Giant	3840	60
4067825 ^b	12.1	—	—	CCDS	Giant	4250	40

Table 3.1—Continued

KIC ID	KIC Parameters			Instrument ^a	Derived from Spectra		
	K _P	log g	T _{eff} [K]		Luminosity Class	T _{eff} [K]	σ _T [K]
4078024	13.8	2.9	4459	SNIFS	Giant	4130	40
4078900	14.4	4.8	3946	SNIFS	Dwarf	3800	50
4136379 ^b	13.3	—	—	SNIFS	Giant	3030	130
4147309 ^b	13.0	—	—	SNIFS	Giant	3520	90
4160669	11.3	0.0	3203	MkIII	Giant	3200	80
4164664 ^b	12.7	—	—	SNIFS	Giant	4040	50
4173278 ^b	10.8	—	—	MkIII	Giant	3760	80
4174532 ^b	10.8	—	—	MkIII	Giant	3670	90
4175398	13.7	4.3	3853	SNIFS	Dwarf	3770	60
4243354	15.4	4.2	3913	SNIFS	Dwarf	3770	60
4247116 ^b	9.2	—	—	CCDS	Giant	3900	60
4282880 ^b	10.8	—	—	MkIII	Giant	3870	70
4371917 ^b	9.2	—	—	CCDS	Giant	4000	60
4382143 ^b	9.6	—	—	CCDS	Giant	3770	70
4385594	11.3	4.5	3822	MkIII	Giant	3870	70
4451217 ^b	9.8	—	—	CCDS	Giant	4130	40
4551429	14.6	4.3	3684	SNIFS	Dwarf	3580	70
4569115	15.5	4.6	3812	SNIFS	Dwarf	3700	60
4579064	14.6	4.4	3729	SNIFS	Giant	3670	50
4655612	14.0	4.8	3934	SNIFS	Dwarf	3730	60
4665808 ^b	10.7	—	—	CCDS	Giant	4200	60
4673368 ^b	11.4	—	—	CCDS	Giant	4350	40
4678401 ^b	10.5	—	—	CCDS	Giant	3600	70
4726192	14.7	4.5	3908	SNIFS	Dwarf	3770	60
4818175 ^b	7.6	—	—	CCDS	Giant	3930	50
4842904 ^b	11.0	—	—	MkIII	Giant	3740	90
4852007 ^b	8.3	—	—	CCDS	Giant	3870	60
4860890 ^b	11.1	—	—	MkIII	Giant	3730	80
4861985 ^b	11.9	—	—	MkIII	Giant	4370	40
4916641	9.4	2.0	4231	CCDS	Giant	4070	60
4927048	8.2	1.7	3941	CCDS	Giant	3800	70
4947596 ^b	11.3	—	—	MkIII	Giant	3770	70
5024699 ^b	12.1	—	—	SNIFS	Giant	3680	80
5032507 ^b	10.4	—	—	CCDS	Giant	3700	80
5079307 ^b	10.4	—	—	MkIII	Giant	3860	80
5088478 ^b	10.4	—	—	MkIII	Giant	3830	90
5093678 ^b	10.7	—	—	MkIII	Giant	3880	70
5109872 ^b	9.8	—	—	CCDS	Giant	4130	60
5112438 ^b	10.7	—	—	MkIII	Giant	3600	70
5129367 ^b	11.6	—	—	MkIII	Giant	3640	60
5171912 ^b	12.0	—	—	CCDS	Giant	4140	40
5197709	8.8	1.8	4230	CCDS	Giant	4070	60
5276467 ^b	9.2	—	—	CCDS	Giant	3720	80
5288939 ^b	10.7	—	—	MkIII	Giant	3810	90
5341903 ^b	9.9	—	—	CCDS	Giant	4080	60
5345216 ^b	13.7	—	—	SNIFS	Giant	3860	60
5393342 ^b	12.9	—	—	SNIFS	Giant	3600	80
5395743 ^b	11.3	—	—	MkIII	Giant	3930	60
5437353	8.1	1.6	4030	CCDS	Giant	3850	60
5598209 ^b	13.3	—	—	SNIFS	Giant	3970	70
5600727	9.3	2.1	3812	CCDS	Giant	3680	80
5631269 ^b	13.5	—	—	SNIFS	Giant	3570	80
5648449 ^b	10.7	—	—	CCDS	Giant	3600	70
5651608 ^b	8.9	—	—	CCDS	Giant	4260	40

Table 3.1—Continued

KIC ID	KIC Parameters			Instrument ^a	Derived from Spectra		
	K _P	log g	T _{eff} [K]		Luminosity Class	T _{eff} [K]	σ _T [K]
5682974 ^b	12.5	—	—	MkIII	Giant	3100	110
5683912 ^b	6.3	—	—	CCDS	Giant	3000	90
5694612 ^b	8.5	—	—	CCDS	Giant	3900	60
5708328 ^b	11.6	—	—	SNIFS	Giant	3800	60
5708837	8.5	1.7	3350	CCDS	Giant	3490	90
5732026 ^b	9.5	—	—	MkIII	Giant	3860	70
5781827 ^b	8.0	—	—	CCDS	Giant	4050	60
5784204	8.5	4.6	3732	CCDS	Giant	3700	80
5791709	9.0	2.0	4100	CCDS	Giant	3900	60
5855851	14.5	4.0	3504	SNIFS	Dwarf	3600	100
5858889	11.0	2.3	3908	MkIII	Giant	3810	70
5895919	14.4	4.7	3813	SNIFS	Dwarf	3890	70
5905446 ^b	10.7	—	—	MkIII	Giant	3650	70
5937264	14.6	4.5	3930	SNIFS	Dwarf	3870	50
5964115 ^b	9.6	—	—	MkIII	Giant	3750	80
5977048 ^b	10.5	—	—	MkIII	Giant	3860	70
6032907	15.3	4.5	3938	SNIFS	Dwarf	3830	70
6033640	10.5	2.1	3990	MkIII	Giant	3810	70
6037983 ^b	11.3	—	—	MkIII	Giant	4010	50
6049470 ^b	10.1	—	—	CCDS	Dwarf	3780	70
6067727 ^b	9.3	—	—	CCDS	Giant	4140	50
6105065 ^b	9.0	—	—	CCDS	Giant	3600	80
6125019	14.4	4.6	3827	SNIFS	Dwarf	3800	60
6127362 ^b	9.6	—	—	CCDS	Giant	3670	70
6129655 ^b	9.5	—	—	MkIII	Giant	3920	50
6146503 ^b	9.2	—	—	CCDS	Giant	3900	60
6187942	15.1	4.3	3691	SNIFS	Dwarf	3780	90
6214095 ^b	9.9	—	—	MkIII	Giant	3780	70
6224062	14.5	4.5	3830	SNIFS	Dwarf	3700	60
6271813 ^b	12.1	—	—	MkIII	Giant	4070	50
6342566 ^b	7.5	—	—	CCDS	Giant	3840	60
6357113	9.4	1.9	4035	CCDS	Giant	3800	60
6360007 ^b	12.2	—	—	MkIII	Giant	3930	60
6363233	14.3	4.4	3889	SNIFS	Dwarf	3820	50
6384975	8.8	4.6	3713	CCDS	Giant	3730	60
6432344 ^b	10.3	—	—	CCDS	Giant	4100	50
6448574 ^b	8.8	—	—	CCDS	Giant	3480	70
6452413 ^b	8.1	—	—	CCDS	Giant	3940	60
6471223	8.2	2.3	3715	CCDS	Giant	3660	60
6503104	15.4	4.3	3662	SNIFS	Dwarf	3320	90
6522800 ^b	8.6	—	—	CCDS	Giant	3330	110
6580131 ^b	7.1	—	—	CCDS	Giant	3950	60
6584408 ^b	11.7	—	—	MkIII	Giant	3930	60
6584424	9.6	2.1	3486	CCDS	Giant	3470	80
6585979 ^b	9.5	—	—	MkIII	Giant	3640	60
6664482 ^b	8.3	—	—	CCDS	Giant	3600	80
6676993	8.8	1.8	4230	CCDS	Giant	4080	60
6695442 ^b	13.4	—	—	SNIFS	Giant	3630	70
6843652 ^b	12.4	—	—	SNIFS	Giant	3860	70
6922834	10.7	2.3	4074	MkIII	Giant	5000	30
6949326	14.7	4.4	3942	SNIFS	Dwarf	3870	60
7007370 ^b	9.3	—	—	CCDS	Giant	4700	40
7033670 ^b	14.6	—	—	SNIFS	Dwarf	3100	30
7033775 ^b	8.5	—	—	CCDS	Giant	3800	60

Table 3.1—Continued

KIC ID	KIC Parameters			Instrument ^a	Derived from Spectra		
	K _P	log g	T _{eff} [K]		Luminosity Class	T _{eff} [K]	σ _T [K]
7037772 ^b	11.0	—	—	MkIII	Giant	3850	60
7048122	9.5	2.2	4177	CCDS	Giant	4030	50
7091114 ^b	9.7	—	—	MkIII	Giant	3920	60
7095218	8.7	4.4	3697	CCDS	Giant	3740	70
7101463	9.6	2.0	4161	MkIII	Giant	3870	70
7102615 ^b	9.7	—	—	MkIII	Giant	3800	60
7185134 ^b	9.1	—	—	CCDS	Giant	3640	60
7206673	9.7	2.0	3921	MkIII	Giant	3830	90
7219652	14.1	4.5	3817	SNIFS	Dwarf	3800	100
7221001 ^b	9.4	—	—	CCDS	Giant	4030	60
7335603	14.8	4.4	3840	SNIFS	Dwarf	3720	60
7345435 ^b	9.3	—	—	CCDS	Giant	4150	40
7351518	9.8	1.9	3993	MkIII	Giant	3980	80
7352201 ^b	8.2	—	—	CCDS	Giant	3750	80
7354482	9.1	1.8	4025	CCDS	Giant	3840	60
7357165 ^b	10.6	—	—	CCDS	Giant	4200	50
7381823 ^b	8.1	—	—	CCDS	Giant	3900	60
7451886	8.8	2.1	3966	CCDS	Giant	3800	80
7505113	10.1	4.5	3697	CCDS	Giant	3330	90
7534293	8.6	1.7	3983	CCDS	Giant	3800	60
7585858 ^b	12.2	—	—	MkIII	Giant	3850	80
7630772	15.0	4.2	3531	SNIFS	Dwarf	3330	80
7702122	8.8	1.7	4208	CCDS	Giant	4070	60
7729057	11.6	2.4	4192	SNIFS	Giant	3990	50
7768995 ^b	9.4	—	—	CCDS	Giant	3800	60
7799575	8.1	4.4	3965	CCDS	Giant	3800	60
7800087	14.5	4.4	3828	SNIFS	Dwarf	3600	70
7820946	14.9	4.5	4007	SNIFS	Dwarf	3880	60
7830098	14.1	4.5	3918	SNIFS	Dwarf	3860	70
7840478 ^b	9.9	—	—	CCDS	Giant	4100	50
7889528	8.2	1.9	4311	CCDS	Giant	4260	40
7910890	9.1	1.9	4070	CCDS	Giant	3930	60
7918217 ^b	10.9	—	—	MkIII	Giant	3630	70
7954259	8.8	1.7	3833	CCDS	Giant	3660	60
7966601 ^b	10.2	—	—	CCDS	Giant	3630	60
7985592 ^b	10.6	—	—	CCDS	Giant	3500	90
7988797 ^b	11.5	—	—	MkIII	Giant	3580	80
8013221	13.6	4.6	3643	SNIFS	Dwarf	3600	70
8015981 ^b	8.6	—	—	CCDS	Giant	3730	70
8024865 ^b	10.7	—	—	MkIII	Giant	3600	80
8039057 ^b	10.8	—	—	MkIII	Giant	4430	40
8040723 ^b	10.9	—	—	MkIII	Giant	4030	50
8091051	10.1	2.1	4219	CCDS	Giant	4080	60
8091423	8.8	2.2	3545	CCDS	Giant	3480	80
8149616	15.2	4.0	3517	SNIFS	Dwarf	3600	110
8158779 ^b	9.7	—	—	MkIII	Giant	3700	90
8178161 ^b	8.2	—	—	CCDS	Giant	4030	60
8209913 ^b	9.5	—	—	MkIII	Giant	3700	70
8226149 ^b	9.8	—	—	CCDS	Giant	4260	40
8254901 ^b	8.2	—	—	CCDS	Giant	3330	90
8297307 ^b	15.7	—	—	SNIFS	Giant	3610	100
8313018 ^b	7.7	—	—	CCDS	Giant	3770	70
8352528	8.6	4.5	3917	CCDS	Giant	3850	60
8389819 ^b	11.4	—	—	MkIII	Giant	3700	70

Table 3.1—Continued

KIC ID	KIC Parameters			Instrument ^a	Derived from Spectra		
	K _P	log g	T _{eff} [K]		Luminosity Class	T _{eff} [K]	σ _T [K]
8393582	14.4	4.5	3887	SNIFS	Dwarf	3790	50
8415336	14.9	4.5	3970	SNIFS	Dwarf	3760	60
8417203	10.8	4.4	3771	MkIII	Giant	3770	70
8423797	9.3	2.2	4039	MkIII	Giant	3890	70
8426324	10.3	2.2	3526	CCDS	Giant	3480	90
8427166 ^b	10.7	—	—	MkIII	Giant	3690	90
8445780 ^b	11.5	—	—	CCDS	Giant	4250	50
8463380 ^b	10.4	—	—	CCDS	Giant	4040	60
8493586 ^b	10.5	—	—	CCDS	Giant	3610	80
8494510	15.7	4.4	3816	SNIFS	Dwarf	3630	60
8510314 ^b	11.2	—	—	MkIII	Giant	3990	50
8556766 ^b	11.6	—	—	SNIFS	Giant	4060	50
8556942 ^b	12.8	—	—	SNIFS	Giant	4000	50
8579358 ^b	8.9	—	—	CCDS	Giant	3730	60
8582121 ^b	10.9	—	—	MkIII	Giant	3630	70
8611876	15.2	4.0	3504	SNIFS	Dwarf	3300	60
8621600	9.5	2.4	4168	CCDS	Giant	4000	70
8631367 ^b	11.4	—	—	MkIII	Giant	4020	50
8653068 ^b	8.4	—	—	CCDS	Giant	3330	100
8701255 ^b	11.0	—	—	MkIII	Giant	3760	70
8719675 ^b	7.7	—	—	CCDS	Giant	3900	50
8733892	9.6	2.0	4275	CCDS	Giant	4170	40
8738899 ^b	9.7	—	—	MkIII	Giant	3780	70
8739252 ^b	9.8	—	—	MkIII	Giant	4000	60
8740378 ^b	8.8	—	—	CCDS	Giant	3960	60
8750712	9.4	1.8	4091	CCDS	Giant	3900	60
8767446 ^b	9.4	—	—	CCDS	Giant	3640	60
8801244	14.2	4.6	3904	SNIFS	Dwarf	3750	60
8814775	14.9	4.1	3535	SNIFS	Dwarf	3340	80
8824683 ^b	9.7	—	—	CCDS	Giant	3760	90
8831759	8.4	4.7	3501	CCDS	Giant	3670	70
8838681 ^b	10.1	—	—	CCDS	Giant	4080	60
8881126	15.8	4.6	3890	SNIFS	Dwarf	3720	60
8885638 ^b	10.9	—	—	MkIII	Giant	3950	70
8894616 ^b	11.5	—	—	MkIII	Giant	4080	50
8912338	14.6	4.4	3881	SNIFS	Dwarf	3870	50
9009407 ^b	10.5	—	—	CCDS	Giant	3480	80
9051345 ^b	9.0	—	—	CCDS	Giant	3350	110
9083661	9.1	2.0	4143	CCDS	Giant	3930	60
9116231 ^b	11.4	—	—	MkIII	Giant	3980	60
9143855	11.0	4.4	3878	MkIII	Giant	4040	60
9172316 ^b	8.9	—	—	CCDS	Giant	3740	70
9175009	14.2	4.6	3836	SNIFS	Dwarf	3870	70
9182817 ^b	11.5	—	—	MkIII	Giant	3900	50
9221176 ^b	13.9	—	—	SNIFS	Giant	4110	40
9228523	8.9	1.8	4112	CCDS	Giant	3900	60
9267368 ^b	12.1	—	—	MkIII	Giant	4030	50
9273312	12.3	2.5	4118	SNIFS	Giant	3900	50
9291963 ^b	13.5	—	—	SNIFS	Giant	4020	50
9326304	8.5	1.6	4119	CCDS	Giant	3960	60
9347339 ^b	9.6	—	—	MkIII	Giant	3760	80
9350124	11.0	2.2	4190	MkIII	Giant	4070	50
9397064	11.4	2.9	3972	SNIFS	Giant	3760	90
9405541	9.7	0.1	3203	CCDS	Giant	3300	110

Table 3.1—Continued

KIC ID	KIC Parameters			Instrument ^a	Derived from Spectra		
	K _P	log g	T _{eff} [K]		Luminosity Class	T _{eff} [K]	σ _T [K]
9413918 ^b	10.5	—	—	MkIII	Giant	3730	70
9456779 ^b	9.0	—	—	CCDS	Giant	4090	60
9489411	14.0	2.2	4499	SNIFS	Giant	3950	60
9528112 ^b	6.8	—	—	CCDS	Giant	3000	20
9529652	8.7	1.8	4122	CCDS	Giant	3930	60
9593633 ^b	11.2	—	—	MkIII	Giant	3700	70
9603366 ^b	10.2	—	—	MkIII	Giant	4040	50
9605196 ^b	9.5	—	—	CCDS	Giant	4100	50
9632503 ^b	9.2	—	—	CCDS	Giant	3960	60
9635876	10.9	4.5	3770	MkIII	Giant	3750	90
9704050 ^b	7.8	—	—	CCDS	Giant	4020	50
9704325 ^b	7.6	—	—	CCDS	Giant	4160	40
9715189 ^b	10.0	—	—	CCDS	Giant	3670	70
9728822 ^b	9.4	—	—	MkIII	Giant	3850	60
9765062	10.0	2.4	4155	MkIII	Giant	3960	70
9790574	13.2	4.6	4033	SNIFS	Dwarf	3910	20
9835672	8.7	1.9	4122	CCDS	Giant	3910	60
9838331 ^b	13.1	—	—	SNIFS	Giant	3840	60
9848470	9.1	1.9	3993	CCDS	Giant	3800	60
9852964 ^b	11.4	—	—	MkIII	Giant	3730	70
9872165 ^b	9.9	—	—	CCDS	Giant	4030	50
9896545	10.1	4.5	3701	CCDS	Giant	3320	100
9904409 ^b	8.9	—	—	CCDS	Giant	4130	60
9963100 ^b	10.2	—	—	CCDS	Giant	3600	80
9991565	14.9	4.4	3936	SNIFS	Dwarf	3940	50
9995317 ^b	8.9	—	—	CCDS	Giant	3950	60
10026881	13.3	4.5	4040	SNIFS	Dwarf	3910	50
10064712 ^b	9.4	—	—	CCDS	Giant	4050	60
10068519 ^b	9.5	—	—	CCDS	Giant	3640	60
10082058	15.7	4.4	3904	SNIFS	Dwarf	3670	70
10122402	12.2	2.4	3993	SNIFS	Giant	3770	80
10129425	12.5	4.5	3940	SNIFS	Dwarf	3900	40
10148717 ^b	9.9	—	—	CCDS	Giant	3600	80
10160830 ^b	12.6	—	—	SNIFS	Giant	3660	70
10166321	14.7	4.5	3936	SNIFS	Dwarf	3860	50
10190244	8.0	1.7	4218	CCDS	Giant	4030	50
10192853 ^b	8.8	—	—	CCDS	Giant	3600	80
10195818	15.2	4.7	3727	SNIFS	Dwarf	3600	70
10224595	14.4	4.2	3528	SNIFS	Dwarf	3250	70
10226239 ^b	12.2	—	—	MkIII	Giant	4090	60
10257435 ^b	11.5	—	—	SNIFS	Giant	3960	60
10336624	12.7	4.1	3541	SNIFS	Dwarf	3510	80
10361019	10.9	2.6	5051	CCDS	Giant	4660	30
10389724 ^b	8.8	—	—	CCDS	Giant	3800	60
10406398 ^b	15.9	—	—	SNIFS	Giant	3310	100
10451006 ^b	9.9	—	—	MkIII	Giant	3640	100
10453983	8.8	2.2	4084	CCDS	Giant	3900	60
10467314 ^b	9.4	—	—	MkIII	Giant	4100	40
10525990	14.4	4.4	3861	SNIFS	Dwarf	3880	100
10527357 ^b	9.1	—	—	CCDS	Giant	3750	80
10532847 ^b	9.2	—	—	CCDS	Giant	4060	60
10553224 ^b	10.1	—	—	MkIII	Giant	3870	70
10590779 ^b	8.7	—	—	CCDS	Giant	4070	60
10592818 ^b	8.9	—	—	CCDS	Giant	4030	50

Table 3.1—Continued

KIC ID	KIC Parameters			Instrument ^a	Derived from Spectra		
	K _P	log g	T _{eff} [K]		Luminosity Class	T _{eff} [K]	σ _T [K]
10593779 ^b	8.9	—	—	CCDS	Giant	3930	60
10596359 ^b	9.6	—	—	CCDS	Giant	3680	80
10618417	9.7	2.4	3996	MkIII	Giant	3920	60
10648847 ^b	8.6	—	—	CCDS	Giant	3760	80
10676126	15.4	4.4	3818	SNIFS	Dwarf	3600	60
10682835	15.9	4.6	4050	SNIFS	Dwarf	3920	50
10717091 ^b	10.3	—	—	MkIII	Giant	3790	60
10735274	9.3	2.5	3925	CCDS	Giant	3670	70
10735305 ^b	8.4	—	—	CCDS	Giant	3570	70
10747553	15.1	4.4	4002	SNIFS	Dwarf	3850	60
10788617 ^b	9.1	—	—	CCDS	Giant	3970	50
10790875 ^b	8.9	—	—	CCDS	Giant	3850	60
10801138 ^b	10.2	—	—	MkIII	Giant	4130	40
10801273	10.6	4.4	3981	CCDS	Dwarf	3970	60
10813670 ^b	10.8	—	—	MkIII	Giant	4140	50
10843322	15.0	4.4	3650	SNIFS	Dwarf	3580	80
10850139	14.2	4.4	3902	SNIFS	Dwarf	3820	50
10850518	14.3	4.6	3847	SNIFS	Dwarf	3900	140
10859767	9.0	1.8	4194	CCDS	Giant	4070	60
10861620 ^b	8.6	—	—	CCDS	Giant	4060	60
10863107 ^b	7.9	—	—	CCDS	Giant	3760	90
10879833 ^b	9.5	—	—	MkIII	Giant	3950	60
10905320	14.3	4.4	4009	SNIFS	Dwarf	3950	50
10934370 ^b	7.5	—	—	CCDS	Giant	4070	60
10990223 ^b	9.1	—	—	CCDS	Giant	3600	70
11031937	9.0	2.0	3991	CCDS	Giant	3760	90
11085850	14.7	4.5	3988	SNIFS	Dwarf	3780	70
11099165	8.9	4.5	3856	CCDS	Giant	3760	80
11126216 ^b	8.5	—	—	CCDS	Giant	3320	110
11180776	14.2	4.5	3884	SNIFS	Dwarf	3940	80
11197047 ^b	11.4	—	—	MkIII	Giant	3700	80
11231223 ^b	9.4	—	—	MkIII	Giant	3730	80
11244150	14.9	4.4	3910	SNIFS	Dwarf	3800	100
11244265 ^b	10.2	—	—	MkIII	Giant	3650	70
11245491 ^b	9.6	—	—	CCDS	Giant	3330	90
11251663 ^b	9.2	—	—	CCDS	Giant	3700	90
11288133	9.3	1.9	4164	CCDS	Giant	4080	60
11349943 ^b	7.7	—	—	CCDS	Giant	3920	60
11389341	14.1	4.6	3750	SNIFS	Dwarf	3720	90
11460413 ^b	9.0	—	—	CCDS	Giant	3920	60
11496589 ^b	9.7	—	—	MkIII	Giant	3990	50
11497648 ^b	9.1	—	—	CCDS	Giant	4050	60
11509173 ^b	12.0	—	—	SNIFS	Giant	4000	50
11567375 ^b	10.6	—	—	MkIII	Giant	4030	50
11704004 ^b	9.2	—	—	CCDS	Giant	3700	90
11713042	14.8	4.6	3816	SNIFS	Dwarf	3720	60
11766491 ^b	9.4	—	—	MkIII	Giant	3880	80
11774310 ^b	10.5	—	—	CCDS	Giant	4250	50
11820505	15.5	4.5	3721	SNIFS	Dwarf	3600	60
11857884 ^b	10.0	—	—	CCDS	Giant	3440	110
11917719 ^b	8.6	—	—	CCDS	Giant	4190	50
12155015	8.6	4.5	3825	CCDS	Giant	3760	90
12217469	8.6	1.8	4274	CCDS	Giant	3960	60
12268739	10.4	2.1	4332	CCDS	Giant	4090	60

Table 3.1—Continued

KIC ID	KIC Parameters			Instrument ^a	Derived from Spectra		
	K_P	$\log g$	T_{eff} [K]		Luminosity Class	T_{eff} [K]	σ_T [K]
12269113 ^b	10.7	—	—	MkIII	Giant	3700	70
12366757 ^b	9.3	—	—	CCDS	Giant	3750	70
12417370	9.0	2.5	4098	CCDS	Giant	3900	60
12459905 ^b	13.5	—	—	SNIFS	Giant	4180	50

^aSNIFS = SuperNova Integral Field Spectrograph, CCDS = Boller & Chivens CCD Spectrograph, MkIII = Mark III spectrograph. SNIFS is attached to the University of Hawaii 2.2-meter telescope, and both CCDS and MkIII at the MDM Observatory 1.3m McGraw-Hill Telescope.

^bNo temperatures or $\log g$ values present in the KIC.

Observations were obtained between June 16 and Aug 28 (2011) with the SuperNova Integral Field Spectrograph (SNIFS, Lantz et al. 2004) at the University of Hawaii 2.2m telescope on Mauna Kea and the Boller and Chivens CCD Spectrograph (CCDS) or the Mark III spectrograph (MkIII) at the MDM Observatory 1.3m McGraw-Hill telescope on Kitt Peak. SNIFS is an optical integral field spectrograph with $R \simeq 1300$ that splits the signal with a dichroic mirror into blue ($3000 - 5200 \text{ \AA}$) and red ($5000 - 9500 \text{ \AA}$) channels. SNIFS images were resampled with microlens arrays, dispersed with grisms, and focused onto blue- and red-sensitive CCDs. Processing of SNIFS data was performed with the SNIFS pipeline, described in detail by Aldering et al. (2006) and Pereira et al. (2010). SNIFS processing included dark, bias, and flat-field corrections, assembling the data into red and blue 3D data cubes, and cleaning them for cosmic rays and bad pixels. After sky subtraction, the spectra are extracted with a PSF model, and wavelengths were calibrated with arc lamp exposures taken at the same telescope pointing as the science data.

The CCDS and MkIII spectrographs cover $5700 - 9300 \text{ \AA}$ and $4400 - 8300 \text{ \AA}$ with $R \simeq 1150$ and $\simeq 2300$, respectively. Standard reduction of data taken with the CCDS and MkIII was performed with IRAF, following the practice of overscan subtraction, division by flat field, and extraction of the spectra. Spectra were wavelength-calibrated against NeArXe comparison arcs. All observations (including SNIFS) were flux-calibrated and telluric lines were removed based on observations of the NOAO primary spectrophotometric standards Feige 66, Feige 110, and BD+284211. All spectra had a median S/N of > 30 (typically $\text{SNR} \simeq 50$) in the $6000 - 7000 \text{ \AA}$ range.

Our spectroscopic set only covers $K_P - J > 2.0$, but we also consider a separate ‘photometric sample’ that includes stars with $0.56 < J - H < 0.66 \cup K_P - J > 2$. This is done so we can ensure coverage of the sample of late K stars used by SL11 (see Section 3.5). The KIC includes JHK photometry from 2MASS (Skrutskie et al. 2006) and visible-wavelength photometry through SDSS $griz$ and $D51$ filters. We add photometry from the Wide-field Infrared Survey Explorer (WISE, Wright et al. 2010), which includes $3.4\mu\text{m}$, $4.6\mu\text{m}$, $12\mu\text{m}$, and $22\mu\text{m}$ bands.

3.3 Luminosity Class

We determine luminosity class by comparing the spectral indices or colors of *Kepler* target stars to those of stars drawn from ‘training sets’ of known giants or dwarfs. We first discuss how we construct our training sets. We then explain our choice of indices and color-color relations, based on previous work on giant/dwarf discrimination and derived empirically from examination of the differences between the dwarf and giant training set. We use the colors and spectroscopic indices of stars in the training sets to construct a likelihood estimator, such that we can calculate the likelihood that a given star is a giant (or dwarf). That calculation is explained in Section 3.3.4.

3.3.1 Training Sets

We construct an uncontaminated set of dwarf stars from a sample of high proper motion-selected late dK and dM stars (LG11). The brightest ($J < 9$) northern stars in the LG11 catalog have visible-wavelength spectra (Lépine et al. 2013), obtained with the same instruments and reduced in the same way as was done for *Kepler* targets observed for this paper. Although the sample from Lépine et al. (2013) includes more than 1500 spectra, we construct our dwarf sample only from the 620 targets with spectra from SNIFS/UH2.2m, which includes the Ca II triplet feature at $8484 - 8662\text{\AA}$.

LG11 use $J - H$, and $H - K$ colors, combined with proper motion from SUPERBLINK (Lépine & Shara 2005) and (for some targets) parallax information from Hipparcos (van Leeuwen & Fantino 2005; van Leeuwen 2007) to remove giant stars. Based on those stars in LG11 with parallaxes, we estimate that fewer than 0.5% of the resulting sample will be giants. However, because of strict cuts in $J - H$ and $H - K$, the LG11 sample is incomplete and biased against dwarfs with much redder or bluer colors. LG11 also use a color cut of $V - J > 2.7$ to select mostly M dwarfs. This excludes some mid- to late-K stars which will be included in our ($K_P - J > 2 \cup 0.58 < J - H < 0.66$) color cut for the photometric sample (see Section 3.2). We therefore add 60 late K and early M dwarfs included in the *Hipparcos* catalog that have UH2.2m spectra but lie outside the cuts imposed by LG11. These stars are confirmed to be dwarfs by their *Hipparcos* parallaxes. We also add 150 M dwarfs with spectra from SDSS, including 50 dwarf from West et al. (2011), with $r - J$ and $J - H$ colors consistent with our targets of interest. We verify that these targets are dwarfs using a cut with reduced proper motion, where the reduced proper motion in the SDSS g band is:

$$H_g = g + 5 \log \mu + 5, \quad (3.1)$$

and μ is the proper motion in arcsec yr $^{-1}$. This quantity is similar to the absolute magnitude, such that giant stars will have much lower reduced proper motions than dwarfs of the same color. We only select SDSS stars with $H_g > 2.2(g - r) + 7.0$, and $\mu > 15$ arcsec yr $^{-1}$, which we determine empirically from our UH2.2m targets with SDSS photometry.

Our sample of >300 giant spectra is constructed from multiple catalogs, specifically Fluks et al. (1994), Danks & Dennefeld (1994), Allen & Strom (1995), Serote Roos et al. (1996), Montes et al. (1999), and Lançon & Wood (2000), as well as 80 bright stars we observed with UH2.2/SNIFS that are confirmed to be giants by *Hipparcos*. Many spectra have significantly higher resolution than our own observations. We convolve these data with

Table 3.2. Definitions of Spectroscopic Indices

Index Name	Band [Å]	Continuum [Å]	Source ^a
Na I (a)	5868-5918	6345-6355	this work ^b
Ba II/Fe I/Mn I/Ti I	6470-6530	6410-6420	Torres-Dodgen & Weaver (1993)
CaH2	6814-6846	7042-7046	Reid et al. (1995)
CaH3	6960-6990	7042-7046	Reid et al. (1995)
TiO5 ^c	7126-7135	7042-7046	Reid et al. (1995)
K I	7669-7705	7677-7691, 7802-7825	this work ^b
Na I (b)	8172-8197	8170-8173, 8232-8235	Schiavon et al. (1997)
Ca II	8484-8662	8250-8300, 8570-8600	Cenarro et al. (2001a)

Note. — Na I, Ba II/Fe I/Mn I/Ti I, K I , and Ca II are measured as equivalent widths, whereas CaH and TiO features are measured as band indices (Reid et al. 1995).

^aPapers where the wavelength definition we use is given.

^bWavelength ranges for Na I (b) and K I were determined from empirical analysis of the giant and dwarf training sets.

^cBecause TiO5 has minimal gravity dependence, we measure other spectroscopic indices with respect to the TiO5 band strength.

a gaussian to match the resolution of our own sample to remove any resolution-dependency in our results. To include sufficient SDSS photometry, we supplement our giant training set by including 200 giant stars with spectra from SDSS all with $r < 16$ and proper motions consistent with zero. We require these SDSS spectra to have spectroscopic indices consistent with the rest of the giant training set. Because we select only SDSS stars with indices consistent with indices from spectra from the rest of the training stars, SDSS giant stars have no effect on our spectroscopic determination of luminosity class. Rather, these SDSS stars are added only for their photometry.

SDSS, 2MASS and WISE colors are available for much of our giant and dwarf training set; however, most lack $D51$ photometry, which covers the gravity-sensitive Mg Ib line at 5200Å. Instead, we synthesize equivalent $g - D51$ colors from the spectra of our training set. We obtain the zero point for the synthesized colors of those stars in our sample which have both spectra and g and $D51$ magnitudes.

3.3.2 Spectroscopic Determination of Luminosity Class

Our determination of luminosity class uses six different gravity-sensitive molecular or atomic indices (Table 3.2 and Figure 3.3). Molecular and atomic indices are ratios of the average flux levels in a specified wavelength region to that of a pseudo-continuum region. Indices are useful for M dwarfs where the continuum is poorly defined. The values of most indices are a function of both gravity *and* temperature of the star. To remove this degeneracy we compare measured indices to the TiO5 spectral index. TiO5, as defined by Reid et al. (1995), is sensitive to spectral type and metallicity (Woolf & Wallerstein 2006; Lépine et al. 2007) but it has minimal gravity dependance (Jao et al. 2008) (see Figure 3.3).

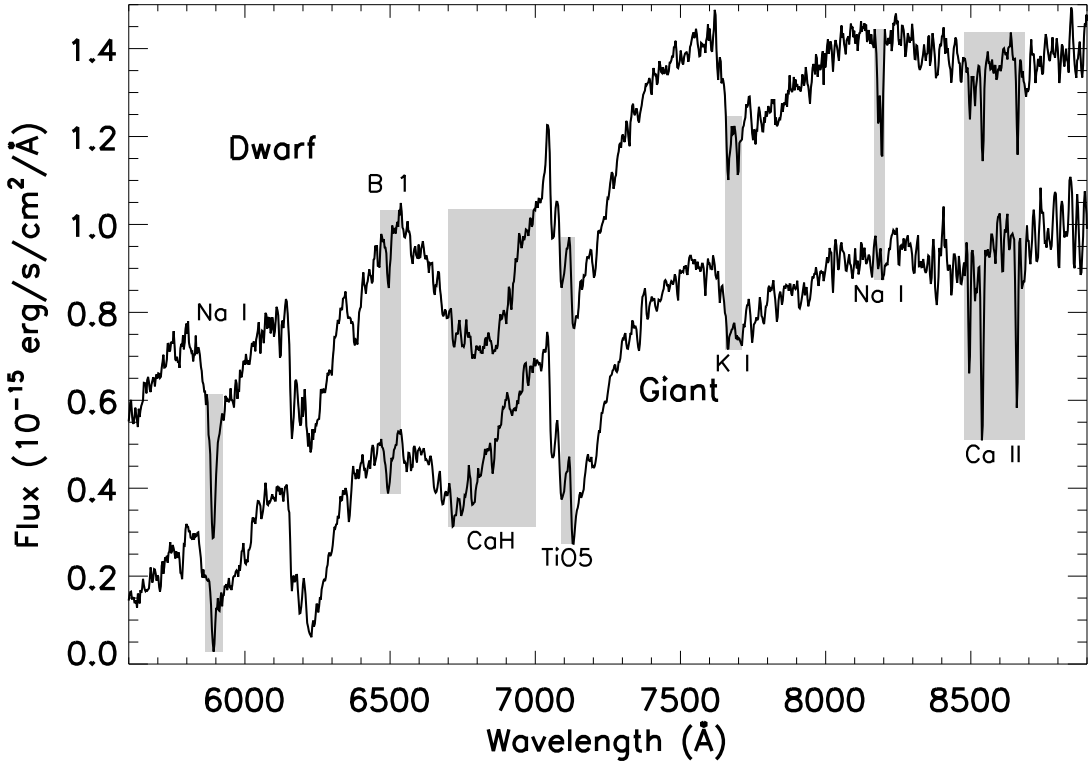


Figure 3.3: SNIFS spectra of an M dwarf (top) and M giant (bottom) of similar T_{eff} ($\simeq 3600$ K) and magnitude ($K_P \simeq 14$). Approximate regions for each of the six indices we use for giant/dwarf discrimination, as well as the TiO₅ band, are marked in grey. B 1 refers to a mix of atomic lines (Ba II, Fe I, Mn I, and Ti I) which overlap at the resolution of SNIFS ($\simeq 1300$). The TiO₅ molecular band is used as a probe of spectral type, although it is also sensitive to metallicity (Lépine et al. 2007). Other atomic and molecular lines are generally much weaker in late type giant stars (Reid & Hawley 2005). Indeed, the Na I (8192-8197 \AA) and K I (7669-7705 \AA) doublets are significantly weaker in the giant spectrum while they are both quite strong in the dwarf.

We show spectra of giant and dwarf stars with similar effective temperatures in Figure 3.3, with the location of each feature labeled. As can be seen, most atomic lines are weaker in giants than in dwarfs. Indeed the Na I doublet (8172-8197Å) and K I (7669-7705Å) lines are quite shallow in giants while relatively deep in dwarfs (Torres-Dodgen & Weaver 1993; Schiavon et al. 1997; Reid & Hawley 2005). Molecular lines provide additional luminosity-dependent spectral signatures. Metal hydride bands, such as the CaH bands defined by Reid et al. (1995) and Lépine et al. (2007) have been used for luminosity classification, although they are less useful for stars earlier than K7. The calcium triplet (8484–8662Å) is a useful indicator of gravity (e.g. Cenarro et al. 2001b; Kraus & Hillenbrand 2009), especially for M stars which emit comparatively more at red wavelengths. Giant and dwarf training sets overlaid on *Kepler* target star indices are shown in Figure 3.4.

3.3.3 Photometric Determination of Luminosity Class

We can use the available photometry to determine the luminosity class of a much larger sample of *Kepler* stars lacking spectra. Brown et al. (2011) primarily use $g - D51$ vs. $g - r$ and $J - K$ vs. $g - i$ colors to separate *Kepler* late-type giants from dwarfs. Both giants and the coolest dwarfs in the sample have relatively weak Mg Ib lines, creating overlap between the dwarf and giant training sets at red $g - r$. A similar effect happens with $J - K$. Near-infrared photometry (JHK) has long been used to separate giants and dwarfs at redder colors (Bessell & Brett 1988), in part due to strong CO and weak Na I and Ca I absorption in giant stars. But for K and early M stars with $J - H < 0.7$ and $H - K < 0.2$, the giant and dwarf sequences overlap, creating a sizable region of ambiguity. At mid-infrared wavelengths, most giant stars have warm dust emission, leading to significantly redder colors in the WISE bandpasses. Other relations can be derived from an examination of our giant and dwarf training sets. $z - K$ vs. $g - J$ follows a similar distribution to that of $J - K$ vs. $g - i$, but the giant and dwarf samples bifurcate at $g - J \simeq 3.0$, which makes this color useful for isolating the reddest giants. Giant and dwarf training sets overlaid on *Kepler* target star colors are shown in Figure 3.5.

3.3.4 Application of training sets to the *Kepler* sample

After each spectral index or color is measured or calculated for *Kepler* targets and both training sets, we identify stars as giants or dwarfs following the same technique as Gilbert et al. (2006). We begin by using the spectral index or color measurements of the training stars to produce a two-dimensional probability distribution function (PDF) for each index (or color). The PDFs are constructed by treating the strength of each index or color (henceforth S) as a Gaussian distributed variable with respect to X . For spectroscopic determination of luminosity class, X is a parameter that primarily relates to the spectral type (although it may have some gravity dependence), while S is a parameter that primarily relates to $\log g$. For the spectroscopic determination of luminosity class, X is the TiO5 band and S is one of our six gravity-sensitive indices (Na I, Ca II, Ba II/Fe I/Mn I/Ti I, K I, or CaH). For photometric determination of luminosity class, X is defined as $g - J$, $g - i$, $J - H$, $g - r$, or $J - 3.4\mu\text{m}$ and S is $z - K$, $J - K$, $H - K$, $g - D51$, or $K - 4.6\mu\text{m}$, respectively. Values of S are binned according to their corresponding X value. Bins in X are designed to contain an equal number of stars (20-25) in each bin, and because of this are not equally

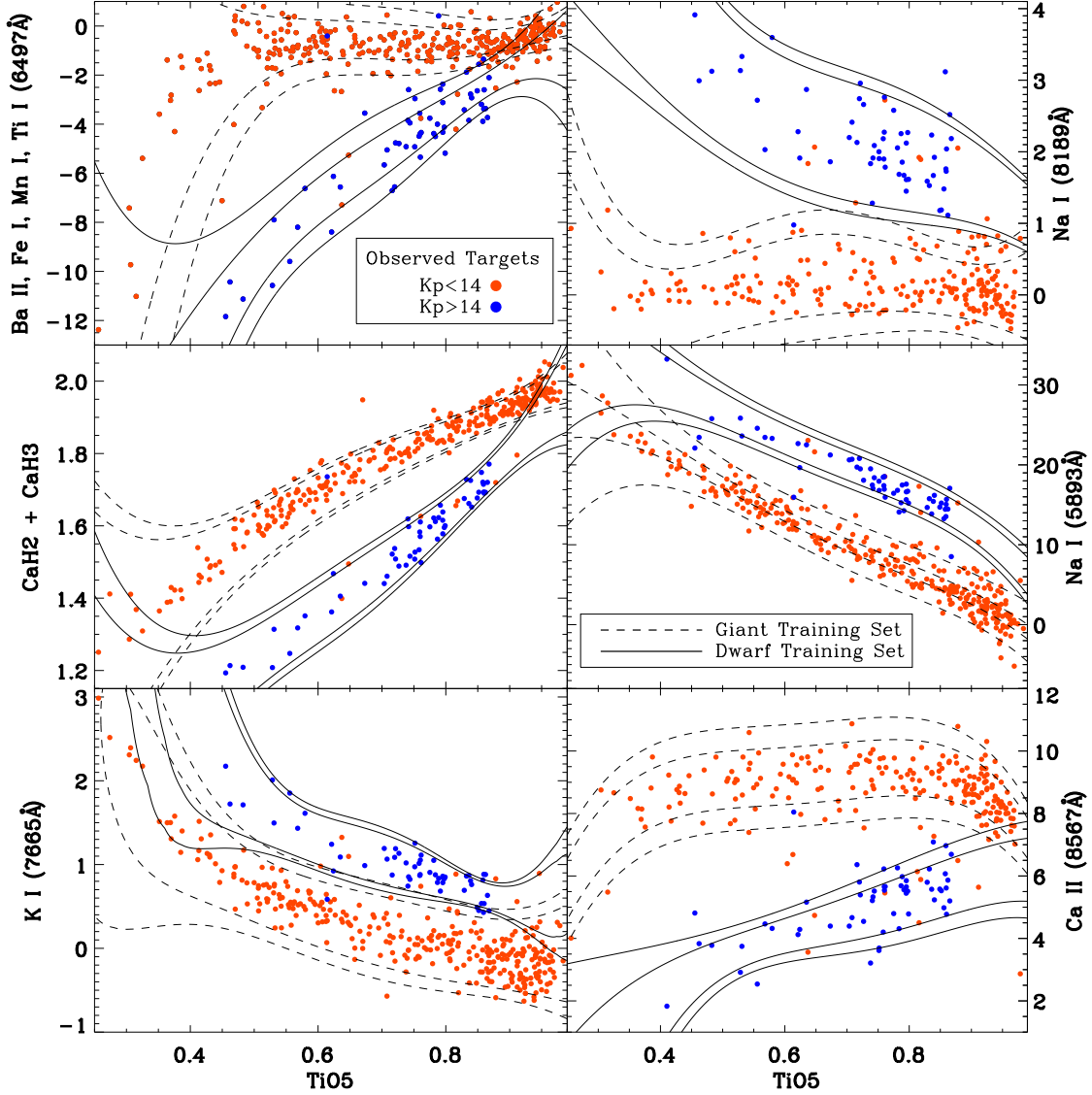


Figure 3.4: Measured strengths of each gravity-sensitive spectral feature vs. the strength of the TiO_5 band for *Kepler* late-type target stars with spectra from this program. Bright ($K_P < 14$) targets are shown as red colored circles while faint ($K_P > 14$) observed targets are shown as blue colored circles. The two-dimensional PDFs defined by our training set of giants (dashed line) and dwarfs (solid line) are overlaid. Contours of the PDF correspond to 68%, and 90%, intervals for the given training set. By using all spectral features, we positively identify each star with spectra as a giant or a dwarf with $> 99\%$ certainty.

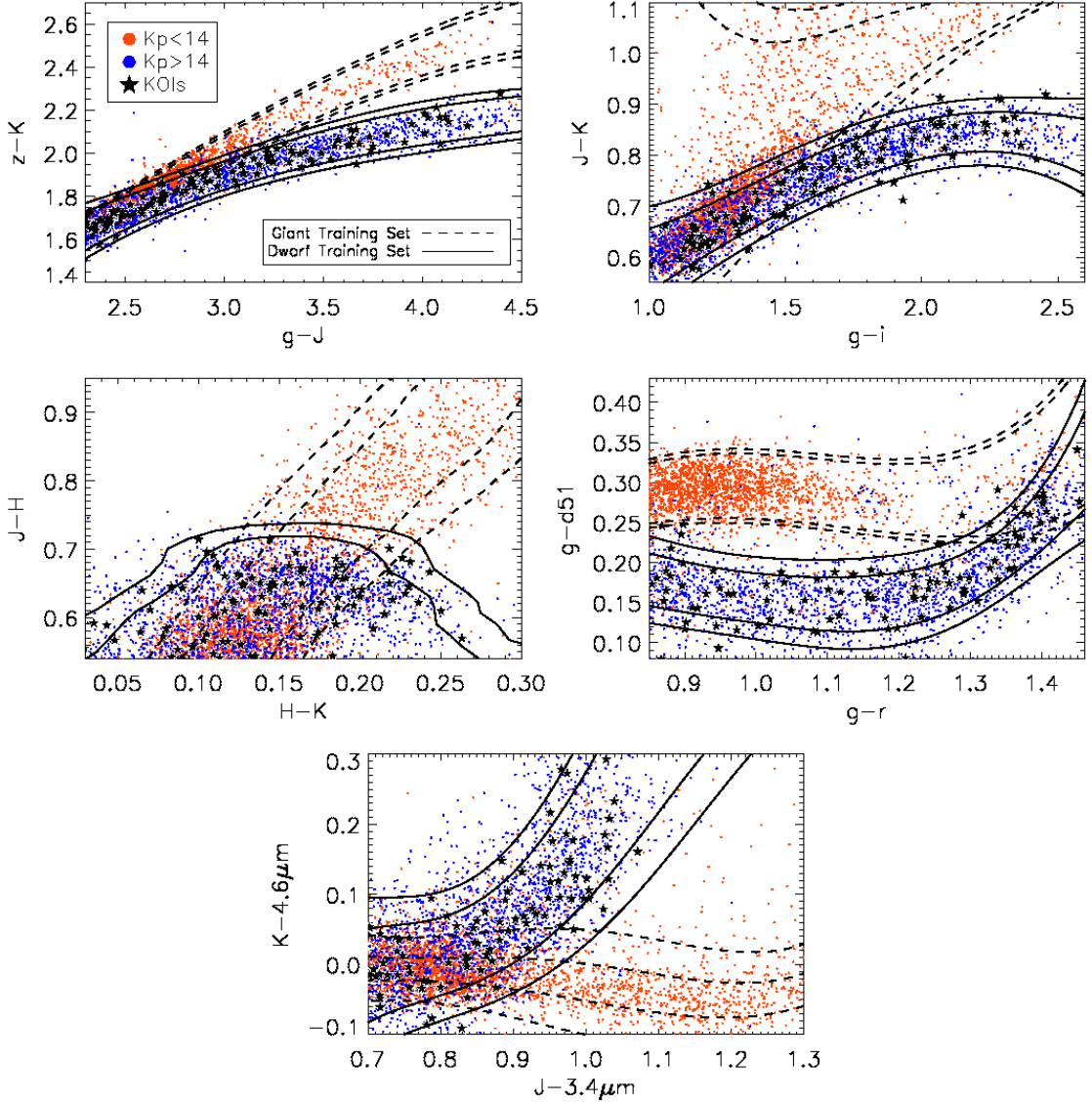


Figure 3.5: Similar to Figure 3.4 except using gravity-sensitive color-color relations. Each dot corresponds to a bright (red) or faint (blue) late-type *Kepler* target star. Contours are shown for the two training sets, corresponding to 68 and 90% PDF intervals. We apply this cut to *Kepler* target stars with $J - H > 0.52$ or $K_p - J > 2.0$, although only a subsample of this set is shown for clarity. Most stars fall well inside either the dwarf or giant sequence, however, even when all color relations are used, $\simeq 3\%$ of the sample still have an ambiguous luminosity class assignments. Most of these stars lack photometry in one or more band.

spaced in X . The mean (\bar{S}) and standard deviation (σ_S) of the distribution is computed in each bin. The two-dimensional PDF takes the form:

$$PDF(X, S) = C \exp \left[\frac{-(S - \bar{S}(X))^2}{2(\sigma_S(X))^2} \right], \quad (3.2)$$

where C is a normalization such that the entire PDF integrates to 1. PDFs for both giant and dwarf training sets overlaid on *Kepler* target star indices or colors are shown in Figures 3.4 and 3.5 for the spectroscopic and photometric sets, respectively.

The likelihood that star i is a dwarf for a given index j is:

$$L_{i,j} = \log_{10} \left(\frac{P_{\text{dwarf}}}{P_{\text{giant}}} \right), \quad (3.3)$$

and the likelihood given all indices is:

$$\langle L_i \rangle = \frac{\sum_j w_j(X) L_{i,j}}{\sum_j w_j(X)}, \quad (3.4)$$

where w_j is a weighting factor. Weights are calculated by determining the efficiency of a given feature at separating giants from dwarfs as a function of X . We take a random subsample (half the total sample) from each training set, and add Poisson noise to the spectra/colors consistent with our observations or given photometric errors. We then apply Equations 3.2 - 3.4 to the subsamples using $w_j(X) = 1$ for all X, j . Values of w_j are then set based on the fraction of dwarfs/giants correctly identified within a training set. $w_j(X) = 1$ if the feature/color identifies 100% of the targets within a given X bin correctly and $w_j(x) = 0$ if the feature/color identifies 50% or less (i.e. no better than guessing) of the targets correctly. Weights are linearly interpolated (based on the fraction of stars correctly identified) between these two values.

Repeating the calculation of L_i using $w_j = 1$ for all j does not change the classification of any stars with spectra (i.e. our results from spectra are essentially independent of our choice of weighting scheme). However, this is not the case for luminosity classes determined from color-color relations. The reason for this is the significant overlap between the PDFs of the color metrics for giant and dwarf training sets (e.g. $2.3 < g - J < 2.8$ and $1.6 < z - K < 1.9$, see Figure 3.5). In overlapping regions, indices or colors will give similar probabilities for a star being a giant or a dwarf, making the metric less useful in giant/dwarf discrimination. This problem is solved by our weighting scheme, as regions where giant and dwarf training sets overlap tend to have lower weights. We show a plot of the weights for the color-color relations in Figure 3.6. Weighting factors are set to 0 if any of the relevant indices/colors for a given star are missing or lie outside the range of our training sets.

We identify all *Kepler* target stars with spectra as a giant or a dwarf with better than 99% ($L_i > 2.0$ or $L_i < -2.0$) confidence. The full list of determined luminosity classes for stars with spectra is given in Table 3.1. For the photometric sample, $\simeq 97\%$ stars are placed into unambiguous giant or dwarf categories ($\langle L_i \rangle > 1.5$ for dwarfs or $\langle L_i \rangle < -1.5$ for giants). However, $\simeq 3\%$ of the sample are more ambiguous, most of which lack photometry in several bands.

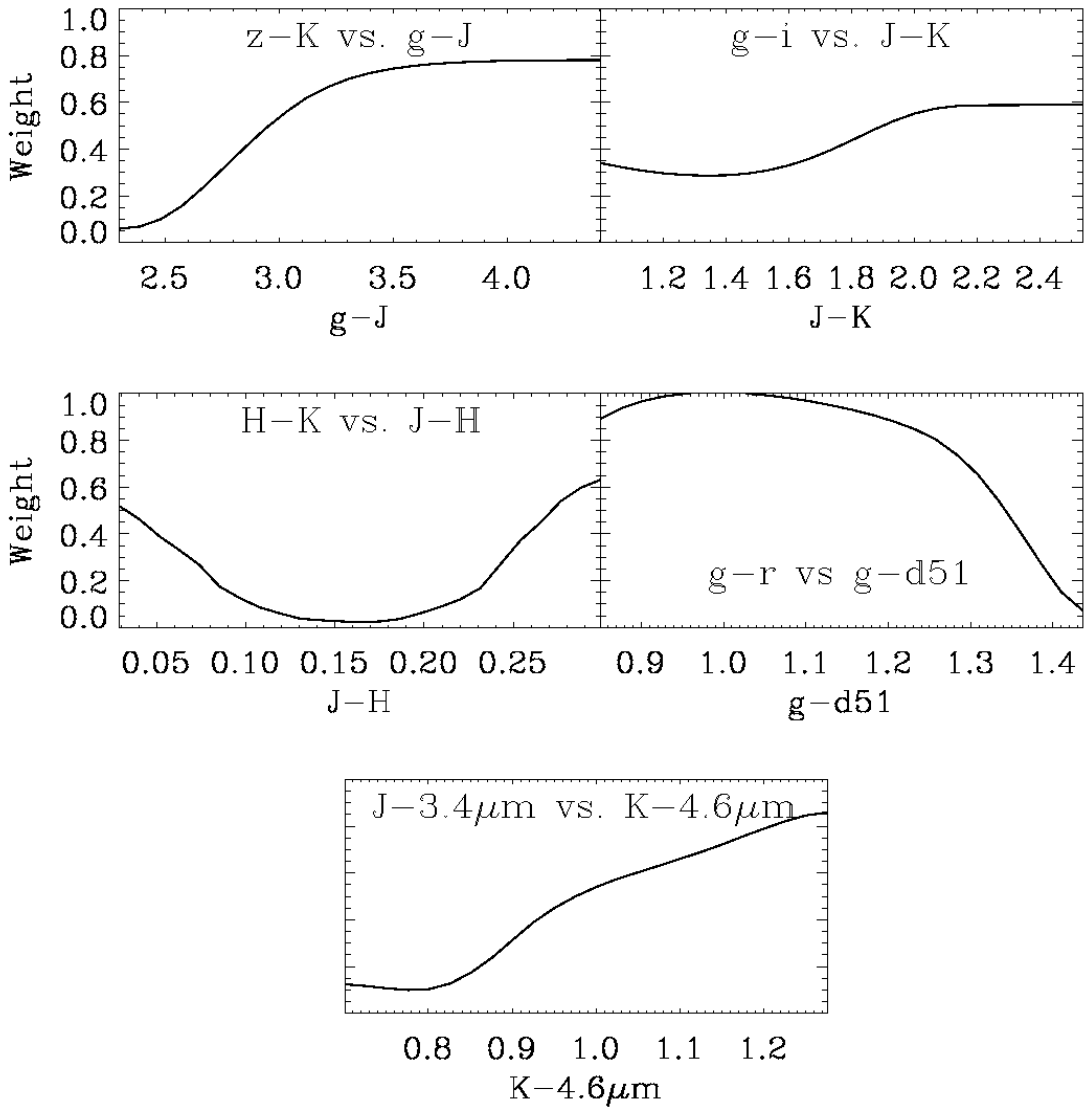


Figure 3.6: Weights for each of the color relations used for our photometric determination of luminosity class. Weights are determined by applying the giant and dwarf PDFs derived from half of the training set to the other half (after adding Poisson noise to the data). Weights are set to 0 for all X outside of our training sets. Weights tend to be low in regions where the giant and dwarf training set PDFs overlap, or in regions where data is sparse.

Since giant/dwarf assignments based on spectroscopy are very accurate, only binomial errors are considered for the spectroscopic sample. For uncertainty estimates from the photometric sample, we re-apply our likelihood calculations using 1000 different subsets of our training sets, adding random (Poisson) noise to the photometry, and then recalculating the giant fraction in each case. The variation in giant fraction is added in quadrature with binomial errors. This does not consider systematic errors (e.g. systematic photometric errors, discrepancies between training sets and *Kepler* target stars, etc).

3.3.5 Giant Star Fraction

We find that, for the coolest *Kepler* stars ($K_P - J > 2$), giant stars dominate the bright ($K_P < 14$) *Kepler* target stars but are relatively rare among dim ($K_P > 14$) targets. The fraction of giants is $96 \pm 1\%$ for bright stars, $7 \pm 3\%$ for dim stars, and $52 \pm 3\%$ for the combined set (based on our spectroscopy). Photometric assignments (considering $K_P - J > 2$) give consistent giant fractions: $97 \pm 2\%$ for bright stars, $11 \pm 3\%$ for dim stars, and $55 \pm 3\%$ for all stars with $K_P - J > 2$. The fractions in each brightness bin decrease somewhat when we apply a KIC $\log g > 4.0$ cut. The giant fraction becomes $74 \pm 8\%$ for bright stars and $3 \pm 2\%$ for dim stars. The fraction of giants for all stars significantly decreases to $10 \pm 2\%$, due mainly to the large number of stars lacking any $\log g$ classification, most of which are giants and all of which are removed by this cut.

3.4 Planet occurrence

Following the work of H12, we calculate the planet occurrence, f , which is defined as the total number of planets, within a given range (in orbital period and radius) and considering all orbital inclinations, per star within a given range (in T_{eff} , $\log g$, and K_P). Planet occurrence will be somewhat higher than the fraction of stars with planets due to the presence of multi-planet systems, but if the rate of planet multiplicity is low, then these two quantities will be nearly identical.

3.4.1 Nonparametric Estimation

We first calculate the planet occurrence following the nonparametric method of Gaidos et al. (2012). The total planet occurrence, f , is the sum of individual planet occurrences (f_i) over all i planets that fall within a given range in orbital period and radius. The most probable occurrence of the i th *Kepler* detected planet in the population of j *Kepler* target stars is:

$$f_i = \frac{1}{\sum_{j=1}^N p_{i,j} d_{i,j}}, \quad (3.5)$$

where $d_{i,j} = 1$ if the S/N of a planet transit around the j th star is sufficient to detect the transit, and 0 otherwise, $p_{i,j}$ is the geometric probability of a transit, and j is summed over all target stars that fall within a given range in T_{eff} , $\log g$, and K_P . We consider a planet

detected ($d_{i,j} = 1$) if:

$$S/N = \frac{\delta}{\sigma_{CDPP}} \sqrt{\frac{N\tau}{30}} \geq 7, \quad (3.6)$$

where δ is the transit depth, N is the number of transits that occur over the observation interval, τ is the transit duration in minutes, and σ_{CDPP} is the 30 minute combined differential photometric precision (CDPP) of *Kepler*. We use Quarter 1-2 30 minute CDPP values from *Kepler*. Our detection threshold $S/N = 7$ matches what is used by Borucki et al. (2011) and Batalha et al. (2013).

For small planets on nearly circular orbits,

$$p = 0.238P^{-2/3}M_*^{-1/3}R_*, \quad (3.7)$$

where P is the orbital period in days and M_* and R_* are the star's mass and radii in solar units. Values for M_* and R_* are computed by interpolating a grid of stellar radii/masses from the Dartmouth Stellar Evolution Database (DSEP Dotter et al. 2008) at estimated values of T_{eff} , [Fe/H], and age. We use DSEP because radii and masses derived from their isochrones are in good agreement (< 0.03 RMS deviation in radius) with current observations from interferometry (Dotter et al. 2008; Feiden et al. 2011).

For exoplanet hosts we use the metallicities given in M12, but for field stars metallicities are drawn from a random gaussian distribution of metallicities with $\overline{[Fe/H]} = -0.07$ and $\sigma_{[Fe/H]} = 0.20$. This distribution is designed to be consistent with the distribution of M dwarfs in the solar neighborhood (Johnson & Apps 2009; Casagrande et al. 2011). Ages are assigned randomly assuming a constant star formation rate (excluding ages < 100 Myr). However, since M dwarfs do not change significantly while on the main sequence, our results are not changed when we fix all ages to 5 Gyr. The resulting stellar radii from the DSEP grid are used in conjunction with values of R_p/R_* from Borucki et al. (2011) to compute planetary radii.

Estimates of T_{eff} are inferred from our optical spectra. We compare our visible spectra to a grid of models of K- and M-dwarf spectra generated by the BT-SETTL version of PHOENIX (Allard et al. 2011). Details of the comparison, sub-grid interpolation, and error calculations are described in Lépine et al. (2013). The grid of models spans T_{eff} of 3000-5000 K in steps of 100 K, log g values of 0.0-5.0 in steps of 0.5 dex, and metallicities of [M/H] = -1.5, -1, -0.5, 0, +0.3, and +0.5. α/Fe is taken to be solar. We report the T_{eff} of the best-fit interpolated model, and the standard deviation of T_{eff} among the set of interpolated models that are nearby in parameter space in Table 3.1.

Our calculated values of T_{eff} are shown in Figure 3.7 vs. the temperature given in the KIC (Brown et al. 2011). BT-SETTL temperatures are systematically lower than KIC temperatures by 110_{-35}^{+15} K for the dwarf stars, and 150_{-35}^{+10} K for the giant stars. Errors are calculated by bootstrap resampling. This is consistent with other determinations using the atmospheric models of Allard et al. (2011), including other determinations on *Kepler* KOI stars (M12). Our calculated temperatures are tightly correlated with KIC temperatures. When KIC temperatures are corrected for our observed offset, the standard deviation of the difference in calculated temperatures ($\sigma_{KIC-Phoenix}$) is 90 K, suggesting that the KIC temperatures for low-mass stars are *more* precise but are less accurate than suggested by Brown et al. (2011). For field stars with visible-wavelength spectra, we adopt our calculated

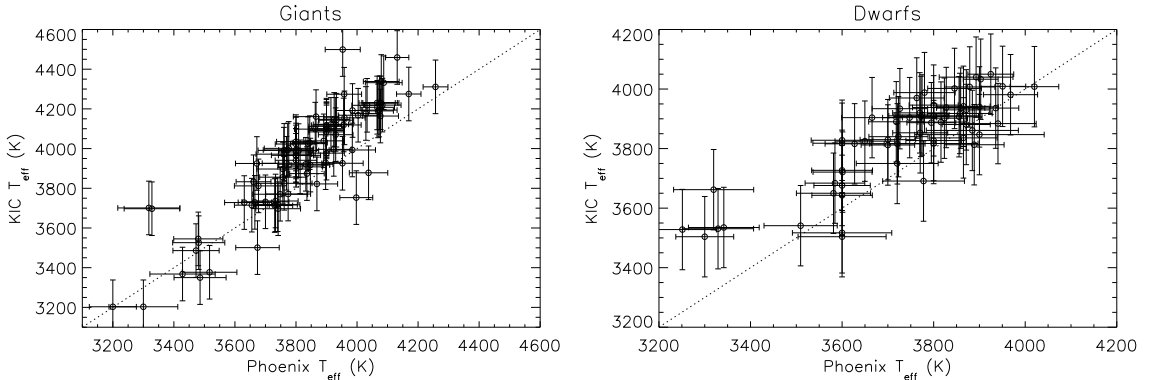


Figure 3.7: Effective temperatures computed by fitting our spectra to models from the BT-SETTL version of PHOENIX (Allard et al. 2011) as a function of the KIC assigned effective temperature for giants (left) and dwarfs (right). The dotted line indicates equality. Errors are estimated as part of our model fitting procedure (errors on KIC temperatures are taken to be 135 K (Brown et al. 2011). For both giants and dwarfs there is a clear 100-200 K offset between our spectroscopically determined temperatures and the KIC temperatures. This is most likely a consequence of the models used, as Castelli & Kurucz (2004) models used to fit KIC photometry to effective temperatures are unreliable below 4000 K.

T_{eff} values, and for stars with exoplanet candidates we use the T_{eff} from M12. For the remaining stars we adjust the KIC effective temperatures of *Kepler* stars downward randomly by 110^{+15}_{-35} K to keep the temperatures consistent with those of the KOI stars and those with spectra in our sample. This offset is randomized to account for errors in the systematic difference between temperatures calculated from our spectra and those listed in the KIC.

Following H12, we compute the planet occurrence with $2R_{\oplus} < R_P < 32_{\oplus}$ and $P < 50$ days around stars with $3400 < T_{eff} < 4100$ using Equations 3.5 - 3.6. Again following H12, we exclude stars with $K_P > 15$ where the accuracy of the planet candidate parameters are more questionable and the false positive rate is higher (Morton & Johnson 2011; Borucki et al. 2011). We calculate the standard deviation of the frequency using a Monte Carlo analysis. Stellar parameters are perturbed randomly (see above) accounting for errors from M12 on KOI metallicity and T_{eff} , and random errors from derived from T_{eff} fits (see Figure 3.7) to our spectra. Other stars are given a random error of 90 K. We perturb transit parameters R_P/R_* and period according to errors given by Borucki et al. (2011). Planetary radii are recalculated from perturbed values of R_P/R_* and R_* .

We remove planets from the KOI sample using the false positive probabilities from Morton & Johnson (2011) (e.g., a planet candidate with a 5% false positive probability is removed in 5% of the simulations). We remove giant stars from the sample using the calculated photometric likelihoods (Section 3.3.3) for each star, such that a star with a 10% likelihood of being a giant star will be removed from the sample in 10% of the Monte Carlo (MC) simulations. This also applies to stars with detected planet candidates, causing the planet to be removed, i.e. we consider the planet detection to be a false positive if the star

is a giant. The number of KOIs and target stars simulated varies somewhat for each Monte Carlo run, but there are typically $\simeq 14$ KOIs around $\simeq 1300$ stars in a given simulation.

We find that there are 0.37 ± 0.08 planets (with $2R_{\oplus} < R_P < 32R_{\oplus}$ and $P < 50$ days) per star in the temperature range $3400 < T_{eff} < 4100$. For comparison we run an additional Monte Carlo simulation but only remove giant stars with KIC $\log g > 4.0$ as in H12. This test yields a planet occurrence of 0.26 ± 0.05 , slightly lower than when giant stars are properly removed. To test how our results depend on our choice of stellar radii model (DSEP) we also run two simulations using the Yonsei-Yale (Demarque et al. 2004) isochrones: one with giant stars removed as explained above and another removing just giants with KIC $\log g > 4.0$. The runs using Yonsei-Yale are included because their models are commonly used to derive radii for *Kepler* targets (e.g. Batalha et al. 2013). However, radii and masses derived from DSEP are a far better match to observations of late-type stars (Dotter et al. 2008; Feiden et al. 2011), and planet occurrence calculated using the DSEP models should be considered more reliable. The resulting Monte Carlo distributions are shown in Figure 3.8.

3.4.2 Parametric Likelihood estimation

We also perform a parametric maximum likelihood estimation of the fraction of stars with planets with radii $2R_{\oplus} < R < 32R_{\oplus}$ and orbital period $P < 50$ d (see H12 for a similar analysis). For discrete, binomial (detection or non-detection) events, the likelihood is expressed as:

$$L = \prod_j^D \rho_j \times \prod_k^{ND} (1 - \rho_k), \quad (3.8)$$

where the first product is of detections, the second is of non-detections, and ρ_i is the probability that a planet with properties in the appropriate ranges orbits the i th star and is detected by *Kepler* to transit. For this formulation, we have assumed that $\rho \ll 1$. We adopt the specific power-law form $dN = CR_i^{-\alpha}P^{-\beta}d\ln R \cdot d\ln P$ for the intrinsic distribution of planets. If both α and β are > 0 then the normalization factor C is given by:

$$C = \frac{f\alpha\beta}{(R_1^{-\alpha} - R_2^{-\alpha}) (P_1^{-\beta} - P_2^{-\beta})}, \quad (3.9)$$

where f is the total planet occurrence. We do not model multi-planet systems; that level of analysis is not justified given the large uncertainties in our parameters.

Following the usual procedure, we maximize the logarithm of L :

$$\begin{aligned} \ln L &= \sum_j^D [\ln C - \alpha \ln R_j - \beta \ln P_j + \ln D_j(R_j, P_j)] \\ &\quad + \sum_k^{ND} \ln [1 - CF_k(\alpha, \beta)] \end{aligned} \quad (3.10)$$

where $D_j(R_j, P_j)$ is the probability of detecting the j th planet around its host star, including the geometric factor (note $D_j(R_j, P_j) = d_j p_j$, see Equation 3.5 and 3.7), and

$$F_k(\alpha, \beta) = \int_{R_1}^{R_2} \int_{P_1}^{P_2} R^{-\alpha} P^{-\beta} D_k(R, P) d\ln R \cdot d\ln P \quad (3.11)$$

If the detection rate is low, then:

$$\begin{aligned} \ln L &\approx \sum_j [\ln C - \alpha \ln R_j - \beta \ln P_j + \ln D_j(R_j, P_j)] \\ &\quad - C \sum_k^{ND} F_k(\alpha, \beta). \end{aligned} \quad (3.12)$$

We then substitute Equation 3.9 for C . Ignoring terms that do not depend on α , and thus do not affect its maximum likelihood value, we find the following quantity must be maximized:

$$\begin{aligned} \ln L_\alpha &= \sum_j [\ln \alpha - \ln (R_1^{-\alpha} - R_2^{-\alpha}) - \alpha \ln R_j] - \\ &\quad \frac{f \alpha \beta \sum_k^{ND} F_k(\alpha, \beta)}{(R_1^{-\alpha} - R_2^{-\alpha}) (P_1^{-\beta} - P_2^{-\beta})}. \end{aligned} \quad (3.13)$$

Likewise,

$$\begin{aligned} \ln L_\beta &= \sum_j [\ln \beta - \ln (P_1^{-\beta} - P_2^{-\beta}) - \beta \ln P_j] - \\ &\quad \frac{f \alpha \beta \sum_k^{ND} F_k(\alpha, \beta)}{(R_1^{-\alpha} - R_2^{-\alpha}) (P_1^{-\beta} - P_2^{-\beta})}. \end{aligned} \quad (3.14)$$

The simultaneous solution for the planet occurrence is found by maximizing the terms that depend on f and is simply

$$f = \frac{N_p (R_1^{-\alpha} - R_2^{-\alpha}) (P_1^{-\beta} - P_2^{-\beta})}{\alpha \beta \sum_k^{ND} F_k(\alpha, \beta)}, \quad (3.15)$$

where N_p is the number of detected planets. Equation 3.15 immediately suggests a reduction in the last terms of Equations 3.13 and 3.14 to N_p , which is independent of α and β and can be ignored.

Because there are too few systems in our sample to get a robust estimate of β , we fix $\beta = 0$ with a cut-off at $P_1 = 1$ d, consistent with the findings of previous analyses (Cumming et al. 2008; Wolfgang & Laughlin 2012, H12). Equation 3.15 becomes:

$$f = \frac{N_p (R_1^{-\alpha} - R_2^{-\alpha}) \ln(P_2/P_1)}{\alpha \sum_k^{ND} F_k(\alpha, \beta = 0)}. \quad (3.16)$$

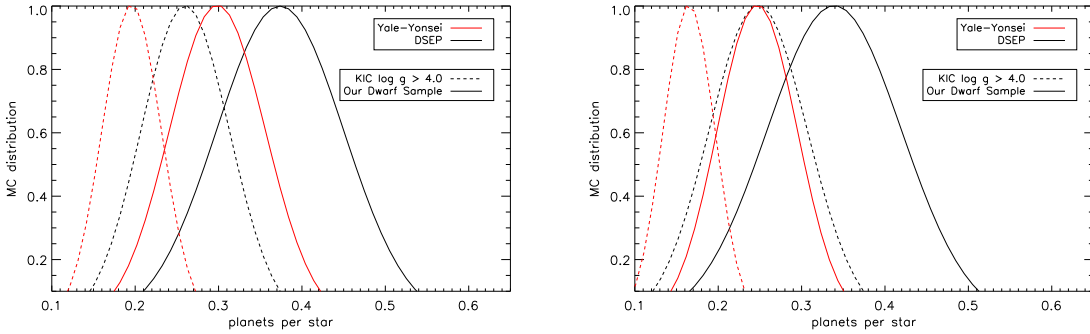


Figure 3.8: Planet occurrence with giant stars removed (solid line) or using KIC $\log g > 4.0$, using isochrones from DSEP (black) or from Yonsei-Yale (red) calculated by Monte Carlo analysis. The left plot is calculated using nonparametric MC estimate, and the right uses a parametric MC estimate. For both plots, we consider planets with radii $2R_{\oplus} < R_P < 32_{\oplus}$ and periods $P < 50$ days, and stars with effective temperatures $3400 < T_{eff} < 4100$. A full description of our analysis is given in Section 3.4.

Artificial Monte Carlo data sets suggest that f is robustly recovered, but that recovered values of α are biased downwards. Using the cool KOIs defined here, stellar parameters derived as explained above, and Monte Carlo data sets generated by sampling with replacement, we find that $f = 0.34 \pm 0.08$, consistent with our nonparametric calculation. As before, we repeat our Monte Carlo simulation but only removing giant stars with KIC $\log g > 4$, and another run using the Yonsei-Yale evolutionary tracks (Demarque et al. 2004) instead of those of DSEP. The resulting Monte Carlo distributions are shown in Figure 3.8.

3.5 Planet-host Metallicities

SL11 use $g - r$ vs. $J - H$ colors to conclude that late-type ($J - H \simeq 0.62$) exoplanet hosts are redder and more metal-rich than stars without transiting planets. Because giant stars have bluer $g - r$ colors at a given $J - H$ color (Bessell & Brett 1988; Gilbert et al. 2006), a significant number of giant star interlopers in their sample will cause field stars to appear metal poor. Giant stars have stellar radii 10-100 times larger than dwarfs, significantly reducing the depth in a light curve for a given transiting planet, making it much less likely that they will appear as KOIs (with the exception of false positives).

We can test their findings by creating a “pure” dwarf sample, and comparing its color distribution to that of the KOI sample. Our $K_p - J > 2$ spectroscopic sample is systematically redder in $J - H$ than the $0.56 < J - H < 0.66$ bin used in SL11, preventing us from making a direct comparison. Instead, we construct samples of giants and dwarfs in the $J - H \simeq 0.62$ bin based on our photometric determination of luminosity class. For both the dwarf and giant samples, we select *Kepler* target stars with photometry in all bands used in our photometric assignment of luminosity class ($J, H, K, D51, g, r$, and all four WISE bands). We then select stars with a $> 90\%$ likelihood of being dwarfs based on

our analysis in Section 3.3.3. The resulting dwarf sample is $\simeq 2500$ stars. This sample may still contain giants. We add Poisson noise to the photometry of both the training sets and the *Kepler* $0.56 < J - H < 0.66$ target star sample, and take random subsamples of both training sets. We then reapply these subsamples to the modified photometry of the *Kepler* sample. We repeat this process 1000 times. By analyzing the number of giant stars in each of these new samples we find that our dwarf sample is $< 1\%$ giant stars at 95% confidence, ignoring possible systematic errors.

We use this dwarf sample, following the method of SL11, to compare the $g - r$ colors at a given $J - H$ (a proxy of effective temperature) of the exoplanet host stars with our dwarf sample. Figure 3.9 shows $g - r$ colors as a function of $J - H$ colors for the dwarf, giant, planet-host, and KIC $\log g > 4.0$ sample. We find no significant difference in color between the KOI stars and our dwarf sample. Unlike the KIC $\log g > 4.0$ sample, *the locus of our photometrically selected dwarf sample is consistent with the locus of the KOI sample at $J - H \simeq 0.62$* . For stars with $K_P - J > 2.0$ we find an offset in $g - r$ color of only -0.05 ± 0.03 between the spectroscopically confirmed dwarfs and late-type KOI stars hosting Earth-to-Neptune sized planets. When we use our photometric sample of dwarfs in the $J - H \simeq 0.62$ bin we find an offset of 0.01 ± 0.02 and we can rule out the offset of 0.08 seen by SL11 with $> 99.7\%$ certainty. Our photometric selection may remove some metal-poor dwarfs. However, even when we include stars $\geq 60\%$ likelihood of being dwarfs, which will necessarily increase the number of interloping giants, the offset is still only 0.03 ± 0.02 (consistent with zero offset).

In spite of the low giant fraction for dim *Kepler* target stars, it is not sufficient to simply repeat the SL11 analysis exclusively for stars with $K_P > 14$. Since SL11 only examine stars with KIC $\log g > 4.0$, it is far more important to investigate the $g - r$ distribution of *misidentified* giants in the $0.56 < J - H < 0.66$ color range (i.e. giant stars that were assigned $\log g > 4$ in the KIC). In fact the fraction of misidentified dim giant stars in their $J - H \simeq 0.62$ bin is higher (12%), than it is for the $K_P - J > 2$ star sample. We show why this is the case in Figure 3.10, which shows the distribution of giants, dwarfs, and misidentified giants in $J - H$ vs. $g - r$ space. Misidentified giants are more concentrated at $0.58 < J - H < 0.63$. Further, the misidentified giants in this $J - H$ range are much more blue than the dwarfs in the same range. Thus by selecting a color bin centered on $J - H = 0.62$, SL11 are over-selecting giant stars, even after applying a KIC $\log g > 4$ cut ($\simeq 15\%$ of this sample are giant stars). This concentration of misidentified giants is the most likely explanation for the color offset seen by SL11, and also explains why the same $g - r$ offset is not seen at redder $J - H$ colors (see Figure 3.9).

3.6 Discussion

We use visible-wavelength spectra to determine the properties of a subset of late-type *Kepler* target stars. We separate giants from dwarfs by comparing our spectra to those of stars with known luminosity class, and determine effective temperatures by comparing with PHOENIX model spectra. We extend our results to a larger collection of *Kepler* stars using photometry from the KIC, 2MASS, and WISE catalogs. We apply our luminosity class determinations to refine estimates of the planet occurrence around stars with $3400 < T_{eff} < 4100$, and

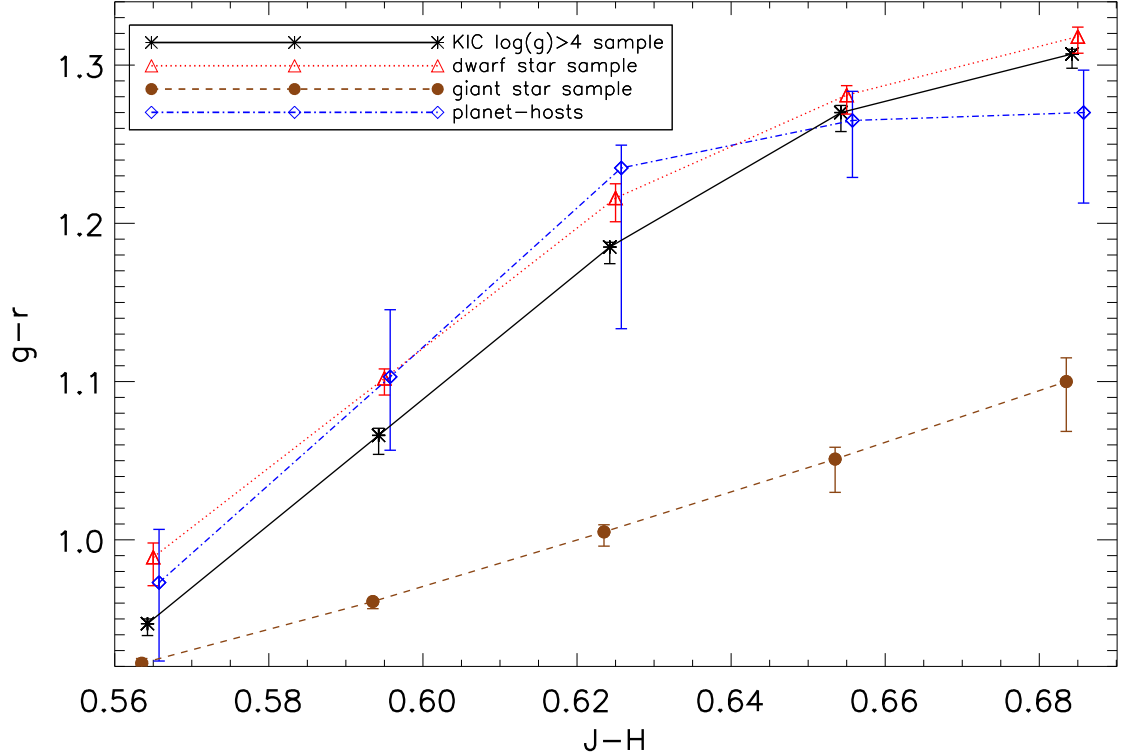


Figure 3.9: Median $g - r$ colors as a function of $J - H$ colors for *Kepler* target stars with: Earth to Neptune sized planet candidates (dotted/dashed line, diamonds), KIC $\log g > 4.0$ (solid line, asterisks), $> 90\%$ likelihood of being dwarfs based on their colors (dotted line, triangles), $> 90\%$ likelihood of being giants (dashed line, circles). The 1σ errors are calculated for the median in each bin by bootstrap resampling. Bins for all data sets are the same, but each point is offset slightly from the bin center for clarity. There is a statistically significant offset between the KIC $\log g > 4.0$ sample and the planet hosts when we consider stars with $0.58 < J - H < 0.66$, however, this offset is no longer present when misidentified giant stars are removed from the sample. Indeed, our dwarf control sample closely tracks the colors of the planet-hosting stellar population.

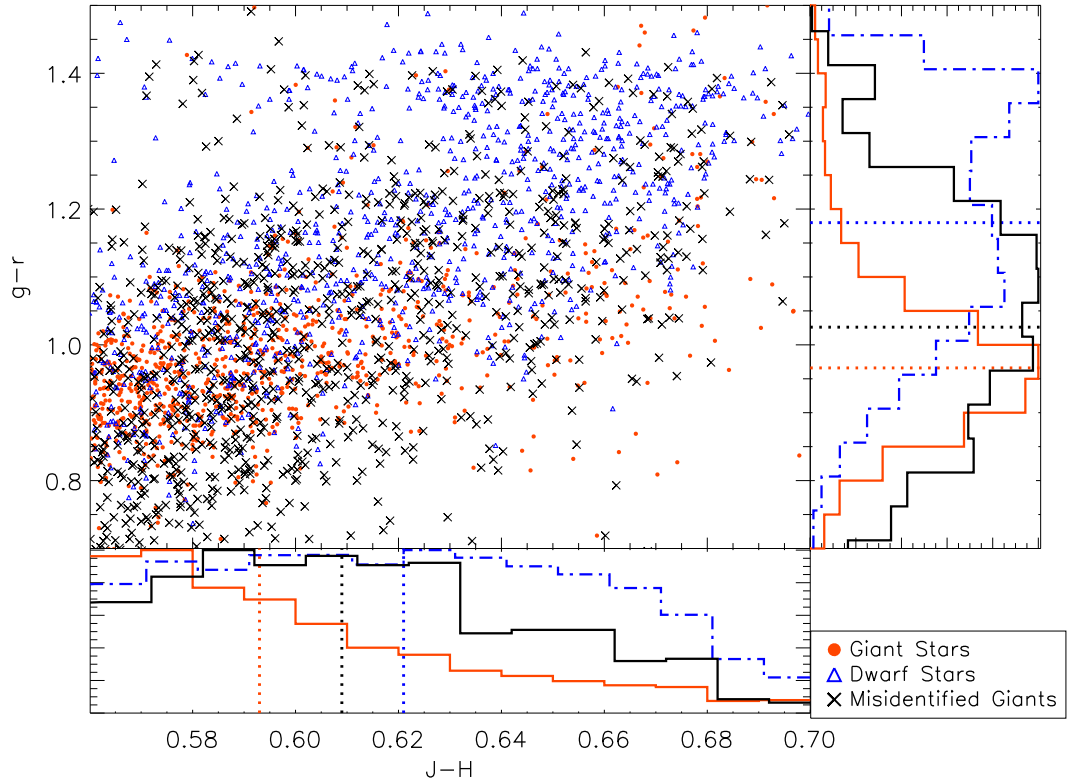


Figure 3.10: Scatter plot of a sample of *Kepler* dwarf stars (blue triangles), giant stars (red circles), and giant stars labeled as dwarfs (KIC $\log g > 4.0$) by the KIC (black crosses) in $g - r$ vs $J - H$ space. An equal number of data points are shown from each subset (giants/dwarfs/misidentified giants) to highlight the *relative* distributions. The histograms on the bottom and right side show the 1-D distribution in each color (coloring matches the center plot). Histograms are normalized to a peak value of 1 and the median of each histogram is marked with a dotted line (of the corresponding color). Although giant stars cover a range of $J - H$ colors, those that were mislabeled as dwarfs are more concentrated around $J - H \simeq 0.61$. The distribution of misidentified giants is bluer than the dwarf distribution. Thus if the misidentified giant stars are not properly removed the dwarf sample will appear bluer (more metal poor) than the KOI distribution (which contains almost no misidentified giants).

compare the colors – and hence metallicities of stars with and without detected Earth and Neptune sized planets. We draw four major conclusions:

1. Among stars redder than $K_P - J = 2$ (\simeq K5 and later), bright ($K_P < 14$) stars are predominantly ($96 \pm 1\%$) giants, while dim stars ($K_P > 14$) are predominantly ($93 \pm 3\%$) dwarfs. These fractions improve somewhat when we consider stars with KIC determined $\log g > 4.0$ ($74 \pm 8\%$ and $97 \pm 2\%$ respectively). Overall, $52 \pm 3\%$ of *Kepler* stars with $K_P - J > 2$ are giants. However, only $10 \pm 2\%$ of said stars with KIC $\log g > 4.0$ are giants, a consequence of the large number of late-type stars lacking any temperature or $\log g$ values in the KIC.

2. KIC effective temperatures, based on the models of Castelli & Kurucz (2004) and *griz* and *JHK* photometry, are systematically higher by 110_{-35}^{+15} K compared to those derived from our own spectra and PHOENIX BT-SETTL atmosphere models (Allard et al. 2011).

3. Adopting the temperature scale from BT-SETTL and radii/masses from the Dartmouth Stellar Evolution Database (Dotter et al. 2008) and removing stars we identify as giants based on nonparametric and parametric Monte Carlo calculations we find a planet occurrence rate of $\simeq 0.36 \pm 0.08$ for planets with radii $2R_\oplus < R_P < 32R_\oplus$ and periods $1 < P < 50$ days per star in the temperature range $3400 < T_{\text{eff}} < 4100$. Using the KIC determined luminosity classes leads to a somewhat lower planet occurrence of 0.26 ± 0.05 .

4. The $g - r$ colors of exoplanet host stars at $J - H \simeq 0.62$ are consistent with an unbiased sample of *Kepler* dwarf stars, ruling out any large difference between hosts of Earth-to-Neptune sized planets and those without any detected planets.

Surprisingly, there are hundreds of stars in our photometric sample that could have been easily identified as giants with KIC photometry, but were assigned $\log g > 4$. The KIC primarily uses $g - D51$ vs $g - r$ colors to identify giants, and many late-type stars with KIC $\log g > 4.0$ have $g - D51$ vs $g - r$ colors consistent with giants (and inconsistent with dwarfs).

Our calculated giant fraction is consistent with other independent measurements. Gaidos et al. (2012) compare radial velocity data from M2K (Apps et al. 2010; Fischer et al. 2012) to *Kepler* results and note that the completeness of the coolest *Kepler* target stars may be quite low ($\simeq 50\%$), much of which could be explained by an underestimate of the frequency of giant stars. Additionally, Ciardi et al. (2011) find that bright *Kepler* M stars are “predominantly giants, regardless of the KIC classification” based on *JHK* photometry alone. Our giant fraction is also consistent with the current understanding of Galactic structure: based on a simulation from TRILEGAL (Girardi et al. 2005), $\simeq 92$ of stars near the center of the *Kepler* field with $K_P < 14$ and $K_P - J > 2.0$ are giants.

Interestingly, we find two KOIs with colors consistent with giant stars. KOI 667 and KOI 977 both fall within our giant training set in multiple color relations, and outside our dwarf training set. M12 identify KOI 977 as a giant, and they also note that KOI 667 consisted of 5 objects within $6''$ which may be contaminating 2MASS or WISE photometry. One of these objects could be an eclipsing binary, diluted by the other stars. KOI 667 also has a relatively high (10%) false positive probability based on Galactic structure models (Morton & Johnson 2011).

Our values of T_{eff} are consistent with results reported elsewhere also using BT-SETTL, including observations of the late-type KOIs with near-infrared spectra M12. These authors find a similar systematic offset of 123_{-32}^{+24} K between their temperatures and KIC assigned

temperatures. KIC temperatures are based on the models of Castelli & Kurucz (2004) and the evolutionary tracks of Girardi et al. (2000), which, although reliable for solar-mass stars, are untrustworthy for stars with $T_{eff} < 3750$ K (Brown et al. 2011).

Our planet occurrence estimate is slightly higher than that of H12, who, using results from *Kepler*, find a planet occurrence rate of 0.30 ± 0.08 for stars with $3600 < T_{eff} < 4100$. The difference is primarily due to reliance on luminosity class determinations by Brown et al. (2011), which we find to be inaccurate. However, the difference is within 1σ . For both our work and that of H12, errors are dominated by the low number of late-type stars (and therefore planets around them) in the *Kepler* field and very high random ($\sim 35\%$) errors in stellar radii.

In addition to random errors (e.g. stellar radii and R_p/R_*) that are included in our Monte Carlo simulation, there may be large systematic uncertainties in atmosphere models and evolutionary tracks, which can change the resulting frequency. When we use the Yonsei-Yale isochrones, it decreases our planet occurrence by $\simeq 0.08$. Interestingly, this difference is similar in size to the random errors in our Monte Carlo analysis ($\simeq 0.08$), and the difference between proper giant removal and using KIC $\log g > 4.0$ ($\simeq 0.10$). This suggests that giant star removal, improved stellar characterization of the dwarf stars, and use of reliable stellar models of late-type stars are of roughly equal importance in characterizing the planet occurrence around very cool stars.

The lack of a strong correlation between host-star metallicity and the presence of Earth-to-Neptune sized planets is consistent with what is found for solar-type stars, e.g. Mayor et al. (2011). This also matches the findings of M12, who determine that among the late-type *Kepler* exoplanet hosts in our sample the median [M/H] is -0.11 ± 0.02 . This distribution is consistent with stars in the solar neighborhood (-0.05 to -0.15 , Johnson & Apps 2009; Schlaufman & Laughlin 2010; Casagrande et al. 2011). A metallicity difference could only be present if *Kepler* target stars are significantly more metal poor than stars in the solar neighborhood. As explained in Gaidos et al. (2012), *Kepler* late K and M stars are < 250 pc from the Sun, and $\lesssim 60$ pc above the galactic plane. Most of the stars will be in the thin disk, and have metallicities similar to that of the solar neighborhood.

Our analysis of the $g - r$ colors of planet hosts contradicts the results of SL11, who find a 4σ difference between $g - r$ colors of late-type exoplanet hosts and stars with no exoplanets present. Their result is most likely an artifact of the large number of stars which were misclassified as dwarfs in the KIC. SL11 state that their result can be reproduced if their sample of KIC $\log g > 4$ stars is between 10% and 30% giants, which they calculate by adding stars with KIC $\log g < 4$ stars (test giant stars) into their control sample, and measuring the resulting $g - r$ color offset. We find that the giant fraction is above 10% for this color range. Further, if the KIC $\log g > 4$ sample that SL11 used was significantly contaminated with giants, the sample will have bluer colors than a true dwarf sample. Adding test giants (to measure the resulting color change) to an already giant-star contaminated sample will create smaller changes in the overall color of a sample than if the sample had contained only dwarf stars. Thus more test giant stars will be required to produce a given color offset, creating an artificially high estimate for the level of giant contamination required to produce the observed color difference.

Although the $g - r$ colors of exoplanet hosts in our sample are consistent with our dwarf sample, we cannot rule out small offsets ($\lesssim 0.05$) in $g - r$ color. It is possible that any

metallicity effect is sufficiently small that it is diluted to non-detection by the large number of undetected exoplanets in the dwarf sample. As *Kepler* continues to discover planets of smaller radii and at larger orbital periods, the answer may become more clear.

References

- Aldering, G., Antilogus, P., Bailey, S., Baltay, C., Bauer, A., Blanc, N., Bongard, S., Copin, Y., Gangler, E., Gilles, S., Kessler, R., Kocevski, D., Lee, B. C., Loken, S., Nugent, P., Pain, R., Pécontal, E., Pereira, R., Perlmutter, S., Rabinowitz, D., Rigaudier, G., Scalzo, R., Smadja, G., Thomas, R. C., Wang, L., Weaver, B. A., & Nearby Supernova Factory. 2006, ApJ, 650, 510
- Allard, F., Homeier, D., & Freytag, B. 2011, in Astronomical Society of the Pacific Conference Series, Vol. 448, 16th Cambridge Workshop on Cool Stars, Stellar Systems, and the Sun, ed. C. Johns-Krull, M. K. Browning, & A. A. West, 91
- Allen, L. E. & Strom, K. M. 1995, AJ, 109, 1379
- Apps, K., Clubb, K. I., Fischer, D. A., Gaidos, E., Howard, A., Johnson, J. A., Marcy, G. W., Isaacson, H., Giguere, M. J., Valenti, J. A., Rodriguez, V., Chubak, C., & Lepine, S. 2010, PASP, 122, 156
- Batalha, N. M., Borucki, W. J., Koch, D. G., Bryson, S. T., Haas, M. R., Brown, T. M., Caldwell, D. A., Hall, J. R., Gilliland, R. L., Latham, D. W., Meibom, S., & Monet, D. G. 2010, ApJ, 713, L109
- Batalha, N. M., Rowe, J. F., Bryson, S. T., Barclay, T., Burke, C. J., Caldwell, D. A., Christiansen, J. L., Mullally, F., Thompson, S. E., Brown, T. M., Dupree, A. K., Fabrycky, D. C., Ford, E. B., Fortney, J. J., Gilliland, R. L., Isaacson, H., Latham, D. W., Marcy, G. W., Quinn, S. N., Ragozzine, D., Shporer, A., Borucki, W. J., Ciardi, D. R., Gautier, III, T. N., Haas, M. R., Jenkins, J. M., Koch, D. G., Lissauer, J. J., Rapin, W., Basri, G. S., Boss, A. P., Buchhave, L. A., Carter, J. A., Charbonneau, D., Christensen-Dalsgaard, J., Clarke, B. D., Cochran, W. D., Demory, B.-O., Desert, J.-M., Devore, E., Doyle, L. R., Esquerdo, G. A., Everett, M., Fressin, F., Geary, J. C., Girouard, F. R., Gould, A., Hall, J. R., Holman, M. J., Howard, A. W., Howell, S. B., Ibrahim, K. A., Kinemuchi, K., Kjeldsen, H., Klaus, T. C., Li, J., Lucas, P. W., Meibom, S., Morris, R. L., Prša, A., Quintana, E., Sanderfer, D. T., Sasselov, D., Seader, S. E., Smith, J. C., Steffen, J. H., Still, M., Stumpe, M. C., Tarter, J. C., Tenenbaum, P., Torres, G., Twicken, J. D., Uddin, K., Van Cleve, J., Walkowicz, L., & Welsh, W. F. 2013, ApJS, 204, 24
- Bean, J. L., Seifahrt, A., Hartman, H., Nilsson, H., Wiedemann, G., Reiners, A., Dreizler, S., & Henry, T. J. 2010, ApJ, 713, 410

Bessell, M. S. & Brett, J. M. 1988, PASP, 100, 1134

Borucki, W. J., Koch, D., Basri, G., Batalha, N., Brown, T., Caldwell, D., Caldwell, J., Christensen-Dalsgaard, J., Cochran, W. D., DeVore, E., Dunham, E. W., Dupree, A. K., Gautier, T. N., Geary, J. C., Gilliland, R., Gould, A., Howell, S. B., Jenkins, J. M., Kondo, Y., Latham, D. W., Marcy, G. W., Meibom, S., Kjeldsen, H., Lissauer, J. J., Monet, D. G., Morrison, D., Sasselov, D., Tarter, J., Boss, A., Brownlee, D., Owen, T., Buzasi, D., Charbonneau, D., Doyle, L., Fortney, J., Ford, E. B., Holman, M. J., Seager, S., Steffen, J. H., Welsh, W. F., Rowe, J., Anderson, H., Buchhave, L., Ciardi, D., Walkowicz, L., Sherry, W., Horch, E., Isaacson, H., Everett, M. E., Fischer, D., Torres, G., Johnson, J. A., Endl, M., MacQueen, P., Bryson, S. T., Dotson, J., Haas, M., Kolodziejczak, J., Van Cleve, J., Chandrasekaran, H., Twicken, J. D., Quintana, E. V., Clarke, B. D., Allen, C., Li, J., Wu, H., Tenenbaum, P., Verner, E., Bruhwiler, F., Barnes, J., & Prsa, A. 2010, Science, 327, 977

Borucki, W. J., Koch, D. G., Basri, G., Batalha, N., Brown, T. M., Bryson, S. T., Caldwell, D., Christensen-Dalsgaard, J., Cochran, W. D., DeVore, E., Dunham, E. W., Gautier, III, T. N., Geary, J. C., Gilliland, R., Gould, A., Howell, S. B., Jenkins, J. M., Latham, D. W., Lissauer, J. J., Marcy, G. W., Rowe, J., Sasselov, D., Boss, A., Charbonneau, D., Ciardi, D., Doyle, L., Dupree, A. K., Ford, E. B., Fortney, J., Holman, M. J., Seager, S., Steffen, J. H., Tarter, J., Welsh, W. F., Allen, C., Buchhave, L. A., Christiansen, J. L., Clarke, B. D., Das, S., Désert, J.-M., Endl, M., Fabrycky, D., Fressin, F., Haas, M., Horch, E., Howard, A., Isaacson, H., Kjeldsen, H., Kolodziejczak, J., Kulesa, C., Li, J., Lucas, P. W., Machalek, P., McCarthy, D., MacQueen, P., Meibom, S., Miquel, T., Prsa, A., Quinn, S. N., Quintana, E. V., Ragozzine, D., Sherry, W., Shporer, A., Tenenbaum, P., Torres, G., Twicken, J. D., Van Cleve, J., Walkowicz, L., Witteborn, F. C., & Still, M. 2011, ApJ, 736, 19

Bouchy, F., Mayor, M., Lovis, C., Udry, S., Benz, W., Berta, J.-L., Delfosse, X., Mordasini, C., Pepe, F., Queloz, D., & Segransan, D. 2009, A&A, 496, 527

Brown, T. M., Latham, D. W., Everett, M. E., & Esquerdo, G. A. 2011, AJ, 142, 112

Casagrande, L., Schönrich, R., Asplund, M., Cassisi, S., Ramírez, I., Meléndez, J., Bensby, T., & Feltzing, S. 2011, A&A, 530, A138

Castelli, F. & Kurucz, R. L. 2004, ArXiv Astrophysics e-prints

Cenarro, A. J., Cardiel, N., Gorgas, J., Peletier, R. F., Vazdekis, A., & Prada, F. 2001a, MNRAS, 326, 959

Cenarro, A. J., Gorgas, J., Cardiel, N., Pedraz, S., Peletier, R. F., & Vazdekis, A. 2001b, MNRAS, 326, 981

Chabrier, G. 2003, PASP, 115, 763

Charbonneau, D., Berta, Z. K., Irwin, J., Burke, C. J., Nutzman, P., Buchhave, L. A., Lovis, C., Bonfils, X., Latham, D. W., Udry, S., Murray-Clay, R. A., Holman, M. J.,

- Falco, E. E., Winn, J. N., Queloz, D., Pepe, F., Mayor, M., Delfosse, X., & Forveille, T. 2009, *Nature*, 462, 891
- Ciardi, D. R., von Braun, K., Bryden, G., van Eyken, J., Howell, S. B., Kane, S. R., Plavchan, P., Ramírez, S. V., & Stauffer, J. R. 2011, *AJ*, 141, 108
- Cumming, A., Butler, R. P., Marcy, G. W., Vogt, S. S., Wright, J. T., & Fischer, D. A. 2008, *PASP*, 120, 531
- Danks, A. C. & Dennefeld, M. 1994, *PASP*, 106, 382
- Demarque, P., Woo, J.-H., Kim, Y.-C., & Yi, S. K. 2004, *ApJS*, 155, 667
- Dotter, A., Chaboyer, B., Jevremović, D., Kostov, V., Baron, E., & Ferguson, J. W. 2008, *ApJS*, 178, 89
- Fabrycky, D. C., Lissauer, J. J., Ragozzine, D., Rowe, J. F., Agol, E., Barclay, T., Batalha, N., Borucki, W., Ciardi, D. R., Ford, E. B., Geary, J. C., Holman, M. J., Jenkins, J. M., Li, J., Morehead, R. C., Shporer, A., Smith, J. C., Steffen, J. H., & Still, M. 2012, ArXiv e-prints
- Feiden, G. A., Chaboyer, B., & Dotter, A. 2011, *ApJ*, 740, L25
- Fischer, D. A., Gaidos, E., Howard, A. W., Giguere, M. J., Johnson, J. A., Marcy, G. W., Wright, J. T., Valenti, J. A., Piskunov, N., Clubb, K. I., Isaacson, H., Apps, K., Lepine, S., Mann, A., Moriarty, J., Brewer, J., Spronck, J. F. P., Schwab, C., & Szymkowiak, A. 2012, *ApJ*, 745, 21
- Fischer, D. A. & Valenti, J. 2005, *ApJ*, 622, 1102
- Fluks, M. A., Plez, B., The, P. S., de Winter, D., Westerlund, B. E., & Steenman, H. C. 1994, *A&AS*, 105, 311
- Gaidos, E., Fischer, D. A., Mann, A. W., & Lépine, S. 2012, *ApJ*, 746, 36
- Gaidos, E., Haghhipour, N., Agol, E., Latham, D., Raymond, S., & Rayner, J. 2007, *Science*, 318, 210
- Gilbert, K. M., Guhathakurta, P., Kalirai, J. S., Rich, R. M., Majewski, S. R., Ostheimer, J. C., Reitzel, D. B., Cenarro, A. J., Cooper, M. C., Luine, C., & Patterson, R. J. 2006, *ApJ*, 652, 1188
- Girardi, L., Bressan, A., Bertelli, G., & Chiosi, C. 2000, *A&AS*, 141, 371
- Girardi, L., Groenewegen, M. A. T., Hatziminaoglou, E., & da Costa, L. 2005, *A&A*, 436, 895
- Gonzalez, G. 1997, *MNRAS*, 285, 403
- Henry, T. J., Kirkpatrick, J. D., & Simons, D. A. 1994, *AJ*, 108, 1437

- Howard, A. W., Marcy, G. W., Bryson, S. T., Jenkins, J. M., Rowe, J. F., Batalha, N. M., Borucki, W. J., Koch, D. G., Dunham, E. W., Gautier, III, T. N., Van Cleve, J., Cochran, W. D., Latham, D. W., Lissauer, J. J., Torres, G., Brown, T. M., Gilliland, R. L., Buchhave, L. A., Caldwell, D. A., Christensen-Dalsgaard, J., Ciardi, D., Fressin, F., Haas, M. R., Howell, S. B., Kjeldsen, H., Seager, S., Rogers, L., Sasselov, D. D., Steffen, J. H., Basri, G. S., Charbonneau, D., Christiansen, J., Clarke, B., Dupree, A., Fabrycky, D. C., Fischer, D. A., Ford, E. B., Fortney, J. J., Tarter, J., Girouard, F. R., Holman, M. J., Johnson, J. A., Klaus, T. C., Machalek, P., Moorhead, A. V., Morehead, R. C., Ragozzine, D., Tenenbaum, P., Twicken, J. D., Quinn, S. N., Isaacson, H., Shporer, A., Lucas, P. W., Walkowicz, L. M., Welsh, W. F., Boss, A., Devore, E., Gould, A., Smith, J. C., Morris, R. L., Prsa, A., Morton, T. D., Still, M., Thompson, S. E., Mullally, F., Endl, M., & MacQueen, P. J. 2012, *ApJS*, 201, 15
- Howard, A. W., Marcy, G. W., Johnson, J. A., Fischer, D. A., Wright, J. T., Isaacson, H., Valenti, J. A., Anderson, J., Lin, D. N. C., & Ida, S. 2010, *Science*, 330, 653
- Jao, W.-C., Henry, T. J., Beaulieu, T. D., & Subasavage, J. P. 2008, *AJ*, 136, 840
- Johnson, J. A., Aller, K. M., Howard, A. W., & Crepp, J. R. 2010, *PASP*, 122, 905
- Johnson, J. A. & Apps, K. 2009, *ApJ*, 699, 933
- Johnson, J. A., Gazak, J. Z., Apps, K., Muirhead, P. S., Crepp, J. R., Crossfield, I. J. M., Boyajian, T., von Braun, K., Rojas-Ayala, B., Howard, A. W., Covey, K. R., Schlawin, E., Hamren, K., Morton, T. D., Marcy, G. W., & Lloyd, J. P. 2012, *AJ*, 143, 111
- Kennedy, G. M. & Kenyon, S. J. 2008, *ApJ*, 673, 502
- Kraus, A. L. & Hillenbrand, L. A. 2009, *ApJ*, 703, 1511
- Kraus, A. L., Tucker, R. A., Thompson, M. I., Craine, E. R., & Hillenbrand, L. A. 2011, *ApJ*, 728, 48
- Lançon, A. & Wood, P. R. 2000, *A&AS*, 146, 217
- Lantz, B., Aldering, G., Antilogus, P., Bonnaud, C., Capoani, L., Castera, A., Copin, Y., Dubet, D., Gangler, E., Henault, F., Lemonnier, J.-P., Pain, R., Pecontal, A., Pecontal, E., & Smadja, G. 2004, in Society of Photo-Optical Instrumentation Engineers (SPIE) Conference Series, Vol. 5249, Society of Photo-Optical Instrumentation Engineers (SPIE) Conference Series, ed. L. Mazuray, P. J. Rogers, & R. Wartmann, 146–155
- Lépine, S. & Gaidos, E. 2011, *AJ*, 142, 138
- Lépine, S., Hilton, E. J., Mann, A. W., Wilde, M., Rojas-Ayala, B., Cruz, K. L., & Gaidos, E. 2013, *AJ*, 145, 102
- Lépine, S., Rich, R. M., & Shara, M. M. 2007, *ApJ*, 669, 1235
- Lépine, S. & Shara, M. M. 2005, *AJ*, 129, 1483

- López-Santiago, J., Montes, D., Gálvez-Ortiz, M. C., Crespo-Chacón, I., Martínez-Arnáiz, R. M., Fernández-Figueroa, M. J., de Castro, E., & Cornide, M. 2010, A&A, 514, A97
- Mann, A. W., Gaidos, E., & Aldering, G. 2011, PASP, 123, 1273
- Mayor, M., Marmier, M., Lovis, C., Udry, S., Ségransan, D., Pepe, F., Benz, W., Bertaux, J., Bouchy, F., Dumusque, X., Lo Curto, G., Mordasini, C., Queloz, D., & Santos, N. C. 2011, ArXiv e-prints
- Montes, D., Ramsey, L. W., & Welty, A. D. 1999, ApJS, 123, 283
- Morton, T. D. & Johnson, J. A. 2011, ApJ, 738, 170
- Muirhead, P. S., Hamren, K., Schlawin, E., Rojas-Ayala, B., Covey, K. R., & Lloyd, J. P. 2012, ApJ, 750, L37
- Pereira, R., Aldering, G., Antilogus, P., Aragon, C., Bailey, S., Baltay, C., Bongard, S., Buton, C., Childress, M., Chotard, N., Copin, Y., Gangler, E., Loken, S., Nugent, P., Pain, R., Pecontal, E., Perlmutter, S., Rabinowitz, D., Rigaudier, G., Runge, K., Scalzo, R., Smadja, G., Fakhouri, H. K., Tao, C., Thomas, R. C., & Wu, C. 2010, in Proc. American Institute of Physics, ed. J.-M. Alimi & A. Fuözfa, Vol. 1241, 259–266
- Reid, I. N., Cruz, K. L., Allen, P., Mungall, F., Kilkenny, D., Liebert, J., Hawley, S. L., Fraser, O. J., Covey, K. R., Lowrance, P., Kirkpatrick, J. D., & Burgasser, A. J. 2004, AJ, 128, 463
- Reid, I. N. & Hawley, S. L. 2005, New light on dark stars : red dwarfs, low-mass stars, brown dwarfs, ed. Reid, I. N. & Hawley, S. L.
- Reid, I. N., Hawley, S. L., & Gizis, J. E. 1995, AJ, 110, 1838
- Rojas-Ayala, B., Covey, K. R., Muirhead, P. S., & Lloyd, J. P. 2012, ApJ, 748, 93
- Santos, N. C., Israeliian, G., & Mayor, M. 2004, A&A, 415, 1153
- Schiavon, R. P., Barbuy, B., Rossi, S. C. F., & Milone, A. 1997, ApJ, 479, 902
- Schlaufman, K. C. & Laughlin, G. 2010, A&A, 519, A105
- . 2011, ApJ, 738, 177
- Serote Roos, M., Boisson, C., & Joly, M. 1996, A&AS, 117, 93
- Skrutskie, M. F., Cutri, R. M., Stiening, R., Weinberg, M. D., Schneider, S., Carpenter, J. M., Beichman, C., Capps, R., Chester, T., Elias, J., Huchra, J., Liebert, J., Lonsdale, C., Monet, D. G., Price, S., Seitzer, P., Jarrett, T., Kirkpatrick, J. D., Gizis, J. E., Howard, E., Evans, T., Fowler, J., Fullmer, L., Hurt, R., Light, R., Kopan, E. L., Marsh, K. A., McCallon, H. L., Tam, R., Van Dyk, S., & Wheelock, S. 2006, AJ, 131, 1163
- Sousa, S. G., Santos, N. C., Mayor, M., Udry, S., Casagrande, L., Israeliian, G., Pepe, F., Queloz, D., & Monteiro, M. J. P. F. G. 2008, A&A, 487, 373

- Torres-Dodgen, A. V. & Weaver, W. B. 1993, PASP, 105, 693
- van Leeuwen, F. 2007, A&A, 474, 653
- van Leeuwen, F. & Fantino, E. 2005, A&A, 439, 791
- Vogt, S. S., Butler, R. P., Rivera, E. J., Haghjhipour, N., Henry, G. W., & Williamson, M. H. 2010, ApJ, 723, 954
- West, A. A., Morgan, D. P., Bochanski, J. J., Andersen, J. M., Bell, K. J., Kowalski, A. F., Davenport, J. R. A., Hawley, S. L., Schmidt, S. J., Bernat, D., Hilton, E. J., Muirhead, P., Covey, K. R., Rojas-Ayala, B., Schlawin, E., Gooding, M., Schluns, K., Dhital, S., Pineda, J. S., & Jones, D. O. 2011, AJ, 141, 97
- Wolfgang, A. & Laughlin, G. 2012, ApJ, 750, 148
- Woolf, V. M. & Wallerstein, G. 2006, PASP, 118, 218
- Wright, E. L., Eisenhardt, P. R. M., Mainzer, A. K., Ressler, M. E., Cutri, R. M., Jarrett, T., Kirkpatrick, J. D., Padgett, D., McMillan, R. S., Skrutskie, M., Stanford, S. A., Cohen, M., Walker, R. G., Mather, J. C., Leisawitz, D., Gautier, III, T. N., McLean, I., Benford, D., Lonsdale, C. J., Blain, A., Mendez, B., Irace, W. R., Duval, V., Liu, F., Royer, D., Heinrichsen, I., Howard, J., Shannon, M., Kendall, M., Walsh, A. L., Larsen, M., Cardon, J. G., Schick, S., Schwalm, M., Abid, M., Fabinsky, B., Naes, L., & Tsai, C.-W. 2010, AJ, 140, 1868
- Yanny, B., Rockosi, C., Newberg, H. J., Knapp, G. R., Adelman-McCarthy, J. K., Alcorn, B., Allam, S., Allende Prieto, C., An, D., Anderson, K. S. J., Anderson, S., Bailer-Jones, C. A. L., Bastian, S., Beers, T. C., Bell, E., Belokurov, V., Bizyaev, D., Blythe, N., Bochanski, J. J., Boroski, W. N., Brinchmann, J., Brinkmann, J., Brewington, H., Carey, L., Cudworth, K. M., Evans, M., Evans, N. W., Gates, E., Gănsicke, B. T., Gillespie, B., Gilmore, G., Nebot Gomez-Moran, A., Grebel, E. K., Greenwell, J., Gunn, J. E., Jordan, C., Jordan, W., Harding, P., Harris, H., Hendry, J. S., Holder, D., Ivans, I. I., Ivezić, Ž., Jester, S., Johnson, J. A., Kent, S. M., Kleinman, S., Kniazev, A., Krzesinski, J., Kron, R., Kuropatkin, N., Lebedeva, S., Lee, Y. S., French Leger, R., Lépine, S., Levine, S., Lin, H., Long, D. C., Loomis, C., Lupton, R., Malanushenko, O., Malanushenko, V., Margon, B., Martinez-Delgado, D., McGehee, P., Monet, D., Morrison, H. L., Munn, J. A., Neilsen, Jr., E. H., Nitta, A., Norris, J. E., Oravetz, D., Owen, R., Padmanabhan, N., Pan, K., Peterson, R. S., Pier, J. R., Platson, J., Re Fiorentin, P., Richards, G. T., Rix, H.-W., Schlegel, D. J., Schneider, D. P., Schreiber, M. R., Schwope, A., Sibley, V., Simmons, A., Snedden, S. A., Allyn Smith, J., Stark, L., Stauffer, F., Steinmetz, M., Stoughton, C., SubbaRao, M., Szalay, A., Szkody, P., Thakar, A. R., Thirupathi, S., Tucker, D., Uomoto, A., Vanden Berk, D., Vidrih, S., Wadadekar, Y., Watters, S., Wilhelm, R., Wyse, R. F. G., Yarger, J., & Zucker, D. 2009, AJ, 137, 4377

Chapter 4

Prospecting in late-type dwarfs: a calibration of infrared and visible spectroscopic metallicities of late-K and M dwarfs spanning 1.5 dex

Published as Mann, Andrew W.; Brewer, John M.; Gaidos, Eric; Lpine, Sbastien; Hilton, Eric J.; 2013, AJ, 145, 52

Abstract

Knowledge of late K and M dwarf metallicities can be used to guide planet searches and constrain planet formation models. However, the determination of metallicities of late-type stars is difficult because visible wavelength spectra of their cool atmospheres contain many overlapping absorption lines, preventing the measurement of equivalent widths. We present new methods, and improved calibrations of existing methods, to determine metallicities of late-K and M dwarfs from moderate resolution ($1300 < R < 2000$) visible and infrared spectra. We select a sample of 112 wide binary systems that contain a late-type companion to a solar-type primary star. Our sample includes 62 primary stars with previously published metallicities, as well as 50 stars with metallicities determined from our own observations. We use our sample to empirically determine which features in the spectrum of the companion are best correlated with the metallicity of the primary. We find $\simeq 120$ features in K and M dwarf spectra that are useful for predicting metallicity. We derive metallicity calibrations for different wavelength ranges, and show that it is possible to get metallicities reliable to < 0.10 dex using either visible, J -, H -, or K - band spectra. We find that the most accurate metallicities derived from visible spectra requires the use of different calibrations for early-type (K5.5–M2) and late-type (M2–M6) dwarfs. Our calibrations are applicable to dwarfs with metallicities of $-1.04 < [\text{Fe}/\text{H}] < +0.56$ and spectral types from K7 to M5. Lastly, we use our sample of wide binaries to test and refine existing calibrations to determine M dwarf metallicities. We find that the ζ parameter, which measures the ratio of TiO can CaH bands, is correlated with $[\text{Fe}/\text{H}]$ for super-solar metallicities, and ζ does not always correctly identify metal-poor M dwarfs. We also find that existing calibrations in the K and H bands are quite reliable for stars with $[\text{Fe}/\text{H}] > -0.5$, but are less useful for more metal-poor stars.

4.1 Introduction

Despite their intrinsic faintness, M dwarfs have become attractive targets for exoplanet searches (e.g., Charbonneau et al. 2009; Apps et al. 2010; Mann et al. 2011), as M dwarfs have smaller radii and lower masses than their solar-type counterparts, allowing for easier detection of low-mass exoplanets (Gaidos et al. 2007). For transiting M dwarf planets with high-precision observations, such as those done by *Kepler* (Borucki et al. 2010; Batalha et al. 2013), errors in planet parameters (primarily planet radius) are directly tied to errors in stellar parameters (e.g., Muirhead et al. 2012), which in turn depend on reliable measurements of stellar temperature and metallicity (Dotter et al. 2008; Demory et al. 2009; Allard et al. 2011). Accurate metallicities are also necessary to study any correlation between metallicity and planet frequency (e.g. Johnson et al. 2010; Mann et al. 2012). Further, because the stellar mass function peaks around mid-M, M dwarfs weigh heavily in any study of Galactic structure. The distribution of M dwarf metallicities can therefore be used to set limits on Milky Way formation models (Woolf & West 2012). However, unlike those of their solar-type counterparts, M-dwarf metallicities are difficult to determine, primarily due to the presence of complex molecular lines in their visible spectra, which result in line confusion and a lack of identifiable continuum, and do not always match with current M dwarf models (Mould 1976; Allard et al. 2011). The visible wavelengths usually used to derive metallicities for solar-type stars are dominated by TiO lines that increase in strength with decreasing effective temperature. These TiO lines obscure the continuum, making equivalent width measurements unreliable, and differ as a function of spectral type. Direct spectral synthesis has been tried on a small sample of stars (Bean et al. 2006; Önehag et al. 2012). However, such spectra is observationally expensive, and spectral synthesis is complicated by incomplete lines lists.

One common technique is to use wide binaries with a solar-type (late-F, G, or early-K) primary and a late-type (late K or M) dwarf companion. Since these stars presumably formed from the same molecular cloud, the metallicity of the M dwarf companion can be assumed to be the same as that of the FGK primary (Bonfils et al. 2005). From this one can create empirical calibrations of observable features to determine metallicities in M dwarfs. Techniques based on absolute photometry (Bonfils et al. 2005; Johnson & Apps 2009; Schlaufman & Laughlin 2010) require parallaxes, which are only available for a handful of the closest and brightest M dwarfs. Molecular indices at visible wavelengths (e.g. Woolf & Wallerstein 2006; Lépine et al. 2013) have proven useful for separating M dwarfs into luminosity/metallicity classes (i.e., dwarf, subdwarf, and extreme subdwarf), but saturate near solar metallicity and are less reliable for late-K and early-M dwarfs.

The use of spectral indices in the infrared has, however, been showing considerable promise. Rojas-Ayala et al. (2010, henceforth R10) showed that [Fe/H] can be inferred for M dwarfs using the Na I doublet and Ca I triplet in moderate resolution ($R \simeq 2700$) K -band spectra and assuming solar relative abundances. Rojas-Ayala et al. (2012, henceforth R12) expanded on this, showing that one can determine [M/H] for early to mid-M dwarfs as accurately as 0.1 dex using the same indices. Further, Terrien et al. (2012, henceforth T12) were able to demonstrate similar precision in the H -band. However, calibrations for both H - and K -band metallicities were derived using a relatively small sample (18 and 22, respectively) of wide binaries. As a result, they were only verified for systems with

near-solar metallicities ($-0.4 \lesssim [\text{Fe}/\text{H}] \lesssim +0.3$), and for a narrow range of spectral types (M0–M4).

In this paper we analyze visible and near-infrared (NIR) observations of 112 late-K and M dwarfs with F, G, or early K star primaries. We determine metallicity estimates for 50 of the FGK stars. We also provide a full list of the 120 features we identify to be metal-sensitive features in visible and NIR spectra, with the expectation that these will be useful for future studies on M dwarf metallicities. In Section 4.2 we present our sample of wide-binary systems, followed by a description of our observations and reduction in Section 4.3. In Section 4.4 we explain how we determine basic properties for both the primary and companion stars. We discuss our search for metal-sensitive features in Section 4.5 and present the results from this analysis in Section 4.6, which includes our calibrations to determine metallicities at a range of wavelengths. We test existing techniques in Section 4.7. Lastly, we summarize the results in Section 8 and discuss possible drawbacks of our analysis as well as prospects for future studies. All wavelengths used in this work are stated as vacuum values.

4.2 Sample

We draw a sample of late K and M dwarfs with comoving FGK stars from a variety of literature sources, specifically Chanamé & Gould (2004), Gould & Chanamé (2004), Lépine & Bongiorno (2007), Schlaufman & Laughlin (2010), and Tokovinin & Lépine (2012). We also identify a number of new common-proper motion (CPM) pairs that contain an FGK star and a late K or M star using proper motions from (in order of preference) *Hipparcos* (van Leeuwen & Fantino 2005; van Leeuwen 2007), SUPERBLINK (Lépine & Shara 2005), or the PPMXL survey (Roeser et al. 2010). We identify new CPM pairs, as well as yet the literature sample, following the techniques of Lépine & Bongiorno (2007) and Dhital et al. (2010). Lépine & Bongiorno (2007) identify CPM pairs using the formula:

$$\Delta X = [(\mu/0.15)^{-3.8} \Delta\theta \Delta\mu]^{0.5}, \quad (4.1)$$

where μ is the absolute proper motion of the primary star in arcsec yr $^{-1}$, $\Delta\theta$ is the separation between the two stars in arcsec, and $\Delta\mu$ is the absolute difference in proper motion between the two stars in arcsec yr $^{-1}$. Lépine & Bongiorno (2007) consider two stars to be physically associated with each other if $\Delta X < 1$, $\Delta\theta < 1500''$, and $\Delta\mu < 100$ mas yr $^{-1}$. We take a more conservative cut and require that our pairs have $\Delta X < 0.9$, $\Delta\theta < 650''$, and $\Delta\mu < 60$ mas yr $^{-1}$ to cut down on the number of chance alignments. This technique takes advantage of the absolute proper motion, and not just the difference in proper motion, of the star, however, it does not factor in associated errors in proper motion. Thus we further force the constraint from Dhital et al. (2010):

$$\left(\frac{\Delta\mu_\alpha}{\sigma_{\Delta\mu_\alpha}} \right)^2 + \left(\frac{\Delta\mu_\delta}{\sigma_{\Delta\mu_\delta}} \right)^2 \leq 2, \quad (4.2)$$

where $\Delta\mu_\alpha$ and $\Delta\mu_\delta$ are the differences in proper motion between the two components (right ascension and declination, respectively) and $\sigma_{\Delta\mu}$ is the error in the proper motion

differences. Equation 4.2 is designed to ensure that the resulting sample has minimal contamination from chance alignment pairs, but at the cost of excluding a large number of true wide binaries. To increase our sample, we add pairs that do not satisfy Equation 2 but have published parallaxes for both the primary and companion star consistent to 1σ of the parallax uncertainty, which strongly suggests that the pair forms a physical system

We remove pairs with $\delta < -45^\circ$ or $\delta > +68^\circ$, since these are outside the reach of some telescopes in Hawaii, and pairs with $\Delta\theta < 3''$ as these will be difficult to observe and may have inaccurate photometry. We further remove pairs with $V_c - J_c < 2.5$ (the subscript c denoting the companion and p the primary). This cut will remove almost all stars earlier than K5 (Lépine & Gaidos 2011) where metallicities can be measured using modified spectral synthesis techniques (Valenti & Piskunov 1996; Valenti & Fischer 2005). We cut out systems with $V_c > 18$, and $K_c > 12$, as the observation time required for these stars is highly prohibitive. For the same reason, we remove systems with $V_p > 12$ unless the primary star already has a published metallicity. The resulting sample contains 262 pairs with primaries with colors in the range $0.8 < V_p - J_p < 2.5$ and/or published temperatures consistent with a late-F, G, or early-K dwarf (Fitzgerald 1970; Ducati et al. 2001). From here we prioritize our observations based on; (1) V_c and K_c magnitudes (to minimize required telescope time), (2) $V_c - J_c$ color (to ensure a range of spectral types), (3) availability of metallicities for the primary star in the literature or V_p magnitude if no literature metallicity is available (see Section 4.3.1), (4) availability of parallax information for the primary or secondary, which makes it more likely that these are true CPM pairs, and (5) metallicity of the primary (if available) to guarantee a range of metallicities for our analysis.

The resulting sample includes 112 stars for which we have obtained infrared spectra (Section 4.3.2), visible wavelength spectra (Section 4.3.3), and metallicities for the primary star from the literature or from our own analysis (Section 4.4.1). Our sample has $-1.04 < [\text{Fe}/\text{H}]_p < 0.56$, and companion star spectral types from K5.5 to M6. We list our sample in Table 4.1.

Table 4.1. Wide Binary Sample

Companion Name	SpT ^a	Name	[Fe/H] ^b	Primary Source ^c	[M/H] ^b	Source ^c
NLTT 738	M2.2	HIP 1224	+0.07 ± 0.03	M13	+0.03 ± 0.03	M13
NLTT 923	M4.1	HIP 1475	-0.05 ± 0.03	VF05	-0.53 ± 0.03	VF05
NLTT 2478	M3.8	HIP 3540	+0.02 ± 0.03	VF05	-0.01 ± 0.03	VF05
NLTT 3598	K7.4	HIP 5110	-0.09 ± 0.03	M13	-0.13 ± 0.03	M13
NLTT 3725	M3.9	HIP 5286	+0.25 ± 0.03	M13	+0.21 ± 0.05	M13
Gl 56.3	K7.6	HIP 6130	-0.01 ± 0.06	C01	+0.01 ± 0.06	C11
NLTT 4568	K7.8	HIP 6431	+0.10 ± 0.03	M13	+0.04 ± 0.03	M13
NLTT 4599	K7.9	HIP 6456	+0.45 ± 0.03	M13	+0.36 ± 0.06	M13
Gl 81.1	M0.1	HIP 9094	+0.12 ± 0.03	VF05	+0.05 ± 0.03	VF05
Gl 100	M2.9	HIP 11565	-0.28 ± 0.04	N12
NLTT 8107	K5.9	HIP 11572	-0.08 ± 0.03	M13	0.00 ± 0.03	M13
Gl 105	M3.9	HIP 12114	-0.12 ± 0.03	VF05	-0.00 ± 0.03	VF05
NLTT 8787	M1.6	HIP 12777	+0.06 ± 0.03	VF05	+0.02 ± 0.03	VF05
Gl 118.2	M3.8	HIP 13642	+0.28 ± 0.03	VF05	+0.21 ± 0.03	VF05
NN 3195	M2.9	HIP 14286	-0.28 ± 0.03	S11	-0.26 ± 0.06	C11
NLTT 10349	M1.0	HIP 15126	-0.92 ± 0.03	M13	-0.66 ± 0.03	M13
NLTT 11125	K7.3	HIP 16467	-0.01 ± 0.03	M13	-0.01 ± 0.03	M13
NLTT 11176	K7.3	HIP 16563	+0.20 ± 0.03	M13	+0.16 ± 0.06	M13
NLTT 11270	M0.4	NLTT 11280	-0.40 ± 0.08	C11	-0.30 ± 0.06	C11
NLTT 11500	M1.8	HIP 17076	-0.52 ± 0.08	C11	-0.44 ± 0.06	C11
PM0355+5214	M2.7	HIP 18366	-0.36 ± 0.05	Ra07	-0.33 ± 0.06	C11
Gl 173.1	M3.2	HIP 21710	-0.34 ± 0.04	N12
Wo 9169	M2.3	HIP 22919	+0.05 ± 0.03	VF05	+0.04 ± 0.03	VF05
PM05003+2507	M1.2	HIP 23259	-0.03 ± 0.08	C11	-0.01 ± 0.06	C11
NN 3348	M4.0	HIP 25662	-0.22 ± 0.03	VF05	-0.10 ± 0.03	VF05
Gl 212	M1.0	HIP 26779	+0.19 ± 0.03	VF05	+0.16 ± 0.03	VF05
NLTT 15511	M3.1	HIP 26907	+0.10 ± 0.06	B06	-0.21 ± 0.06	M13
NLTT 15601	M2.6	HIP 27253	+0.45 ± 0.03	VF05	+0.27 ± 0.03	VF05
NLTT 15974	K5.7	HIP 28671	-1.04 ± 0.05	Ra07
Gl 231.1	M3.7	HIP 29860	-0.04 ± 0.03	VF05	-0.08 ± 0.03	VF05
NLTT 16628	M1.4	HIP 31127	-0.54 ± 0.03	M13	-0.45 ± 0.03	M13
PM0636+3751W	M3.1	HIP 31597	+0.09 ± 0.03	M13	+0.08 ± 0.03	M13
NN 3408	M0.9	HIP 32423	-0.26 ± 0.03	M13	-0.21 ± 0.04	M13
Gl 250	M2.3	HIP 32984	+0.14 ± 0.03	VF05	-0.01 ± 0.03	VF05
PM0719+6644N	K7.7	HIP 35449	+0.21 ± 0.03	M13	+0.18 ± 0.03	M13
Gl 297.2	M2.3	HIP 40035	-0.04 ± 0.05	F08	-0.03 ± 0.06	C11
NLTT 19115	M1.5	HIP 40298	-0.07 ± 0.03	M13	-0.09 ± 0.03	M13
NLTT 19184	M3.0	HIP 40497	-0.20 ± 0.07	M04	-0.19 ± 0.06	C11
PM0850+3505	M0.2	HIP 43426	+0.24 ± 0.08	C11	+0.22 ± 0.06	C11
Gl 324	M4.1	HIP 43587	+0.31 ± 0.03	VF05	+0.25 ± 0.03	VF05
PM0902+0602	M1.4	NLTT 12373	-0.08 ± 0.05	M13	-0.00 ± 0.08	M13
PM0915+2321	M1.4	HIP 45406	+0.31 ± 0.07	R007	+0.22 ± 0.06	C11
NLTT 21492	M1.6	HIP 45863	-0.12 ± 0.03	M13	-0.13 ± 0.03	M13
NLTT 21671	M4.0	HIP 46134	+0.21 ± 0.07	R007	+0.21 ± 0.06	C11
NLTT 23002	M0.2	NLTT 23002	-0.15 ± 0.03	M13	-0.11 ± 0.03	M13
PM1000+3155	M6.0	HIP 49081	+0.20 ± 0.03	VF05	+0.11 ± 0.03	VF05
NLTT 24144	M1.5	HIP 50802	-0.01 ± 0.03	M13	-0.06 ± 0.03	M13
Gl 394	K7.1	HIP 51459	-0.07 ± 0.03	VF05	-0.05 ± 0.03	VF05
NN 3628	M4.1	HIP 53008	+0.13 ± 0.07	R007	-0.22 ± 0.06	C11
NLTT 26194	M0.4	HIP 54155	+0.16 ± 0.03	M13	+0.11 ± 0.07	M13
NLTT 27152	M0.5	HIP 55486	+0.46 ± 0.03	M13	+0.42 ± 0.03	M13
NLTT 28036	M2.2	HIP 56729	-0.09 ± 0.03	M13	-0.04 ± 0.03	M13
NLTT 28180	M1.6	HIP 56930	-0.12 ± 0.03	M13	-0.17 ± 0.05	M13

Table 4.1—Continued

Companion Name	SpT ^a	Name	[Fe/H] ^b	Primary Source ^c	[M/H] ^b	Source ^c
PM1204+1728S	M3.7	HIP 58919	+0.05 ± 0.08	C11	+0.05 ± 0.06	C11
NLTT 29641	K5.7	HIP 59080	-0.16 ± 0.03	M13	-0.13 ± 0.03	M13
NLTT 29745	M0.2	HIP 59233	-0.80 ± 0.05	Ra07	-0.70 ± 0.06	C11
NLTT 30986	M1.8	HIP 61081	-0.54 ± 0.03	M13	-0.42 ± 0.03	M13
NLTT 31037	M0.1	HIP 61189	+0.11 ± 0.03	M13	+0.05 ± 0.03	M13
PM1237+3549	M1.8	HIP 61589	-0.05 ± 0.03	M13	-0.08 ± 0.05	M13
NLTT 33176	K7.5	HIP 64345	-0.57 ± 0.03	M13	-0.39 ± 0.03	M13
NLTT 33528	M0.7	HIP 64797	-0.12 ± 0.03	M13	-0.13 ± 0.03	M13
NLTT 34150	M3.0	HIP 65636	+0.13 ± 0.03	M13	+0.01 ± 0.03	M13
NLTT 34357	M0.1	HIP 65963	-0.14 ± 0.03	M13	-0.08 ± 0.03	M13
NLTT 36190	M1.8	HIP 68799	-0.03 ± 0.03	M13	-0.06 ± 0.03	M13
NLTT 36893	M0.6	HIP 69893	-0.90 ± 0.08	C11	-0.77 ± 0.06	C11
NLTT 36969	M4.3	HIP 70016	-0.18 ± 0.03	VF05	-0.15 ± 0.03	VF05
NLTT 37004	M0.1	HIP 70100	+0.15 ± 0.03	M13	+0.13 ± 0.03	M13
NLTT 37283	M2.0	HIP 70426	+0.09 ± 0.03	M13	+0.03 ± 0.04	M13
Gl 549	M2.5	HIP 70497	-0.00 ± 0.05	LH05	-0.01 ± 0.06	C11
PM1425+2035W	M4.8	HIP 70520	-0.58 ± 0.05	Ra07	-0.40 ± 0.06	C11
NLTT 37349	M4.0	HIP 70623	+0.56 ± 0.03	VF05	+0.46 ± 0.03	VF05
NLTT 39578	M2.8	HIP 74396	-0.09 ± 0.03	M13	-0.07 ± 0.03	M13
NLTT 39754	M2.8	HIP 74734	-0.32 ± 0.03	M13	-0.27 ± 0.03	M13
NLTT 39942	K7.5	HIP 75069	-0.38 ± 0.03	M13	-0.34 ± 0.03	M13
NLTT 40401	M0.7	HIP 75783	-0.17 ± 0.08	C11	-0.12 ± 0.06	C11
NLTT 40692	M4.1	HIP 76315	+0.11 ± 0.03	VF05	-0.08 ± 0.03	VF05
PM15393-1016	M2.1	HIP 76668	-0.06 ± 0.03	M13	-0.14 ± 0.03	M13
Gl 611	M3.8	HIP 78775	-0.69 ± 0.03	VF05	-0.49 ± 0.03	VF05
NLTT 42006	K7.9	HIP 78969	+0.19 ± 0.03	M13	+0.12 ± 0.03	M13
Gl 615.2	M2.7	HIP 79607	-0.06 ± 0.03	VF05	-0.05 ± 0.03	VF05
NLTT 42396	M3.5	HIP 79629	-0.25 ± 0.04	M13	-0.25 ± 0.06	M13
Gl 654	M1.8	HIP 83591	-0.41 ± 0.03	VF05	-0.30 ± 0.03	VF05
NLTT 44569	M3.8	HIP 84616	-0.12 ± 0.03	M13	-0.09 ± 0.03	M13
PM1742+1643	M1.7	PM1742+1645	-0.09 ± 0.03	M13
NLTT 45430	M3.3	HIP 86974	+0.30 ± 0.03	VF05	+0.24 ± 0.03	VF05
NLTT 45473	M1.5	HIP 87082	-0.05 ± 0.03	M13	-0.03 ± 0.05	M13
PM18006+6832	K7.5	HIP 88188	+0.05 ± 0.04	M13	-0.04 ± 0.07	M13
NLTT 45791	M2.1	HIP 88194	-0.06 ± 0.03	VF05	-0.06 ± 0.03	VF05
NLTT 45826	M2.2	HIP 88365	-0.66 ± 0.03	M13	-0.34 ± 0.03	M13
PM18247-0620	M3.2	HIP 90246	-0.01 ± 0.03	M13	-0.08 ± 0.03	M13
NLTT 46858	M1.3	HIP 91605	-0.51 ± 0.08	C11	-0.45 ± 0.06	C11
PM19321-1119	M4.1	HIP 96085	+0.05 ± 0.03	VF05	-0.05 ± 0.03	VF05
Gl 768.1B	M3.4	HIP 97675	+0.16 ± 0.03	VF05	+0.12 ± 0.03	VF05
Gl 777	M4.3	HIP 98767	+0.21 ± 0.03	VF05	+0.19 ± 0.03	VF05
Gl 783.2	M3.9	HIP 99452	-0.15 ± 0.03	VF05	-0.09 ± 0.03	VF05
NLTT 49011	M2.6	HIP 99965	+0.14 ± 0.08	C11	+0.13 ± 0.06	C11
Gl 797	M2.6	HIP 102040	-0.09 ± 0.03	VF05	-0.09 ± 0.03	VF05
NLTT 50489	M1.7	HIP 104097	-0.38 ± 0.03	M13	-0.27 ± 0.03	M13
NLTT 52304	M0.5	HIP 107920	+0.03 ± 0.07	Ro07	+0.15 ± 0.06	C11
PM2157+2854	M1.9	HIP 108388	+0.21 ± 0.07	Ro07
NLTT 52593	M4.2	HIP 108506	+0.16 ± 0.03	VF05	+0.08 ± 0.03	VF05
PM2206+4322W	M3.6	PM2206+4322E	+0.30 ± 0.03	M13	+0.15 ± 0.03	M13
NN 4269	M4.0	HIP 109926	+0.01 ± 0.05	F08	+0.04 ± 0.06	C11
PM2231+4509	M2.8	HIP 111148	-0.00 ± 0.03	VF05	-0.02 ± 0.03	VF05
NLTT 54820	M2.0	HIP 112447	-0.22 ± 0.03	VF05	-0.16 ± 0.03	VF05
Wo 9801	M3.2	HIP 112935	-0.18 ± 0.04	T05	-0.05 ± 0.06	C11

Table 4.1—Continued

Companion Name	SpT ^a	Name	[Fe/H] ^b	Primary Source ^c	[M/H] ^b	Source ^c
G1 889	M3.5	HIP 114156	-0.04 ± 0.08	M13	-0.06 ± 0.05	M13
NLTT 56041	K5.5	HIP 114420	+0.18 ± 0.08	C11	+0.18 ± 0.06	C11
NLTT 57309	M2.8	HIP 116421	-0.40 ± 0.03	VF05	-0.20 ± 0.03	VF05
NLTT 57675	M3.6	HIP 116906	-0.03 ± 0.03	VF05	-0.02 ± 0.03	VF05
PM2355+0041W	M1.8	HIP 117960	+0.12 ± 0.03	M13	+0.06 ± 0.03	M13
NLTT 58659	K7.1	HIP 118282	-0.67 ± 0.03	M13	-0.47 ± 0.03	M13

^aSpectral types derived from TiO and CaH indices, (see Lépine et al. (2013)). Continuous spectral types (to 0.1) are used for plotting/binning/calculations, even though spectral types are only accurate to ±0.2 (and by convention should be rounded to the nearest 0.5).

^b[M/H] and [Fe/H] values shown here include our applied corrections (see Section 4.4).

^cMetallicity sources: C01 = Cayrel de Strobel et al. (2001), M04 = Mishenina et al. (2004), LH05 = Luck & Heiter (2005), VF05 = Valenti & Fischer (2005), T05 = Takeda et al. (2005), B06 = Bean et al. (2006), Ra07 = Ramírez et al. (2007), Ro07 = Robinson et al. (2007), F08 = Fuhrmann (2008), S11 = da Silva et al. (2011), C11 = Casagrande et al. (2011), N12 = Neves et al. (2012), M13 = analysis of CFHT/ESPaDOnS spectra as part of this program.

Note that all metallicities sources are from high-resolution spectra, with the exception of Ro07, which uses moderate-resolution spectra, and C11, which uses Strömgren photometry.

4.3 Observations and Reduction

4.3.1 ESPaDOnS/CFHT

Between 2011 January and 2012 April, 60 F-, G- and early K-type stars were observed using the ESPaDOnS spectrograph attached to the Canada France Hawaii Telescope (CFHT; Donati 2003) on Mauna Kea. Observations were taken in the star+sky mode, which gave a resolution of $R \simeq 65000$ and a wavelength range from $0.37\mu\text{m}$ to $1.05\mu\text{m}$. All observations were designed to achieve a signal-to-noise ratio (S/N) of > 100 at $0.67\mu\text{m}$, and typical S/N was > 150 (per resolving element). The data were reduced automatically using the *Libre-ESpRIT* pipeline described in Donati et al. (1997).

4.3.2 SpeX/IRTF

We obtained near-infrared spectra of our sample of companions using the SpeX spectrograph (Rayner et al. 2003) attached to the NASA Infrared Telescope Facility (IRTF) on Mauna Kea. SpeX observations were taken in the short cross-dispersed (SXD) mode using the $0.3 \times 15''$ slit, yielding simultaneous coverage from 0.8 to $2.4\mu\text{m}$ and a resolution of $R \simeq 2000$. The star was placed at two positions along the slit (A and B). Exposures were taken with an ABBA slit-nodding pattern, with at least 6 exposures in total. Integration times were no longer than 120 s for each exposure to minimize the effect of changes in atmospheric H₂O. Thus for faint stars more than 6 exposures were required to get sufficient S/N. S/N in the *H*- and *K*-bands was > 100 in all cases, and typically > 150 (per resolving element). To correct for telluric lines, we observed an A0V-type star within 30 minutes and 0.1 air mass of the target observation (and usually much closer in time and air mass). Often the same

A0V star was used to remove telluric lines for more than one target. To remove effects from large telescope slews, we obtained flat-field and argon lamp calibration sequences after each A0V star.

Spectra were extracted and reduced using the SpeXTool package (Cushing et al. 2004), which performed flat-field correction, wavelength calibration, sky subtraction, and extraction of the one-dimensional (1D) spectrum. Multiple exposures were stacked using the IDL routine *xcombxspec*. A telluric correction spectrum was constructed from each A0V star using the *xtellcor* package (Vacca et al. 2003), and then applied to the relevant target spectra.

Reduced spectra were put in vacuum wavelengths using the formula from Ciddor (1996). We put spectra in the star's rest frame by comparing them to a spectrum of the template star HD36395 (an M1.5 dwarf, also in rest frame/vacuum) taken from the IRTF spectral library (Cushing et al. 2005; Rayner et al. 2009). We cross-correlated each spectrum with the template, in orders 3 – 7 separately (order 8 is ignored because it is too smooth and has relatively poor S/N), yielding 6 radial velocities (RVs). We shifted the spectrum by the average (after removing any 5σ outliers) of each set of RVs.

4.3.3 SNIFS/UH2.2m

We obtained a visible spectrum of each companion with the SuperNova Integral Field Spectrograph (SNIFS, Lantz et al. 2004) on the University of Hawaii 2.2m telescope atop Mauna Kea. SNIFS has $R \simeq 1300$ and splits the signal with a dichroic mirror into blue ($0.32\text{--}0.52\,\mu\text{m}$) and red ($0.52\text{--}0.95\,\mu\text{m}$) channels. SNIFS data processing is performed with a data reduction pipeline, described in detail in Bacon et al. (2001) and Aldering et al. (2006). SNIFS processing includes dark, bias, and flat-field corrections, assembling the data into red and blue three-dimensional data cubes, and cleaning them for cosmic rays and bad pixels. Wavelengths are calibrated with arc lamp exposures taken at the same telescope pointing as the science data. The calibrated spectrum is then sky-subtracted, and a 1-D spectrum is extracted using a point-spread function model. Corrections are applied to the spectrum for instrument response, and for telluric lines based on observations of the Feige 66, Feige 110, BD+284211, or BD+174708 spectrophotometric standards (Oke 1990) that are taken over the course of each night.

Approximate spectral types are determined by the HAMMER software package (Covey et al. 2007). The spectra are then shifted to zero radial velocity by cross-correlating with templates from Bochanski et al. (2007) of the corresponding spectral type. Late-K stars are cross-correlated using an M0 template.

4.3.4 Construction of a combined M dwarf Spectrum

We use the overlapping region in our SpeX and SNIFS data ($0.81\text{--}0.96\,\mu\text{m}$) to combine the visible and NIR spectra. We normalize each SNIFS spectrum by a constant, C , which is equal to the ratio of the median flux of the SNIFS spectra in overlapping region to the median flux of the SpeX spectra in the overlapping region. We also find that there is a systematic offset in wavelength between the visible wavelength and NIR spectra in the overlapping region. This amounts to a RV shift of $\simeq 30\,\text{km s}^{-1}$ between the SNIFS and SpeX spectra. The most likely explanation for this is a small difference in the RV templates

used for our SpeX and SNIFS data, taken from Rayner et al. (2009) and Bochanski et al. (2007) respectively. We choose to shift the visible wavelength data to match with the NIR data (which has higher resolution and therefore gives more reliable RVs) by adding an additional RV correction of -30 km s^{-1} to each SNIFS spectrum. Given the modest resolution of SNIFS data, this correction is unlikely to significantly change our results. The offset corresponds to $< 1 \text{ \AA}$, which is significantly less than the resolving power of SNIFS, and is similar in size to random errors in our RV measurements.

4.4 Deriving Stellar Parameters

4.4.1 FGK Metallicities

We draw primary star metallicities from a variety of sources in the literature. We list the adopted metallicity and literature source for each binary in Table 4.1. In total, 33 primary star metallicities come from the SPOCS catalog (Valenti & Fischer 2005), 50 from observations taken as part of this project with CFHT/ESPaDOnS, and 29 from other literature sources. SPOCS consists of high-resolution echelle spectra of > 1000 F-, G-, and K-type stars obtained with the Keck, Lick, or Anglo-Australian Telescope. Valenti & Fischer (2005) fit the observed spectrum to a synthetic spectrum using the software package SME (Spectroscopy Made Easy, Valenti & Piskunov 1996), which provides a set of observational parameters (T_{eff} , [Fe/H], [M/H], $\log g$, etc.) for each star. We adopt an uncertainty of 0.03 dex for their derived [M/H] and [Fe/H] values.

To determine the stellar parameters of primaries observed with CFHT/ESPaDOnS we model each spectrum using the SME software (Valenti & Piskunov 1996), fitting the spectrum to a set of tuned lines from the SPOCS catalog (Valenti & Fischer 2005). We simultaneously solve for surface gravity, effective temperature, projected rotational velocity, and metallicity in addition to individual abundances of Fe, Na, Si, Ni, and Ti. Solar values are assumed for all of the initial models and after obtaining an initial fit, we then perturb T_{eff} by $\pm 100 \text{ K}$ and fit again. Our final model parameters are χ^2 -weighted averages of three runs. Corrections based on Vesta and stellar binary observations as detailed in Valenti & Fischer (2005) are then applied.

For stars with good parallax measurements (*Hipparcos* stars or their companions), we use Yonsei-Yale (Y²) isochrones (Demarque et al. 2004) to better constrain the surface gravity (Valenti et al. 2009). After we determine the stellar parameters as above, we use distance and B and V magnitudes to derive bolometric luminosity and, combined with the SME T_{eff} , the stellar radius. Bolometric corrections are obtained by interpolating in the high temperature grid of VandenBerg & Clem (2003), and B , V magnitudes were drawn from *Hipparcos* (van Leeuwen & Fantino 2005). The SME determined ratio of Si to Fe is used as a proxy for alpha element enhancement. A best-fit evolutionary model is found by interpolating in the Y² grid which yielded a surface gravity for the star. This $\log g$ is compared to the value determined using SME and if the two did not match, a new set of SME models is found with the gravity fixed to the isochrone value. The process is repeated until the $\log g$ values agree to within 0.001 dex. Final stellar parameters (T_{eff} , $\log g$, [M/H], etc.) for stars observed as part of our program are listed in Table 4.2.

Table 4.2. Parameters of Primary Stars observed at CFHT

Name	T_{eff}	\pm	$\log g$	\pm	[Fe/H]	\pm	[M/H]	\pm	χ^2_{red}	Run Type ^a
HIP 1224	5141	44	4.53	0.06	+0.07	0.03	+0.03	0.03	2.9	ITER
HIP 5110	4648	44	4.61	0.06	-0.09	0.03	-0.13	0.03	6.0	ITER
HIP 5286	4676	53	4.60	0.06	+0.25	0.03	+0.21	0.05	14.7	ITER
HIP 6431	4858	44	4.57	0.06	+0.10	0.03	+0.04	0.03	6.3	ITER
HIP 6456	5222	52	4.44	0.06	+0.45	0.03	+0.36	0.06	6.8	ITER
HIP 11572	5093	44	4.51	0.06	-0.08	0.03	+0.00	0.03	3.6	ITER
HIP 15126	5285	44	4.64	0.06	-0.92	0.03	-0.66	0.03	2.2	ITER
HIP 16467	5539	44	4.33	0.06	-0.01	0.03	-0.01	0.03	2.1	ITER
HIP 16563	5788	44	4.52	0.06	+0.20	0.03	+0.16	0.06	4.4	ITER
HIP 31127	5158	44	3.83	0.06	-0.54	0.03	-0.45	0.03	3.1	ITER
HIP 31597	5428	44	4.44	0.06	+0.09	0.03	+0.08	0.03	2.0	ITER
HIP 32423	4817	44	4.64	0.06	-0.26	0.03	-0.21	0.04	5.6	ITER
HIP 35449	6156	44	4.36	0.06	+0.21	0.03	+0.18	0.03	1.9	ITER
HIP 40298	5618	44	4.51	0.06	-0.07	0.03	-0.09	0.03	1.7	ITER
NLTT 12373	5838	93	4.62	0.09	-0.08	0.05	-0.00	0.08	2.2	VESTA
HIP 45863	5172	44	4.51	0.06	-0.12	0.03	-0.13	0.03	4.3	ITER
NLTT 23002	5259	44	4.58	0.06	-0.15	0.03	-0.11	0.03	3.1	VESTA
HIP 50802	4472	44	4.70	0.06	-0.01	0.03	-0.06	0.03	13.1	ITER
HIP 54155	5547	50	4.54	0.06	+0.16	0.03	+0.11	0.07	2.9	ITER
HIP 55486	5371	44	4.51	0.06	+0.46	0.03	+0.42	0.03	9.6	ITER
HIP 56729	5421	44	4.47	0.06	-0.09	0.03	-0.04	0.03	2.7	ITER
HIP 56930	5025	44	4.61	0.06	-0.12	0.03	-0.17	0.05	7.0	ITER
HIP 59080	5423	44	4.41	0.06	-0.16	0.03	-0.13	0.03	4.9	ITER
HIP 61081	5298	44	4.59	0.06	-0.54	0.03	-0.42	0.03	2.5	ITER
HIP 61189	4655	44	4.93	0.06	+0.11	0.03	+0.05	0.03	16.6	VESTA
HIP 61589	5700	44	4.49	0.06	-0.05	0.03	-0.08	0.05	2.3	ITER
HIP 64345	5495	44	4.40	0.06	-0.57	0.03	-0.39	0.03	1.8	ITER
HIP 64797	5041	44	4.60	0.06	-0.12	0.03	-0.13	0.03	15.1	ITER
HIP 65636	4619	44	4.64	0.06	+0.13	0.03	+0.01	0.03	13.4	ITER
HIP 65963	5478	44	4.52	0.06	-0.14	0.03	-0.08	0.03	1.7	ITER
HIP 68799	5492	44	4.42	0.06	-0.03	0.03	-0.06	0.03	2.7	ITER
HIP 70100	4886	44	4.57	0.06	+0.15	0.03	+0.13	0.03	9.9	ITER
HIP 70426	4801	44	4.58	0.06	+0.09	0.03	+0.03	0.04	12.8	ITER
HIP 74396	5124	44	4.60	0.06	-0.09	0.03	-0.07	0.03	3.5	ITER
HIP 74734	5822	44	4.34	0.06	-0.32	0.03	-0.27	0.03	2.1	ITER
HIP 75069	5196	44	4.61	0.06	-0.38	0.03	-0.34	0.03	2.8	ITER
HIP 76668	4636	44	4.65	0.06	-0.06	0.03	-0.14	0.03	13.7	ITER
HIP 78969	4899	44	4.58	0.06	+0.19	0.03	+0.12	0.03	9.0	ITER
HIP 79629	5600	50	4.48	0.06	-0.25	0.04	-0.25	0.06	2.0	ITER
HIP 84616	4826	44	4.62	0.06	-0.12	0.03	-0.09	0.03	6.4	ITER
PM1742+1645	5492	44	4.50	0.06	-0.09	0.03	+0.01	0.03	4.2	VESTA
HIP 87082	5795	44	4.40	0.06	-0.05	0.03	-0.03	0.05	2.7	ITER
HIP 88188	5299	53	4.54	0.06	+0.05	0.04	-0.04	0.07	3.2	ITER
HIP 88365	5371	44	4.59	0.06	-0.66	0.03	-0.34	0.03	3.7	ITER
HIP 90246	4494	44	4.69	0.06	-0.01	0.03	-0.08	0.03	11.3	ITER
HIP 104097	4428	44	4.72	0.06	-0.38	0.03	-0.27	0.03	15.1	ITER
PM2206+4322E	5652	44	4.62	0.06	+0.30	0.03	+0.15	0.03	6.2	VESTA
HIP 114156	4314	66	4.72	0.06	-0.04	0.08	-0.06	0.05	15.5	ITER
HIP 117960	5252	44	4.54	0.06	+0.12	0.03	+0.06	0.03	4.0	ITER
HIP 118282	5178	44	4.64	0.06	-0.67	0.03	-0.47	0.03	2.0	ITER

^aITER: parameters determined using *Hipparcos* parallaxes and Y^2 isochrones. VESTA: parameters determined using classical SME fitting (no parallax information included) with a correction using Vesta as described in Valenti & Fischer (2005).

Table 4.3. Corrections Applied to Primary Star Metallicities

Source	Control Stars	$\Delta[\text{Fe}/\text{H}]$	σ_{control}	No. of Stars Used ^a
VF05	...	0.00	0.03	33
CFHT	...	0.00	0.03 ^b	50
C01	294	0.02	0.07	1
M04	178	0.04	0.08	1
LH05	174	0.02	0.06	1
T05	127	0.01	0.05	1
B06	33	0.07	0.07	1
Ra07	112	0.08	0.05	4
Ro07	127	0.00	0.07	5
F08	165	0.03	0.06	2
C11 ^c	614	0.00	0.08	10
S11	50	0.03	0.04	1
N12 ^d	125	0.00	0.05	2

Note. — Number of stars from listed source used in our final wide binary sample.

^aNumber of stars from listed source used in our final wide binary sample.

^bTypical uncertainty. Errors for individual stars listed in Table 4.2.

^cMetallicities determined from Strömgren photometry.

^dBased on a control sample from Santos et al. (2004) and Sousa et al. (2011), on which abundances in N12 are anchored.

Our analysis of the ESPaDOnS spectra is designed to keep our metallicities consistent with those from the SPOCS catalog (both are based on SME analysis and use the same set of spectral lines). As an extra check on consistency we have obtained CFHT spectra for three stars in the SPOCS sample. The derived stellar parameters from these three spectra are consistent (within errors) with those listed in the SPOCS catalog, confirming that there is no systematic offset between metallicities from SPOCS and CFHT.

Metallicities from other literature sources are not necessarily determined in the same way as our spectral analysis, and thus may have small systematic inconsistencies. We correct for this by checking for overlap between the SPOCS samples and any given literature source. For us to use a metallicity derived from any other literature source we require; (1) at least 30 stars in both samples that can be used as a control sample to check for differences, (2) metallicities for our primary stars from the literature source fall within the range of metallicities of the control sample, (3) the mean difference between the SPOCS metallicities and the literature metallicities in the control sample $\Delta[\text{Fe}/\text{H}]_{\text{control}} \leq 0.07$ dex, and (4) the resulting scatter in the control sample $\sigma_{\text{control}} \leq 0.08$ dex. These limits are designed to keep uncertainties in the primary star metallicities well below the precision already obtained for determining M dwarf metallicities (e.g., R12 and T12). We adopt σ_{control} as the uncertainty in [Fe/H] for a given literature source. As an example, we show metallicities from both Ramírez et al. (2007) and SPOCS in Fig. 4.1. We list all sources of metallicities, the adopted systematic offset (which we apply for all calculations in this paper) for that source, and the adopted uncertainty in Table 4.3.

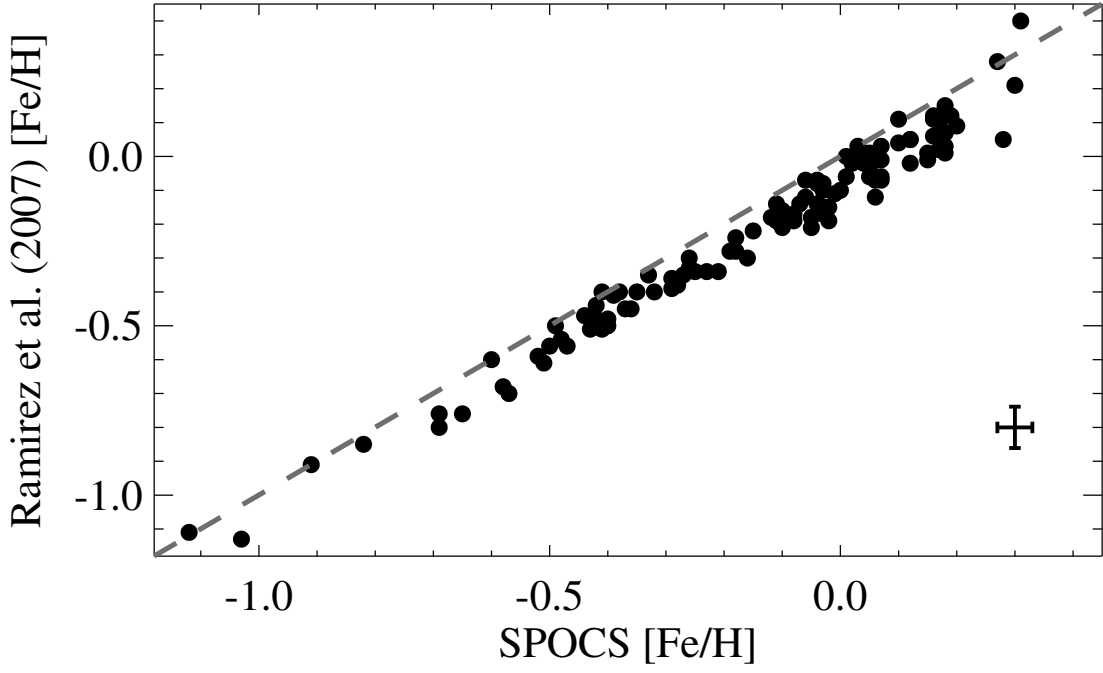


Figure 4.1: Comparison of metallicities from Ramírez et al. (2007) and those from SPOCS (Valenti & Fischer 2005) for the 112 stars present in both samples. The $[\text{Fe}/\text{H}]$ values are quite consistent once corrected for a systematic offset of 0.08 dex. The remaining scatter is only $\simeq 0.06$ dex. Assuming SPOCS $[\text{Fe}/\text{H}]$ values are accurate to 0.03 dex, this implies $[\text{Fe}/\text{H}]$ metallicities from Ramírez et al. (2007) are accurate to $\simeq 0.05$ dex. We perform a similar analysis for all other metallicity sources (see Table 4.3).

4.4.2 Late-K/M Dwarf Spectral Types

We determine M dwarf spectral types using indices at both visible and NIR wavelengths. We use the empirical spectral type–band index relations from Lépine et al. (2013), which have been calibrated to work on the SNIFS/UH2.2m. Lépine et al. (2013) determined spectral types accurate to $\simeq 0.2$ subtypes based on empirical relations between spectral type and the strengths of TiO and CaH bands (Reid et al. 1995). It has been shown that CaH is sensitive to spectral type, and that TiO is sensitive to both spectral type and metallicity (Woolf & Wallerstein 2006). As a result, for stars with $[Fe/H] < -0.5$ (the metallicity of the primary star) we base our visible wavelength spectral types solely on relations using CaH bands.

R12 showed that one can determine temperatures and spectral types using a modified version of the H₂O-K (H₂O-K2, Covey et al. 2010) index. R12 calibrated their spectral types based on *K*-band spectra of stars from the Research Consortium on Nearby Stars Measuring (RECONS; Henry et al. 1994). Their calibration is accurate to $\simeq 0.6$ subtypes.

Fig. 4.2 compares the spectral types derived from visible wavelength indices versus those derived using the H₂O-K2 index. Although there is good agreement between the two techniques for the later-type stars in our sample, for stars earlier than M1 (as determined by TiO and CaH bands), spectral types determined from H₂O-K2 are systematically later than those from visible wavelength indices. The H₂O features become quite weak in the spectra of late-K and early-M stars and R12 caution using it on stars with $T_{\text{eff}} > 4000$. Further, the spectral-type calibration from R12 does not include any K stars, and is therefore unreliable for the warmest stars in our sample. As a result, we choose to use spectral types determined from our visible wavelength spectra for the entire sample.

4.5 Identifying Metal-Sensitive Indices

To determine which features in the companion dwarf spectra best correlate with metallicity we perform a systematic analysis of our sample of spectra and metallicities. Our analysis proceeds as follows:

1. A center wavelength is selected, starting at the blue end of the spectrum ($\simeq 0.33 \mu\text{m}$) and incrementally increasing by $0.00015 \mu\text{m}$ (1.5\AA) after all other steps are complete. This process is repeated until the center is at the red end of the spectrum ($\simeq 2.4 \mu\text{m}$) and excludes the gap in all SpeX spectra at $1.85 \mu\text{m}$.
2. For each feature center, we select a feature width starting at $0.002 \mu\text{m}$ (20\AA), and then increased incrementally by $0.00015 \mu\text{m}$ (1.5\AA) after completing all following steps. We use 20\AA as a minimum, as features smaller than this have considerable Poisson noise (making their measurement difficult). We use an upper limit of $0.01 \mu\text{m}$ (100\AA) for the feature width, as regions of the spectra larger than this likely contain multiple features that should be treated separately.
3. The equivalent width is calculated for each feature using the approximation:

$$\text{EW}_{\lambda} \simeq \sum_{i=0}^{n-1} \left[1 - \frac{F(\lambda_i)}{F_c(\lambda_i)} \right] \Delta\lambda_i, \quad (4.3)$$

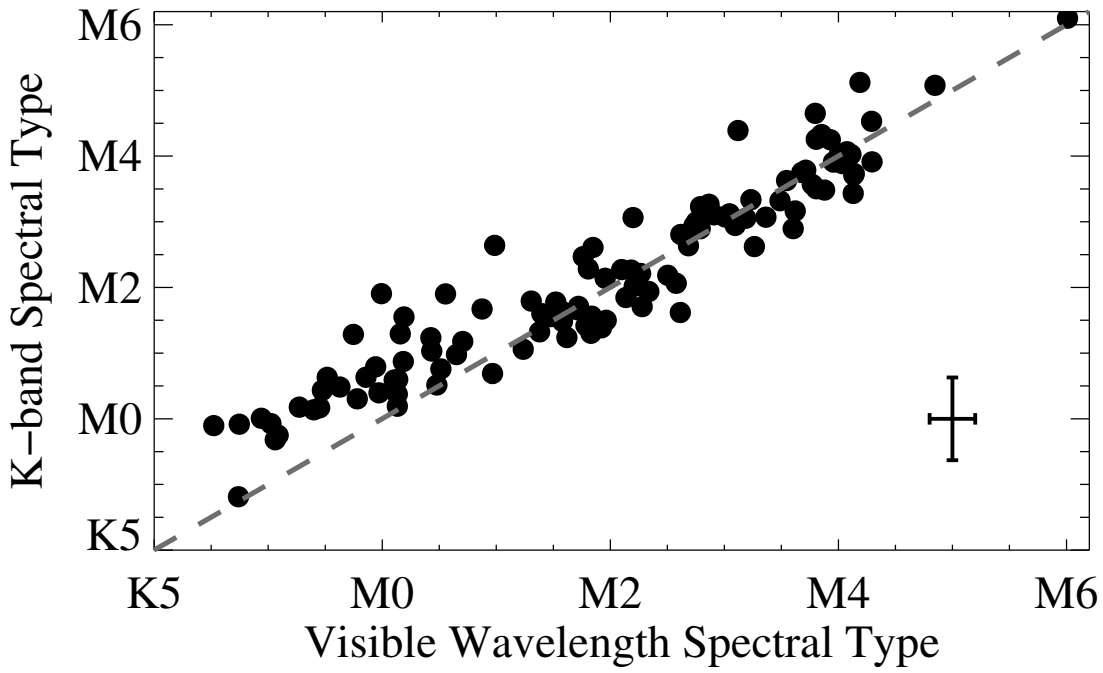


Figure 4.2: Spectral types derived from the $\text{H}_2\text{O-K2}$ index (RA12) vs. those derived from TiO and CaH indices at visible wavelengths. The dashed line indicates a perfect agreement and typical errors are shown in the bottom right of the plot. For spectral types later than M1 the different techniques agree, but for earlier-type stars the $\text{H}_2\text{O-K2}$ index tends to return a later spectral type than visible wavelength indices.

where λ_i is the wavelength at pixel i , F is the flux at λ_i , F_c is the pseudo-continuum at λ_i , and the sum is computed over all n pixels within a given feature. We compensate for the low resolution by interpolating the spectrum near the edge to a much higher resolution ($R > 10,000$). We experiment with different techniques to calculate the pseudo-continuum (see below). The list of continuum regions used is listed in Table 4.4, many of which are taken from T12.

4. A temperature-sensitive parameter τ , is calculated from each spectrum. τ is defined based on the center wavelength of the selected feature from step (2). Specifically, τ is set to be the K -band H₂O (H₂O-K2) index as defined by R12 if the feature is centered in the K band, the H band H₂O (H₂O-H) index as defined by T12 if the feature is in the H band, or the Color1 index from Hawley et al. (2002) if the feature is drawn from visible wavelengths. If the feature falls within the J-band, we use a new H₂O-J index defined as:

$$\text{H}_2\text{O}-\text{J} = \frac{\langle \mathcal{F}(1.210 - 1.230) \rangle / \langle \mathcal{F}(1.313 - 1.333) \rangle}{\langle \mathcal{F}(1.313 - 1.333) \rangle / \langle \mathcal{F}(1.331 - 1.351) \rangle}, \quad (4.4)$$

where $\langle \mathcal{F}(a - b) \rangle$ indicates the median flux level in a wavelength range between a and b (in μm). H₂O-J is defined to select regions relatively clear of atomic or molecular features and to correlate well with the H₂O-K and H₂O-H indices.

5. Using least-squares, the best fit is found for the equation:

$$[\text{Fe}/\text{H}]_i = A + B \times \text{EW}_i + C \times \tau_i, \quad (4.5)$$

where $[\text{Fe}/\text{H}]_i$ is the metallicity of i th primary star (assumed to be the metallicity of the companion M dwarf), EW_i is the calculated equivalent width of the selected feature in the i th late-K or M dwarf companion spectrum, and A , B , and C are fitting parameters. The quality of the fit is measured by the adjusted square of the multiple correlation coefficient (R_{ap}^2), which is defined as:

$$R_{\text{ap}}^2 = 1 - \frac{(n - 1) \sum (y_{i,\text{model}} - y_i)^2}{(n - p) \sum (y_i - \bar{y})^2}, \quad (4.6)$$

where p is the number of changeable parameters (i.e. A , B , and C), n is the number of data points in the fit, y_i is the metallicity of the i th primary star, $y_{i,\text{model}}$ is the metallicity of the i th star predicted by the fit, and \bar{y} is the average of y_i . A R_{ap}^2 closer to 1 implies that the model accurately explains the variance of the sample, while $R_{\text{ap}}^2=0$ implies that it can explain none. For Equation 4.5, $p = 3$, $y_i = [\text{Fe}/\text{H}]_i$, and $y_{i,\text{model}} = A + B \times \text{EW}_i + C \times \tau_i$. Note that for $n \gg p$, $R_{\text{ap}}^2 \simeq R^2$.

6. To asses the significance of the assigned R_{ap}^2 value, $[\text{Fe}/\text{H}]$ (or $[\text{M}/\text{H}]$) values are randomly reassigned among the stars, and step 5 is repeated 1000 times (re-randomizing the metallicities each time). The resulting distribution of the 1000 R_{ap}^2 values gives the level above which the R_{ap}^2 value (determined from non-random metallicities) can be considered significant. We consider the given feature center to be

Table 4.4. Continuum Regions Used

Visible μm	J-Band μm	H-Band μm	K-Band μm
0.4035–0.4080	0.9790–0.9890	1.4440–1.4480	1.8860–1.8900
0.4135–0.4180	1.0610–1.0650	1.4644–1.4710	1.9350–1.9400
0.4425–0.4450	1.1260–1.1300	1.4921–1.4965	1.9610–1.9700
0.4610–0.4625	1.1530–1.1580	1.5060–1.5090	2.0500–2.0540
0.4680–0.4700	1.1890–1.1930	1.5190–1.5220	2.0800–2.0870
0.5269–0.5299	1.2140–1.2180	1.5920–1.5960	2.1330–2.1351
0.5660–0.5675	1.2250–1.2300	1.6230–1.6310	2.1530–2.1590
0.6586–0.6607	1.2550–1.2634	1.6935–1.6980	2.1670–2.1720
0.7041–0.7049	1.2700–1.2730	1.7530–1.7570	2.1940–2.1985
0.7390–0.7500	1.2950–1.2970	...	2.2130–2.2190
0.8100–0.8160	1.3040–1.3070	...	2.2450–2.2520
0.8230–0.8300	1.3214–1.3270	...	2.2717–2.2781
0.8590–0.8620	1.4090–1.4150	...	2.2850–2.2900
0.8890–0.8920	2.3050–2.3105
0.9100–0.9120	2.3600–2.3640
0.9220–0.9255	2.3710–2.3760
...	2.3950–2.4050

a *bona-fide* metal sensitive feature if R_{ap}^2 is higher than the 99.9% highest R_{ap}^2 value from the randomly assigned metallicities (henceforth R_{rand}^2).

For each increment in feature center and width, we record the resulting R_{ap}^2 and R_{rand}^2 . We show the resulting distribution of R^2 and R_{rand}^2 values as a function of the feature's central wavelength in Fig. 4.3.

We repeat our analysis using various methods of fitting for the pseudo-continuum. Better estimates of the continuum should result in more accurate line measurements, and therefore higher R_{ap}^2 values for the same features. In one experiment we tried to fit the global spectrum with a high order (> 10) polynomial. We tested fitting each band (visible, *JHK*) with 3rd through 6th order polynomials, as well as with 3rd through 6th order Legendre polynomials. Interestingly, we found we had the best (highest R_{ap}^2 with respect to R_{rand}^2) results when fitting the pseudo-continuum using a linear fit (using the IDL code `linfit`) of the continuum regions immediately blueward and redward of the selected feature. We use this fitting procedure for all calibrations derived in Section 4.6.

We run additional experiments to test the influence of spectral type on determination of metallicities: we repeat our analysis on just the early-type stars in our sample (K5.5–M2.0) and again with just the late-type stars (M2.0–M6). The split roughly corresponds to our median spectral type (\simeq M2). It is possible to parse our data into smaller spectral type

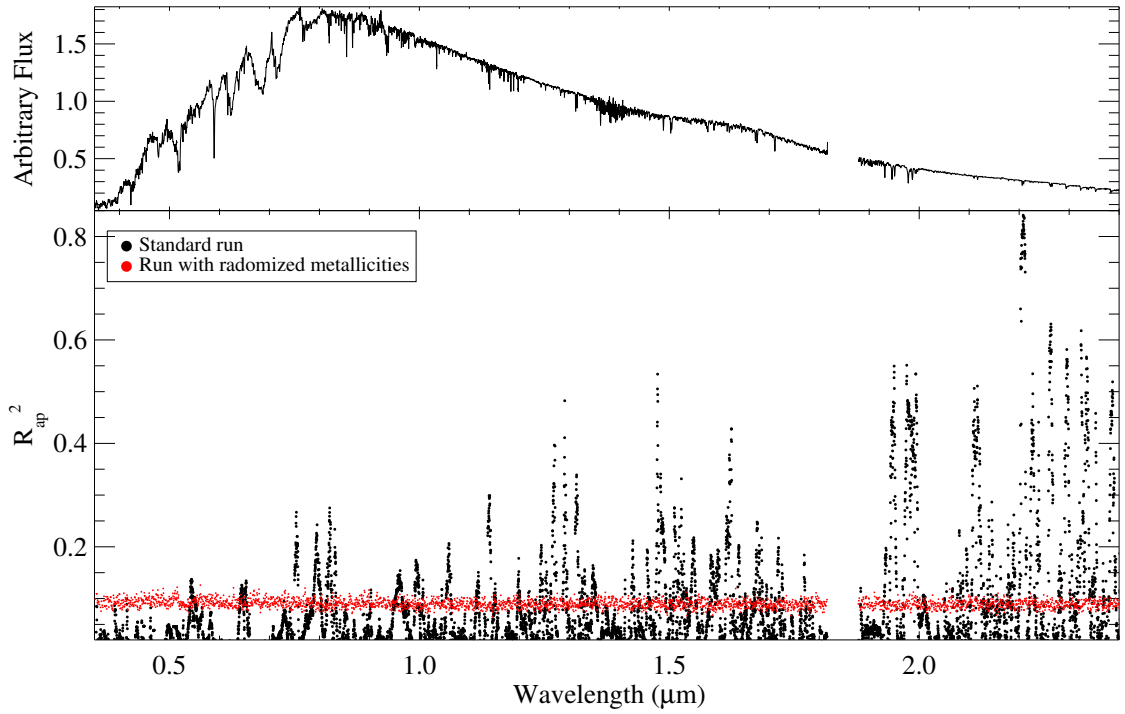


Figure 4.3: Results of our systematic search to find the features that best correlate with $[Fe/H]$ in late-K or M dwarf spectra. Feature centers (shown on the X axis) and widths are changed incrementally covering a range of widths (20 \AA to 100 \AA) and feature centers ($0.35 \mu\text{m}$ to $2.4 \mu\text{m}$). Red points indicate the R^2_{rand} values derived from randomly reassigning primary star metallicities and repeating our process 1000 times (the 99.9% highest resulting R^2_{ap} values are shown). In this particular analysis, we fit for $[Fe/H]$, and fit the pseudo-continuum using just the continuum regions immediately blueward and redward of a given feature. A range of feature widths are shown, which results in some range to the distribution for a given central wavelength. Although there are $> 400,000$ unique combinations of feature center and width, only 15,000 are shown for simplicity.

ranges, although this will proportionately shrink each sample. Thus this would make it difficult to identify metal sensitive features that have not been previously discovered.

Lastly, we rerun our analysis using [M/H] rather than [Fe/H] for the metallicity of the primary star. R12 were able to derive better fits between *K*-band atomic lines and [M/H] than for [Fe/H], perhaps due to variations in $[\alpha/\text{Fe}]$ creating discrepancies between the actual measured quantities (Na and Ca in the case of R12) and Fe abundances. However, many of the literature sources we draw from do not provide [M/H] values for the primary stars (just [Fe/H]). As a result, there are 5 fewer binaries when using [M/H] and 16 primary stars have a different source for their [M/H] values than their [Fe/H] values (see Table 4.1 for a full list of [Fe/H] and [M/H] sources used).

We consider a feature to be metal-sensitive if a given feature's center and width has an R_{ap}^2 value above its corresponding R_{rand}^2 value. This criterion ensures that no features are identified simply by coincidence.

Once features are identified, we then attempt to derive a calibration for a given wavelength range (e.g., J-band) by solving the equation (by least squares):

$$[\text{Fe}/\text{H}]_i = A + \sum_{j=1}^N (B_j \times \text{EW}_{i,j}) + C \times \tau_i, \quad (4.7)$$

where $[\text{Fe}/\text{H}]_i$ is the metallicity of the i th primary star, N is the total number of features of interest among M_λ features identified as metal-sensitive in a given wavelength range, τ_i is the temperature sensitive parameter selected based on the wavelength regime (see above), $\text{EW}_{i,j}$ is the equivalent width of the j th feature measured for the i th star, and A , C , and the B_j 's are fitting parameters. We find the best fit for $N=1,2,3,\dots < M_\lambda$ until the increase in R_{ap}^2 is negligible ($\Delta R_{\text{ap}}^2 < 0.03$) or it is clear from visual inspection of the data that the adding of further variables is over fitting the data. This limit is usually hit at $N = 3 - 4$. Although we use [Fe/H] in Equations 4.5 and 4.7, we also perform the same procedure using [M/H].

4.6 Determination of M dwarf Metallicities

The first thing our analysis gives us is a catalog of metal-sensitive features, which we list in order of λ_c in Table 4.5. In total we find 120 features that are statistically significant predictors of metallicity, although only 20 of these are used in our final calibrations. We identify a number of previously known metal-sensitive features, as well as many of new ones. One of the most metal-sensitive features is the Na I doublet in the *K*-band ($2.208 \mu\text{m}$), already identified by R10. Our analysis identifies the Ca I ($1.616 \mu\text{m}$ and $1.621 \mu\text{m}$) and K I ($1.5176 \mu\text{m}$) lines shown to be metal-sensitive by T12. In fact, our analysis locks on to very similar wavelength centers and widths as those found by T12 for both *H*-band and *K*-band features. Since our analysis covers all wavelengths and is completely blind (e.g., they have no a-priori line lists or knowledge of feature size) this suggests that our purely empirical analysis is identifying metal-sensitive atomic and molecular lines.

Table 4.5. Metal-sensitive Features

F#	Center λ [μm]	Width [Å]	R_{ap}^2					
			All	[Fe/H] Early	Late	All	[M/H] Early	Late
...	0.3980	23	...	0.42	0.18	...	0.38	...
...	0.4098	35	...	0.30	0.26	...	0.24	...
...	0.4148	68	0.10	0.28	0.36	...	0.21	0.28
...	0.4342	23	...	0.23	...	0.10	0.30	...
...	0.4444	41	...	0.31	0.26	...	0.28	...
F01	0.4648	23	...	0.56	0.54	...
...	0.5384	20	0.13	0.39	0.31	...
...	0.5444	53	0.15	0.41	...	0.13	0.36	...
...	0.5524	77	0.11	0.42	0.20	0.10	0.39	0.22
F02	0.5608	20	...	0.43	0.30	...
F03	0.6118	20	0.14	0.20	0.26	0.15	0.26	0.39
F04	0.6232	20	0.28	0.41
...	0.6356	20	...	0.33	0.38	0.16	0.24	0.54
F05	0.6416	41	0.13	...	0.42	0.22	...	0.57
...	0.6526	20	0.16	0.23	0.24	0.19	...	0.34
...	0.6888	35	0.32	0.12	...	0.47
...	0.7024	29	...	0.31	0.28	0.43
F06	0.7540	20	0.30	0.51	0.39	0.28	0.44	0.38
...	0.7942	20	0.30	0.37	0.29	0.35	0.32	0.39
...	0.8008	23	0.19	...	0.31	0.26	...	0.44
F07	0.8208	35	0.36	0.77	0.23	0.31	0.69	0.22
...	0.8266	98	0.31	0.40	0.24	0.35	0.41	0.28
F08	0.8684	26	0.14	0.63	0.23	0.15	0.53	0.18
...	0.8870	20	0.16	0.36	0.22	0.21	0.28	0.30
...	0.9025	20	0.16	0.29	...	0.17	0.20	...
...	0.9189	20	0.15	0.19	0.23	0.23	0.26	0.32
...	0.9507	20	0.12	0.25	0.34	0.27
...	0.9559	20	0.17	0.32	0.26	0.14	0.27	0.22
...	0.9627	20	0.16	0.32	0.23	0.12	0.23	0.21
...	0.9719	20	0.22	0.33	0.30	0.20	0.27	0.24
...	0.9931	68	0.18	0.23	0.22
...	1.0569	41	0.23	0.44	...	0.23	0.43	...
...	1.0639	86	0.21	0.48	...	0.25	0.49	...
...	1.0834	20	0.13	0.48	...	0.14	0.51	...
...	1.1176	50	0.18	0.35	...	0.18	0.31	...
F09	1.1396	26	0.35	0.46	0.28	0.27	0.35	0.19
...	1.1794	20	0.14	0.33	0.21	...
...	1.1880	20	0.12	0.34	0.22	...
...	1.1986	23	0.20	0.32	...	0.14	0.22	...
...	1.2432	23	0.26	0.68	0.22	0.22	0.62	...
...	1.2532	23	0.23	0.41	0.25	0.17	0.26	0.21
F10	1.2698	98	0.42	0.47	0.37	0.43	0.47	0.35
F11	1.2908	20	0.51	0.63	0.41	0.41	0.55	0.26
F12	1.3148	50	0.39	0.72	0.23	0.31	0.66	0.25
...	1.3292	20	0.31	0.46	0.22	0.28	0.41	0.29
F13	1.3344	23	0.15	0.42	0.31	0.16	0.35	0.38
...	1.3472	55	0.18	0.30	0.26	0.24	0.42	0.30
...	1.3500	20	0.17	0.31	0.21	0.21	0.38	0.23
...	1.3780	44	...	0.20	...	0.16	0.27	...
...	1.3986	26	0.14	0.28	...	0.21	0.33	...
...	1.4276	50	0.27	0.42	...	0.25	0.35	...
...	1.4366	53	0.14	0.32	0.26	0.11	0.26	0.24
F14	1.4766	41	0.54	0.60	0.44	0.45	0.51	0.29
F15	1.4836	23	0.43	0.73	0.18	0.36	0.66	0.25
...	1.4942	98	0.28	0.59	...	0.24	0.60	...
...	1.5000	65	0.14	0.52	...	0.13	0.52	0.22
F16	1.5172	33	0.48	0.70	0.48	0.48	0.69	0.45
...	1.5256	59	0.40	0.75	0.24	0.34	0.69	...
...	1.5314	26	0.26	0.71	...	0.22	0.65	...
...	1.5468	29	0.25	0.58	...	0.20	0.53	...
...	1.5522	23	0.26	0.57	...	0.21	0.56	...
...	1.5628	23	0.16	0.42	...	0.14	0.37	...
...	1.5840	47	0.27	0.60	0.19	0.27	0.60	0.19
...	1.5940	86	0.20	0.58	0.24	0.21	0.57	...
...	1.5978	20	0.29	0.68	...	0.23	0.61	...
F17	1.6158	23	0.60	0.88	0.28	0.55	0.86	0.22
...	1.6202	23	0.48	0.85	0.21	0.46	0.80	0.27

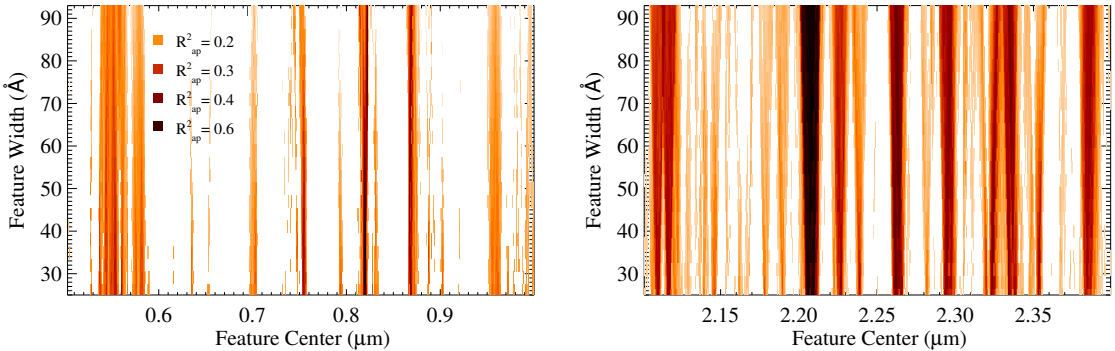


Figure 4.4: Distribution of R_{ap}^2 values as a function of feature center and width for the K -band (left) and red end of the visible wavelengths (right). The visible wavelength distribution is based on our analysis using just K5.5–M2 dwarfs. Data points which do not have $R_{ap}^2 > R_{rand}^2$ are white (i.e. not shown). Surprisingly, there is not much change in R_{ap}^2 as a function of the selected width for a given feature in the K -band, however we do see a trend towards smaller widths in the visible wavelengths.

Because our only restriction was the size of the feature ($\leq 100 \text{ \AA}$), our technique can easily identify areas of the spectrum corresponding to several, even unrelated lines. Some of these regions may be associated with doublets/triplets from the same atomic species, with broad molecular bands, or with sets of lines that are blended at our resolution. Some features in Table 4.5 may not correspond to any one specific element or molecule, but simply to a region of the spectrum that undergoes overall changes as a function of the metallicity of the star.

We show the distribution of R_{ap}^2 values as a function of feature width and center for two example wavelength regions in Fig. 4.4. Interestingly, features in the H and K band features yield similar R_{ap}^2 for a wide range of a feature's widths. However, the opposite is seen in the visible end of the spectrum, where features perform better near the minimum feature width (20 \AA). This is most likely due to crowding at visible wavelengths.

We find far better metal-sensitive features by doing a separate analysis for earlier-type dwarfs (K5.5–M2) and for later type dwarfs (M2–M6). Specifically, the best fit we achieve when fitting for $[\text{Fe}/\text{H}]$ using all stars in our sample yields $R_{ap}^2 = 0.54$, whereas when we split up the sample by spectral type we achieve $R_{ap}^2 = 0.84$ for K5.5–M2.0 and $R_{ap}^2 = 0.68$ for M2.0–M6.0. This is not unexpected, many of the most metal-sensitive features for K5.5–M2 dwarfs become blended with molecular bands (which grow as a function of spectral type) at the resolution of SNIFS. Further, features blueward of 0.5 μm tend to have very low S/N for stars later than M2, and are not to be very useful. This also suggests that better results could be achieved on later type M dwarfs with modest improvements in resolution, to better distinguish the lines.

We find the best empirical fits to Equation 4.7 for each wavelength regime (visible, J , H , and K) and metallically metric ($[\text{Fe}/\text{H}]$ and $[\text{M}/\text{H}]$). They are:

$$[\text{Fe}/\text{H}]_{V,e} = 0.53F_{07} + 0.26F_{01} - 0.16F_{02} \quad (4.8)$$

Table 4.5—Continued

F#	Center λ [μm]	Width [\AA]	R_{ap}^2					
			All	[Fe/H] Early	Late	All	[M/H] Early	Late
...	1.6380	59	0.22	0.46	...	0.29	0.54	0.31
...	1.6446	20	0.15	0.58	...	0.15	0.54	...
...	1.6522	20	0.16	0.46	...	0.18	0.44	...
...	1.6660	23	0.20	0.36	0.24	0.14	0.29	...
...	1.6758	23	0.29	0.63	0.23	0.20	0.55	...
...	1.6817	26	0.25	0.51	0.22	0.18	0.41	0.19
...	1.7003	23	0.21	0.55	0.38	0.18	0.48	0.26
...	1.7115	23	0.15	0.56	0.35	0.21	0.46	0.24
...	1.7189	80	0.26	0.28	0.42	0.29	0.33	0.31
F18	1.7261	32	0.24	0.39	0.26	0.18	0.38	0.19
...	1.7303	20	0.19	0.46	...	0.11	0.46	...
...	1.7405	23	...	0.42	...	0.10	0.42	...
...	1.7629	38	0.15	0.34	...	0.17	0.32	0.25
...	1.7707	23	0.21	0.44	...	0.21	0.42	...
...	1.8807	32	0.16	0.41	...	0.16	0.33	...
...	1.9507	29	0.61	0.77	0.51	0.51	0.65	0.36
...	1.9753	77	0.57	0.77	0.42	0.44	0.60	0.30
...	1.9863	29	0.51	0.75	0.41	0.38	0.55	0.31
...	1.9931	29	0.54	0.72	0.39	0.43	0.56	0.28
...	2.0513	62	0.18	0.36	...	0.21	0.25	0.19
...	2.0675	41	0.16	0.34	...	0.12
...	2.0831	95	0.24	0.47	0.20	0.20	0.25	...
...	2.0965	29	0.29	0.37	0.31	0.17	0.25	...
...	2.1063	92	0.45	0.61	0.23	0.44	0.51	0.24
...	2.1103	29	0.54	0.69	0.35	0.52	0.55	0.38
...	2.1173	32	0.53	0.69	0.32	0.48	0.53	0.30
...	2.1375	47	0.25	0.42	0.19	0.21	0.33	0.28
...	2.1469	29	0.33	0.40	0.35	0.42	0.35	0.40
...	2.1697	74	0.18	0.35	...	0.11
...	2.1783	29	0.35	0.59	...	0.27	0.40	...
...	2.1895	32	0.32	0.47	0.18	0.27	0.49	...
F19	2.2079	68	0.86	0.88	0.83	0.78	0.72	0.68
...	2.2271	29	0.54	0.74	0.42	0.46	0.57	0.29
...	2.2391	29	0.47	0.60	0.18	0.41	0.47	0.20
...	2.2640	59	0.66	0.89	0.47	0.57	0.71	0.40
...	2.2823	32	0.28	0.36	0.27	0.27	0.27	0.28
...	2.2968	74	0.58	0.68	0.52	0.55	0.52	0.50
...	2.3014	70	0.53	0.65	0.41	0.47	0.47	0.42
F20	2.3242	38	0.63	0.75	0.58	0.56	0.57	0.50
F21	2.3342	35	0.61	0.73	0.55	0.57	0.58	0.49
...	2.3430	44	0.37	0.52	0.38	0.36	0.41	0.35
...	2.3536	29	0.58	0.68	0.52	0.52	0.49	0.51
...	2.3678	44	0.17	...	0.42	0.22	...	0.45
F22	2.3844	35	0.54	0.69	0.35	0.50	0.51	0.32

Note. — Here we show only the features used in our final calibrations. The full version of the table with *all* metal-sensitive features identified by our analysis will be available electronically.

^a... denotes that the feature did not have an R_{ap}^2 value above the R_{rand}^2 value, and thus is not considered a statistically significant metal-sensitive feature.

^bFull: K5.5–M6.0, early: K5.5–M2.0, late: M2.0–M6.0.

$$\begin{aligned}
& -0.784(\text{Color1}) - 0.34 \\
[\text{M}/\text{H}]_{\text{V,e}} &= 0.38F_{07} + 0.21F_{01} + 0.29F_{08} \\
& -0.504(\text{Color1}) - 0.79
\end{aligned} \tag{4.9}$$

$$\begin{aligned}
[\text{Fe}/\text{H}]_{\text{V,l}} &= -0.20F_{05} + 0.48F_{08} + 0.24F_{07} \\
& + 0.14F_{03} - 0.204(\text{Color1}) - 0.32
\end{aligned} \tag{4.10}$$

$$\begin{aligned}
[\text{M}/\text{H}]_{\text{V,l}} &= -0.065F_{05} - 0.071F_{04} - 0.30F_{06} \\
& + 0.719(\text{Color1}) - 0.24
\end{aligned} \tag{4.11}$$

$$\begin{aligned}
[\text{Fe}/\text{H}]_{\text{J}} &= 0.29F_{10} + 0.21F_{09} + 0.26F_{12} \\
& - 0.26F_{13} - 0.190(\text{H}_2\text{O}-\text{J}) - 1.03
\end{aligned} \tag{4.12}$$

$$\begin{aligned}
[\text{M}/\text{H}]_{\text{J}} &= 0.32F_{10} + 0.46F_{11} + 0.076F_{09} \\
& + 1.213(\text{H}_2\text{O}-\text{J}) - 1.97
\end{aligned} \tag{4.13}$$

$$\begin{aligned}
[\text{Fe}/\text{H}]_{\text{H}} &= 0.40F_{17} + 0.51F_{14} - 0.28F_{18} \\
& - 1.460(\text{H}_2\text{O}-\text{H}) + 0.71
\end{aligned} \tag{4.14}$$

$$\begin{aligned}
[\text{M}/\text{H}]_{\text{H}} &= 0.38F_{17} + 0.40F_{16} + 0.41F_{15} \\
& + 0.194(\text{H}_2\text{O}-\text{H}) - 0.76
\end{aligned} \tag{4.15}$$

$$\begin{aligned}
[\text{Fe}/\text{H}]_{\text{K}} &= 0.19F_{19} + 0.069F_{22} + 0.083F_{20} \\
& + 0.218(\text{H}_2\text{O}-\text{K}) - 1.55
\end{aligned} \tag{4.16}$$

$$\begin{aligned}
[\text{M}/\text{H}]_{\text{K}} &= 0.12F_{19} + 0.086F_{22} + 0.13F_{21} \\
& + 0.245(\text{H}_2\text{O}-\text{K}) - 1.18
\end{aligned} \tag{4.17}$$

where $F\#$ refer to the equivalent width of the corresponding feature listed in Table 4.5, the subscripts refer to the wavelength bands where the calibration is useful (V referring to visible wavelengths). An additional subscript is added (e or l) for calibrations in visible wavelengths to denote which formula is valid for early (K5.5 to M2) and late (M2 to M6) dwarfs. All equations assume feature equivalent widths are calculated in Angstroms.

We show the primary star metallicity as a function of the derived metallicity for the companion dwarf for each of the 10 calibrations in Figure 4.5 and list reduced χ^2 , R_{ap}^2 , root mean square error (RMSE), in Table 4.6. The RMSE indicates how useful a model is at prediction (lower numbers indicate the fit is a better predictor) and is defined as:

$$\text{RMSE} = \sqrt{\sum_{i=0}^n \frac{(y_{i,\text{model}} - y_i)^2}{(n-p)}}. \tag{4.18}$$

Lower R_{ap}^2 and higher RMSE values may in part be due to differences in S/N as a function of wavelength. We estimate measurement noise sources by adding synthetic noise to each spectrum consistent with the observed S/N of that spectrum, then recalculating the metallicity of the M dwarf using the appropriate equation above. The standard deviation in the metallicity estimate from 1000 different additions of noise pattern is assumed to be the measurement error. This error is what we use for our calculation of the

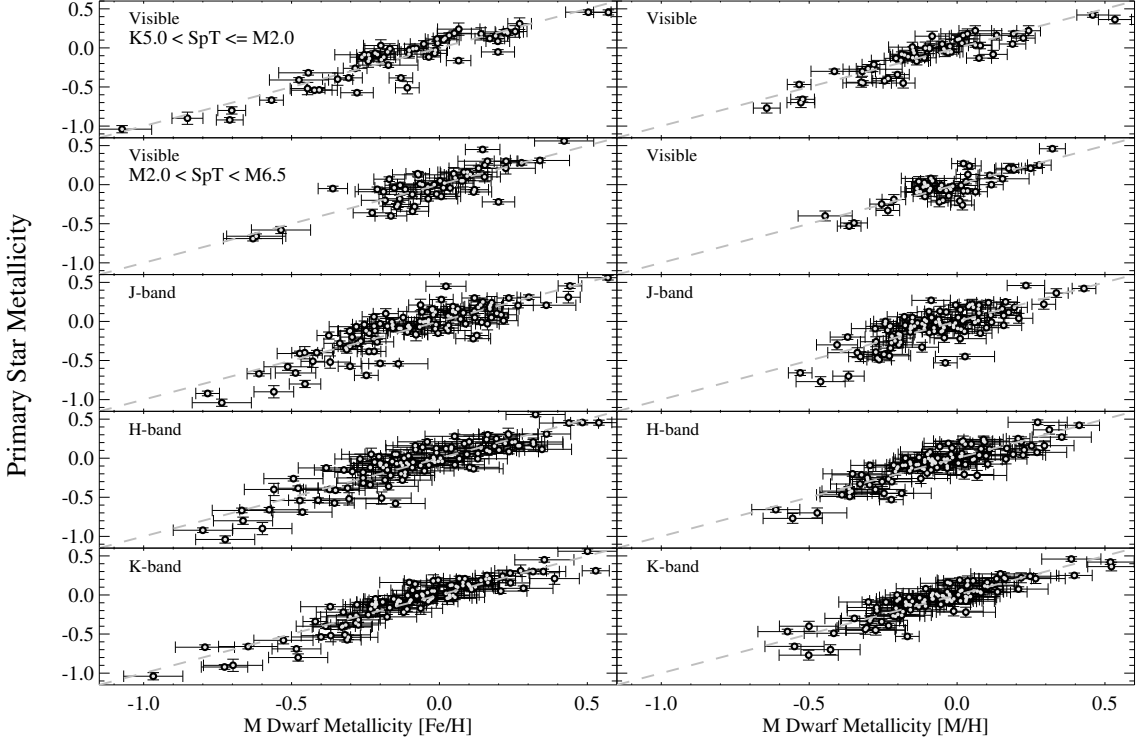


Figure 4.5: Metallicity for the primary star vs. derived metallicity of the late K or M dwarf companion based on Equations (4.8)-(4.17). Calibrations for $[Fe/H]$ are shown on the left plots, while those for $[M/H]$ are shown on the right plots. Statistics on the quality of the fit can be found in Table 4.6. Y axis error bars shown are based on 1σ Gaussian errors for the primary star metallicity (see Section 4.4.1). Error bars for the K/M dwarf metallicity are the 1σ standard deviation of 1000 recalculations of the K/M dwarf metallicity after adding noise to each spectrum consistent with its S/N.

reduced χ^2 for each fit. Thus the reduced χ^2 values probe how much of the noise comes from measurement (errors). A reduced χ^2 close to 1 would suggest that most or all of the error from the fit is due to measurement (e.g. Poisson) noise.

The dependence on τ varies significantly between equations. This is most likely due to different features capturing some of the temperature-dependence and/or that the Color1 and H_2O indices are not accurately modeling temperature dependencies across the full sample. It is also interesting that some coefficients of features are negative. This may be due to a combination of factors, including changes in $[Fe/H]$ versus $[\alpha/Fe]$ (e.g. Ca is an α element) or complex relations between T_{eff} and $[Fe/H]$, that vary for each feature. Whatever the case, since these fits are purely empirical, we should be cautious not to over-interpret the physical meaning of any particular coefficient or feature.

Table 4.6. Metallicity Calibration Statistics

Eqn. #	Band	λ (μm)	SpT Range	Type	R_{ap}^2	RMSE	σ	χ_{Red}^2
4.8	Optical	0.35–1.00	K5.0–M2.0	[Fe/H]	0.84	0.07	0.13	8.8
4.9	Optical	0.35–1.00	K5.0–M2.0	[M/H]	0.80	0.06	0.11	6.4
4.10	Optical	0.35–1.00	M2.0–M6	[Fe/H]	0.68	0.06	0.14	7.1
4.11	Optical	0.35–1.00	M2.0–M6	[M/H]	0.65	0.06	0.11	7.8
4.12	J	1.00–1.44	K5.0–M5.0	[Fe/H]	0.71	0.07	0.16	11.4
4.13	J	1.00–1.44	K5.0–M5.0	[M/H]	0.55	0.08	0.15	9.4
4.14	H	1.44–1.80	K5.0–M5.0	[Fe/H]	0.77	0.07	0.14	3.7
4.15	H	1.44–1.80	K5.0–M5.0	[M/H]	0.73	0.06	0.12	4.2
4.16	K	1.80–2.45	K5.0–M5.0	[Fe/H]	0.86	0.06	0.11	4.7
4.17	K	1.80–2.45	K5.0–M5.0	[M/H]	0.77	0.05	0.10	3.8

Table 4.7. Assessment of Previous Metallicity Indicators

Technique	Type	R_{ap}^2	RMSE	Eqn #
$\zeta_{\text{TiO/CaH}}$	[Fe/H]	0.58	0.28	4.26
$\zeta_{\text{TiO/CaH}}$	[M/H]	0.61	0.23	4.27
$J - K$	[Fe/H]	0.30	0.19	4.29
$J - K$	[M/H]	0.25	0.16	4.30
H -Band	[Fe/H]	0.74	0.14	4.31
H -Band	[M/H]	0.71	0.12	4.32
K -Band	[Fe/H]	0.76	0.14	4.33
K -Band	[M/H]	0.75	0.13	4.34

4.7 Assessing and Recalibrating Existing Techniques

In addition to defining our own metallicity calibrations, we can use our sample to test existing metallicity estimators, as well as improve the existing calibrations. Like before, we use R_{ap}^2 , and RMSE as our standard metrics to asses the quality of a calibration. We summarize our refits in Table 4.7.

4.7.1 $\zeta_{\text{TiO/CaH}}$

Much effort has gone into determine M dwarf metallicities using visible wavelength spectra. Most of this has been focused on the $\zeta_{\text{TiO/CaH}}$ (henceforth ζ) parameter (e.g. Lépine et al. 2007; Woolf et al. 2009; Dhital et al. 2012). However, the setup of our analysis means that we would not be able to identify ζ at all, because ζ is based on spectroscopic indices (not equivalent widths). Band indices (e.g., TiO5, CaH3, etc.) are calculated from the ratio of

the flux in region a to the flux in region b using the approximation:

$$\text{Index} \simeq \frac{[\sum_{i=a} F(\lambda_i)]/[w_a]}{[\sum_{i=b} F(\lambda_i)]/[w_b]}, \quad (4.19)$$

where w_a and w_b are the widths of region a and b in angstroms, respectively. The sums are computed over all pixels i in region a and b , respectively. Our analysis only makes use of equivalent widths (see Equation 4.3). Further, we do not allow high order terms, while ζ generally requires 3rd or 4th order polynomials of the CaH index (e.g. Lépine et al. 2013). However, this does not prevent us from using our data to test the performance of ζ .

We calculate the CaH2, CaH3, and TiO5 indices following the definitions from Reid et al. (1995). We compute corrected indices (CaH_c , CaH_c , and TiO5_c) using the formula from Lépine et al. (2013), which include corrections for the SNIFS instrument. We use these to compute ζ following the formula as defined by Lépine et al. (2007):

$$\zeta = \frac{1 - \text{TiO5}}{1 - [\text{TiO5}]_{Z_\odot}}, \quad (4.20)$$

where $[\text{TiO5}]_{Z_\odot}$ is a function of $\text{CaH} = \text{CaH2} + \text{CaH3}$. We use the formula for $[\text{TiO5}]_{Z_\odot}$ from Lépine et al. (2013).

$$\begin{aligned} [\text{TiO5}]_{Z_\odot} &= 0.622 - 1.906(\text{CaH}_c) \\ &\quad + 2.211(\text{CaH}_c)^2 - 0.588(\text{CaH}_c)^3. \end{aligned} \quad (4.21)$$

We plot the primary star metallicities as a function of the derived ζ values as filled points in Fig. 4.6. ζ shows a weak trend with metallicity in both $[\text{Fe}/\text{H}]$ and $[\text{M}/\text{H}]$. From this we derive the following relationships:

$$[\text{Fe}/\text{H}] = 0.98\zeta - 1.04 \quad (4.22)$$

$$[\text{M}/\text{H}] = 0.68\zeta - 0.74 \quad (4.23)$$

Like before, we randomly reassign the metallicities to different CPM pairs, and attempt to compute an R_{rand}^2 value. We find that both Equations 4.23 and 4.23 give $R_{\text{ap}}^2 < R_{\text{rand}}^2$. Further, the ζ parameter only correctly identifies one companion as a subdwarf (LHS 1812/PM06032+1921S). Although this is the most metal-poor star in our sample, there are 12 other stars in our sample with $[\text{Fe}/\text{H}] < -0.5$ but ζ values consistent with solar metallicity ($\zeta > 0.825$). According to Woolf et al. (2009), M dwarfs with $[\text{Fe}/\text{H}] < -0.34$ should have $\zeta < 0.825$, and be labeled as sdM, suggesting a problem with these stars. If we remove these pairs, we derive the following relations:

$$[\text{Fe}/\text{H}] = 1.26\zeta - 1.25 \quad (4.24)$$

$$[\text{M}/\text{H}] = 0.88\zeta - 0.89 \quad (4.25)$$

These formulae are highly significant; they yield R_{ap}^2 values of 0.58 and 0.52, and RMSE values of 0.22 and 0.20, respectively. This suggests that ζ may be useful at predicting

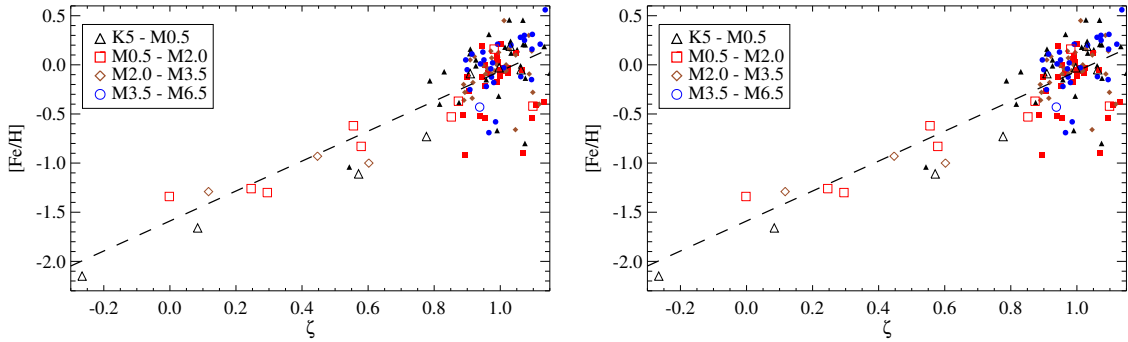


Figure 4.6: Metallicity of the primary star ($[{\rm Fe}/{\rm H}]$ to the left and $[{\rm M}/{\rm H}]$ to the right) vs. the ζ parameter as defined by Lépine et al. (2007) and using the calibration of Lépine et al. (2013). It has been shown that the effectiveness of ζ varies as a function of spectral type, so we break up our sample into four spectral type ranges in the plot. The best-fit lines from Equations 4.25 and 4.25 are shown as dotted lines. We add in a sample of 22 stars from Woolf et al. (2009, open symbols) to our own wide binary sample (filled points). Our measurements of ζ do accurately identify metal-poor stars identified in Woolf et al. (2009), however, ζ only identifies one of our wide binary stars as a subdwarf.

metallicities for $[{\rm Fe}/{\rm H}] > +0.05$ (the limit of the Woolf et al. (2009) calibration), provided the high-zeta, low-metallicity stars can be explained.

Woolf et al. (2009, using $R \simeq 3000$ spectra) derive a relation between metallicity and the ζ parameter using a mix of wide binaries (for which the primary star metallicity is known) and single (K/M) stars with high-resolution spectra, analyzed using the MOOG software (Sneden 1973) with NEXTGEN models (Hauschildt et al. 1999). Although many of their wide binaries are also in our binary sample (including LHS 1812), there is insufficient overlap between the stars in Woolf & Wallerstein (2005, 2006), and Woolf et al. (2009) and those from SPOCS or our CFHT samples to detect any systematic offsets between the two samples. This is further complicated by fact that Woolf et al. (2009) have very few subdwarf binaries in their sample (most of their subdwarfs are single stars). To test whether these low-metallicity, high- ζ dwarfs are anomalous, we observed an additional set of stars from Woolf et al. (2009).

In total we observed 22 stars used in the Woolf et al. (2009) calibration with SNIFS. We specifically select stars to cover a wide range of metallicities to get a wide range of ζ values. We list the 22 stars in Table 4.8 and show them in Fig. 4.6 as unfilled points. These 22 points form a clear metallicity sequence, showing that the revised ζ can reproduce the results of Woolf et al. (2009) and that ζ can be measured using modest resolution spectra.

Assuming the metallicities from Woolf et al. (2009) are reliable and consistent with our own, we use the combined set of our binaries and the 22 additional late-type dwarfs from Woolf et al. (2009) to derive the following relations:

$$[{\rm Fe}/{\rm H}] = 1.55\zeta - 1.62 \quad (4.26)$$

$$[{\rm M}/{\rm H}] = 1.29\zeta - 1.35 \quad (4.27)$$

Table 4.8. Stars Observed from Woolf et al. (2009)

Name	[Fe/H] ^a	$\sigma_{\text{[Fe/H]}}^a$	[M/H] ^a	ζ^b
LHS 38	-0.43	0.05	-0.40	0.94
HIP 1386	0.16	0.10	0.15	0.98
HIP 59514	-0.05	0.08	-0.03	1.06
HIP 89490	-0.53	0.08	-0.44	0.85
HIP 98906	-0.62	0.10	-0.52	0.56
HIP 105932	-0.37	0.05	-0.30	0.87
HD 18143B	0.19	0.11	0.18	1.03
HD 88230	-0.03	0.18	-0.05	1.00
HD 95735	-0.42	0.07	-0.40	1.10
GJ 129	-1.66	0.05	-1.33	0.08
GJ 1177B	-0.09	0.10	-0.06	0.91
GJ 3212	-0.08	0.05	-0.06	0.70
LHS 364	-1.41	0.04	-1.15	0.00
GJ 9722	-0.83	0.04	-0.70	0.58
LHS 174	-1.11	0.05	-0.95	0.57
LHS 182	-2.15	0.03	-1.88	-0.27
LHS 491	-0.93	0.08	-0.78	0.45
LHS 3084	-0.73	0.05	-0.64	0.78
LHS 156	-1.00	0.04	-0.85	0.60
LHS 161	-1.30	0.04	-1.06	0.29
LHS 318	-1.26	0.05	-1.03	0.25
LSPMJ2205+5353	-1.29	0.08	-1.06	0.12

^aDetermined from Woolf & Wallerstein (2005), Woolf & Wallerstein (2006), or Woolf et al. (2009).

^bDetermined from SNIFS spectra.

which we show in Fig. 4.6 as dashed lines. The resulting fits yield R_{ap}^2 values of 0.58 and 0.61, respectively, both well above the R_{rand}^2 (0.17 and 0.14, respectively). The RMSE values are 0.28 and 0.23, although it is notably higher for dwarfs with $\zeta > 0.825$ and lower for dwarfs with $\zeta < 0.825$. If we remove the 11 stars with $[\text{Fe}/\text{H}] < -0.5$ but $\zeta > 0.825$, ζ follows a clear trend over the full range of metallicities covered. Interestingly, these 11 dwarfs appear to follow a completely different sequence in $[\text{Fe}/\text{H}]$ (or $[\text{M}/\text{H}]$) versus ζ , and are well separated from their single-star, metal-poor counterparts, suggesting that they are unique in some way. However, further inspection of these 11 pairs does not reveal anything that could explain their discrepancy: none exhibit H- α significant emission (likely inactive), they cover a wide range of spectral types (K7–M5), and they have metallicities from 5 different sources (including from SPOCS and our own CFHT spectra). We revisit the issue of these stars in Section 4.8.

4.7.2 $J - K$ Metallicities

Johnson et al. (2012) find a relation between the $J - K$ and $V - K$ colors and the metallicity of M dwarfs, based in part on relations noted by Leggett (1992) and Lépine & Shara (2005). They find a best fit relation of:

$$[\text{Fe}/\text{H}] = -0.050 + 3.520\Delta(J - K), \quad (4.28)$$

where $\Delta(J - K)$ is defined as:

$$\Delta(J - K) = \begin{cases} (J - K) - 0.835 & : V - K < 5.5 \\ (J - K) - \sum_{i=0} a_i(V - K)^i & : V - K \geq 5.5 \end{cases}$$

and $\{a\} = \{1.637, -0.2910, 0.02557\}$. Johnson et al. (2012) note that this metallicity relation is only valid for stars with $-0.1 < \Delta(J - K) < 0.1$ and $V - K > 3.8$, but that this technique yields metallicities accurate to ± 0.15 dex. When we apply these two restrictions to our sample, we have 118 M dwarfs with known metallicities for their primary stars. This includes stars without SNIFS/IRTF spectra that were therefore not included earlier analyses.

We find a higher RMSE of 0.20 dex, and an R_{ap}^2 of 0.20. One possible issue is the quality of V magnitudes in our sample, which come from a variety of sources. However, when we remove stars with $V - K \geq 5.5$ unless they have more reliable V magnitudes from *Tycho* (Høg et al. 2000), the quality of the fit does not change in any significant way (for stars with $V - K < 5.5$, $\Delta(J - K)$ is independent of V so these are not removed).

We attempt to improve on the calibration and derive a relation for $[\text{M}/\text{H}]$ and find:

$$[\text{Fe}/\text{H}] = -0.11 + 3.14\Delta(J - K) \quad (4.29)$$

$$[\text{M}/\text{H}] = -0.09 + 2.14\Delta(J - K) \quad (4.30)$$

which results in a slightly improved RMSE = 0.19 and 0.16, and improved $R_{\text{ap}}^2 = 0.30$ and 0.25 for $[\text{Fe}/\text{H}]$ and $[\text{M}/\text{H}]$ respectively. These R_{ap}^2 values are significantly larger than the R_{rand}^2 values (0.08 and 0.09). The major difference between our fit and that of Johnson et al. (2012) is that they fix the constant term to -0.05 in order to keep $[\text{Fe}/\text{H}] = -0.05$

at $\Delta(J - K) = 0$, consistent with a volume limited sample of stars from Johnson & Apps (2009), whereas we make no such restrictions.

4.7.3 *K*-band Metallicities

R10 have shown that one could derive M dwarf metallicities from *K*-band spectra using the Na I and Ca I lines (at $2.21\mu\text{m}$ and $2.26\mu\text{m}$). T12 refine the calibration of R12 using SpeX data, and find that metallicities derived this way are accurate to ± 0.12 dex. However, both R12 and T12 use relatively few wide binary pairs (18 and 22, respectively), and there is significant overlap in their two samples. Our sample has overlap with theirs, but is large enough to serve as a robust check on their calibrations. Because the work of T12 was optimized for SpeX, we perform our test on their calibration. We follow their method as closely as possible (including altering our continuum fitting procedure to match theirs).

We find that following the calibration of T12 yields $\text{RMSE} = 0.16$ and $R_{\text{ap}}^2 = 0.69$. We improve this calibration, and find a best fit of the form:

$$\begin{aligned} [\text{Fe}/\text{H}] = & 0.19 \times \text{EW}_{Na} + 0.074 \times \text{EW}_{Ca} \\ & + 2.13 \times (\text{H}_2\text{O}-\text{K}) - 3.18 \end{aligned} \quad (4.31)$$

This new form yields metallicities accurate to $\text{RMSE} = 0.14$ and $R_{\text{ap}}^2 = 0.76$. The new calibration noticeably improves the fit for stars with $-0.3 < [\text{Fe}/\text{H}] < +0.0$, however, both calibrations do a relatively poor job fitting the most metal-poor stars ($[\text{Fe}/\text{H}] < -0.5$) in the sample. Adding square terms improves the fit only negligibly ($\Delta R_{\text{ap}}^2 < 0.02$) and does not significantly improve the results for the most metal-poor stars. This, combined with our results from Section 4.6, suggests that fitting metal-poor stars requires a different set of lines, rather than simply higher order terms. Improvements may also be possible by deriving a separate calibration for $[\text{Fe}/\text{H}] < -0.5$, however, our sample has only 12 stars in this range, which is insufficient to derive a reliable calibration.

We also find a calibration for determining $[\text{M}/\text{H}]$ of the form:

$$\begin{aligned} [\text{M}/\text{H}] = & 0.16 \times \text{EW}_{Na} + 0.039 \times \text{EW}_{Ca} \\ & + 2.29 \times (\text{H}_2\text{O}-\text{K}) - 3.04 \end{aligned} \quad (4.32)$$

which gives $\text{RMSE} = 0.13$ and $R_{\text{ap}}^2 = 0.75$.

4.7.4 *H*-band Metallicities

In addition to refining the calibration of RA10, T12 derive metallicities from *H*-band spectra. The technique relies on the Ca and K lines in the *H*-band and a separate H₂O band defined for the *H*-band (H₂O-H). As we did with *K*-band metallicities in Section 4.7.3, we use our sample to test the quality of the T12 technique. As before, we follow their prescription, including using the same continuum regions to fit the continuum to a 4th order Legendre polynomial.

We find the T12 calibration gives $\text{RMSE} = 0.16$, and $R_{\text{ap}}^2 = 0.71$. As before, we improve this calibration, and find a best fit of the form:

$$\begin{aligned} [\text{Fe}/\text{H}] &= 0.55 \times \text{EW}_K + 0.32 \times \text{EW}_{Ca} \\ &\quad + 1.1 \times (\text{H}_2\text{O}-\text{H}) - 2.09, \end{aligned} \quad (4.33)$$

The new calibration gives an almost negligible improvement over T12; yielding $\text{RMSE} = 0.14$, and $R_{\text{ap}}^2 = 0.74$.

As with the K -band metallicities, adding square terms improves the fit negligibly (increase in $R_{\text{ap}}^2 < 0.01$), again suggesting that more lines are needed to fit the metal-poor stars.

Fitting these features to $[\text{M}/\text{H}]$ we find a best fit of the form:

$$\begin{aligned} [\text{M}/\text{H}] &= 0.41 \times \text{EW}_K + 0.24 \times \text{EW}_{Ca} \\ &\quad + 1.04 \times (\text{H}_2\text{O}-\text{H}) - 1.77, \end{aligned} \quad (4.34)$$

which gives $\text{RMSE} = 0.12$ and $R_{\text{ap}}^2 = 0.71$.

4.8 Summary and Discussion

We present our sample of 112 late-K and M dwarfs in wide binary systems which we use to locate the most metal-sensitive features and recalibrate existing methods to determine late K and M dwarf metallicities. We combine published metallicities of 62 of the primary stars with 50 from our own CFHT spectra. We use moderate-resolution visible and NIR spectra of the late K and M dwarfs to identify the largest possible set of metal-dependent spectral features in late K to mid M dwarfs for each of the JHK and visible wavelength bands. We utilize the metallicities of the primaries to calibrate these metal-dependent features and obtain optimal relationships to estimate metallicity in M dwarfs. Our sample covers a wide range of spectral types (from K5 to M6) and 1.5 dex in metallicity. This enables us to search for dependencies on spectral type, which was previously impossible with the relatively small samples used. We draw 5 important conclusions from our analysis:

1. It is possible to determine accurate ($\text{RMSE} < 0.1$ dex) metallicities for late-K to mid-M dwarfs using modest resolution spectra ($1000 < R < 2000$) from a variety of different wavelengths. Although features in the K -band perform best, metallicities can be estimated from spectra of any of the four wavelength regions.
2. Determining reliable metallicities at visible wavelengths requires different calibrations depending on the spectral type of the star. The results are most accurate for K5.5-M2 dwarfs, most likely because the atomic lines we use are less contaminated by molecular lines and the pseudo-continuum is easier to estimate for these dwarfs. It is not known if our calibrations are applicable for stars later than M6. This will be the subject of a future investigation on metallicities for late M and brown dwarfs.

3. Existing methods to determine metallicities using H - and K -band spectra (e.g. those from T12) work well for stars of near solar-metallicity, but have difficulties with most metal-poor stars in our sample ($[\text{Fe}/\text{H}] < -0.5$), even after applying our re-calibrations. Instead, determining metallicities for these stars requires the use of additional lines/features to improve the fit. This is most likely due to differences in $[\alpha/\text{Fe}]$, which are not being accurately captured by the K, Ca, and Na lines (Na and K are not α elements) used by R10 and T12.

4. We are approaching the limits of what is possible with moderate resolution spectra. There is a diminishing return on adding additional lines to a given fit after 3-4 features, even if there are many more metal-sensitive features present in a given wavelength range. Thus going to higher S/N or adding more wide binaries of near solar-metallicity is unlikely to improve the calibration. However, improvements could probably be made by including later spectral types (later than M5), getting more $[\text{M}/\text{H}]$ values, a larger number of more metal-poor stars ($[\text{Fe}/\text{H}] < -1.0$), or obtaining spectra with higher resolution.

5. Although the ζ parameter, commonly used to place stars into metallicity classes, correctly identifies metal-poor stars used in Woolf et al. (2009), classifications based on ζ incorrectly identify 12 of the 13 K/M companions with $[\text{Fe}/\text{H}] < -0.5$ as near solar-metallicity. This suggests that the ζ parameter is sensitive to stellar characteristics other than temperature and metallicity (e.g., activity, gravity, etc.), and may incorrectly identify some metal-poor stars as having near-solar abundances.

Our calibrations may be useful for both existing and future catalogs of M dwarf spectra. In particular, our calibration for visible wavelength spectra can be used on existing catalogs of local M dwarfs such as Lépine et al. (2013) to better probe the metallicity distribution of the local neighborhood especially since this sample is mostly early M-dwarfs, where our calibration performs best. Sloan Digital Sky Survey also has $\simeq 70,000$ visible wavelength spectra of M dwarfs (West et al. 2011; Bochanski et al. 2011) with similar resolution to our own, which could be used in conjunction with our calibrations to map out the metallicity distribution of the sample. Work has already been done in this area to confirm the existence of an ‘M dwarf problem’ (Woolf & West 2012), but this depends on less metallicities derived from ζ parameter.

Although our fits have better RMSE values for $[\text{M}/\text{H}]$ than they do for $[\text{Fe}/\text{H}]$, this does not necessarily mean those fits are superior. In fact, the R_{ap}^2 values for fits to $[\text{M}/\text{H}]$ are all inferior to those calibrations done on $[\text{Fe}/\text{H}]$. The reason is that the distribution of values for $[\text{Fe}/\text{H}]$ is not the same as it is for $[\text{M}/\text{H}]$. Some of the most metal-poor stars do not have $[\text{M}/\text{H}]$ values, and those that do generally have higher $[\text{M}/\text{H}]$ values due to large differences in α abundance (as determined for the primary star).

We confirm the claim of Johnson et al. (2012), that one can get approximate M dwarf metallicities using $J - K$ versus $V - K$ colors. However, the technique has a limited range of metallicities ($-0.4 < [\text{Fe}/\text{H}] < +0.2$) and is only accurate to $\simeq 0.2$ dex. Thus this technique is probably best used in special applications, such as biasing a planet-search towards metal-rich M dwarfs.

One possible explanation for the poor performance of ζ on our sample compared to that of Woolf et al. (2009) is the presence of unresolved binaries. It is likely that most wide binaries form as higher order systems (Kouwenhoven et al. 2010). Thus many of our wide pairs may include unresolved M+M dwarf pairs. There is evidence of radius inflation in low-mass eclipsing binary systems (López-Morales 2007; Irwin et al. 2011; Kraus et al. 2011) and may also be cooler than their single star counterparts (Boyajian et al. 2012). Further, atmospheric models indicate that the TiO₅ and CaH₂/CaH₃ indices, on which ζ is based, are sensitive to temperature and gravity (Jao et al. 2008; Allard et al. 2011). However, none of our most metal-poor companions show H- α emission, whereas radius inflation in tight binaries is usually associated with high chromospheric activity (López-Morales 2007; Kraus et al. 2011; Stassun et al. 2012). Additional metallicities of M-dwarf with known multiplicity (e.g., low-mass eclipsing binaries and spectroscopic binaries) are needed to confirm if this is the source of the discrepancy.

Another complication is the possibility of having false binaries (chance alignments) in our sample. We can estimate the number of interlopers by cross referencing our sample with that of Tokovinin & Lépine (2012). Tokovinin & Lépine (2012) calculate the probability that stars with commiserate proper motions are actually physically associated with each other (P_{phys}). Although Tokovinin & Lépine (2012) caution that their probabilities are purely based on models (and therefore only approximate), the numbers can be used to give a rough estimate of contamination from chance alignments. By summing up P_{phys} values for all of our binaries included in the Tokovinin & Lépine (2012) sample we find that $> 90\%$ of our binaries are physically associated with each other. However, some of the pairs with low P_{phys} values have parallax information for both the primary and companion that are consistent with each other. If we assume pairs with consistent parallaxes have $P_{\text{phys}} = 1$ and repeat our calculation, we find that 94% of our binaries are physically associated with each other. Although our metal-poor stars ($[\text{Fe}/\text{H}] < -0.5$) tend to be more distant, and therefore only 3 of the 13 are listed in Tokovinin & Lépine (2012), two of them have $P_{\text{phys}} > 93\%$ (the other has $P_{\text{phys}} = 72\%$). Three more of our $[\text{Fe}/\text{H}] < -0.5$ stars have parallaxes that are consistent with the primary to 1σ , indicating that even our metal-poor stars are almost all physical pairs.

We do not claim to have identified every single metal-sensitive feature at the resolution of our spectra, however, the nature of our analysis means that it is unlikely that we missed any of the most useful ones. We perform a rough test on our recovery rate by introducing artificial metal-sensitive lines of various usefulness and repeating our analysis. Specifically, we select a sample of the most metal-sensitive features (those used in Equations (8)-(17)) and insert them elsewhere in the spectrum of the stars. When moving features from NIR to visible wavelengths we convolve the lines with a Gaussian profile to reduce the resolution of the feature (features moved into the NIR are not changed). We then repeat our analysis as described in Section 4.5. We find that metal-sensitive features are sometimes not identified when they are placed on very strong telluric features, blueward of $0.4 \mu\text{m}$ (where the S/N is very low), or when they overlap with other strong features (e.g., the Mg Ib line) that make clean measurements difficult. We also note that features identified as metal-sensitive in the NIR appear less metal-sensitive (although they are still identified) when placed in visible wavelengths; this is likely due to the lower resolution and/or difficulties measuring features that are convolved with strong molecular lines in the visible. In spite of these exceptions,

we still recover $> 88\%$ of the lines on average, and $> 93\%$ when we exclude telluric regions and low S/N regions of the spectrum. This indicates that our analysis is quite robust, and that expanding on our findings will require observations later-type stars (past M5), more metal-poor stars, or higher resolution visible spectra.

References

- Aldering, G., Antilogus, P., Bailey, S., Baltay, C., Bauer, A., Blanc, N., Bongard, S., Copin, Y., Gangler, E., Gilles, S., Kessler, R., Kocevski, D., Lee, B. C., Loken, S., Nugent, P., Pain, R., Pécontal, E., Pereira, R., Perlmutter, S., Rabinowitz, D., Rigaudier, G., Scalzo, R., Smadja, G., Thomas, R. C., Wang, L., Weaver, B. A., & Nearby Supernova Factory. 2006, *ApJ*, 650, 510
- Allard, F., Homeier, D., & Freytag, B. 2011, in Astronomical Society of the Pacific Conference Series, Vol. 448, 16th Cambridge Workshop on Cool Stars, Stellar Systems, and the Sun, ed. C. Johns-Krull, M. K. Browning, & A. A. West, 91
- Apps, K., Clubb, K. I., Fischer, D. A., Gaidos, E., Howard, A., Johnson, J. A., Marcy, G. W., Isaacson, H., Giguere, M. J., Valenti, J. A., Rodriguez, V., Chubak, C., & Lepine, S. 2010, *PASP*, 122, 156
- Bacon, R., Copin, Y., Monnet, G., Miller, B. W., Allington-Smith, J. R., Bureau, M., Carollo, C. M., Davies, R. L., Emsellem, E., Kuntschner, H., Peletier, R. F., Verolme, E. K., & de Zeeuw, P. T. 2001, *MNRAS*, 326, 23
- Batalha, N. M., Rowe, J. F., Bryson, S. T., Barclay, T., Burke, C. J., Caldwell, D. A., Christiansen, J. L., Mullally, F., Thompson, S. E., Brown, T. M., Dupree, A. K., Fabrycky, D. C., Ford, E. B., Fortney, J. J., Gilliland, R. L., Isaacson, H., Latham, D. W., Marcy, G. W., Quinn, S. N., Ragozzine, D., Shporer, A., Borucki, W. J., Ciardi, D. R., Gautier, III, T. N., Haas, M. R., Jenkins, J. M., Koch, D. G., Lissauer, J. J., Rapin, W., Basri, G. S., Boss, A. P., Buchhave, L. A., Carter, J. A., Charbonneau, D., Christensen-Dalsgaard, J., Clarke, B. D., Cochran, W. D., Demory, B.-O., Desert, J.-M., Devore, E., Doyle, L. R., Esquerdo, G. A., Everett, M., Fressin, F., Geary, J. C., Girouard, F. R., Gould, A., Hall, J. R., Holman, M. J., Howard, A. W., Howell, S. B., Ibrahim, K. A., Kinemuchi, K., Kjeldsen, H., Klaus, T. C., Li, J., Lucas, P. W., Meibom, S., Morris, R. L., Prša, A., Quintana, E., Sanderfer, D. T., Sasselov, D., Seader, S. E., Smith, J. C., Steffen, J. H., Still, M., Stumpe, M. C., Tarter, J. C., Tenenbaum, P., Torres, G., Twicken, J. D., Uddin, K., Van Cleve, J., Walkowicz, L., & Welsh, W. F. 2013, *ApJS*, 204, 24
- Bean, J. L., Sneden, C., Hauschildt, P. H., Johns-Krull, C. M., & Benedict, G. F. 2006, *ApJ*, 652, 1604
- Bochanski, J. J., Hawley, S. L., & West, A. A. 2011, *AJ*, 141, 98

- Bochanski, J. J., West, A. A., Hawley, S. L., & Covey, K. R. 2007, AJ, 133, 531
- Bonfils, X., Delfosse, X., Udry, S., Santos, N. C., Forveille, T., & Ségransan, D. 2005, A&A, 442, 635
- Borucki, W. J., Koch, D., Basri, G., Batalha, N., Brown, T., Caldwell, D., Caldwell, J., Christensen-Dalsgaard, J., Cochran, W. D., DeVore, E., Dunham, E. W., Dupree, A. K., Gautier, T. N., Geary, J. C., Gilliland, R., Gould, A., Howell, S. B., Jenkins, J. M., Kondo, Y., Latham, D. W., Marcy, G. W., Meibom, S., Kjeldsen, H., Lissauer, J. J., Monet, D. G., Morrison, D., Sasselov, D., Tarter, J., Boss, A., Brownlee, D., Owen, T., Buzasi, D., Charbonneau, D., Doyle, L., Fortney, J., Ford, E. B., Holman, M. J., Seager, S., Steffen, J. H., Welsh, W. F., Rowe, J., Anderson, H., Buchhave, L., Ciardi, D., Walkowicz, L., Sherry, W., Horch, E., Isaacson, H., Everett, M. E., Fischer, D., Torres, G., Johnson, J. A., Endl, M., MacQueen, P., Bryson, S. T., Dotson, J., Haas, M., Kolodziejczak, J., Van Cleve, J., Chandrasekaran, H., Twicken, J. D., Quintana, E. V., Clarke, B. D., Allen, C., Li, J., Wu, H., Tenenbaum, P., Verner, E., Bruhweiler, F., Barnes, J., & Prsa, A. 2010, Science, 327, 977
- Boyajian, T. S., von Braun, K., van Belle, G., McAlister, H. A., ten Brummelaar, T. A., Kane, S. R., Muirhead, P. S., Jones, J., White, R., Schaefer, G., Ciardi, D., Henry, T., López-Morales, M., Ridgway, S., Gies, D., Jao, W.-C., Rojas-Ayala, B., Parks, J. R., Sturmann, L., Sturmann, J., Turner, N. H., Farrington, C., Goldfinger, P. J., & Berger, D. H. 2012, ApJ, 757, 112
- Casagrande, L., Schönrich, R., Asplund, M., Cassisi, S., Ramírez, I., Meléndez, J., Bensby, T., & Feltzing, S. 2011, A&A, 530, A138
- Cayrel de Strobel, G., Soubiran, C., & Ralite, N. 2001, A&A, 373, 159
- Chanamé, J. & Gould, A. 2004, ApJ, 601, 289
- Charbonneau, D., Berta, Z. K., Irwin, J., Burke, C. J., Nutzman, P., Buchhave, L. A., Lovis, C., Bonfils, X., Latham, D. W., Udry, S., Murray-Clay, R. A., Holman, M. J., Falco, E. E., Winn, J. N., Queloz, D., Pepe, F., Mayor, M., Delfosse, X., & Forveille, T. 2009, Nature, 462, 891
- Ciddor, P. E. 1996, Appl. Opt., 35, 1566
- Covey, K. R., Ivezić, Ž., Schlegel, D., Finkbeiner, D., Padmanabhan, N., Lupton, R. H., Agüeros, M. A., Bochanski, J. J., Hawley, S. L., West, A. A., Seth, A., Kimball, A., Gogarten, S. M., Claire, M., Haggard, D., Kaib, N., Schneider, D. P., & Sesar, B. 2007, AJ, 134, 2398
- Covey, K. R., Lada, C. J., Román-Zúñiga, C., Muench, A. A., Forbrich, J., & Ascenso, J. 2010, ApJ, 722, 971
- Cushing, M. C., Rayner, J. T., & Vacca, W. D. 2005, ApJ, 623, 1115
- Cushing, M. C., Vacca, W. D., & Rayner, J. T. 2004, PASP, 116, 362

- da Silva, R., Milone, A. C., & Reddy, B. E. 2011, *A&A*, 526, A71
- Demarque, P., Woo, J.-H., Kim, Y.-C., & Yi, S. K. 2004, *ApJS*, 155, 667
- Demory, B.-O., Ségransan, D., Forveille, T., Queloz, D., Beuzit, J.-L., Delfosse, X., di Folco, E., Kervella, P., Le Bouquin, J.-B., Perrier, C., Benisty, M., Duvert, G., Hofmann, K.-H., Lopez, B., & Petrov, R. 2009, *A&A*, 505, 205
- Dhital, S., West, A. A., Stassun, K. G., & Bochanski, J. J. 2010, *AJ*, 139, 2566
- Dhital, S., West, A. A., Stassun, K. G., Bochanski, J. J., Massey, A. P., & Bastien, F. A. 2012, *AJ*, 143, 67
- Donati, J.-F. 2003, in *Astronomical Society of the Pacific Conference Series*, Vol. 307, *Astronomical Society of the Pacific Conference Series*, ed. J. Trujillo-Bueno & J. Sanchez Almeida, 41
- Donati, J.-F., Semel, M., Carter, B. D., Rees, D. E., & Collier Cameron, A. 1997, *MNRAS*, 291, 658
- Dotter, A., Chaboyer, B., Jevremović, D., Kostov, V., Baron, E., & Ferguson, J. W. 2008, *ApJS*, 178, 89
- Ducati, J. R., Bevilacqua, C. M., Rembold, S. B., & Ribeiro, D. 2001, *ApJ*, 558, 309
- Fitzgerald, M. P. 1970, *A&A*, 4, 234
- Fuhrmann, K. 2008, *MNRAS*, 384, 173
- Gaidos, E., Haghhipour, N., Agol, E., Latham, D., Raymond, S., & Rayner, J. 2007, *Science*, 318, 210
- Gould, A. & Chanamé, J. 2004, *ApJS*, 150, 455
- Hauschildt, P. H., Allard, F., & Baron, E. 1999, *ApJ*, 512, 377
- Hawley, S. L., Covey, K. R., Knapp, G. R., Goliowski, D. A., Fan, X., Anderson, S. F., Gunn, J. E., Harris, H. C., Ivezić, Ž., Long, G. M., Lupton, R. H., McGehee, P. M., Narayanan, V., Peng, E., Schlegel, D., Schneider, D. P., Spahn, E. Y., Strauss, M. A., Szkody, P., Tsvetanov, Z., Walkowicz, L. M., Brinkmann, J., Harvanek, M., Hennessy, G. S., Kleinman, S. J., Krzesinski, J., Long, D., Neilsen, E. H., Newman, P. R., Nitta, A., Snedden, S. A., & York, D. G. 2002, *AJ*, 123, 3409
- Henry, T. J., Kirkpatrick, J. D., & Simons, D. A. 1994, *AJ*, 108, 1437
- Høg, E., Fabricius, C., Makarov, V. V., Urban, S., Corbin, T., Wycoff, G., Bastian, U., Schwerkendiek, P., & Wicenec, A. 2000, *A&A*, 355, L27
- Irwin, J. M., Quinn, S. N., Berta, Z. K., Latham, D. W., Torres, G., Burke, C. J., Charbonneau, D., Dittmann, J., Esquerdo, G. A., Stefanik, R. P., Oksanen, A., Buchhave, L. A., Nutzman, P., Berlind, P., Calkins, M. L., & Falco, E. E. 2011, *ApJ*, 742, 123

- Jao, W.-C., Henry, T. J., Beaulieu, T. D., & Subasavage, J. P. 2008, AJ, 136, 840
- Johnson, J. A., Aller, K. M., Howard, A. W., & Crepp, J. R. 2010, PASP, 122, 905
- Johnson, J. A. & Apps, K. 2009, ApJ, 699, 933
- Johnson, J. A., Gazak, J. Z., Apps, K., Muirhead, P. S., Crepp, J. R., Crossfield, I. J. M., Boyajian, T., von Braun, K., Rojas-Ayala, B., Howard, A. W., Covey, K. R., Schlawin, E., Hamren, K., Morton, T. D., Marcy, G. W., & Lloyd, J. P. 2012, AJ, 143, 111
- Kouwenhoven, M. B. N., Goodwin, S. P., Parker, R. J., Davies, M. B., Malmberg, D., & Kroupa, P. 2010, MNRAS, 404, 1835
- Kraus, A. L., Tucker, R. A., Thompson, M. I., Craine, E. R., & Hillenbrand, L. A. 2011, ApJ, 728, 48
- Lantz, B., Aldering, G., Antilogus, P., Bonnaud, C., Capoani, L., Castera, A., Copin, Y., Dubet, D., Gangler, E., Henault, F., Lemonnier, J.-P., Pain, R., Pecontal, A., Pecontal, E., & Smadja, G. 2004, in Society of Photo-Optical Instrumentation Engineers (SPIE) Conference Series, Vol. 5249, Society of Photo-Optical Instrumentation Engineers (SPIE) Conference Series, ed. L. Mazuray, P. J. Rogers, & R. Wartmann, 146–155
- Leggett, S. K. 1992, ApJS, 82, 351
- Lépine, S. & Bongiorno, B. 2007, AJ, 133, 889
- Lépine, S. & Gaidos, E. 2011, AJ, 142, 138
- Lépine, S., Hilton, E. J., Mann, A. W., Wilde, M., Rojas-Ayala, B., Cruz, K. L., & Gaidos, E. 2013, AJ, 145, 102
- Lépine, S., Rich, R. M., & Shara, M. M. 2007, ApJ, 669, 1235
- Lépine, S. & Shara, M. M. 2005, AJ, 129, 1483
- López-Morales, M. 2007, ApJ, 660, 732
- Luck, R. E. & Heiter, U. 2005, AJ, 129, 1063
- Mann, A. W., Gaidos, E., & Aldering, G. 2011, PASP, 123, 1273
- Mann, A. W., Gaidos, E., Lépine, S., & Hilton, E. J. 2012, ApJ, 753, 90
- Mishenina, T. V., Soubiran, C., Kovtyukh, V. V., & Korotin, S. A. 2004, A&A, 418, 551
- Mould, J. R. 1976, A&A, 48, 443
- Muirhead, P. S., Hamren, K., Schlawin, E., Rojas-Ayala, B., Covey, K. R., & Lloyd, J. P. 2012, ApJ, 750, L37
- Neves, V., Bonfils, X., Santos, N. C., Delfosse, X., Forveille, T., Allard, F., Natário, C., Fernandes, C. S., & Udry, S. 2012, A&A, 538, A25

- Oke, J. B. 1990, AJ, 99, 1621
- Önehag, A., Heiter, U., Gustafsson, B., Piskunov, N., Plez, B., & Reiners, A. 2012, A&A, 542, A33
- Ramírez, I., Allende Prieto, C., & Lambert, D. L. 2007, A&A, 465, 271
- Rayner, J. T., Cushing, M. C., & Vacca, W. D. 2009, ApJS, 185, 289
- Rayner, J. T., Toomey, D. W., Onaka, P. M., Denault, A. J., Stahlberger, W. E., Vacca, W. D., Cushing, M. C., & Wang, S. 2003, PASP, 115, 362
- Reid, I. N., Hawley, S. L., & Gizis, J. E. 1995, AJ, 110, 1838
- Robinson, S. E., Ammons, S. M., Kretke, K. A., Strader, J., Wertheimer, J. G., Fischer, D. A., & Laughlin, G. 2007, ApJS, 169, 430
- Roeser, S., Demleitner, M., & Schilbach, E. 2010, AJ, 139, 2440
- Rojas-Ayala, B., Covey, K. R., Muirhead, P. S., & Lloyd, J. P. 2010, ApJ, 720, L113
- . 2012, ApJ, 748, 93
- Santos, N. C., Israelian, G., & Mayor, M. 2004, A&A, 415, 1153
- Schlaufman, K. C. & Laughlin, G. 2010, A&A, 519, A105
- Sneden, C. A. 1973, PhD thesis, THE UNIVERSITY OF TEXAS AT AUSTIN.
- Sousa, S. G., Santos, N. C., Israelian, G., Mayor, M., & Udry, S. 2011, A&A, 533, A141
- Stassun, K. G., Kratter, K. M., Scholz, A., & Dupuy, T. J. 2012, ApJ, 756, 47
- Takeda, Y., Ohkubo, M., Sato, B., Kambe, E., & Sadakane, K. 2005, PASJ, 57, 27
- Terrien, R. C., Mahadevan, S., Bender, C. F., Deshpande, R., Ramsey, L. W., & Bochanski, J. J. 2012, ApJ, 747, L38
- Tokovinin, A. & Lépine, S. 2012, AJ, 144, 102
- Vacca, W. D., Cushing, M. C., & Rayner, J. T. 2003, PASP, 115, 389
- Valenti, J. A., Fischer, D., Marcy, G. W., Johnson, J. A., Henry, G. W., Wright, J. T., Howard, A. W., Giguere, M., & Isaacson, H. 2009, ApJ, 702, 989
- Valenti, J. A. & Fischer, D. A. 2005, ApJS, 159, 141
- Valenti, J. A. & Piskunov, N. 1996, A&AS, 118, 595
- van Leeuwen, F. 2007, A&A, 474, 653
- van Leeuwen, F. & Fantino, E. 2005, A&A, 439, 791
- VandenBerg, D. A. & Clem, J. L. 2003, AJ, 126, 778

- West, A. A., Morgan, D. P., Bochanski, J. J., Andersen, J. M., Bell, K. J., Kowalski, A. F., Davenport, J. R. A., Hawley, S. L., Schmidt, S. J., Bernat, D., Hilton, E. J., Muirhead, P., Covey, K. R., Rojas-Ayala, B., Schlawin, E., Gooding, M., Schluns, K., Dhital, S., Pineda, J. S., & Jones, D. O. 2011, AJ, 141, 97
- Woolf, V. M., Lépine, S., & Wallerstein, G. 2009, PASP, 121, 117
- Woolf, V. M. & Wallerstein, G. 2005, MNRAS, 356, 963
- . 2006, PASP, 118, 218
- Woolf, V. M. & West, A. A. 2012, MNRAS, 422, 1489

Chapter 5

Testing the Metal of Late-Type Kepler Planet Hosts with Iron-Clad Methods

Published as Mann, Andrew W.; Gaidos, Eric; Kraus, Adam; Hilton, Eric J.; 2013, ApJ, 770, 43

Abstract

It has been shown that F, G, and early K dwarf hosts of Neptune-sized planets are not preferentially metal-rich. However, it is less clear whether the same holds for late K and M dwarf planet hosts. We report metallicities of *Kepler* targets and candidate transiting planet hosts with effective temperatures below 4500 K. We use new metallicity calibrations to determine [Fe/H] from visible and near-infrared spectra. We find that the metallicity distribution of late K and M dwarfs monitored by *Kepler* is consistent with that of the solar neighborhood. Further, we show that hosts of Earth- to Neptune-sized planets have metallicities consistent with those lacking detected planets and rule out a previously claimed 0.2 dex offset between the two distributions at 6σ confidence. We also demonstrate that the metallicities of late K and M dwarfs hosting multiple detected planets are consistent with those lacking detected planets. Our results indicate that multiple terrestrial and Neptune-sized planets can form around late K and M dwarfs with metallicities as low as 0.25 of the solar value. The presence of Neptune-sized planets orbiting such low-metallicity M dwarfs suggests that accreting planets collect most or all of the solids from the disk and that the potential cores of giant planets can readily form around M dwarfs. The paucity of giant planets around M dwarfs compared to solar-type stars must be due to relatively rapid disk evaporation or a slower rate of core accretion, rather than insufficient solids to form a core.

5.1 Introduction

The NASA *Kepler* mission (Borucki et al. 2010) has discovered more than 2000 exoplanet candidates (also called *Kepler* Objects of Interest or KOIs, Batalha et al. 2013), enabling the study of exoplanet statistics based on large data sets. Among other science results, *Kepler* data has been used to estimate planet occurrence (e.g., Howard et al. 2012; Fressin et al. 2013), constrain the distribution of planet densities (Gaidos et al. 2012; Wolfgang & Laughlin 2012), study the architecture of multi-planet systems (Fabrycky et al. 2012), and

search for correlations (or non-correlations) between the radius of planets and the metallicity of their host stars for F, G, and early K dwarfs (Buchhave et al. 2012).

It is well established that the presence of Jovian planets is correlated with the metallicity of the host star (Gonzalez 1997; Santos et al. 2001; Fischer & Valenti 2005). This is generally interpreted as supporting the core accretion mechanism for giant planet formation; metal-rich stars are assumed to have had metal-rich disks in which the higher density of solids allowed faster core accretion and the formation of giant planets before the disks dissipated. Buchhave et al. (2012) showed that Earth- to Neptune-sized planets are present around FGK dwarfs spanning a range of metallicities ($-0.6 < [\text{Fe}/\text{H}] < +0.5$). However, Buchhave et al. (2012) did not measure the metallicity of a control sample of *Kepler* field stars. If *Kepler* is biased towards more metal-poor stars (compared to the solar neighborhood), the stars hosting Neptune-sized planets investigated by Buchhave et al. (2012) could be more metal-rich than non-hosts. Further, the Buchhave et al. (2012) sample contains no stars with $T_{\text{eff}} < 4500$ K, and cannot draw conclusions about the role of metallicity on the frequency of Neptune-sized planets around late K and M dwarfs.

Laughlin et al. (2004) and Adams et al. (2005) argued that the core-accretion model of planet formation predicts that late K and M dwarfs have significantly fewer giant planets than their solar-type counterparts. Disks around M dwarfs have longer dynamical (orbital) times (resulting in slower planet growth, Pollack et al. 1996), lower surface densities (Hartmann et al. 1998; Scholz et al. 2006), and less total disk mass (Williams & Cieza 2011) than those around their solar-mass counterparts. Laughlin et al. (2004) and Adams et al. (2005) predicted that although M dwarfs should have fewer giant planets, Neptune-like objects and terrestrial-type planets should be common around such stars.

There are theoretical reasons to suspect the presence of Neptunes around M dwarfs should be correlated with stellar metallicity, even if this is not the case for FGK dwarfs. Numerical simulations indicate that the initial surface density of solids in a disk (for which stellar metallicity is a proxy) controls the mass and number of planets. Kokubo et al. (2006) found that the mass of the largest and second largest planet in a planetary system should scale almost linearly with the disk surface density and that the total number of planets decreases with surface density, even in the absence of giant planets. Because the surface density of solids in a planet-forming disk should scale with the metallicity, their results suggest that metal-rich systems host larger (non-Jovian) but fewer planets. Since the disk mass scales roughly linearly with the stellar mass (although with considerable scatter; Williams & Cieza 2011), it is possible that even metal-poor FGK dwarf disks have sufficient solid material to produce Neptune sized planets, as was found observationally (Sousa et al. 2008; Buchhave et al. 2012). Schlaufman & Laughlin (2010) asserted that because of the smaller disk mass around late K and M dwarfs, metallicity is more critical for the formation of Neptunes around these stars. They claimed this requirement should manifest itself as a correlation between the presence of Neptune-sized planets and the metallicity of late K or M dwarfs.

Indeed, Schlaufman & Laughlin (2011) found that late K and M dwarfs hosting super-Earth- to Neptune-sized transiting planet candidates from *Kepler* have redder $g - r$ (for a fixed $J - H$) color than those with no detected transit. Based on a comparison between two open stellar clusters with different metallicities, Schlaufman & Laughlin (2011) claimed

that the $g - r$ color offset is due to a difference in metallicity of $\simeq 0.2$ dex, in agreement with the theoretical case laid out in Schlaufman & Laughlin (2010).

Complicating the issue, the clusters used by Schlaufman & Laughlin (2011) to calibrate their color-metallicity relation contain very few late K and M stars. West et al. (2004) and Bochanski et al. (2013) found that the metallicity dependence of $g - r$ reverses sign at late K/early M spectral types, and that cooler stars have *bluer* $g - r$ colors if they are more metal rich. Mann et al. (2012) explained that the origin of the $g - r$ color difference between the KOI and non-KOI sample observed by Schlaufman & Laughlin (2011) is an artifact of giant star contamination in their non-KOI sample. But the question of whether KOI M dwarfs are more metal-rich than non-KOIs remains open.

Compared to solar-type stars, M dwarf metallicities are difficult to determine, primarily due to the presence of complex molecular lines in their visible spectra, which result in line confusion and a lack of identifiable continuum, and do not always match with current M dwarf models (Allard et al. 2011). Previous techniques to determine M dwarf metallicities using color-magnitude diagrams (Johnson & Apps 2009; Schlaufman & Laughlin 2010) require astrometric parallaxes, which are largely unavailable for *Kepler* targets. Visible-light spectroscopic techniques were developed (e.g., the ζ index, Lépine et al. 2007; Dhital et al. 2012), and are a reliable indicator of whether an M dwarf is a sub-dwarf or ultra sub-dwarf. However, ζ saturates near solar metallicity (Woolf et al. 2009; Mann et al. 2013), making it unreliable for measuring metallicities higher than that of the Sun. Rojas-Ayala et al. (2010) and Terrien et al. (2012) demonstrated that atomic lines in the K - and H -bands (respectively) can be used to estimate metallicities for M dwarfs. They calibrated their methods using ~ 20 wide binaries, but their samples were restricted in both spectral type (M0-M4), and metallicity ($-0.5 < [\text{Fe}/\text{H}] < +0.4$). Recently, Mann et al. (2013) (henceforth M13) used 110 wide binaries spanning K5 to M6, and $-1.04 < [\text{Fe}/\text{H}] < +0.56$, and derive improved calibrations to determine metallicities using visible, J -, H -, or K -band spectra.

Using the techniques of Rojas-Ayala et al. (2012), Muirhead et al. (2012a) estimated metallicities for late K and M planet candidate hosts. Muirhead et al. (2012a) found that late K and M KOIs' metallicities are consistent with the solar neighborhood ($\simeq -0.10$, Casagrande et al. 2008), but did not measure the metallicity of the overall field for comparison. Dressing & Charbonneau (2013) fitted *grizJHK* colors from the Kepler Input Catalog (KIC, Batalha et al. 2010; Brown et al. 2011) to the stellar models of Dotter et al. (2008) to determine R_* , M_* , T_{eff} , and $[\text{Fe}/\text{H}]$ for M dwarf *Kepler* targets. However, the colors of late K and early-M dwarfs are usually not reliable indicators of metallicity (Lépine et al. 2013; Mann et al. 2013), and metallicities from Dressing & Charbonneau (2013) show weak or no significant correlation with those from Muirhead et al. (2012a).

In this paper we investigate whether the size and multiplicity of planets around late-type dwarfs depend on the metallicity of the host star. In Section 5.2 we describe our sample of planet candidate hosts and our comparison sample of dwarfs with no detected transit. In Section 5.3 we detail our visible and near-infrared observations of *Kepler* stars. We derive a new calibration in Section 5.4 to determine $[\text{Fe}/\text{H}]$ from visible wavelength spectra. We then apply this calibration, and others from M13, to calculate the $[\text{Fe}/\text{H}]$ of the KOI and non-KOI samples. In Section 5.5 we report the metallicity distributions of late K and M dwarf hosts of Earth-, Neptune-, and Jovian-sized planets, hosts of multiple

detected planets, and dwarfs with no detected transits. In Section 5.6 we conclude with a brief discussion of possible complications and the consequences of our findings.

5.2 Sample

5.2.1 KOI Sample

We selected KOIs from Batalha et al. (2013) with $K_P - J > 1.85$, where K_P is the magnitude in the *Kepler* bandpass, and J is from the Two Micron All Sky Survey (2MASS, Skrutskie et al. 2006). This sample includes all dwarfs with $T_{eff} < 4100$ K and some as warm as 4500 K (Mann et al. 2012). We excluded four KOIs that are probably false positives. KOI-977 is a giant star (Muirhead et al. 2012a). KOI-1902 has a V-like transit shape, and flux variations indicative of an eclipsing binary. In the latest planet candidate release, KOI-1164 has been added to the false positive list¹. The light curve of KOI-256 shows no limb-darkening, which is indicative of a stellar eclipse, rather than a planetary transit. As a test, we obtained two spectra of KOI-256 6h apart (see Section 5.3 for a description of observations). The spectra show a radial velocity difference of $> 100 \text{ km s}^{-1}$, suggesting that the transit is an eclipsing white dwarf-M dwarf binary, later confirmed by Muirhead et al. (2013). The remaining sample of KOIs contains 157 planet candidates orbiting 106 dwarfs.

5.2.2 *Kepler* Non-KOI Sample

Mann et al. (2012) show that $> 90\%$ of the bright ($K_P < 14$), and $\simeq 7\%$ of the faint ($K_P > 14$), late K and M ($K_P - J > 2.0$) *Kepler* targets are giant stars. *JHK* colors are sometimes used to identify giant stars (e.g., Lépine & Gaidos 2011), however, these colors are known to be metal-sensitive (Leggett 1992; Muirhead et al. 2012b), and the giant and dwarf branches overlap in *JHK* color space for K type stars (Bessell & Brett 1988). Instead, we screen out giants stars using their reduced proper motion, defined as:

$$H_J = J + 5 \log \mu + 5, \quad (5.1)$$

where μ is the total proper motion in arcseconds yr $^{-1}$ and the J magnitude is taken from 2MASS.

We computed proper motions for each *Kepler* target star using all available astrometry from the USNO-B1.0 (Monet et al. 2003), 2MASS (Skrutskie et al. 2006), and SDSS (Ahn et al. 2012) catalogs, using the algorithm described in Kraus & Hillenbrand (2007). We obtained the astrometry for each star from the Vizier archive using the IDL routine queryvizier.pro (Landsman 1993), and then combined the astrometry epochs from all surveys using a weighted least-squares fit. Our algorithm tested the goodness of each fit for each proper motion and rejected all astrometry outliers at $> 3\sigma$. Most of these outliers were found in the photographic survey data, not in 2MASS or SDSS, due to the heavy weight assigned to the modern CCD-based epochs. The resulting catalog has proper

¹<http://exoplanetarchive.ipac.caltech.edu/>

motion uncertainties a factor of ~ 2 smaller than those from USNO-B alone (~ 3 mas yr^{-1} vs. 6–7 mas yr^{-1}).

For bright ($R \lesssim 12$) stars, many of which are saturated in one or more of the above surveys, we adopted proper motions from the Third USNO CCD Astrograph Catalog (UCAC3, Zacharias et al. 2010). UCAC3 extends to $R = 16$, though the proper motion errors become quite large at $R > 13\text{--}14$. The typical errors in the UCAC3 proper motions are $\sim 1\text{--}3$ mas yr^{-1} for stars as faint as $R \simeq 12$ and ~ 6 mas yr^{-1} for those as faint as $R \simeq 16$.

We use stars with known luminosity class from Mann et al. (2012) to test possible reduced proper motion cuts. Figure 5.1 shows the reduced proper motions for the giant and dwarf samples, excluding those stars for which the errors in total proper motion are > 25 mas yr^{-1} and those that had potential contamination from a nearby star. A proper motion cut of $H_J > 7.5$ excludes only 1 dwarf (of 52) in the sample, and includes only 3 giant stars (of 278).

To establish the metallicity of *Kepler* target late K and M dwarfs, we randomly selected 100 stars observed by *Kepler* in Quarters 1 through 8 that have no detected planets (non-KOIs) for NIR spectroscopy with the criteria $K_P - J > 1.85$ and $H_J > 7.5$ (see Section 5.3 for a description of the observations). Spectra of three of these 100 contain strong CO features at ~ 2.35 μm indicative of giant stars (Cushing et al. 2005; Rayner et al. 2009), and were excluded from our analysis.

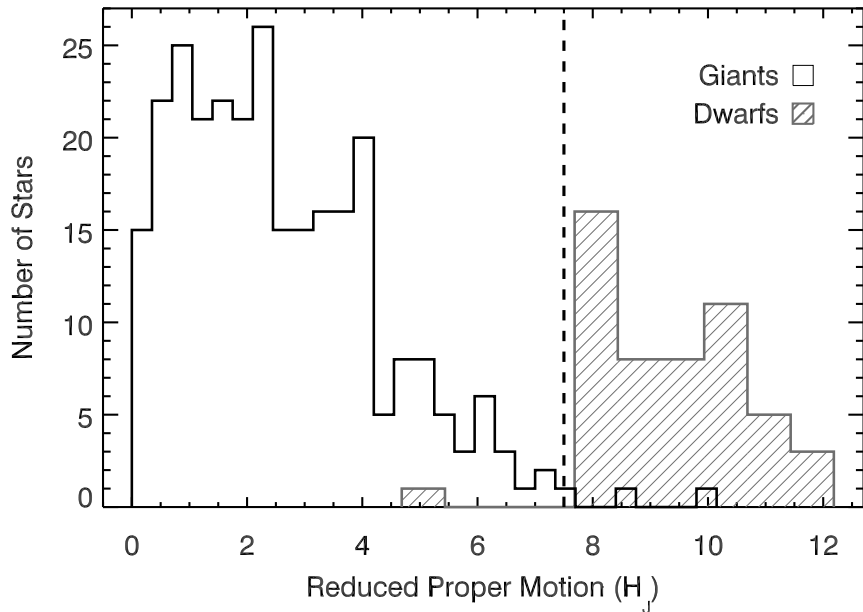


Figure 5.1: Distribution of reduced proper motions for spectroscopically confirmed late K and M giants (black) and dwarfs (grey, hashed) from Mann et al. (2012). Stars with questionable proper motions (error in proper motion > 25 mas yr^{-1}) were excluded. We utilized a reduced proper motion cut of $H_J > 7.5$ (shown as a vertical dashed line) to remove interloping giant stars from our non-KOI sample.

5.3 Observations And Reduction

Spectra of KOIs were obtained with the SuperNova Integral Field Spectrograph (SNIFS, Lantz et al. 2004) on the University of Hawaii 2.2m telescope atop Mauna Kea. SNIFS covers 3200 Å to 9700 Å at a resolution of $1000 < R < 1300$. Signal-to-noise ratio (S/N) was > 80 redward of 6000 Å for each target. The SNIFS processing pipeline (Bacon et al. 2001) automatically performed basic data reduction. This included dark, bias, and flat-field corrections, removing of bad pixels and cosmic rays, and sky subtraction. The SNIFS pipeline used arcs taken at the same position as the target to wavelength-calibrate the data. Spectrophotometric standards from Oke (1990), taken over the course of each night, were used in conjunction with a model of the atmosphere above Mauna Kea (Buton et al. 2013) to correct for instrument response and atmospheric extinction. We shifted the spectra in wavelength to the rest frames of their emitting star by cross correlating them with a similar spectral type template from the Sloan Digital Sky Survey (Bochanski et al. 2007).

We obtained near-IR spectra of the 100 non-KOI targets using the SpeX spectrograph (Rayner et al. 2003) attached to the NASA Infrared Telescope Facility (IRTF) on Mauna Kea. SpeX observations were taken in the short cross-dispersed mode using the 0.3'' slit, which yielded a resolution of $R \simeq 2000$ from 0.8 to 2.4 μ m. S/N in the H - and K -bands was typically > 80 . To correct for telluric lines, we observed an A0V-type star within 30 minutes of time and 0.1 airmass of the target observation. To remove effects from large telescope slews, we obtained flat-field and argon lamp calibration sequences after each A0V star. Spectra were extracted and reduced using the SpeXTool package, which performed flat-field correction, wavelength calibration, and sky subtraction (Cushing et al. 2004). Telluric corrections were computed from each A0V star using the *xteLLcor* package (Vacca et al. 2003), and then applied to the relevant target spectra. We then placed each spectrum in the star's rest frame by cross-correlating it to a spectrum of a template star (of a similar spectral type) from the IRTF spectral library (Cushing et al. 2005; Rayner et al. 2009).

5.4 Determination of [Fe/H] and R_*

M13 provide empirical calibrations for calculating [Fe/H] from indices in visible, J -, H -, or K - band spectra of late K and M dwarfs. However, M13 have higher S/N observations ($S/N \simeq 150$) than those obtained for the much fainter targets observed in this program. As a result, when we applied the calibrations from M13 on features blueward of 6000 Å (NIR calibrations are less affected) the resulting errors were large ($\gtrsim 0.1$ dex) from measurement noise alone.

To mitigate S/N errors, we took the calibrator (wide binary) sample of M13 and repeated their process of defining a visible wavelength metallicity calibration. However, we restricted ourselves to indices redward of 6000 Å where the S/N of our observations is the highest. We then derived the following calibration:

$$\begin{aligned} [\text{Fe}/\text{H}] = & 0.68F1 + 0.53F2 - 0.32F3 \\ & - 1.0\text{Color1} - 0.26, \end{aligned} \quad (5.2)$$

where Color1 is a temperature sensitive index from Hawley et al. (2002), and F1, F2, and F3 correspond to the equivalent widths of features at 8191-8225 Å, 8860-8880 Å, and 9179-9199 Å, respectively². We used the pseudo-continuum regions defined in M13. Figure 5.2 shows the primary star metallicity as a function of the K/M dwarf metallicity derived from Equation 5.2. Equation 5.2 has a root mean square error (RMSE) of 0.08 dex, and an adjusted square of the multiple correlation coefficient (R_{ap}^2) of 0.82, indicating it is roughly as reliable as the corresponding calibration from M13 (RMSE=0.07 and $R_{\text{ap}}^2=0.84$).

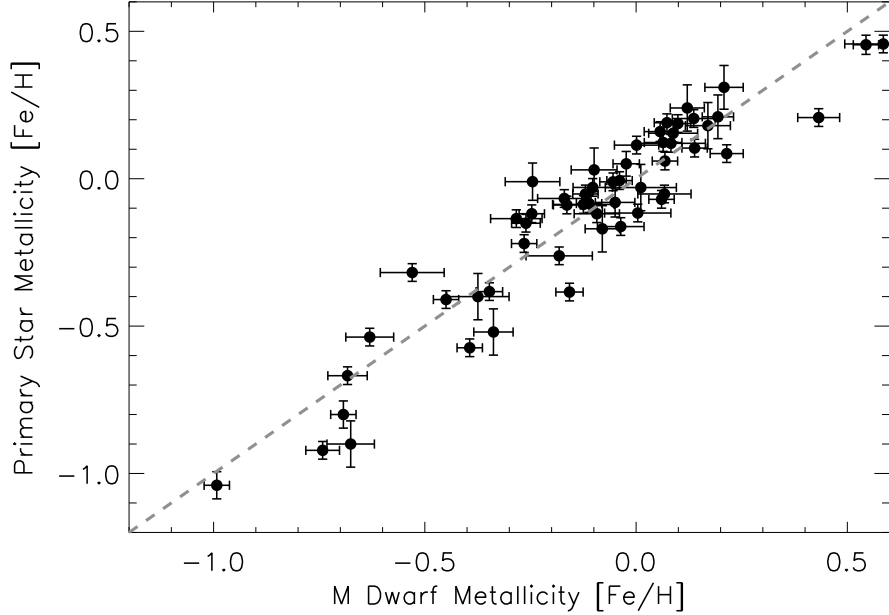


Figure 5.2: Metallicity of the primary (FGK) dwarf from M13 vs. metallicity for the late K or M dwarf companion derived using Equation 5.2. The dashed line indicates equality. The binary sample covers the full range of metallicities and spectral types in our KOI and non-KOI sample.

Metallicities of the non-KOI sample were calculated as the weighted means of the J -, H -, and K -band calibrations outlined in M13. Weights were based on the measurement errors in each band added in quadrature with the errors from each calibration (e.g., the J -band calibration has a significantly higher RMSE than the H - and K -band calibrations).

Using metallicities from two different sources (visible and NIR) engenders the risk of systematic differences. However, the empirical relations we utilized are calibrated using an identical set of wide binaries. As a check, we selected a sample of 55 late K to mid-M dwarfs from Lépine et al. (2013) that have both visible wavelength spectra from SNIFS and NIR spectra from SpeX. The scatter between [Fe/H] values derived using visible and NIR spectra are consistent with combined measurement and calibration errors for these two techniques ($\sigma = 0.14$ dex). More importantly, there is no significant offset between metallicities derived from the two methods (median difference in metallicity is 0.01 ± 0.02 dex).

²Note: all wavelengths in this work are reported in vacuum

We compare our metallicities of our KOI sample with values from Muirhead et al. (2012a) in Figure 5.3a. Our metallicities are consistent with their's for stars with $[\text{Fe}/\text{H}] > -0.3$. However, for more metal-poor stars, metallicities from our analysis are systematically lower and the scatter between metallicity estimates is higher. Note that we report $[\text{Fe}/\text{H}]$ values while Muirhead et al. (2012a) uses $[\text{M}/\text{H}]$. Increasing $[\alpha/\text{Fe}]$ with decreasing $[\text{Fe}/\text{H}]$ may, in part, explain this discrepancy. The calibrator (wide binary) sample of Rojas-Ayala et al. (2012), on which Muirhead et al. (2012a) is based, has a paucity of stars with $[\text{Fe}/\text{H}] < -0.5$. The result is that their calibration assigns metallicities that are systematically too high for stars with $[\text{Fe}/\text{H}] < -0.4$. As can be seen in Figure 5.2, our calibration performs well for dwarfs even with $[\text{Fe}/\text{H}] < -0.5$.

Table 5.1. KOI Stellar Parameters

KOI	<i>Kepler</i> ID	[Fe/H]	$\sigma_{\text{[Fe/H]}}$	R_* R_\odot	σ_{R_*} R_\odot
227	6185476	-0.21	0.08	0.60	0.03
247	11852982	+0.11	0.08	0.53	0.04
248 ^a	5364071	+0.13	0.05	0.57	0.04
249	9390653	-0.30	0.08	0.37	0.06
250 ^a	9757613	-0.10	0.08	0.59	0.03
251 ^a	10489206	-0.03	0.08	0.48	0.05
252	11187837	-0.08	0.09	0.50	0.05
253	11752906	+0.41	0.07	0.55	0.04
254	5794240	+0.27	0.08	0.49	0.05
255	7021681	-0.23	0.09	0.55	0.04
314 ^a	7603200	-0.07	0.08	0.52	0.04
430	10717241	-0.12	0.09	0.64	0.03
463	8845205	-0.35	0.08	0.36	0.06
478	10990886	+0.20	0.08	0.48	0.05
503	5340644	-0.11	0.09	0.62	0.03
531	10395543	+0.09	0.08	0.61	0.03
571 ^a	8120608	-0.17	0.06	0.52	0.05
596	10388286	-0.04	0.08	0.43	0.05
610	5686174	-0.06	0.09	0.61	0.03
641	5131180	+0.29	0.09	0.62	0.03
663 ^a	6425957	-0.34	0.08	0.62	0.03
719	9950612	-0.27	0.05	0.69	0.03
736 ^a	10340423	-0.05	0.10	0.61	0.03
739	10386984	-0.09	0.05	0.57	0.04
775 ^a	11754553	+0.04	0.06	0.61	0.03
778	11853255	-0.33	0.08	0.61	0.03
781	11923270	-0.01	0.08	0.42	0.05
784 ^a	12066335	-0.24	0.07	0.60	0.03
812 ^a	4139816	-0.51	0.07	0.57	0.03
817 ^a	4725681	-0.01	0.07	0.49	0.04
818	4913852	+0.23	0.06	0.43	0.05
854	6435936	+0.21	0.06	0.44	0.06
868	6867155	+0.12	0.06	0.64	0.03
877 ^a	7287995	-0.05	0.08	0.64	0.03
886 ^a	7455287	-0.25	0.07	0.46	0.05
898 ^a	7870390	-0.20	0.07	0.58	0.03
899 ^a	7907423	-0.26	0.05	0.44	0.06
936 ^a	9388479	+0.10	0.08	0.45	0.05
940	9479273	-0.36	0.13	0.78	0.03
947	9710326	-0.17	0.08	0.48	0.05
952 ^a	9787239	-0.02	0.06	0.47	0.05
961 ^a	8561063	-0.52	0.09	0.14	0.04
1024	2715135	-0.06	0.06	0.64	0.03
1078 ^a	10166274	-0.06	0.09	0.56	0.04
1085	10118816	-0.38	0.09	0.53	0.04
1141	8346392	-0.14	0.07	0.58	0.03
1146	8351704	-0.41	0.05	0.49	0.05
1201	4061149	-0.45	0.09	0.42	0.05
1202	3444588	-0.03	0.10	0.60	0.03
1298	10604335	-0.21	0.10	0.62	0.03
1361	6960913	+0.10	0.07	0.64	0.03
1393	9202151	+0.14	0.06	0.49	0.05
1397	9427402	-0.30	0.06	0.55	0.04
1408	9150827	-0.12	0.06	0.60	0.03

Table 5.1—Continued

KOI	<i>Kepler</i> ID	[Fe/H]	$\sigma_{\text{[Fe/H]}}$	R_* R_\odot	σ_{R_*} R_\odot
1422 ^a	11497958	-0.16	0.07	0.41	0.05
1427	11129738	-0.26	0.08	0.60	0.03
1459	9761199	-0.03	0.08	0.57	0.04
1475 ^a	4770365	-0.19	0.09	0.62	0.03
1515 ^a	7871954	-0.62	0.09	0.58	0.03
1577	12506770	-0.23	0.13	0.63	0.03
1584	9941066	-0.06	0.06	0.61	0.03
1588	5617854	-0.30	0.09	0.61	0.03
1649	11337141	-0.44	0.09	0.46	0.05
1681	5531953	-0.45	0.07	0.45	0.05
1686	6149553	-0.19	0.05	0.33	0.06
1702	7304449	-0.16	0.06	0.30	0.05
1713 ^a	8230616	-0.32	0.08	0.63	0.03
1725	10905746	-0.30	0.08	0.42	0.06
1843 ^a	5080636	+0.25	0.09	0.44	0.04
1867 ^a	8167996	-0.03	0.08	0.51	0.04
1868	6773862	-0.35	0.08	0.57	0.04
1874 ^a	8978528	-0.43	0.06	0.61	0.03
1876	11622600	-0.44	0.09	0.65	0.03
1879	8367644	+0.15	0.09	0.51	0.05
1880	10332883	-0.05	0.09	0.52	0.04
1907	7094486	-0.11	0.09	0.55	0.03
1908 ^a	5706966	-0.20	0.05	0.64	0.03
2006	10525027	-0.36	0.08	0.51	0.04
2036 ^a	6382217	-0.04	0.07	0.53	0.03
2057	9573685	-0.07	0.06	0.53	0.04
2058	10329835	-0.09	0.09	0.52	0.04
2078	9351316	+0.03	0.07	0.63	0.03
2090	11348997	+0.08	0.09	0.42	0.06
2101	9411412	-0.13	0.07	0.64	0.03
2114	6921944	+0.37	0.10	0.64	0.03
2124	11462341	-0.19	0.08	0.61	0.03
2130	2161536	+0.02	0.12	0.57	0.03
2156	2556650	-0.59	0.07	0.47	0.05
2174 ^a	8261920	-0.01	0.08	0.63	0.03
2179 ^a	10670119	-0.11	0.06	0.42	0.06
2191	5601258	+0.06	0.06	0.46	0.05
2238	8229458	-0.29	0.09	0.51	0.04
2256	9112931	-0.46	0.06	0.62	0.03
2283	10206675	+0.09	0.08	0.60	0.03
2306	6666233	+0.62	0.08	0.49	0.04
2329	11192235	-0.22	0.11	0.52	0.04
2347	8235924	+0.05	0.08	0.58	0.04
2417	9654468	-0.13	0.07	0.69	0.03
2418	10027247	+0.16	0.08	0.39	0.05
2453	8631751	-0.48	0.07	0.44	0.06
2527	7879433	-0.22	0.09	0.64	0.03
2542	6183511	-0.15	0.06	0.34	0.06
2588	12156347	-0.15	0.12	0.61	0.03
2626	11768142	-0.43	0.08	0.42	0.05
2650 ^a	8890150	-0.08	0.06	0.54	0.04
2662	3426367	-0.15	0.09	0.35	0.06

^aMulti-planet candidate system as listed in the Batalha et al. (2013) catalog.

Table 5.2. non-KOI Stellar Parameters

<i>Kepler</i> ID	[Fe/H]	$\sigma_{\text{[Fe/H]}}$
1721911	+0.37	0.07
1996399	+0.07	0.06
2010738	+0.21	0.12
2850521	-0.68	0.11
3233853	-0.01	0.05
3342894	+0.17	0.09
3533220	-0.19	0.06
3935942	+0.04	0.05
4543236	-0.19	0.06
4543619	-0.55	0.12
4553205	+0.08	0.05
4682420	-0.39	0.12
5000970	-0.26	0.07
5165017	-0.02	0.06
5252367	-0.18	0.13
5513769	-0.05	0.09
5779809	-0.26	0.10
6021570	-0.02	0.12
6037009	-0.10	0.11
6102385	-0.59	0.13
6110166	-0.09	0.05
6153404	-0.03	0.09
6470362	-0.41	0.06
6592335	-0.03	0.13
6600771	+0.16	0.15
6946682	-0.25	0.13
7813530	-0.47	0.07
7908791	-0.29	0.09
8153154	-0.17	0.07
8174116	+0.12	0.11
8233490	-0.22	0.09
8297307	-0.42	0.08
8552739	+0.05	0.06
8941398	-0.07	0.05
9012329	+0.18	0.10
9032388	-0.08	0.11
9388780	-0.15	0.13
9391356	-0.05	0.10
9945070	-0.36	0.07
10195818	-0.15	0.05
10200508	+0.42	0.13
10334540	-0.11	0.12
10529055	-0.02	0.05
10579570	-0.07	0.13
10713157	+0.02	0.06
10713284	+0.16	0.07
11018954	-0.02	0.06
11026972	-0.88	0.10
11122711	-0.68	0.13
11124523	-0.17	0.06
11229244	-0.10	0.12
11240969	-0.44	0.05
11441938	+0.11	0.10
11450068	-0.10	0.05

In Figure 5.3b we compare metallicities from Dressing & Charbonneau (2013) with ours for all overlapping (KOI and non-KOI) targets. Dressing & Charbonneau (2013) [Fe/H] values are inconsistent with (reduced $\chi^2 > 3$), and show no correlation with our values. Dressing & Charbonneau (2013) themselves note significant disagreement with their metallicities and those reported in Muirhead et al. (2012a), highlighting the difficulties of estimating M dwarf metallicities from photometry and stellar models alone.

We calculated stellar radii using the $T_{\text{eff}}\text{-}R_*$ relationship given in Boyajian et al. (2012). We determined T_{eff} for each KOI by fitting BT-SETTL models (Allard et al. 2011) to our visible wavelength spectra following the technique outlined in Lépine et al. (2013), except that we only included models with metallicities $\leq 2\sigma$ different from those we derived from Equation 5.2. Stellar radii in Batalha et al. (2013) are based on temperatures in the KIC (Brown et al. 2011) and Yonsei-Yale isochrones (Demarque et al. 2004). However, radii from Demarque et al. (2004) are known to be inaccurate for late K and M dwarfs (Boyajian et al. 2012), and KIC temperatures have been shown to be too high for late K and M dwarfs (Mann et al. 2012). Instead, Boyajian et al. (2012) derive their $T_{\text{eff}}\text{-}R_*$ using empirical measurements of radii of K and M dwarfs from long-baseline interferometry. They obtain [Fe/H] values for their targets from the literature, and find no discernible metallicity dependence in their $T_{\text{eff}}\text{-}R_*$ relation. This contradicts stellar evolutionary models such as Dotter et al. (2008), which show a strong metallicity dependence for the $T_{\text{eff}}\text{-}R_*$ relation for late K and M dwarfs. We chose to use the relation from Boyajian et al. (2012), rather than the Dotter et al. (2008) models, because Boyajian et al. (2012) is based on empirical measurements rather than evolutionary models.

Our stellar radii are $0.06R_\odot$ larger than those of Muirhead et al. (2012a). Their stellar radii for stars with $T_{\text{eff}} < 3900$ are consistent with ours at $\leq 1.2\sigma$. The discrepancy is larger (typically $> 1.5\sigma$) for warmer stars because their temperatures are underestimated: the H₂O index utilized by Muirhead et al. (2012a) to calculate T_{eff} saturates at 3800–4000 K (Rojas-Ayala et al. 2012; Dressing & Charbonneau 2013). However, Muirhead et al. (2012a) stellar radii are still $< 3\sigma$ consistent even at warm temperatures. Our stellar radii are on average $0.02R_\odot$ larger than those of Dressing & Charbonneau (2013) with no significant trend in T_{eff} . This offset is smaller than the typical errors from our own measurements (median $\sigma_{R_*} \simeq 0.04R_\odot$). Resulting T_{eff} , R_* , and associated errors for KOIs in this program are listed in Table 5.1.

We adopted the R_{planet}/R_* values reported by Batalha et al. (2013). Dressing & Charbonneau (2013) refit the *Kepler* light curves for M dwarf KOIs and find that there are significant problems with some of the transit parameters reported in Batalha et al. (2013). However, these problems are primarily in a/R_* (where a is the semi-major axis) and impact parameter, whereas the median R_{planet}/R_* value from Dressing & Charbonneau (2013) is only 3% smaller than those of Batalha et al. (2013). Further, the differences in R_{planet}/R_* between Dressing & Charbonneau (2013) and Batalha et al. (2013) are small compared to errors in R_{planet}/R_* reported by Batalha et al. (2013) ($\simeq 13\%$) and errors in stellar radii ($\simeq 7\%$). Moreover Dressing & Charbonneau (2013) only refit transits of M dwarfs, while our sample includes many late K dwarfs.

Table 5.2—Continued

<i>Kepler</i> ID	[Fe/H]	$\sigma_{\text{[Fe/H]}}$
11703956	-0.25	0.11
3218308	+0.23	0.14
3328254	-0.24	0.17
3344220	-0.09	0.16
3357261	+0.30	0.17
3438817	+0.33	0.12
4078900	-0.51	0.15
4175398	-0.12	0.11
4243354	-0.33	0.12
4551429	+0.18	0.12
4569115	+0.25	0.13
4655612	-0.36	0.14
4726192	-0.09	0.16
6224062	-0.06	0.14
6363233	-0.19	0.15
6503104	+0.11	0.05
6949326	+0.04	0.13
7033670	-0.20	0.08
7630772	+0.18	0.10
7800087	+0.34	0.13
8013221	-0.24	0.12
8393582	-0.70	0.16
8415336	-0.21	0.14
8494510	-0.12	0.13
8611876	-0.12	0.09
8814775	-0.16	0.10
8881126	-0.42	0.21
8912338	+0.01	0.16
9991565	-0.28	0.14
10082058	-0.23	0.12
10129425	-0.31	0.13
10166321	+0.08	0.13
10195818	-0.00	0.11
10224595	-0.07	0.07
10336624	+0.01	0.14
10676126	-0.00	0.09
10747553	-0.20	0.09
10843322	-0.38	0.10
10850139	-0.52	0.09
10850518	+0.35	0.10
10905320	-0.42	0.14
11713042	-0.58	0.12
11820505	+0.17	0.14

Note. — Table 5.2 is published in its entirety in the electronic edition of the *Astrophysical Journal*, and can be downloaded with the arXiv version of the manuscript. A portion is shown here for guidance regarding its form and content.

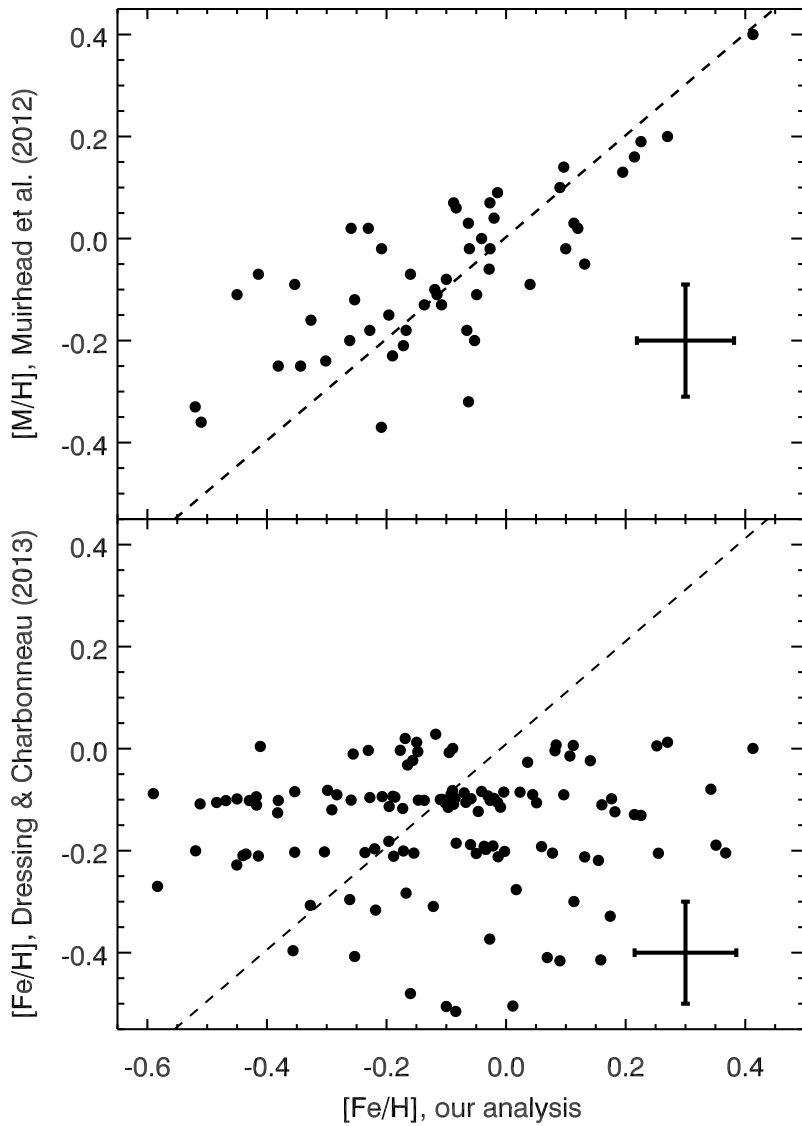


Figure 5.3: Metallicities from Muirhead et al. (2012a) (top) or from Dressing & Charbonneau (2013) (bottom) as a function of those derived from our own program. The dashed lines indicate equality. We have added artificial scatter ($\simeq 0.01$ dex) to metallicities from Dressing & Charbonneau (2013) for clarity. Typical errors are shown in the bottom right of each plot. Note that Muirhead et al. (2012a) use $[M/H]$ instead of $[Fe/H]$. Our metallicities are mostly within 1σ (reduced $\chi^2 \simeq 1$) of those from Muirhead et al. (2012a), with the exception of those with $[Fe/H] < -0.3$ which are more discrepant. Our $[Fe/H]$ values greatly differ (reduced $\chi^2 > 3$) from those of Dressing & Charbonneau (2013).

5.5 Results

We list [Fe/H] values and stellar radii for the KOI sample in Table 5.1, and [Fe/H] values for the non-KOIs in Table 5.2. Figure 5.4 compares the metallicity distributions of dwarfs with no detected transit (non-KOI sample), as well as metallicities for different planet-size samples (Earths, Neptunes, and Jupiters). We summarize the metallicities for each distribution in Table 5.3, and compare with the non-KOI sample using the Kolmogorov-Smirnov (KS) and Cramér-von Mises-Anderson (CMA) tests. Systems with multiple detected planets are placed into size bins (Earth-, Neptune-, and Jupiter-size) according to the largest detected planet in the system. We also list the metallicity distribution of these multi-planet systems, according to the Batalha et al. (2013) catalog, in Table 5.3.

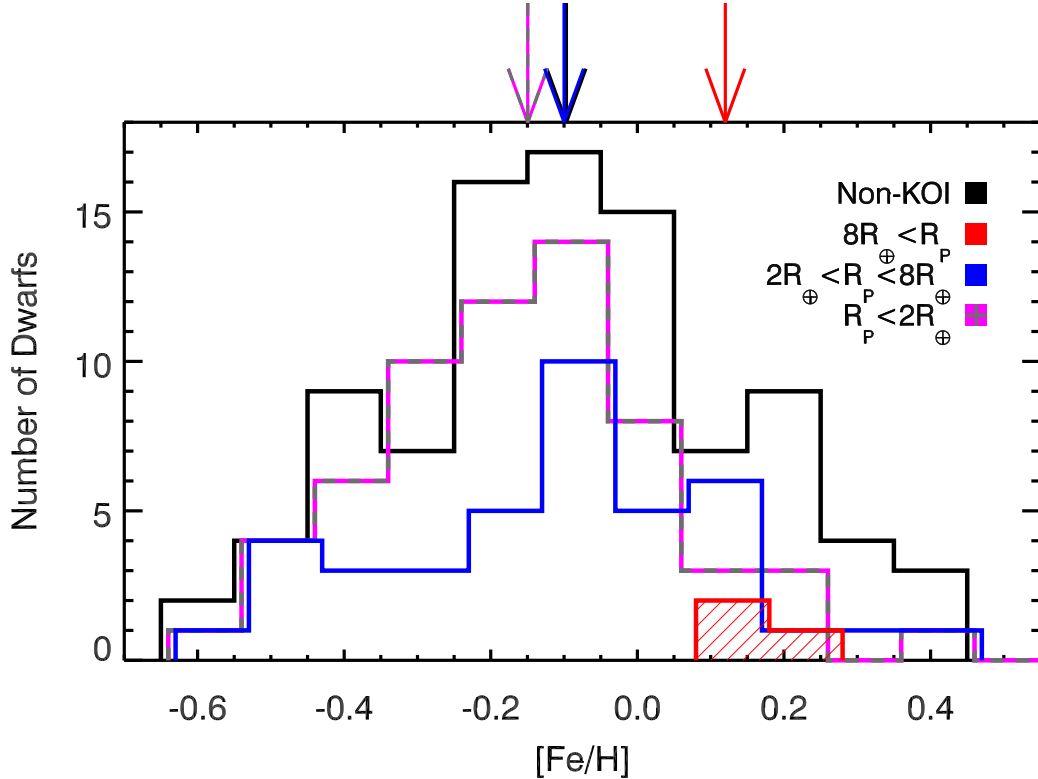


Figure 5.4: Metallicity distribution of *Kepler* late K and M targets with no detected transit (black), Earth-sized KOIs ($R_P < 2R_{\oplus}$, magenta-grey dashed), Neptune sized KOIs ($2R_{\oplus} < R_P < 8R_{\oplus}$, blue), and Jupiter-sized KOIs ($8R_{\oplus} < R_P$, red, hashed). Bin sizes and locations are identical for all distributions, but the histograms are slightly offset for clarity. Arrows above the plot indicate the median of each distribution. Note that the black and blue arrows are nearly overlapping. For multi-planet systems we use the radius of the largest detected planet in the system.

Metallicities of stars hosting Jupiter-sized planets are significantly higher than those with no detected transit, which is consistent with previous findings based on radial velocity

Table 5.3. Summary of Metallicity Distributions

Planet-type	Planet sizes R_{\oplus}	N	[Fe/H] median	KS ^a	CMA ^b σ
Jupiters	$R_p > 8$	3	$+0.12 \pm 0.07$	2.0%	3.2
Neptunes	$2.0 < R_p \leq 8$	40	-0.10 ± 0.04	96.9%	0.2
Neptunes2	$2.5 < R_p \leq 8$	17	-0.12 ± 0.06	99.5%	0.1
Neptunes3	$3.0 < R_p \leq 8$	6	-0.03 ± 0.11	99.5%	0.2
Earths	$R_p \leq 2$	63	-0.15 ± 0.03	33.9%	1.2
Multis ^c	all	31	-0.10 ± 0.04	39.4%	0.8
Non-KOI	not detected	97	-0.10 ± 0.03

^aProbability that the distribution is drawn from the same parent population as the non-KOI sample based on a Kolmogorov-Smirnov (KS) test.

^bDifference between distribution and non-KOI distribution (in standard deviations) as determined by the Cramér-von Mises-Anderson statistic (Anderson 1962).

^cSystems with more than one transiting planet detected in the Batalha et al. (2013) catalog.

surveys of M dwarfs (e.g., Johnson et al. 2010). Because there are only 3 giant planets in the sample, the difference between the Jupiter and non-KOI sample is at the edge of statistical significance, with a difference between the median [Fe/H] values of 0.22 ± 0.073 (3.0σ).

The distribution of metallicities for dwarfs hosting Neptune-sized planets is consistent with the non-KOI sample for all metrics. We rule out the 0.2 dex offset reported by Schlaufman & Laughlin (2011) between the metallicity of stars hosting non-Jovian ($R_p \leq 8R_{\oplus}$) planets and the non-KOI sample at $> 6\sigma$, and at $> 4\sigma$ if we consider just Neptune-sized planets ($2.0 \leq R_p \leq 8R_{\oplus}$).

The distribution for the Earth-sized hosts is slightly more metal poor (by 0.05 dex) than the non-KOI sample, although the offset is not significant ($\sigma = 0.04$ dex). Our detected offset is consistent with predictions from Gaidos & Mann (2013), who use Dotter et al. (2008) models and *Kepler* target stars to show that M dwarfs hosting small planets have [Fe/H] values $\simeq 0.02$ dex lower than those without planets, because for a given $g - r$ color, metal-poor K and M dwarfs will have smaller radii than metal-rich dwarfs (making small planets easier to detect). If the relations from Boyajian et al. (2012) are correct (i.e., metallicity is negligible factor in R_* for a given T_{eff}) then this detection bias is smaller, but still present, since Boyajian et al. (2012) find that the color- R_* and color- T_{eff} relations for K and M dwarfs have a significant metallicity dependence.

5.6 Discussion

In this paper we present our comparison between metallicities of late K and M *Kepler* target stars and planet candidate hosts. We used techniques of (or modified techniques of) Mann et al. (2013) to calculate [Fe/H]. We then investigated correlations between stellar metallicity and the presence, multiplicity, and size of any detected planets. We draw four main conclusions:

- The metallicity distribution of late K and M *Kepler* targets is indistinguishable from that of the solar neighborhood.
- Late K and M *Kepler* dwarfs hosting giant planets are more metal-rich than those without detected planets.
- Late K and M hosts where the largest detected planet is Earth- or Neptune-sized have metallicities consistent with those dwarfs with no detected transit.
- Late K and M dwarfs hosting multiple detected planets are not significantly more metal-rich or metal-poor than those with no detected transit.

An important effect is the presence of non-detected planets in the control (non-KOI) sample, which dilutes any metallicity offset between the two samples. Suppose metallicity is a bimodal distribution with stars harboring planets having metallicity greater by $\Delta_{[\text{Fe}/\text{H}]}$ than those without planets. The observed metallicity offset (O) between the KOI sample and the non-KOI sample is:

$$O = \Delta_{[\text{Fe}/\text{H}]} \frac{(1-f)}{(1-ft)}, \quad (5.3)$$

where, f is the fraction of stars with planets, and t is the probability of detecting the planet (e.g., the geometric transit probability). For transiting planets, ft is small, and the denominator $\simeq 1$. In the case that f approaches 1, $O \simeq 0$, because the non-KOI sample is completely diluted with undetected planets. This may be the case when considering Earth-to super-Earth-sized planets and all orbital periods around M dwarfs (Swift et al. 2013). In the case of giant planets, which are relatively rare (2% for period < 85 days; Fressin et al. 2013), dilution is negligible and $O \simeq \Delta_{[\text{Fe}/\text{H}]}$. For Neptunes, Fressin et al. (2013) find that $\sim 25\%$ of stars harbor a Neptune ($2 R_\oplus < R_p \leq 8 R_\oplus$) and periods < 85 days (note that only 1 of the planets in our sample has a period $\gg 85$ days). In this case $O \simeq 0.75\Delta_{[\text{Fe}/\text{H}]}$, which has little effect on our conclusions.

We examined how our results change as a function of how we define Earth-, Neptune-, and Jupiter-sized planets. There are no KOIs in our sample with radii between $6R_\oplus$ and $9R_\oplus$, so our choice of a Neptune-Jupiter boundary is unimportant. We investigated the effect of changing the Earth-Neptune boundary by considering two sub-samples; Neptunes2, defined as $2.5 R_\oplus < R_p \leq 8 R_\oplus$, and Neptunes3, defined as $3.0 R_\oplus < R_p \leq 8 R_\oplus$. All three Neptune samples are consistent with each other and the non-KOI sample at 1σ , demonstrating that our results are not sensitive to how we define Earth- and Neptune-sized planets.

Fressin et al. (2013) show that the *Kepler* planet search algorithm is missing planets that should have been detected based on their S/N. However, this only alters our results if the metallicity distribution of missing planets is significantly different than that of the detected planets. To check the effect of incompleteness, we considered a subsample with transit detections of $S/N > 16$ as reported by Batalha et al. (2013), where Fressin et al. (2013) suggest the detection efficiency of the *Kepler* pipeline is $\simeq 100\%$. In this case, the sample shrinks from 157 planet candidates around 106 dwarfs to 132 candidates around 93 dwarfs. Most of the candidates removed by this cut are $R_p \leq 2R_\oplus$. We reran all analyses on this subsample and find that none of our conclusions are changed.

Our results disagree with those of Schlaufman & Laughlin (2011), who claim that late K and M *Kepler* stars hosting small planets are more metal-rich than non-hosting late K and M stars. In place of spectroscopic metallicities Schlaufman & Laughlin (2011) use $g - r$ vs. $J - H$ colors, which been shown to be positively correlated with metallicity for F, G, and early-K dwarfs (e.g., An et al. 2009). However, West et al. (2004) and Bochanski et al. (2013) see a *negative* correlation between $g - r$ color and metallicity for M dwarfs. The stars in our sample are in the transition region (mostly K5-M2), where the PHOENIX stellar atmosphere models predict little or no trend of $g - r$ color with metallicity (Lépine et al. 2013).

We used our sample (both KOIs and non-KOIs) to investigate how $g - r$ correlates with metallicity for our range of spectral types. In Figure 5.5a we show the $g - r$ colors for the metal-poor ($[\text{Fe}/\text{H}] < -0.1$) and metal-rich ($[\text{Fe}/\text{H}] > -0.1$) samples for three different $J - H$ bins centered at $J - H = 0.575, 0.625$, and 0.675 . $[\text{Fe}/\text{H}] = -0.1$ was selected to divide the samples because this is the median metallicity of our sample. The late-type dwarf bin used by Schlaufman & Laughlin (2011) is centered at $J - H = 0.62$. The distribution of $g - r$ colors of the two metallicity samples are consistent at $< 2\sigma$ in each of the three $J - H$ bins. We use a slightly different parsing in Figure 5.5b, where we show $[\text{Fe}/\text{H}]$ vs. $g - r$ color for two $J - H$ bins. In each bin a least-squares linear fit to the data yield slopes that are

not significantly different from 0. The fit yields coefficients of determination (R^2) of 0.01 and 0.07 for the $0.65 > J - H$ and $0.65 < J - H$ bins, respectively. An F-test comparing $[\text{Fe}/\text{H}] - [\text{Fe}/\text{H}]$ to that of $[\text{Fe}/\text{H}] - [\text{Fe}/\text{H}]_{\text{fit}}$ gives respective differences in the variances of only 0.50 and 0.48σ . These results strongly suggest that $g - r$ vs. $J - H$ is not a good predictor of $[\text{Fe}/\text{H}]$ for late-type dwarfs.

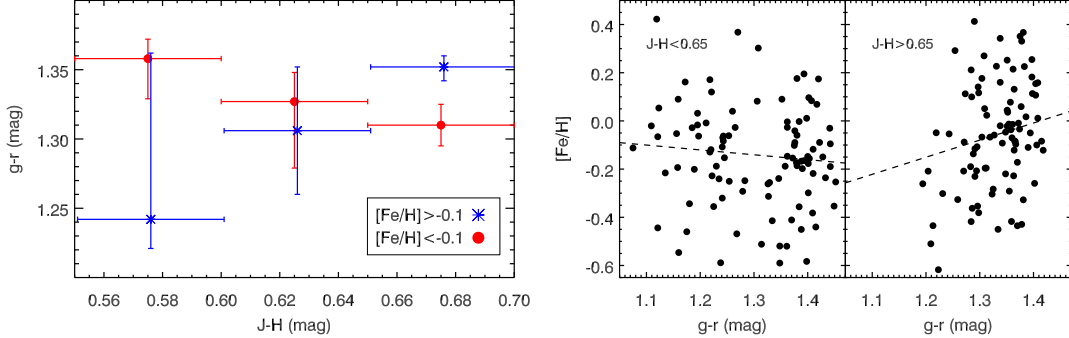


Figure 5.5: Left: median $g - r$ colors of the metal-rich (blue) and metal-poor (red) samples of *Kepler* dwarfs for three $J - H$ color bins centered at 0.575, 0.625, and 0.675. Bin sizes and locations are identical for all distributions, but are slightly offset for clarity. The scatter in $g - r$ colors for a given metallicity range and $J - H$ bin are determined through bootstrap resampling. For all three $J - H$ bins, the two metallicity groups are indistinguishable at 2σ . Right: $[\text{Fe}/\text{H}]$ vs. $g - r$ for two different $J - H$ bins, with the best-fit line shown. For both bins, the best fit lines are consistent with a slope of 0, and yield coefficients of determination (R^2) of 0.01 and 0.07, respectively. An F-test detects no significant improvement from the regression for either bin. Thus no significant correlation between $g - r$ vs. $J - H$ and $[\text{Fe}/\text{H}]$ is found.

Our results have some important theoretical implications. Theoretical studies have suggested there is a minimum metallicity for a protoplanetary disk to form planets (e.g., Gonzalez et al. 2001; Johnson & Li 2012). Assuming the metallicity of the protoplanetary disk matches that of the star later in its evolution, this suggests that low-metallicity stars should not harbor planets. Johnson & Li (2012) estimate that the minimum metallicity to form a planet around a solar-type star is $[\text{Fe}/\text{H}]_{\min} \simeq -1.5 + \log(a)$, where a is the semi-major axis in AU. For the planets in our paper ($a \lesssim 0.1$) $[\text{Fe}/\text{H}]_{\min}$ is approximately -2.5 . Because M dwarfs have less massive, we expect that $[\text{Fe}/\text{H}]_{\min}$ will be higher for these stars. Our results show that Earth and Neptune-sized planets are able to form around stars with metallicities as low as $[\text{Fe}/\text{H}] \simeq -0.6$, similar to what is seen for FGK dwarfs (Buchhave et al. 2012). But it is likely that we are not probing sufficiently metal-poor dwarfs to detect the proposed planet formation threshold.

Our results also indicate that, for small planets, multiplicity is not correlated with metallicity. Interestingly, two of the four KOIs with $[\text{Fe}/\text{H}] < -0.5$ have ≥ 3 detected planets (KOI-961 has 3 and KOI-812 has 4), suggesting the accretion process must be efficient in collecting solids from the disk. A minimum mass solar nebula contains about $64M_{\oplus}$ of rock/metal/ices. Assuming that the disk mass is $\sim 0.1M_{*}$ (Williams & Cieza 2011),

and that the amount of metals in a disk scales with its mass and the stellar metallicity, a disk around an early M dwarf with $[Fe/H] = -0.5$ contains $\sim 10M_{\oplus}$ of solids. KOI-812 (as an example) contains four detected planets with radii from 1.3 to $2.4R_{\oplus}$. Most of these are likely rocky, or are composed of rocky cores with a thin hydrogen envelopes (Gaidos et al. 2012). If we assume a mass-radius relationship of $M_P \simeq R_P^2$, with M_P and R_P in Earth units, then the total mass in KOI-812's planets is $15.5 \pm 3.1M_{\oplus}$. Although some of this mass is hydrogen (and thus not affected by the amount of solids in the disk), this analysis does not consider undetected planets at higher semi-major axes. Thus our results suggest that the progenitors of these planets must have been very efficient in accreting most of the available solid material from the disk.

The core accretion scenario of giant planet formation requires the formation of a $\simeq 5 - 10M_{\oplus}$ core (Pollack et al. 1996; Hubickyj et al. 2005) in the $\sim 2 - 6$ Myr timescale on which disks are observed to dissipate (Haisch et al. 2001; Evans et al. 2009). The scarcity of giant planets around M dwarfs (especially metal-poor M dwarfs) means that either giant planets cores do not form around these stars, or that they do not form in time. The existence of objects that are likely $5 - 10M_{\oplus}$ (or have rocky cores of this size), even around metal-poor M dwarfs, suggests that the latter is the more viable explanation.

References

- Adams, F. C., Bodenheimer, P., & Laughlin, G. 2005, Astronomische Nachrichten, 326, 913
- Ahn, C. P., Alexandroff, R., Allende Prieto, C., Anderson, S. F., Anderton, T., Andrews, B. H., Aubourg, É., Bailey, S., Balbinot, E., Barnes, R., & et al. 2012, ApJS, 203, 21
- Allard, F., Homeier, D., & Freytag, B. 2011, in Astronomical Society of the Pacific Conference Series, Vol. 448, 16th Cambridge Workshop on Cool Stars, Stellar Systems, and the Sun, ed. C. Johns-Krull, M. K. Browning, & A. A. West, 91
- An, D., Johnson, J. A., Beers, T. C., Pinsonneault, M. H., Terndrup, D. M., Delahaye, F., Lee, Y. S., Masseron, T., & Yanny, B. 2009, ApJ, 707, L64
- Anderson, T. W. 1962, Annual Math Statistics, 33, 1148
- Bacon, R., Copin, Y., Monnet, G., Miller, B. W., Allington-Smith, J. R., Bureau, M., Carollo, C. M., Davies, R. L., Emsellem, E., Kuntschner, H., Peletier, R. F., Verolme, E. K., & de Zeeuw, P. T. 2001, MNRAS, 326, 23
- Batalha, N. M., Borucki, W. J., Koch, D. G., Bryson, S. T., Haas, M. R., Brown, T. M., Caldwell, D. A., Hall, J. R., Gilliland, R. L., Latham, D. W., Meibom, S., & Monet, D. G. 2010, ApJ, 713, L109
- Batalha, N. M., Rowe, J. F., Bryson, S. T., Barclay, T., Burke, C. J., Caldwell, D. A., Christiansen, J. L., Mullally, F., Thompson, S. E., Brown, T. M., Dupree, A. K., Fabrycky, D. C., Ford, E. B., Fortney, J. J., Gilliland, R. L., Isaacson, H., Latham, D. W., Marcy, G. W., Quinn, S. N., Ragozzine, D., Shporer, A., Borucki, W. J., Ciardi, D. R., Gautier, III, T. N., Haas, M. R., Jenkins, J. M., Koch, D. G., Lissauer, J. J., Rapin, W., Basri, G. S., Boss, A. P., Buchhave, L. A., Carter, J. A., Charbonneau, D., Christensen-Dalsgaard, J., Clarke, B. D., Cochran, W. D., Demory, B.-O., Desert, J.-M., Devore, E., Doyle, L. R., Esquerdo, G. A., Everett, M., Fressin, F., Geary, J. C., Girouard, F. R., Gould, A., Hall, J. R., Holman, M. J., Howard, A. W., Howell, S. B., Ibrahim, K. A., Kinemuchi, K., Kjeldsen, H., Klaus, T. C., Li, J., Lucas, P. W., Meibom, S., Morris, R. L., Prša, A., Quintana, E., Sanderfer, D. T., Sasselov, D., Seader, S. E., Smith, J. C., Steffen, J. H., Still, M., Stumpe, M. C., Tarter, J. C., Tenenbaum, P., Torres, G., Twicken, J. D., Uddin, K., Van Cleve, J., Walkowicz, L., & Welsh, W. F. 2013, ApJS, 204, 24

- Bessell, M. S. & Brett, J. M. 1988, PASP, 100, 1134
- Bochanski, J. J., Savcheva, A., West, A. A., & Hawley, S. L. 2013, AJ, 145, 40
- Bochanski, J. J., West, A. A., Hawley, S. L., & Covey, K. R. 2007, AJ, 133, 531
- Borucki, W. J., Koch, D., Basri, G., Batalha, N., Brown, T., Caldwell, D., Caldwell, J., Christensen-Dalsgaard, J., Cochran, W. D., DeVore, E., Dunham, E. W., Dupree, A. K., Gautier, T. N., Geary, J. C., Gilliland, R., Gould, A., Howell, S. B., Jenkins, J. M., Kondo, Y., Latham, D. W., Marcy, G. W., Meibom, S., Kjeldsen, H., Lissauer, J. J., Monet, D. G., Morrison, D., Sasselov, D., Tarter, J., Boss, A., Brownlee, D., Owen, T., Buzasi, D., Charbonneau, D., Doyle, L., Fortney, J., Ford, E. B., Holman, M. J., Seager, S., Steffen, J. H., Welsh, W. F., Rowe, J., Anderson, H., Buchhave, L., Ciardi, D., Walkowicz, L., Sherry, W., Horch, E., Isaacson, H., Everett, M. E., Fischer, D., Torres, G., Johnson, J. A., Endl, M., MacQueen, P., Bryson, S. T., Dotson, J., Haas, M., Kolodziejczak, J., Van Cleve, J., Chandrasekaran, H., Twicken, J. D., Quintana, E. V., Clarke, B. D., Allen, C., Li, J., Wu, H., Tenenbaum, P., Verner, E., Bruhweiler, F., Barnes, J., & Prsa, A. 2010, Science, 327, 977
- Boyajian, T. S., von Braun, K., van Belle, G., McAlister, H. A., ten Brummelaar, T. A., Kane, S. R., Muirhead, P. S., Jones, J., White, R., Schaefer, G., Ciardi, D., Henry, T., López-Morales, M., Ridgway, S., Gies, D., Jao, W.-C., Rojas-Ayala, B., Parks, J. R., Sturmann, L., Sturmann, J., Turner, N. H., Farrington, C., Goldfinger, P. J., & Berger, D. H. 2012, ApJ, 757, 112
- Brown, T. M., Latham, D. W., Everett, M. E., & Esquerdo, G. A. 2011, AJ, 142, 112
- Buchhave, L. A., Latham, D. W., Johansen, A., Bizzarro, M., Torres, G., Rowe, J. F., Batalha, N. M., Borucki, W. J., Brugamyer, E., Caldwell, C., Bryson, S. T., Ciardi, D. R., Cochran, W. D., Endl, M., Esquerdo, G. A., Ford, E. B., Geary, J. C., Gilliland, R. L., Hansen, T., Isaacson, H., Laird, J. B., Lucas, P. W., Marcy, G. W., Morse, J. A., Robertson, P., Shporer, A., Stefanik, R. P., Still, M., & Quinn, S. N. 2012, Nature, 486, 375
- Buton, C., Copin, Y., Aldering, G., Antilogus, P., Aragon, C., Bailey, S., Baltay, C., Bongard, S., Canto, A., Cellier-Holzem, F., Childress, M., Chotard, N., Fakhouri, H. K., Gangler, E., Guy, J., Hsiao, E. Y., Kerschhaggl, M., Kowalski, M., Loken, S., Nugent, P., Paech, K., Pain, R., Pécontal, E., Pereira, R., Perlmutter, S., Rabinowitz, D., Rigault, M., Runge, K., Scalzo, R., Smadja, G., Tao, C., Thomas, R. C., Weaver, B. A., Wu, C., & Nearby SuperNova Factory. 2013, A&A, 549, A8
- Casagrande, L., Flynn, C., & Bessell, M. 2008, MNRAS, 389, 585
- Cushing, M. C., Rayner, J. T., & Vacca, W. D. 2005, ApJ, 623, 1115
- Cushing, M. C., Vacca, W. D., & Rayner, J. T. 2004, PASP, 116, 362
- Demarque, P., Woo, J.-H., Kim, Y.-C., & Yi, S. K. 2004, ApJS, 155, 667

- Dhital, S., West, A. A., Stassun, K. G., Bochanski, J. J., Massey, A. P., & Bastien, F. A. 2012, AJ, 143, 67
- Dotter, A., Chaboyer, B., Jevremović, D., Kostov, V., Baron, E., & Ferguson, J. W. 2008, ApJS, 178, 89
- Dressing, C. D. & Charbonneau, D. 2013, ApJ, 767, 95
- Evans, N. J., Dunham, M. M., Jørgensen, J. K., Enoch, M. L., Merín, B., van Dishoeck, E. F., Alcalá, J. M., Myers, P. C., Stapelfeldt, K. R., Huard, T. L., Allen, L. E., Harvey, P. M., van Kempen, T., Blake, G. A., Koerner, D. W., Mundy, L. G., Padgett, D. L., & Sargent, A. I. 2009, ApJS, 181, 321
- Fabrycky, D. C., Lissauer, J. J., Ragozzine, D., Rowe, J. F., Agol, E., Barclay, T., Batalha, N., Borucki, W., Ciardi, D. R., Ford, E. B., Geary, J. C., Holman, M. J., Jenkins, J. M., Li, J., Morehead, R. C., Shporer, A., Smith, J. C., Steffen, J. H., & Still, M. 2012, ArXiv e-prints
- Fischer, D. A. & Valenti, J. 2005, ApJ, 622, 1102
- Fressin, F., Torres, G., Charbonneau, D., Bryson, S. T., Christiansen, J., Dressing, C. D., Jenkins, J. M., Walkowicz, L. M., & Batalha, N. M. 2013, ApJ, 766, 81
- Gaidos, E., Fischer, D. A., Mann, A. W., & Lépine, S. 2012, ApJ, 746, 36
- Gaidos, E. & Mann, A. W. 2013, ApJ, 762, 41
- Gonzalez, G. 1997, MNRAS, 285, 403
- Gonzalez, G., Brownlee, D., & Ward, P. 2001, Icarus, 152, 185
- Haisch, Jr., K. E., Lada, E. A., & Lada, C. J. 2001, ApJ, 553, L153
- Hartmann, L., Calvet, N., Gullbring, E., & D'Alessio, P. 1998, ApJ, 495, 385
- Hawley, S. L., Covey, K. R., Knapp, G. R., Golimowski, D. A., Fan, X., Anderson, S. F., Gunn, J. E., Harris, H. C., Ivezić, Ž., Long, G. M., Lupton, R. H., McGehee, P. M., Narayanan, V., Peng, E., Schlegel, D., Schneider, D. P., Spahn, E. Y., Strauss, M. A., Szkody, P., Tsvetanov, Z., Walkowicz, L. M., Brinkmann, J., Harvanek, M., Hennessy, G. S., Kleinman, S. J., Krzesinski, J., Long, D., Neilsen, E. H., Newman, P. R., Nitta, A., Snedden, S. A., & York, D. G. 2002, AJ, 123, 3409
- Howard, A. W., Marcy, G. W., Bryson, S. T., Jenkins, J. M., Rowe, J. F., Batalha, N. M., Borucki, W. J., Koch, D. G., Dunham, E. W., Gautier, III, T. N., Van Cleve, J., Cochran, W. D., Latham, D. W., Lissauer, J. J., Torres, G., Brown, T. M., Gilliland, R. L., Buchhave, L. A., Caldwell, D. A., Christensen-Dalsgaard, J., Ciardi, D., Fressin, F., Haas, M. R., Howell, S. B., Kjeldsen, H., Seager, S., Rogers, L., Sasselov, D. D., Steffen, J. H., Basri, G. S., Charbonneau, D., Christiansen, J., Clarke, B., Dupree, A., Fabrycky, D. C., Fischer, D. A., Ford, E. B., Fortney, J. J., Tarter, J., Girouard, F. R., Holman, M. J., Johnson, J. A., Klaus, T. C., Machalek, P., Moorhead, A. V., Morehead, R. C.,

- Ragozzine, D., Tenenbaum, P., Twicken, J. D., Quinn, S. N., Isaacson, H., Shporer, A., Lucas, P. W., Walkowicz, L. M., Welsh, W. F., Boss, A., Devore, E., Gould, A., Smith, J. C., Morris, R. L., Prsa, A., Morton, T. D., Still, M., Thompson, S. E., Mullally, F., Endl, M., & MacQueen, P. J. 2012, *ApJS*, 201, 15
- Hubickyj, O., Bodenheimer, P., & Lissauer, J. J. 2005, *Icarus*, 179, 415
- Johnson, J. A., Aller, K. M., Howard, A. W., & Crepp, J. R. 2010, *PASP*, 122, 905
- Johnson, J. A. & Apps, K. 2009, *ApJ*, 699, 933
- Johnson, J. L. & Li, H. 2012, *ApJ*, 751, 81
- Kokubo, E., Kominami, J., & Ida, S. 2006, *ApJ*, 642, 1131
- Kraus, A. L. & Hillenbrand, L. A. 2007, *AJ*, 134, 2340
- Landsman, W. B. 1993, in *Astronomical Society of the Pacific Conference Series*, Vol. 52, *Astronomical Data Analysis Software and Systems II*, ed. R. J. Hanisch, R. J. V. Brissenden, & J. Barnes, 246
- Lantz, B., Aldering, G., Antilogus, P., Bonnaud, C., Capoani, L., Castera, A., Copin, Y., Dubet, D., Gangler, E., Henault, F., Lemonnier, J.-P., Pain, R., Pecontal, A., Pecontal, E., & Smadja, G. 2004, in *Society of Photo-Optical Instrumentation Engineers (SPIE) Conference Series*, Vol. 5249, *Society of Photo-Optical Instrumentation Engineers (SPIE) Conference Series*, ed. L. Mazuray, P. J. Rogers, & R. Wartmann, 146–155
- Laughlin, G., Bodenheimer, P., & Adams, F. C. 2004, *ApJ*, 612, L73
- Leggett, S. K. 1992, *ApJS*, 82, 351
- Lépine, S. & Gaidos, E. 2011, *AJ*, 142, 138
- Lépine, S., Hilton, E. J., Mann, A. W., Wilde, M., Rojas-Ayala, B., Cruz, K. L., & Gaidos, E. 2013, *AJ*, 145, 102
- Lépine, S., Rich, R. M., & Shara, M. M. 2007, *ApJ*, 669, 1235
- Mann, A. W., Brewer, J. M., Gaidos, E., Lépine, S., & Hilton, E. J. 2013, *AJ*, 145, 52
- Mann, A. W., Gaidos, E., Lépine, S., & Hilton, E. J. 2012, *ApJ*, 753, 90
- Monet, D. G., Levine, S. E., Canzian, B., Ables, H. D., Bird, A. R., Dahn, C. C., Guetter, H. H., Harris, H. C., Henden, A. A., Leggett, S. K., Levison, H. F., Luginbuhl, C. B., Martini, J., Monet, A. K. B., Munn, J. A., Pier, J. R., Rhodes, A. R., Riepe, B., Sell, S., Stone, R. C., Vrba, F. J., Walker, R. L., Westerhout, G., Brucato, R. J., Reid, I. N., Schoening, W., Hartley, M., Read, M. A., & Tritton, S. B. 2003, *AJ*, 125, 984
- Muirhead, P. S., Hamren, K., Schlawin, E., Rojas-Ayala, B., Covey, K. R., & Lloyd, J. P. 2012a, *ApJ*, 750, L37

- Muirhead, P. S., Johnson, J. A., Apps, K., Carter, J. A., Morton, T. D., Fabrycky, D. C., Pineda, J. S., Bottom, M., Rojas-Ayala, B., Schlawin, E., Hamren, K., Covey, K. R., Crepp, J. R., Stassun, K. G., Pepper, J., Hebb, L., Kirby, E. N., Howard, A. W., Isaacson, H. T., Marcy, G. W., Levitan, D., Diaz-Santos, T., Armus, L., & Lloyd, J. P. 2012b, *ApJ*, 747, 144
- Muirhead, P. S., Vanderburg, A., Shporer, A., Becker, J., Swift, J. J., Lloyd, J. P., Fuller, J., Zhao, M., Hinkley, S., Pineda, J. S., Bottom, M., Howard, A. W., von Braun, K., Boyajian, T. S., Law, N., Baranec, C., Riddle, R., Ramaprakash, A. N., Tendulkar, S. P., Bui, K., Burse, M., Chordia, P., Das, H., Dekany, R., Punnadi, S., & Johnson, J. A. 2013, *ApJ*, 767, 111
- Oke, J. B. 1990, *AJ*, 99, 1621
- Pollack, J. B., Hubickyj, O., Bodenheimer, P., Lissauer, J. J., Podolak, M., & Greenzweig, Y. 1996, *Icarus*, 124, 62
- Rayner, J. T., Cushing, M. C., & Vacca, W. D. 2009, *ApJS*, 185, 289
- Rayner, J. T., Toomey, D. W., Onaka, P. M., Denault, A. J., Stahlberger, W. E., Vacca, W. D., Cushing, M. C., & Wang, S. 2003, *PASP*, 115, 362
- Rojas-Ayala, B., Covey, K. R., Muirhead, P. S., & Lloyd, J. P. 2010, *ApJ*, 720, L113
- . 2012, *ApJ*, 748, 93
- Santos, N. C., Israelian, G., & Mayor, M. 2001, *A&A*, 373, 1019
- Schlaufman, K. C. & Laughlin, G. 2010, *A&A*, 519, A105
- . 2011, *ApJ*, 738, 177
- Scholz, A., Jayawardhana, R., & Wood, K. 2006, *ApJ*, 645, 1498
- Skrutskie, M. F., Cutri, R. M., Stiening, R., Weinberg, M. D., Schneider, S., Carpenter, J. M., Beichman, C., Capps, R., Chester, T., Elias, J., Huchra, J., Liebert, J., Lonsdale, C., Monet, D. G., Price, S., Seitzer, P., Jarrett, T., Kirkpatrick, J. D., Gizis, J. E., Howard, E., Evans, T., Fowler, J., Fullmer, L., Hurt, R., Light, R., Kopan, E. L., Marsh, K. A., McCallon, H. L., Tam, R., Van Dyk, S., & Wheelock, S. 2006, *AJ*, 131, 1163
- Sousa, S. G., Santos, N. C., Mayor, M., Udry, S., Casagrande, L., Israelian, G., Pepe, F., Queloz, D., & Monteiro, M. J. P. F. G. 2008, *A&A*, 487, 373
- Swift, J. J., Johnson, J. A., Morton, T. D., Crepp, J. R., Montet, B. T., Fabrycky, D. C., & Muirhead, P. S. 2013, *ApJ*, 764, 105
- Terrien, R. C., Mahadevan, S., Bender, C. F., Deshpande, R., Ramsey, L. W., & Bochanski, J. J. 2012, *ApJ*, 747, L38
- Vacca, W. D., Cushing, M. C., & Rayner, J. T. 2003, *PASP*, 115, 389

- West, A. A., Hawley, S. L., Walkowicz, L. M., Covey, K. R., Silvestri, N. M., Raymond, S. N., Harris, H. C., Munn, J. A., McGehee, P. M., Ivezić, Ž., & Brinkmann, J. 2004, AJ, 128, 426
- Williams, J. P. & Cieza, L. A. 2011, ARA&A, 49, 67
- Wolfgang, A. & Laughlin, G. 2012, ApJ, 750, 148
- Woolf, V. M., Lépine, S., & Wallerstein, G. 2009, PASP, 121, 117
- Zacharias, N., Finch, C., Girard, T., Hambly, N., Wycoff, G., Zacharias, M. I., Castillo, D., Corbin, T., DiVittorio, M., Dutta, S., Gaume, R., Gauss, S., Germain, M., Hall, D., Hartkopf, W., Hsu, D., Holdenried, E., Makarov, V., Martinez, M., Mason, B., Monet, D., Rafferty, T., Rhodes, A., Siemers, T., Smith, D., Tilleman, T., Urban, S., Wieder, G., Winter, L., & Young, A. 2010, AJ, 139, 2184

Chapter 6

Conclusions

6.1 Summary

The focus of this dissertation work was to better understand planets orbiting late-type (late K and M) dwarfs, including the development of new techniques to locate planets transiting nearby late-type stars, and calibrating techniques to constraining late K and M dwarf parameters. Measuring fundamental properties for these stars is exceptionally difficult, due to both their intrinsic faintness and the presence of complex molecular bands in their atmospheres. This is a particular problem for exoplanet work, as the parameters of any orbiting planet are linked to the parameters of the host star (e.g. transit depth $\propto R_P/R_*$). Thus our knowledge of the planet is often limited by our knowledge of the physical characteristics of the star it orbits, particularly for high-precision transit or Doppler measurements, (e.g. *Kepler* targets), where accurate stellar parameters prove to be even more critical. Further, making statistical statements such as planet occurrence rates and role of stellar metallicity and mass on planet formation requires an understanding of not just the stellar hosts, but the population of stars with no detected planet.

In most cases, models of FGK stars can be used to determine stellar parameters with the requisite accuracy to characterize their orbiting planets. However, M dwarf atmospheric and evolutionary models are based on incomplete line lists and do not match empirical data (Allard et al. 2011; Boyajian et al. 2012). Instead, this work focused on measuring M dwarf parameters (metallicity, T_{eff} , and radius) using purely empirical techniques.

A common trick to measure metallicities is to use wide binary systems containing an FGK primary and an M dwarf companion. Since the primary and companion are coeval, the primary star metallicity (determined through known techniques) is identical to that of the companion. As explained in Ch. 4, I built a sample of 110 FGK+M wide binary systems, which represent roughly a factor of 5 increase over previous work (Rojas-Ayala et al. 2012). For the FGK primaries without published metallicities, I used spectral synthesis on high-resolution spectra to derive the metallicity (Valenti & Piskunov 1996). For each of the M dwarfs, I obtained moderate resolution ($1300 < R < 2000$) near infrared and optical spectra. I then performed a systematic analysis of the companion spectra to determine what features in the M dwarf spectra are the best indicators of [Fe/H] and [M/H]. This work enables metallicity determinations using easily obtainable visible or near infrared spectra accurate to < 0.08 dex, and can be applied to existing catalogs such as West et al. (2011) and Lépine et al. (2013).

A large part of this program was to apply the metallicity calibration to *Kepler* targets. Although *Kepler* target star selection was heavily biased against M stars, *Kepler* planet candidates around late-type stars far outnumber those found through ground-based work, and thus are the most useful to ascertain statistical information about the planet population. Such science products as the planet occurrence rate, however, require an understanding of both the planet hosts and the stars around which no planet is detected.

Basic information about the *Kepler* target stars can be pulled from the *Kepler* Input Catalog (KIC, Brown et al. 2011), which is based on *grizHJK* photometry. Unfortunately, most KIC colors are insensitive (or weakly sensitive to) stellar surface gravity, particularly for the late-type stars. With this in mind, I began a program to characterize a subsample of the K and M stars currently being observed by *Kepler*. Using a combination of spectra and photometry, I showed that $96\% \pm 1\%$ of the bright ($K_P < 14$) *Kepler* target stars are actually giants, including $74 \pm 8\%$ of the bright, late-type stars characterized as dwarfs in the KIC ($\log g_{KIC} > 4.0$).

The presence of these previously misidentified giant stars skewed the results coming out of *Kepler*. Transits are more difficult to detect around giant stars, so this finding increases the calculated planet occurrence. My findings also had an effect on searching for a correlation between the presence (or properties of planets) and the metallicity of the host star. It is known that the frequency of giant planets is correlated to the metallicity of the host star. Using early *Kepler* results Schlaufman & Laughlin (2011) claimed that the $g - r$ and $J - H$ colors of *Kepler* targets implied a correlation between the occurrence of Earth-to Neptune-sized planets to the metallicity of their (K and M dwarf) host star. Late-type giant stars have bluer $g - r$ colors than dwarfs of the same $J - H$ color (much like metal-poor dwarfs have bluer colors than metal rich dwarfs). Since none of the planet candidates are orbiting giant stars, Schlaufman & Laughlin (2011) actually compared a set of (bluer) giant and dwarf stars to a set of pure dwarfs. Once the giants were correctly removed, any correlation between the metallicity and the frequency results vanished (see Ch. 3).

A more rigorous investigation of planet-metallicity correlations for *Kepler* late K and M dwarfs could be done using spectra. Thus I acquired spectra of a sample of 100 late-type *Kepler* target stars with no detected planet, but are confirmed to be dwarfs by their high proper motions. I combine this with a sample of 95 of the coolest *Kepler* planet hosts. A comparison of the metallicity of the sample shows *no significant correlation* between the presence of small planets and the metallicity of the late-type star, contrary to what is predicted by some theoretical arguments (Gonzalez et al. 2001). This suggests that planet formation must be very efficient in collecting material from the disk, since planets are forming in environments with a paucity of the solid materials utilized for building planets.

6.2 Future Outlook

One of the most interesting conclusions of my dissertation was the level of giant star contamination in the *Kepler* M star target list. The bigger issue is simply understanding systematics in the *Kepler* sample. What other erroneous results will researchers come to due to misunderstood or underestimated errors in the *Kepler* target list? It is unlikely that the F, G, and early K stars targeted by *Kepler* contain many giants (FGK giants are extraordinarily rare), however, the *Kepler* Input Catalog (KIC) might be plagued by other

systematic errors. Many of the FGK stars called dwarfs by the KIC may in fact be sub-giant stars (Gaidos & Mann 2013) and this has been shown with spectroscopy by Everett et al. (2013). Asteroseismology studies of *Kepler* objects also reveal systematic errors in the radius estimates in the KIC (Verner et al. 2011).

The paucity of reliable stellar parameters have spurred a large number of follow-up programs to better characterize the planet-hosts (*Kepler* objects of interest or KOIs) and identify (or rule out) false-positives. These studies are essential to find interesting systems, but largely ignore characterizing the non-host stars. However, to gather accurate statistical information on the population (e.g. planet occurrence, correlations between host star and planet properties) requires reliable stellar parameters for not just the KOIs, but *the entire target catalog*.

My next project will be to improve the utility of *Kepler* data by constructing a catalog of high quality spectra of *Kepler* target stars. In particular, I plan on using available multi-object moderate to high resolution spectrographs to collect spectra on a large and representative sample of *Kepler* targets. My own survey of the late-type target stars, Mann et al. (2012), is both evidence that such a project is necessary, and a proof of concept. Although there are others working on better characterizing the whole population, they are focused primarily on expanding and reanalyzing *photometry* in the KIC (Everett et al. 2012; Gaidos 2013), whereas my proposed catalog will gather much more useful spectroscopy. Given that planetary and stellar astronomers will likely be mining *Kepler* light curves for the next decade, I expect that such a catalog will be useful for a wide variety of purposes even after parallaxes from *GAIA* become available. Further, now that the *Kepler* mission is ending more attention will be paid to a careful study of the stellar parameters. Thus the full utility of such a catalog is not yet known, but I have designed this program with some specific, attainable science goals in mind.

Statistical study of spin-orbit alignment: Part of this project is to get a comparison sample of high-resolution spectra to see how the planet-host $v \sin(i)$ distribution compares to that of the parent population. The *Kepler* light curves can be used with spot models to determine the rotation period of the star, which combined with $v \sin(i)$ can yield the inclination of the stars rotation. Errors on this technique tend to be $> 20^\circ$ for an individual system (Gaidos et al. 2000), but by analyzing thousands of stars, one can perform a robust comparison between the inclinations of stellar planet hosts. One would expect these distributions to be very different, as the detection of a transit implies that the planet has an inclination near 90° , and presumably the planetary orbits should be similarly inclined to stellar rotation. However, this is not true for large, close-in planets (Winn et al. 2010), and different planet formation models make varying predictions on how $v \sin(i)_{\text{planet-hosts}}$ compares to $v \sin(i)_{\text{non-hosts}}$ (e.g. Bate et al. 2010).

Planet Occurrence: The planet occurrence (the number of planets per star) is (very roughly) the number of detected planets divided by the number of stars around which the given planet could have been detected (corrected for geometric probability and other statistical considerations). Programs to improve the parameters of *Kepler* host stars are trying to get a better handle on the numerator of this equation. My program is aimed at the better constraining the (largely neglected) denominator. Specifically my program will: a) lower the errors on radii of the target stars using high-resolution spectra of the Mg I line or moderate resolution spectra of a range of indices, b) identify tight binary systems where the

non-transiting star will dilute the transit signal, c) set limits on the fraction of sub-giants in the target star list, most of which are impossible to identify using available photometry (Brown et al. 2011). All of these issues change the planet occurrence calculation, although the largest source of error is the 35% errors in stellar radii from the KIC, as the stellar radius is one of the major factors in determining if a planet could be detected around a given star.

Understanding planet-metallicity correlations: It is well established that there exists a correlation between the occurrence of giant planets and the metallicity of the host star (Fischer & Valenti 2005). *Kepler* data can probe smaller planets (Earths and Neptunes), but measuring any correlation between the presence of small planets and the metallicity of the host star requires both metallicities for the planet hosts and for a much larger, representative sample of stars with no detected planet. A large sample is needed for a comparison because many stars have planets that do not transit. It may be that the *Kepler* target stars are metal-poor compared to the solar neighborhood. This could explain why *Kepler* has found roughly a factor of 2 less Jupiter-sized planets than what is predicted from radial velocity surveys (Wright et al. 2012; Howard et al. 2012).

Spectroscopic Binary Fraction: It has been suggested that planets which form in tight binaries will be significantly different from those that form around single stars (Kraus et al. 2012). Further, the chaotic environment of close binaries likely impedes or at least alters the planet formation process. This could be tested by determining the fraction of KOIs in binaries, and comparing it to the binary fraction in the field star population (which is not necessarily the same as for the solar neighborhood due to selection effects and differences in the stellar populations). Such a comparison would require accounting for the increased difficulty of finding planets around SBs because the second star will dilute the transit signal. *Kepler* light curves will find eclipsing binaries, but miss the majority of tight binary systems, and high-resolution follow-up of the KOIs tells us nothing about the field star population. High-resolution, multi-epoch observations of the field stars could provide a very accurate fraction of tight binaries.

Planet size distribution: Different theories and planet formation models predict disparate occurrence rates of Jupiter-, Neptune-, and Earth-sized planets (e.g. Mordasini et al. 2009). Existing *Kepler* data is insufficient to distinguish the three populations due to high errors in both planet hosts and target stars with no detected planets (Howard et al. 2012). By reducing the errors on the target star population one can correct for the intrinsic frequency of each planet type (i.e. recalculate the occurrence of each type of object with higher accuracy). I show a sample simulation in Figure 6.1.

This program requires a combination of low and moderate resolution spectra for a large ($> 20,000$) sample of *Kepler* target stars spanning a range of temperatures, masses, metallicities, and positions with respect to the galactic plane. (Note that the samples targeted for high-resolution and low-resolution spectra need not be the same, but some overlap is a good idea). Such a program sounds ambitious, but could be done relatively cheaply (especially considering the significant science gains) using the proper combination of multi-object spectrographs. Although this can be accomplished with a range of instruments, Hectospec and Hectochelle on the Multiple Mirror Telescope (MMT) are particularly useful for this project. Hectospec can collect moderate resolution spectra of up to 300 stars (simultaneously) within $\lesssim 1$ square degree at $R > 1000$. Following the techniques outlined

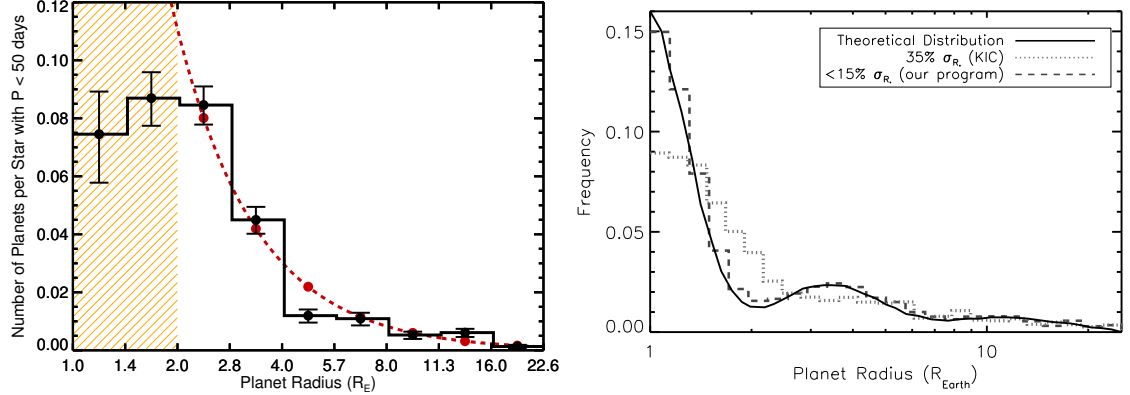


Figure 6.1: Left: distribution of observed planet candidates from *Kepler*. The red dashed line indicates the best fit, and the shaded region designates the range of planetary radii where the sample is thought to be incomplete (plot taken from Howard et al. 2012). Right: theoretical distribution of planetary radii as determined by Mordasini et al. (2009) (black). The same distribution as it would be seen by *Kepler* (without improvements in target star parameters) is shown as a dotted line (comparable to what is currently seen in *Kepler* data). The dashed bins are the observed distribution assuming 8% errors on KOI radii (*Kepler* follow-up) and < 15% errors on stellar radii for 20,000 non-KOI stars (this program). This assumes $\simeq 500$ more planet candidates will be found by *Kepler* over the course of the mission and that the proposed program can correct for any systematic errors in the KIC.

in Robinson et al. (2006), spectra similar to what Hectospec produces can be used to determine $\log g$ to 0.14 dex, [Fe/H] to 0.07 dex and T_{eff} to 82K (or better), and correct for any systematic errors in the overall sample due to degeneracies in fundamental parameters with just photometry.

Similarly, Hectochelle can be used to acquire up to 240 spectra at $R \simeq 34,000$ over a selected 150 Å range. Based on data from the SPOCS catalog, I find that by centering on gravity-sensitive Mg I b lines, one could measure $\log g$ to 0.09 dex and $v \sin(i)$ to < 10 km/s (there is very little metallicity information in this range, but T_{eff} can be constrained using the existing photometry and atmospheric models). The target list will include a sample of well characterized KOIs (with Keck HIRES data) and astroseismology targets to correct for any systematic biases from our analysis (since these will have independently determined stellar parameters). Despite the fact that the number of targets required is quite large, the *Kepler* field is just above galactic plane, and thus is sufficiently dense to use all 240-300 fibers. In fact, given the relatively small amount of telescope time compared to the extremely high science benefits, it is rather surprising that the *Kepler* team is not currently undertaking such a project themselves.

References

- Allard, F., Homeier, D., & Freytag, B. 2011, in Astronomical Society of the Pacific Conference Series, Vol. 448, 16th Cambridge Workshop on Cool Stars, Stellar Systems, and the Sun, ed. C. Johns-Krull, M. K. Browning, & A. A. West, 91
- Bate, M. R., Lodato, G., & Pringle, J. E. 2010, MNRAS, 401, 1505
- Boyajian, T. S., von Braun, K., van Belle, G., McAlister, H. A., ten Brummelaar, T. A., Kane, S. R., Muirhead, P. S., Jones, J., White, R., Schaefer, G., Ciardi, D., Henry, T., López-Morales, M., Ridgway, S., Gies, D., Jao, W.-C., Rojas-Ayala, B., Parks, J. R., Sturmann, L., Sturmann, J., Turner, N. H., Farrington, C., Goldfinger, P. J., & Berger, D. H. 2012, ApJ, 757, 112
- Brown, T. M., Latham, D. W., Everett, M. E., & Esquerdo, G. A. 2011, AJ, 142, 112
- Everett, M. E., Howell, S. B., & Kinemuchi, K. 2012, PASP, 124, 316
- Everett, M. E., Howell, S. B., Silva, D. R., & Szkody, P. 2013, ArXiv e-prints
- Fischer, D. A. & Valenti, J. 2005, ApJ, 622, 1102
- Gaidos, E. 2013, ArXiv e-prints
- Gaidos, E. & Mann, A. W. 2013, ApJ, 762, 41
- Gaidos, E. J., Henry, G. W., & Henry, S. M. 2000, AJ, 120, 1006
- Gonzalez, G., Brownlee, D., & Ward, P. 2001, Icarus, 152, 185
- Howard, A. W., Marcy, G. W., Bryson, S. T., Jenkins, J. M., Rowe, J. F., Batalha, N. M., Borucki, W. J., Koch, D. G., Dunham, E. W., Gautier, III, T. N., Van Cleve, J., Cochran, W. D., Latham, D. W., Lissauer, J. J., Torres, G., Brown, T. M., Gilliland, R. L., Buchhave, L. A., Caldwell, D. A., Christensen-Dalsgaard, J., Ciardi, D., Fressin, F., Haas, M. R., Howell, S. B., Kjeldsen, H., Seager, S., Rogers, L., Sasselov, D. D., Steffen, J. H., Basri, G. S., Charbonneau, D., Christiansen, J., Clarke, B., Dupree, A., Fabrycky, D. C., Fischer, D. A., Ford, E. B., Fortney, J. J., Tarter, J., Girouard, F. R., Holman, M. J., Johnson, J. A., Klaus, T. C., Machalek, P., Moorhead, A. V., Morehead, R. C., Ragozzine, D., Tenenbaum, P., Twicken, J. D., Quinn, S. N., Isaacson, H., Shporer, A., Lucas, P. W., Walkowicz, L. M., Welsh, W. F., Boss, A., Devore, E., Gould, A., Smith, J. C., Morris, R. L., Prsa, A., Morton, T. D., Still, M., Thompson, S. E., Mullally, F., Endl, M., & MacQueen, P. J. 2012, ApJS, 201, 15

- Kraus, A. L., Ireland, M. J., Hillenbrand, L. A., & Martinache, F. 2012, *ApJ*, 745, 19
- Lépine, S., Hilton, E. J., Mann, A. W., Wilde, M., Rojas-Ayala, B., Cruz, K. L., & Gaidos, E. 2013, *AJ*, 145, 102
- Mann, A. W., Gaidos, E., Lépine, S., & Hilton, E. J. 2012, *ApJ*, 753, 90
- Mordasini, C., Alibert, Y., Benz, W., & Naef, D. 2009, *A&A*, 501, 1161
- Robinson, S. E., Strader, J., Ammons, S. M., Laughlin, G., & Fischer, D. 2006, *ApJ*, 637, 1102
- Rojas-Ayala, B., Covey, K. R., Muirhead, P. S., & Lloyd, J. P. 2012, *ApJ*, 748, 93
- Schlaufman, K. C. & Laughlin, G. 2011, *ApJ*, 738, 177
- Valenti, J. A. & Piskunov, N. 1996, *A&AS*, 118, 595
- Verner, G. A., Chaplin, W. J., Basu, S., Brown, T. M., Hekker, S., Huber, D., Karoff, C., Mathur, S., Metcalfe, T. S., Mosser, B., Quirion, P.-O., Appourchaux, T., Bedding, T. R., Bruntt, H., Campante, T. L., Elsworth, Y., García, R. A., Handberg, R., Régulo, C., Roxburgh, I. W., Stello, D., Christensen-Dalsgaard, J., Gilliland, R. L., Kawaler, S. D., Kjeldsen, H., Allen, C., Clarke, B. D., & Girouard, F. R. 2011, *ApJ*, 738, L28
- West, A. A., Morgan, D. P., Bochanski, J. J., Andersen, J. M., Bell, K. J., Kowalski, A. F., Davenport, J. R. A., Hawley, S. L., Schmidt, S. J., Bernat, D., Hilton, E. J., Muirhead, P., Covey, K. R., Rojas-Ayala, B., Schlawin, E., Gooding, M., Schluns, K., Dhital, S., Pineda, J. S., & Jones, D. O. 2011, *AJ*, 141, 97
- Winn, J. N., Fabrycky, D., Albrecht, S., & Johnson, J. A. 2010, *ApJ*, 718, L145
- Wright, J. T., Marcy, G. W., Howard, A. W., Johnson, J. A., Morton, T. D., & Fischer, D. A. 2012, *ApJ*, 753, 160